Development of a geophysical and geochemical methodology for, the characterization of hydrocarbon contamination of soil and groundwater

Mohamad Abbas

Normandie Université

THÈSE

Pour obtenir le diplôme de doctorat

SCIENCES DE L'UNIVERS
Préparée au sein de « Université de Rouen Normandie »

Développement des méthodologies géophysique et géochimique pour la caractérisation d'un site contaminé par des hydrocarbures

Présentée et soutenue par
Mohamad ABBAS

Thèse soutenue publiquement le (21/12/17) devant le jury composé de		
M. / Rachid ABABOU	PR / Université de Toulouse	Rapporteur
M. / LE BORGNE Tanguy	PR / Université de Rennes 1	Rapporteur
Mme / Fabienne PETIT	PR / Université de Rouen Normandie	Examinateur
M. / Mohamed KRIMISSA	Doct Ingénieur / EDF R&D	Examinateur
Mme / Anne PANTET	PR/ Université du Havre	Examinateur
M. / Carsten LEVEN-PFISTER	Ass PR / Université de Tuebingen	Examinateur
M. / Abderrahim JARDANI	McF HDR / Université de Rouen Normandie	Directeur de thèse
M. / Jean-Paul DUPONT	PR / Université de Rouen Normandie	Codirecteur de thèse

Thèse dirigée par Abderrahim JARDANI (codirigée par Jean-Paul DUPONT), UMR 6143 M2C Morphodynamique Continentale et Côtière.

UNIVERSITÉ DE ROUEN NORMANDIE

EdNBISE
Ecole doctorale Normande
Biologie Intégrative,
Santé, Environnement

M2C

Development of a geophysical and geochemical methodology for the characterization of hydrocarbon contamination of soil and groundwater

By

Mohamad Abbas

A thesis submitted in partial fulfilment of the requirements for the award of

Doctor of Philosophy

Faculty of science

University of Rouen, France

December, 2017

Acknowledgments

First of all, I would like to kindly thank Dr. Abderrahim Jardani and Prof. Jean Paul Dupont for their valuable supervision throughout my PhD project. I would like to acknowledge Mr. Michele Simon for his help during the various laboratory experiments and field surveys. Special thanks for my cousin and childhood friend Eng. Ahmad Hammoud for his continuous support and encouragement, and for being beside during the good and hard times throughout my scientific career. I am heartily grateful to my parents, brothers and sister who believed in me and provided me with all means of support and motivation. I am sincerely thankful to my uncle Eng. Ibrahim Hammoud for giving me the opportunity to study abroad through his financial support during my Master's studies. I'm grateful to my friends in Germany, France and Lebanon, especially Dr. Ahmad Kaiss, Mr. Kassem Jouny and Dr. Ali El Hassan who provided continuous support throughout my studies. My thanks are due to my colleagues and professors at the University of Tuebingen who provided me with the needed background and skills to complete my PhD studies.

Finally, I would like to dedicate this achievement to my father Hani Abbas and my mother Sanaa Hammoud as a modest but not enough present in return for all their sacrifices and efforts that made me what I am now.

Résumé

La contamination par les hydrocarbures peut altérer les propriétés physicochimiques et biologiques du sous-sol, par conséquent le diagnostic et l'évolution des contaminants peuvent être surveillés en couplant les analyses géochimiques et les techniques géophysiques. Dans ce travail, différentes méthodes géophysiques de sub-surface telles que la tomographie de résistivité électrique, la polarisation induite, le géoradar et le potentiel spontané ont été utilisées d'une manière combinée pour localiser les zones impactées par les hydrocarbures du site de l'ancienne raffinerie de Petit Couronne. Les investigations géophysiques par la tomographie de résistivité électrique en 2D ont révélés la présence des anomalies de fortes valeurs de conductivité et chargeabilité électrique associés aux zones contaminées de l'aquifère. Les résultats obtenus avec les profils d'ERT et IP indiquent que la contamination a modifié les parties capacitives et ohmiques de la conduction électrique dans les sédiments contaminés. Cette signature très conductrice des zones contaminées est due aux processus de biodégradation des hydrocarbures qui minéralisent les eaux de l'aquifère. Les panaches d'hydrocarbures ont été identifiés sur les profils de géoradar par une forte atténuation des amplitudes de signaux électromagnétiques. Les profils de potentiel spontané ont aussi fourni une cartographie spatiale des zones contaminées par leurs signatures électriques négatives qui est associées aux processus d'oxydoréduction et biodégradation à l'interface entre la zone non saturée et saturée. Une carte de potentiel redox a été reconstruite à partir de l'inversion des données résiduelles de potentiel spontané grâce au calcul des composantes de la densité du courant électrique. La contribution redox dans l'aquifère contaminé s'explique par des dipôles verticaux répartis sur la frange capillaire juste au-dessus de la nappe phréatique, en favorisant le mécanisme de la biogéobatterie sur ce site. L'ensemble de ces résultats ont été confirmés par les mesures géochimiques menées au niveau des forages. L'étude a montré que les altérations biologiques des hydrocarbures ont modifié les propriétés chimiques de l'eau porale et que l'étendue de la contamination des eaux souterraines peut être délimitée à partir du contraste géophysique observé entre les zones contaminées et les zones non contaminées. La combinaison des différentes méthodes géophysiques avec des analyses géochimiques ponctuelles au niveau des forages ont permis de mieux comprendre les différents processus qui sont à l'origine de modifications des propriétés biogéochimiques dans les sols et les eaux souterraines.

Mots clés: hydrocarbures, biodégradation, résistivité électrique, potentiel spontané, géoradar.

Abstract

The presence of hydrocarbon contamination in the subsurface can modify the physiochemical and biological properties of soil and groundwater. The sensitivity of geophysical methods to biogeochemical changes occurring in contaminated media can be used to monitor hydrocarbon contamination in a fast and inexpensive way. As such, geophysical methods including, electrical resistivity tomography, induced polarization, ground penetrating radar, self-potential and magnetic susceptibility were used in this work to characterize the hydrocarbon contamination and investigate its effects on the soil and groundwater geophysical and geochemical properties at a site impacted by an aged hydrocarbon plume. The geophysical response to hydrocarbon contamination varies according to factors related to the contaminant in question and to the contaminated environment. Therefore, to achieve a better interpretation, the field geophysical data were constrained by geochemical soil boring data which showed that biodegradation is occurring in the site. This was shown through observing elevated total dissolved solids concentrations, elevated groundwater electrical conductivity values, negative redox potential values and depleted terminal electron acceptors concentrations in the contaminated locations. Throughout the investigation, the geophysical measurements supported the conductive model and consistently recorded low resistivity anomalies, high chargeability values and attenuated GPR reflections in the contaminated zones. Additionally, significant negative self-potential anomalies associated with oxidation-reduction processes coupled to the biodegradation of hydrocarbons were recorded in the groundwater contaminated zone. Based on this observation, a redox potential map of the contaminated site was constructed by the inversion of the field self potential data. Throughout the process, a groundwater model was first calibrated to remove the electrokinetic component from the SP signal. Then, the obtained residual self potential data was inverted for the electrical current density by using an inversion algorithm which includes minimizing a cost function with a data misfit contribution and a regularizer. As a result, the obtained current density was used to construct a map of redox potential showing the borders and the redox front of the contaminant plume. The redox contribution was explained by vertical dipoles distributed across the capillary fringe, supporting further the mechanism of bio-geo-battery which was created due to the existence of a strong redox potential gradient between the highly reducing conditions within the plume and the oxidizing conditions outside the plume. Furthermore, elevated magnetic susceptibility values were recorded in the biologically active transition zone where bio-precipitation of iron minerals is occurring. Given these results, this study showed that biological alterations of hydrocarbons induced subtle changes in the pore water biogeochemistry, which consequently modified the geophysical properties of the contaminated sediments. The extent of groundwater contamination was delineated according to the geophysical contrast between the contaminated and clean zones. Moreover, the combination of the different geophysical methods, constrained by the geochemical point measurements, provided insight on the different processes which might have modified the soil and groundwater biogeochemical properties at the contaminated site.

Key words: Hydrocarbons, biodegradation, electrical resistivity, ground penetrating radar, self-potential.

Table of contents

List of Figures

Chapter 1

Introduction

1.1. Problem and methods

Land contamination in industrialized countries is a major concern for the governmental and environmental authorities that are monitoring and remediating contaminated lands, as it is considered as a major risk for the general public inhabiting these lands. In France, almost 1600 sites have been contaminated due to a wide variety of industrial activities including those dealing with the processing of hydrocarbon's products (Donnes Basol et Basias). Contamination from hydrocarbon products such as gasoline, diesel and heavy oils is a major current environmental issue of great concern in France. The contamination may occur through spills which may result of blowouts, equipment failure, operator's errors, corrosion, sabotage, pigging operations, tank rehabilitation, heavy rainfall, flooding and others. These events may occur during the industrial activities or after the facilities closure, where their waste products and remaining residues can present a major hazard for the environment. The spilled hydrocarbon products percolate the subsurface and the underlying strata, and as a result, both the soil and groundwater may be negatively affected as the hydrocarbon substances mix with them.

The polluted sites constitute a source of major risk on the human health because some pollutants are carcinogens and can be inhaled or ingested. Therefore, proper waste management and monitoring techniques have to be developed to anticipate undesirable impacts on the contaminated environment. The rehabilitation or remediation of contaminated sites is crucial since it will help restore the quality of the contaminated environment in order to make it usable again by its inhabitants. Thereby, the French governmental laws require the establishment of a remediation procedure of polluted sites according to published official notices (e.g., Notice of the 8th of February 2007). Generally, such procedure includes, determining the locations of pollution sources, quantifying the pollution, identifying the risk of the contaminant transport and remediating the site in later stages.

The characterization of hydrocarbon contamination is classically done through chemical and biological analysis of soil and groundwater samples recovered from boreholes. However, these invasive techniques are expensive, time-consuming and provide data with limited spatial and temporal resolution. This encouraged the development of cost-effective and fast complementary methods which can be used for investigating contaminated lands. As such, geophysical techniques hold a great promise as inexpensive and non-invasive tools which can be used in hydrocarbon contamination studies (Atekwana et al., 2000; Atekwana and Atekwana, 2010; Naudet et al., 2004; Sauck, 2000; Sogade et al., 2006).

By using geophysical techniques, it is possible to gather large scale data that cannot be provided by other conventional methods. Geophysical methods are a set of indirect methods which can provide information on the spatial distribution of the subsurface physical parameters (e.g., electrical conductivity, permittivity, magnetic susceptibility, etc.) that can be modified due to the presence of contaminants. For example, the hydrocarbon contaminated zone can be electrically different from the surrounding media and can produce significant anomalies in geoelectrical

measurements (Atekwana and Atekwana, 2010). However, the geophysical methods are not directly related to chemical parameters such as the contaminant distribution or nature, and thus can't be used as stand-alone methods. To achieve a better interpretation, the geophysical data should be constrained by classical sampling geochemical investigations to relate the geophysical response to the subsurface chemical, biological and physical conditions.

Tomographic geophysical methods came up in the early 1980s after the development of proper instrumental devices, computing facilities and inversion algorithms (Loke, 1991). This allowed geophysicists to perform 1D, 2-D and 3-D surveys with reasonable computation time and costs. The possibility to get large-scale information and the further development of cross-hole methods demonstrated the geophysical methods as promising techniques which can be used for different environmental applications. In the past decades, the development of geophysical techniques for the study of hydrocarbon contamination was particularly done on the geoelectrical and electromagnetic methods. These methods have the advantage of being able to measure several parameters which are sensitive to the presence of the contaminant and its alterations of the host environment. These techniques which include, induced polarization (IP), ground penetrating radar (GPR), electrical resistivity tomography (ERT) and self-potential (SP) have been successfully used in hydrogeophysical studies to map contaminants plumes in the vadose and saturated zones (Cassiani et al., 2006 ; Daily et al., 1992; Daily et al., 1995; Ramirez et al., 1993), to monitor the evolution of contaminant plumes during the remediation process (Benson et al., 1997; Bermejo et al., 1997; Daniels et al., 1992; Maxwell and Schmok, 1995; Vanhala, 1997) and to highlight the impact of hydrocarbon contamination and its associated biodegradation processes on the soil and groundwater chemical and biological properties (Atekwana et al., 2000, Atekwana et al., 2005; Naudet et al, 2004; Sauck et al., 1998).

However, the application of geophysical techniques at hydrocarbon contaminated sites over the last two decades has yielded dramatically variable results. This is due to the fact that geophysical attributes are affected by factors related to the contaminant itself and by factors related to the contaminated environment such as the thickness and depth of the impacted zone, the dynamic field conditions and the extent of the bacterial activity (Atekwana et al., 2000). Shortly after a contamination event, fresh oil spills are suggested to increase the bulk electrical resistivity of contaminated media as explained by the insulating layer model (Mazac et al., 1990; DeRyck et al., 1993). On the other hand, after few years, the contamination is referred to as an aged contamination and is considered to be associated with a decrease in the bulk electrical resistivity due to biodegradation processes, as demonstrated by the conductive layer model (Atekwana et al., 2000; Sauck et al., 1998). Moreover, as the biodegradation of hydrocarbons is associated with redox reactions (e.g., iron reduction), the electron transfer between the reduced and oxidized zones can generate a natural electrical current which can be detected by the SP method (Tim and Möller, 2001; Naudet et al., 2003, 2004; Naudet and Revil, 2005; Revil et al., 2010). The reduction of iron may also induce changes in the magnetic iron mineral content of contaminated sediments, which

can display distinct magnetic susceptibility signatures (Kappler and Straub, 2005; Lovley and Anderson, 2000; Weber et al., 2006).

Geophysical methods can also be implemented at the laboratory scale to investigate the influence of the different biological and chemical mechanisms on the different geophysical signatures. Laboratory geoelectrical measurements were able to detect and differentiate between different types of hydrocarbons (e.g., Revil et al., 2011) and to highlight the influence of the subsurface biogeochemical processes on the geophysical signals (e.g., Abdel Aal et al., 2004). The joint interpretation of geophysical methods has been used in a variety of land contamination studies and successfully reduced the ambiguity of geophysical interpretations by detecting well recognizable geophysical anomalies associated with contaminant plumes (e.g., Atekwana et al., 2000; Benson and Stubben, 1995; Grumman and Daniels, 1995; Mazác et al., 1990).

1.2. Study objective

The main objective of this thesis is to characterize a hydrocarbon contaminated site through performing large-scale geophysical investigations, constrained by laboratory and field geochemical measurements. We aim to define the geophysical response to hydrocarbon contamination under the site geological and biological conditions and to develop a geophysical methodology which can describe the contamination extent and adverse its effects on the soil and groundwater chemical, physical and biological properties. The study also aims to find a good combination of fast and low-cost methods that can be used to follow the remediation process which is planned to proceed in 2018. Throughout this study, large-scale geophysical data were correlated with geochemical point measurements collected from a number of boreholes installed on the site.

This aims to establish a reasonable relationship between geophysical methods such as ERT, GPR, IP, SP and MS and geochemical parameters (e.g., hydrocarbon content, total dissolved solids, redox potential, groundwater electrical conductivity, concentration of dissolved oxygen, etc.) that can be modified due to the presence of hydrocarbon contaminants. This relationship will be used in later stages to follow the efficiency of the remediation process and the temporal evolution of the contaminant plume in a fast and cost-effective way by using time-lapse geophysical surveys. The study is expected to contribute to the body of literature by providing case studies that show the geophysical responses to hydrocarbon contamination under our site conditions, as it is the first study where the 5 methods were combined on the same profile lines and under the same conditions.

1.3. Thesis Structure

In this chapter, we present a bibliographic study which describes the hydrocarbon contamination in terms of its physiochemical properties, its partitioning behavior, its impact on the soil and groundwater chemical and biological properties and its impact on the different

geophysical signals. The presence of hydrocarbons as a carbon source for microorganisms can induce biological and chemical processes that can modify the hydrocarbons properties and impact the host environment in many different ways. The way by which the contaminants can impact the subsurface depends on factors such as the time of residence and the oil spill history. Therefore, it is important to highlight the impact of the contamination on the short-term (recent contamination) and on the long term, where biological processes (e.g., bacterial degradation) are occurring. This chapter presents previous laboratory and field studies that attempted to characterize contaminated lands by using different geophysical methods. It also presents studies that explained the influence of the different biological and chemical processes associated with hydrocarbon contamination on the different geophysical signals. The second chapter describes the study site in terms of history, geology, location, pollution sources and type of contaminants. The second chapter also describes a geochemical study which was done by using the site boreholes and presents maps of geochemical parameters which describe the chemical and biological conditions of soil and groundwater. The third chapter outlines the different geophysical methods used in the framework of this thesis by explaining the origins of the measured signals and the principles and implementations of the different techniques. The fourth chapter presents a study where data acquired from geophysical methods including, SP, IP, ERT and GPR were interpreted jointly and constrained by maps of geochemical parameters (paper 1). This chapter aims to define the geophysical response to hydrocarbon contamination and delineate its borders according to the geophysical contrast between the contaminated and clean zones. This chapter also aims to assess the impact of the pollution and its consequent biodegradation processes on the soil and groundwater biological and chemical properties. Chapter 5 shows a field and a numerical modeling study which aims to map the distribution of the groundwater redox potential from the inversion of SP field data (paper 2). Chapter 6 presents a study showing the variation of magnetic susceptibility (MS) signatures of contaminated sediments with respect to the sampling depth and contaminant distribution. Chapter 7 shows an application of the GPR method which aims to map underground utilities (pipes, concrete slabs, etc.) to help planning the installation of new boreholes. Finally, chapter 8 outlines the conclusion of this work and the future plan and prospective.

1.4. Hydrocarbons: nature and partitioning behavior

The hydrocarbons are organic molecules composed of a number of carbon atoms (C) associated with one or more hydrogen atom (H). The general formula of a hydrocarbon compound is C_aH_b, where ‘a’ is the number of C molecules and b is the number of H molecules. Petroleum hydrocarbons represent 65% to 95 % of crude oil fractions and are classified into 4 main classes: saturated hydrocarbons, aromatic hydrocarbons, resins hydrocarbons (e.g., carbazoles, sulfoxides, amides, etc.) and asphaltenes (e.g., phenols, fatty acids, ketones, esters, etc.). Saturated and aromatic hydrocarbons, which are considered as potential pollution threats, constitute a big fraction of the refined oil products that are commonly used in the industry. For example, gasoline which is used as fuel for engines combustion is essentially formed of alkanes and aromatic BTEX

hydrocarbons (Benzene, Toluene, Ethylbenzene and Xylenes). The BTEX products consist of a single benzene ring, have low solubility in water and exhibit a density of less than 1 g/mL.

The distribution of hydrocarbons in the subsurface depends on the product density. Hydrocarbons with a density of less than 1 mg/L such as BTEX are referred to as Light Non-Aqueous Phase Liquids (LNAPL), whereas those of a density greater than 1 mg/L are known as Dense Non-Aqueous Phase Liquids (DNAPL). The near subsurface is a porous medium which contains different phases according to the constituents of its pore spaces. The water table separates the saturated zone from the non-saturated (vadose) zone. The interface between these two zones contains the capillary fringe and the transition zone. The oil products partition in the subsurface in 4 different phases: free phase, residual phase, dissolved phase and vapor phase (Sau Atekwana, 2010) (Figure 1.1).

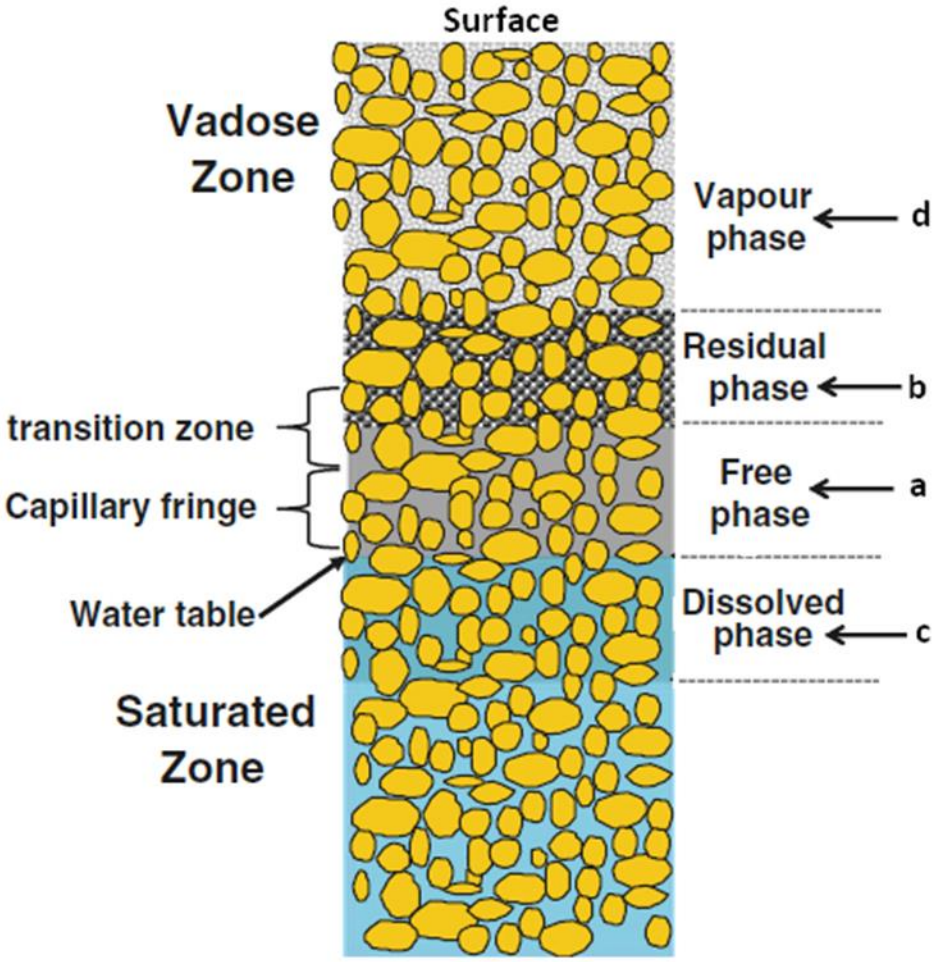

Figure 1.1: Schematic of the distribution of the different contamination (LNAPL) phases in the subsurface (Atekwana and Atekwana, 2010).

Figure 1.2 shows the different possible scenarios of the LNAPL and DNAPL partitioning into the different phases after the occurrence of oil spills:

a. Free phase: as the percolating LNAPL reaches the interface between the vadose and saturated zones, it floats on the water table due to its lower density compared to water and forms the so-called free phase. The hydrocarbons partially replace the water and air in the capillary fringe and transition zones with a hydrocarbon saturation of approximately 50% (Sauck, 2000). The free phase can extend to a large distance in the lateral direction and can have a thickness ranging from few centimeters to several meters, depending on the size of the spill and on the permeability of the aquifer material.

b. Residual phase: this phase consists of the spill part which didn't drain by gravity and residually saturated the pore spaces while the spill was traversing the vadose zone down to the water table. Therefore, the residual phase is limited to the spill source zone but it may be present at locations far from the source zone where the extended free phase can rise up due to tidal fluctuations of the water table. The groundwater table fluctuations due to seasonal recharge or the presence of an open water body close to the aquifer move the residual and the free phases up and down in accordance with the water level movement. As a result, part of the free phase will be trapped in the residual zone as the water level rises up, and part of it will be trapped in the upper portion of the saturated zone as the water level drops down. This pattern of trapped hydrocarbons is referred to as the smear zone (Sauck, 2000; Lee et al., 2001).

c. Dissolved phase: this phase is located in the saturated zone and is determined by the solubility of the hydrocarbons fractions. The soluble fractions at the source area can form a plume of dissolved hydrocarbons with decreasing concentrations as the dissolved plume moves away from the source zone (Atekwana and Atekwana, 2010). The advective transport process that develops due to the hydraulic gradient spreads the dissolved plume from the source zone in the groundwater flow direction. Generally, the LNAPL fractions have very low solubility values and therefore the concentration of hydrocarbons in the dissolved phase will be much lower than that of the free phase.

d. Vapor phase: this phase is located in the upper part of the vadose zone and just above the residual phase. This phase is loaded with vapors of the volatile fractions of hydrocarbons.

The four phases are generally present together only in the source zone where the spill initially occurred. As we move further in the lateral direction from the source zone, the contamination extends as a dissolved phase plume. In the case of a DNAPL spill, the hydrocarbons percolate through the vadose and saturated zones. The spill reaches the underlying aquitard, where the free phase follows the aquitard topography. The DNAPL non-soluble fractions will be trapped in basins hydraulically disconnected from each other, while the soluble fractions will form a plume in the groundwater flow direction (Figure 1.2). Previous studies such as Pinder and Gray (2008) described the physical mechanisms and the associated equations of the LNAPL and DNAPL spills transport and partitioning in the saturated and non-saturated zones (For example, see section "5.3.1" of Pinder and Gray (2008) which depicts a numerical example of the partitioning of a DNAPL spill into a water-saturated porous reservoir).

.

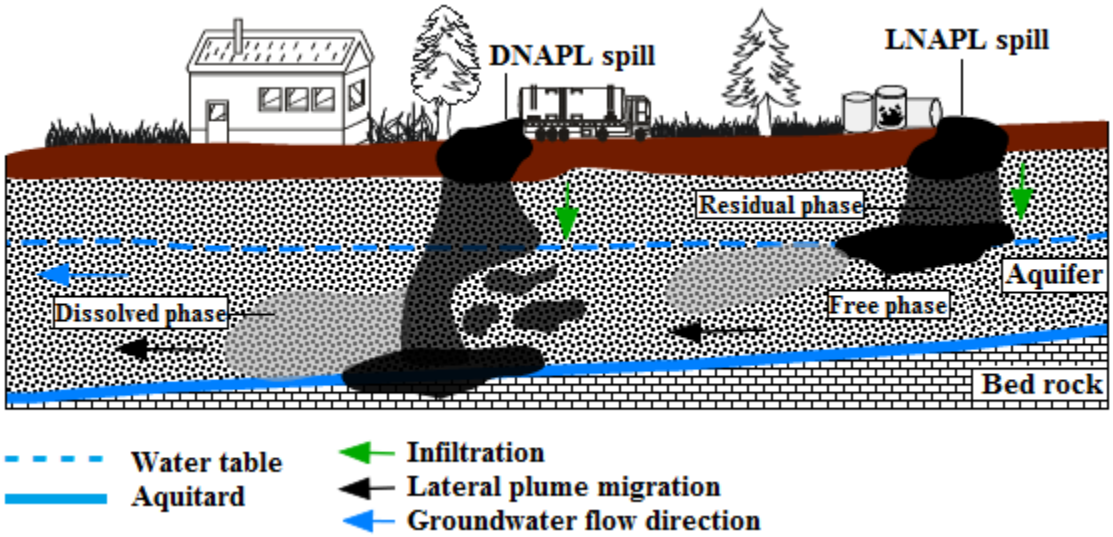

Figure 1.2: Schematic of the partitioning of LNAPL and DNAPL into dissolved, free and residual phases after the occurrence of oil spills.

1.5. Bacterial Biodegradation of Hydrocarbons

Microbial biodegradation of petroleum hydrocarbons is a natural mechanism by which hydrocarbon pollutants are cleaned up from the environment by the gradual breaking down of the organic compound chemical structure through several chemical and biological mechanisms (Das and Chandran, 2011). Hydrocarbons can be primarily biodegraded by microorganisms such as bacteria, yeast and fungi. However, bacteria are considered to be the most active degraders of oil spills in polluted environments (Rahman et al., 2003). Previous studies isolated many bacterial genera (e.g., *Acinetobacter sp., Arthrobacter, Burkholderia, Gordonia, Brevibacterium, Aeromicrobium, Dietzia, Burkholderia, Mycobacterium, Pseudomonas, Sphingomonas, Rhodococcus, etc.)* that proved to be capable of degrading hydrocarbons in soil systems (e.g., Throne-Holst et al., 2007; Chaillan et al., 2004; Daugulis and McCracken, 2003; Floodgate, 1984).

Bacterial biodegradation of hydrocarbons can occur under aerobic and anaerobic conditions, where the aerobic degradation is the dominant and most rapid process if sufficient amount of oxygen is available. The aerobic degradation pathway involves an oxidative intracellular attack catalyzed by enzymes such as oxygenase and peroxidase (Fritsche and Hofrichter, 2000). The pollutant is converted into metabolic intermediates by a step by step peripheral degradation process (Figure 1.3). This process leads to the formation of cell biomass and production of by-products such as CO_2 and H_2O.

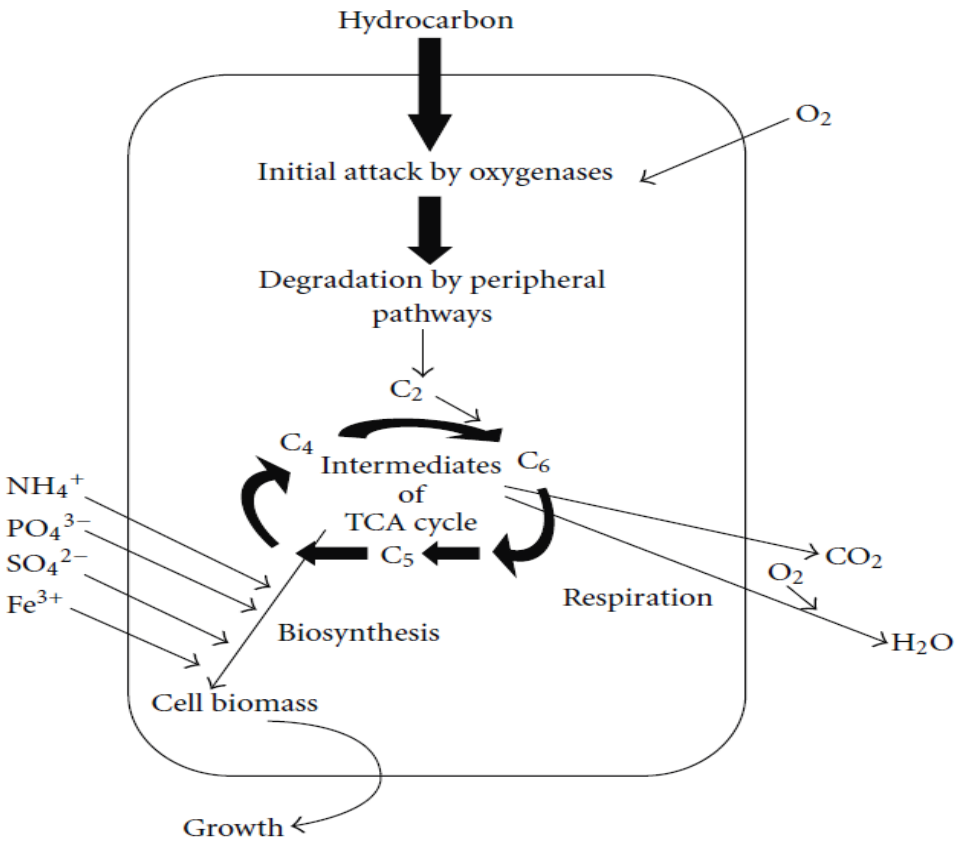

Figure 1.3: Aerobic biodegradation main principles (Fritsche and Hofrichter, 2000; Das and Chandran, 2011).

1.5.1. Controlling Factors

Different factors that can influence and limit the hydrocarbon biodegradation process have been recognized and reported (e.g., Cooney et al., 1985; Brusseau, 1998). The presence of microorganisms capable of degrading hydrocarbons is the main requirement, and the limiting factors are mainly those which sustain bacterial optimal growth rates and efficient metabolic activity.

Availability

Petroleum hydrocarbons availability to microorganisms is an important limiting factor because hydrocarbons bind to soil grains and are difficult to remove. The availability of hydrocarbons to microorganisms is defined as their susceptibility to microbial attacks (Barathi and Vasudevan, 2001). Linear alkanes and small aromatics are generally known to have higher susceptibility than heavy molecular weight compounds. For example, polycyclic aromatic hydrocarbons are heavy and hard to be degraded (Perry, 1984; Atlas and Bragg, 2009; Ulrici, 2000).

Temperature

The temperature is considered as an important factor because it directly affects the pollutants physical properties, as well as the diversity and activity of microorganisms (Venosa and Zhu, 2003). Low temperatures can decrease the solubility of hydrocarbons, increase the oil viscosity and reduce the volatility of low molecular weight compounds. These conditions can reduce the bioavailability and delay the biodegradation process. Additionally, very high temperatures can decrease the oxygen solubility which may reduce the metabolic activity of aerobic microorganisms. Previous studies reported that the biodegradation rate decreases with decreasing temperature and recorded the highest degradation rates in soil systems at temperatures ranging from 30 to 40℃ (Bartha and Bossert, 1984; Cooney, 1984).

Nutrients and electron acceptors

The successful growth and cellular metabolism require the presence of mineral nutrients such as nitrogen, phosphate and iron, despite the presence of degradable carbon source (Cooney, 1984). The availability of nitrogen and phosphorus was reported to be a limiting factor for oil degradation in contaminated environments (Atlas, 1985). In previous studies, the addition of nutrients in nutrient deficient environments was necessary to enhance the cellular metabolic processes and accelerate the biodegradation of oil pollutants (Mitsch et al., 1993; Choi et al., 2002; Kim et al., 2005). As the carbon source presents an electron donor during the redox reactions coupled to the biodegradation process, the oxidation of organic carbon requires the presence of terminal electron acceptors (TEAs) such as O_2, NO_3^-, SO_4^{2-}, Fe (III), Mn (IV) and CO_2. The availability of electron acceptors is considered as an important limiting factor for aerobic and anaerobic biodegradation processes which are associated with the sequential utilization of TEAs (Das and Chandran, 2011).

1.5.2. Impact on the subsurface chemical and biological conditions

Over long periods of time, the hydrocarbon contamination can be subjected to physical, chemical and biological alterations that can impact the host environment in many different ways (Sauck et al., 1998). The growth and proliferation of bacterial populations, their metabolic processes and their attachment to mineral surfaces can have a profound effect on the aquifer and soil chemical and physical properties (Bennet et al., 1996). A review done by Atekwana and Atekwana (2010) presented a conceptual model showing the implications of the presence of bacterial populations and their corresponding metabolic processes on the physiochemical and biological properties of the contaminated subsurface (Figure 1.4). The presence of excess organic carbon as a carbon source enhances the bacterial growth and metabolism, which leads to an increase in the bacterial populations and to the production of biofilms that accumulate on mineral surfaces (Bekkins et al., 1999).

Biofilms are a group of microbial cells embedded together in an extracellular polymeric matrix which determines its physiochemical properties. In oil contaminated environments, continuous biofilms may form on the water table where the oxygen and nutrients are most available

(Revil et al., 2010). This enhanced number of bacterial cells coating the mineral surfaces can lead to the clogging of pore spaces and to a consequent decrease in both the permeability and the porosity (Abdel Aal et al., 2010).

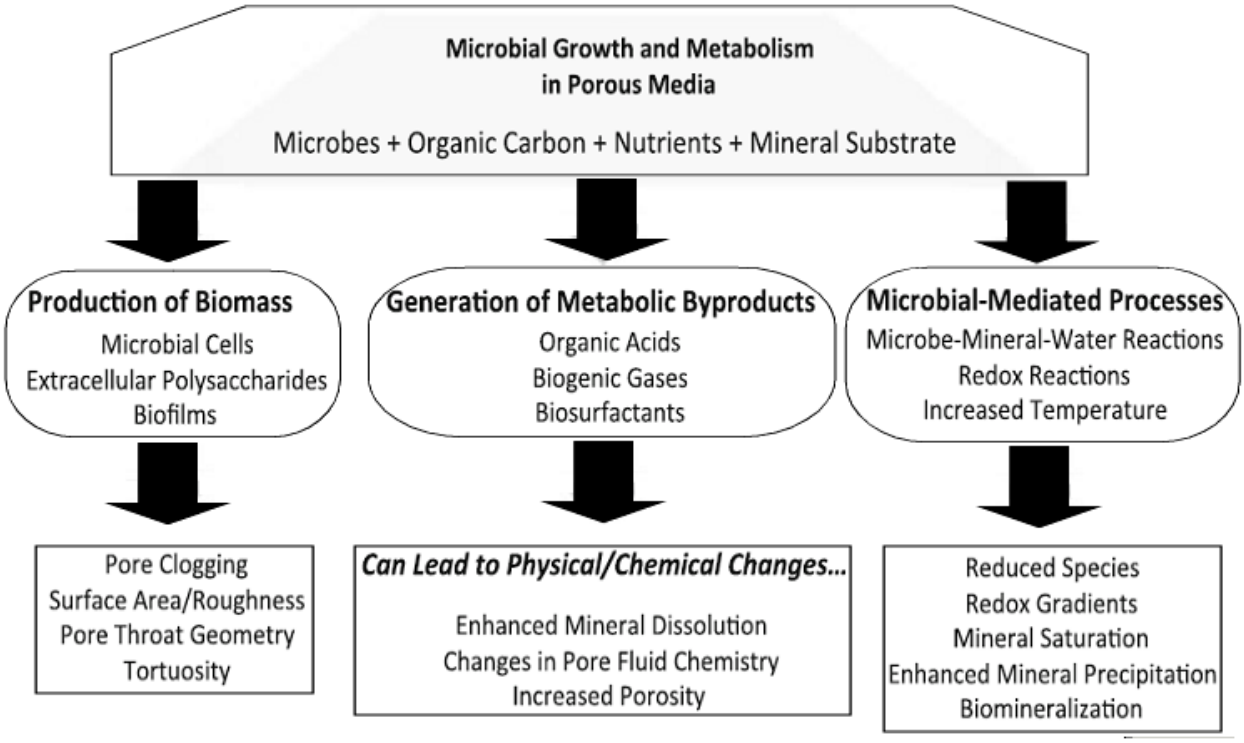

Figure 1.4: Conceptual diagram showing the physiochemical impact of microbial growth and activity in porous media (modified after Atekwana and Atekwana, 2010).

Bacteria derive their energy through oxidizing organic carbon for their growth and reducing TEAs for their respiration (Huling et al., 2002). The reduction of TEAs such as nitrate (most energetically preferred), manganese, iron, sulfate and carbon dioxide (less energetically preferred) are referred to as terminal electron acceptor processes (TEAPS) (Vroblesky and Chapelle, 1994). Oxygen is the electron acceptor for aerobic metabolism, but the low concentration of dissolved oxygen in the aquifer is rapidly consumed by bacterial respiration in the upgradient close to the contamination source, converting this area to anaerobic. Since re-oxygenation by oxygen diffusion from the atmosphere is relatively slow, anaerobic bacteria utilize other TEAs to oxidize the organic matter. Hydrocarbon biodegradation by anaerobic bacteria follows a sequential utilization of electron acceptors, where the most energetically preferred reaction proceeds in the plume until all the required electron acceptors are depleted (Semple et al., 2007; Tiehm and Schulze, 2003). Then, the next most preferred reaction proceeds until its required electron acceptors are depleted. Therefore, if the biodegradation has been occurring for some time, it is expected to get data with very low concentrations (zero sometimes) for the most energetic electron acceptors (e.g., oxygen, nitrate and sulfate). In this sense, the depletion of electron acceptors was used as an indication of

intrinsic bioremediation by a study done at a contaminated site near Rocky Point, North Carolina (Borden, 1994).

The sequential utilization of electron acceptors will create a zonation pattern of TEAPS. In cases where the aquifer has an old contamination, it is expected that methanogenesis (less energetically preferred) is the predominant TEAP at the upgradient in the core of the plume. This is because the alternative potential electron acceptors have been already depleted. However, the zonation depends on the availability of TEAs and on the competition of microorganisms for these TEAs. For example, Fe^{3+} is considered to provide the greatest accepting potential capacity and to be the most abundant electron acceptor in shallow aquifers. The presence of Fe^{3+} can exclude methanogenesis because iron reducers can outcompete the methanogenic community for the organic carbon. As a result, the reduction of Fe^{3+} will be the predominant TEAP in the core of the plume. The consumption of electron acceptors through microbial respiration in the vicinity of the plume causes a change in the redox chemistry of pore fluids. Baedeker et al. (1993) showed that the plume is more reducing than the surrounding media. Therefore, the area within the plume is anoxic and reducing, while the area outside the plume is oxic and oxidizing.

The reduction of electron acceptors by the TEAPs leads to the production of reduced redox species (e.g., Mg^{2+}, Fe^{2+}, etc.) and metabolic by-products such as organic acids, carbonic acids, biogenic gases and biosurfactants. An example would be the reaction of CO_2 (reduced from the electron acceptors) with water which produces carbonic acids (Soltani et al., 2004). Organic acids such as benzoic, dimethylcyclohexanoic, cyclohexanoic, mythelbenzoic and toluic acids were identified in an aquifer impacted by a crude oil spill near Bemidji, Minnesota (Baedecker et al., 1987). Organic and carbonic acids cause etching and dissolution of minerals surfaces and reduce the pH of the contaminated medium, which leads to leaching of soluble salts present at the grains coatings (McMahon et al., 1995). These weathering and dissolution processes lead to the accumulation of ions in the pores fluids. The production of ions through minerals dissolution, in addition to the production of reduced redox species, may lead to a significant increase in the concentrations of total dissolved solids (TDS) (Atekwana et al., 2004b).

McMahon et al. (1995) observed enhanced concentrations of ions such as calcium, magnesium and iron which are one to two times higher than background values at a site impacted by an oil plume in Hanahan, South Carolina. The dissolution patterns of the quartz and orthoclase grains were evident in SEM images of soil samples taken from the same site. Several previous studies reported enhanced Ca^{2+} concentrations and a leachate plume of enhanced TDS concentrations below LNAPL impacted zones (e.g., Atekwana 2004a; Sauck, 2000). The authors attributed this increase to the minerals dissolution processes during bacterial biodegradation of hydrocarbons. Moreover, the production of cationic and anionic biosurfactants and organic acids increases the electrolyte concentration of pore fluids by directly adding ions into solution (Cassidy et al., 2001; Davis and Atekwana, 2006). The enhanced mineral dissolution can also impact the

grain surface physical properties by increasing the porosity and the permeability (McMahon and Chapelle, 1991).

The Reduction of TEAs such as iron and sulfate by iron and sulfate-reducing bacteria can result in the precipitation of different mineral phases (Fredrickson et al., 1998; Hansel et al., 2003). The ferrous ion produced during the reduction of iron can result in the precipitation of secondary minerals such as siderite, magnetite and goethite. Iron sulfide minerals can be also precipitated through the reaction of the ferrous ion with the sulfide produced by sulfate-reducing bacteria. In this sense, previous studies linked the biological precipitation of iron minerals (e.g., siderite, pyrite and amorphous iron sulfide) in hydrocarbon contaminated groundwater to the bacterial reduction of iron and sulfate (Cozarelli et al., 1999; Prommer et al., 1999).

1.6. Previous investigations: impact on the geophysical signals

1.6.1. Fresh Hydrocarbons

At the initial stage of contamination, fresh spills were suggested to impact the subsurface only by the physical replacement of water in the saturated zone and air in the vadose zone by hydrocarbons. At this stage, chemical and biological alterations of hydrocarbons are negligible and the controlling factor is the contrast in physical properties between the hydrocarbons and the surrounding media. Petroleum hydrocarbons are characterized by an electrical conductivity of approximately 0.001 mS/m and a relative permittivity of approximately 2 to 3. On the other hand, clean water has an electrical conductivity of approximately 0.1 to 1 mS/S and a relative permittivity of around 80 (Atekwana and Atekwana, 2010). Therefore the partial replacement of water by oil can decrease the electrical conductivity and the relative permittivity of contaminated sediments. These assumptions gave the basis of the insulating layer model which assumed that contaminated sediments would exhibit a higher resistivity and a lower relative permittivity than the surrounding clean media. This model received wide support from field studies and laboratory experiments which reported enhanced GPR reflections and high apparent resistivity anomalies associated with contaminated groundwater and soils (Benson, 1995; Benson et al., 1997; Campbell et al., 1996; Olhoeft, 1992; DeRyck et al., 1993; Schneider and Greenhouse, 1992; Schneider et al., 1993; Endres and Greenhouse, 1996).

DeRyck et al. (1993) used electrical resistivity probes to follow the change of electrical resistivity with respect to water saturation after the injection of kerosene into a polyethylene tank filled with sand. The study showed a decrease of water saturation due to the replacement of water by kerosene. The accumulation of kerosene which replaced water at the capillary fringe (between 70 and 110 cm) was shown to be associated with a large increase (from 200 to around 700 ohm.m) in the electrical resistivity with increased pooling of kerosene (Figure 1.5).

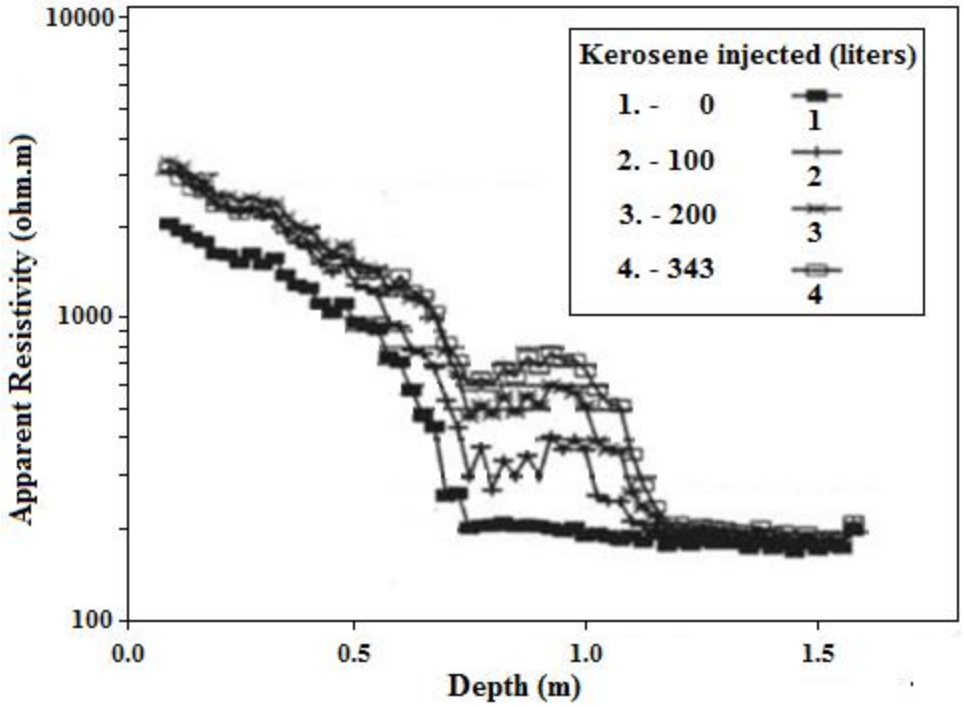

Figure 1.5: Plot of the bulk electrical resistivity relative to depth obtained from a controlled kerosene spill experiment. A high resistivity layer was obtained between 70 and 110 cm and was attributed to kerosene accumulation in the capillary fringe (modified after DeRyck et al., 1993).

Similarly, field studies reported high electrical resistivity anomalies associated with areas of known hydrocarbon plumes (Benson et al., 1997; Osella et al., 2002). In a controlled fresh spill experiment, Campbell et al. (1996) observed an increase in amplitude (brightness) of GPR reflections associated with increased pooling of gasoline. The study attributed this response to the replacement of the high relative permittivity water by the lower relative permittivity hydrocarbons. This produced a high velocity GPR layer which was responsible for the bright reflections (Figure 1.6). Similarly, a study done by Lopes de Castro and Branco (2003) over a fresh gasoline spill in Fortaleza (Brazil) reported enhanced GPR reflections in the contamination residual, free and dissolved phases. Enhanced GPR reflections were also reported at hydrocarbon contaminated sites by studies such as Benson (1995) and Benson and Mutsoe (1996).

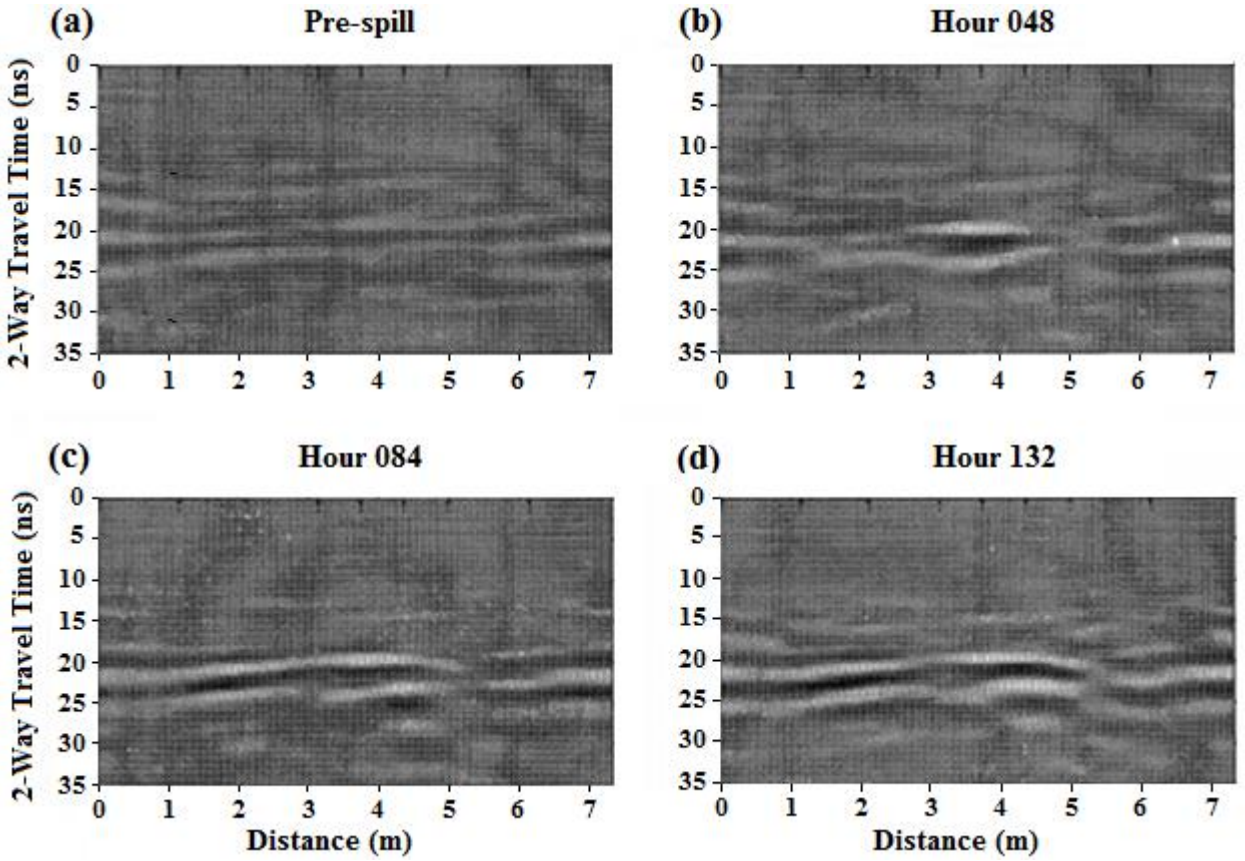

Figure 1.6: GPR profiles from a controlled spill experiment showing the temporal response of the GPR prior to and after the injection of a gasoline spill. The results show bright reflections which increased over time during the increased pooling of gasoline at the water table (20-25 ns) (modified after Atekwana and Atekwana, 2010; Campbell, 1996).

1.6.2. Altered Hydrocarbons

After sufficient time has passed, the geophysical properties of hydrocarbon contaminated sites will be determined by the type of physical, chemical and biological alterations of hydrocarbons (Sauck et al., 1998; Atekwana et al., 2000). The hydrocarbon contamination is then referred to as "aged contamination" and the extent to which these alterations can take place depends on conditions such as lithology, moisture, temperature and microbial activity (Atekwana and Atekwana, 2010).

Electrical Resistivity

As discussed earlier in section 1.5.2, bacterial biodegradation processes can induce significant changes in the sediments and pore fluids composition. Sauck et al. (1998) suggested a conductive electrical response due to the biogeochemical processes associated with an aged hydrocarbon contamination instead of the resistive response associated with a fresh contamination (insulating layer model). This temporal change in the resistivity behavior is attributed to the minerals dissolution by biodegradation by-products, and to the consumption of TEAs that may

accumulate ions into solution. These processes can lead to a significant increase in the concertation of TDS which will enhance the ionic strength and the electrolytic conductivity of pore fluids. According to the conductive model, these modifications in the pore fluid chemistry can lead to an increase in the bulk electrical conductivity of contaminated media. Additionally, the bio-precipitation of mineral phases can also increase the bulk electrical conductivity and impact electrical resistivity measurements (Slater et al., 2007).

Cassidy et al. (2001) investigated the evolution of electrolytic conductivity in columns contaminated with diesel over 120 days. The experiment consisted of an anaerobic column embedded with nutrients and an aerobic column with no added nutrients. As a result, a significant increase of electrolytic conductivity was observed in the anaerobic column with active biodegradation. Allen et al. (2007) showed a direct correlation between the increase of bulk electrical conductivity and the presence of specific microbial populations in LNAPL contaminated sediments. In a study done at a contaminated site in Carson City, Michigan, Atekwana et al. (2004a) showed higher bulk electrical conductivity values in contaminated locations compared to uncontaminated locations. The higher electrical conductivity was coincident with a high percentage of oil degrading microbes (5-55 percent of the heterotrophic microbial community) and high concentrations of organic acids (Figures 1.7 and 1.8).

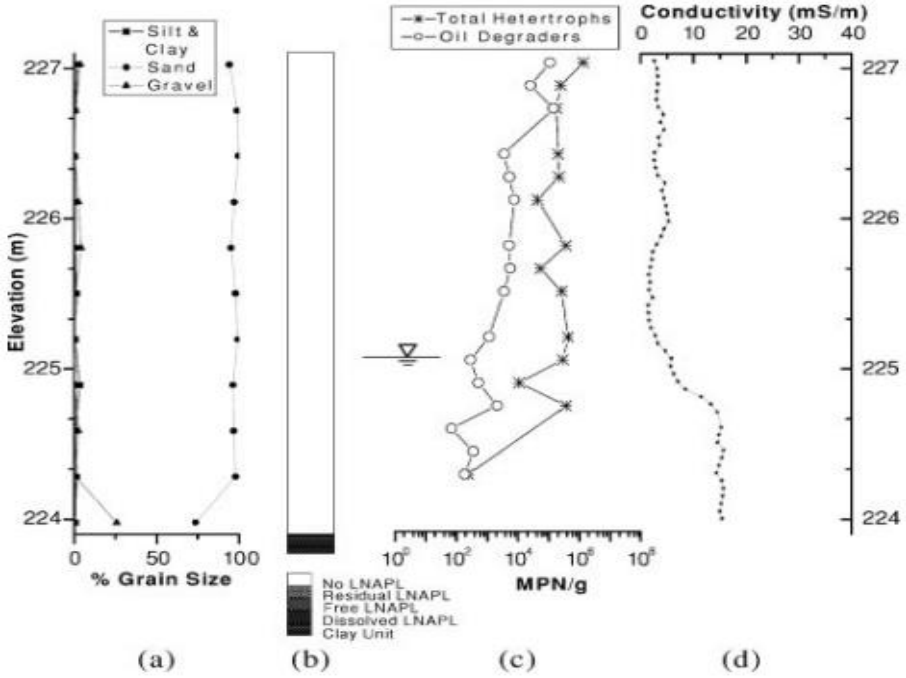

Figure 1.7: The *insitu* electrical conductivity variation (d) with respect to the LNAPL distribution (b) grain size distribution (a) and microbial populations distribution (c) at a clean location in the Carson City site (Atekwana et al., 2004a).

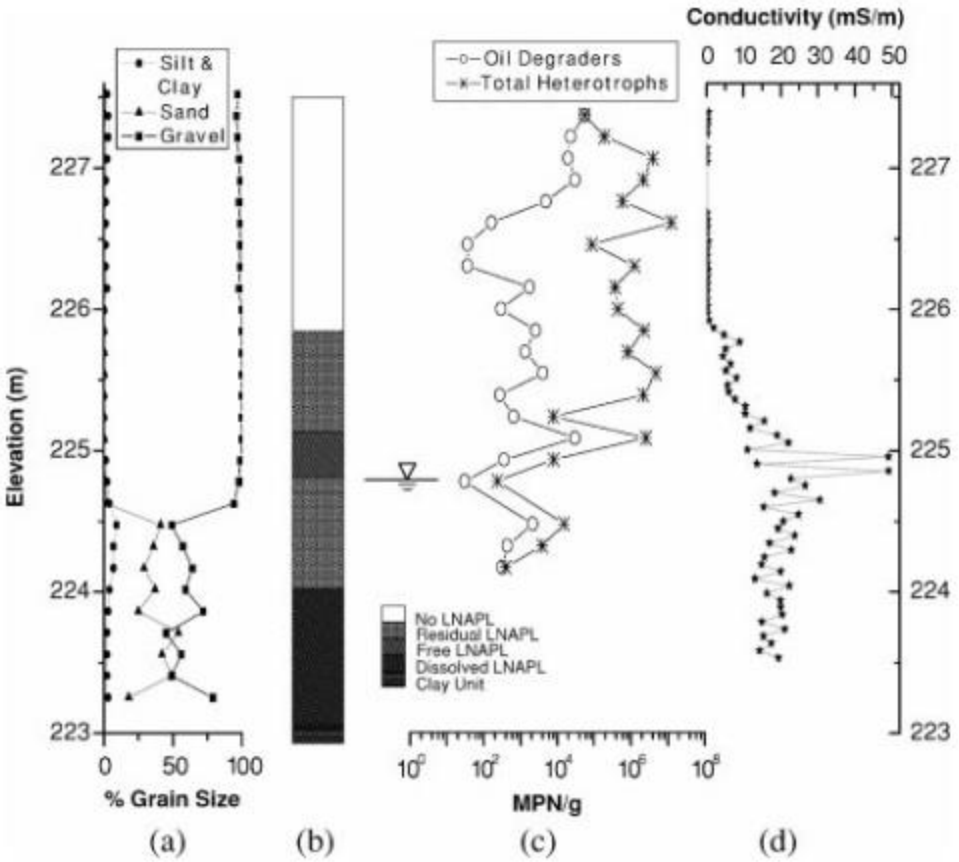

Figure 1.8: The *insitu* electrical conductivity variation (d) with respect to the LNAPL distribution (b) grain size distribution (a) and microbial populations distribution (c) at a contaminated location in the Carson City site (Atekwana et al., 2004a).

Additionally, in two other studies done at the same site, Legall (2002) showed that electron acceptors (manganese, iron, nitrate and sulfate) are depleted and Atekwana et al. (2003) showed increased TDS concentrations. The higher TDS concentrations observed at the contaminated locations were attributed to the higher concentrations of calcium, silica, bicarbonate ions, magnesium and sodium observed by Legall (2002). Moreover, SEM images of contaminated soil samples from the Carson City site showed extensive development of bacterial biofilms and showed that mineral surfaces are highly etched and pitted (Figure 1.9). Thus, these images provided evidence on the alteration of mineral surfaces through enhanced mineral weathering by bacterial processes. Therefore, the presence of oil degrading microbial populations in accordance with higher concentrations of organic acids attributed the high electrical conductivity values to the observed higher TDS concentrations resulting from enhanced mineral weathering by organic acids.

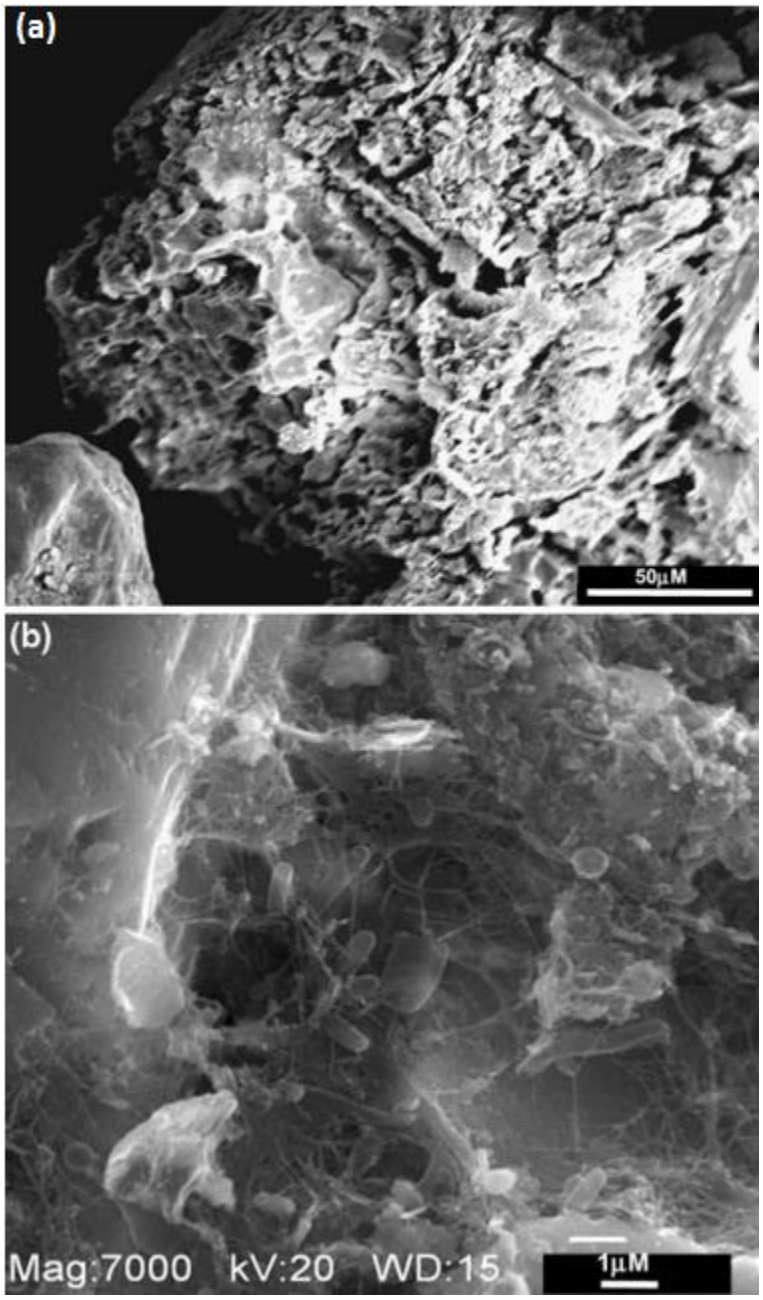

Figure 1.9: Scanning electron microscope images of contaminated soil samples taken from the Carson City site. The images show etched and pitted mineral surfaces (a) and extensive development of bacterial biofilms (b) (Atekwana et al., 2004a; Atekwana and Atekwana, 2010).

To validate the field results, Atekwana et al. (2004d) conducted a meso-scale biodegradation experiment on two biotic sand columns extracted from the Carson City site. One column was embedded with 4 liters of diesel and the other was kept clean. The results were similar to those of the field investigation, with the highest increase (>120%) of bulk electrical conductivity occurring at the capillary fringe and the smear zone, concurrent with the diesel free and residual phases (Figure 1.10). A smaller increase (10 %) was observed in the saturated zone where the contaminant

is in the dissolved phase. The microbial analyses recorded the highest population of oil degrading bacteria in accordance with the highest bulk electrical conductivity values in the capillary fringe and smear zone. The zone impacted by the residual phase of hydrocarbons (transition zone) was reported as the zone of most active biodegradation (Werkema et al., 2003). At this zone, the fluctuating water table smears the hydrocarbons and makes them readily available for bacterial activity (Lee et al., 2001).

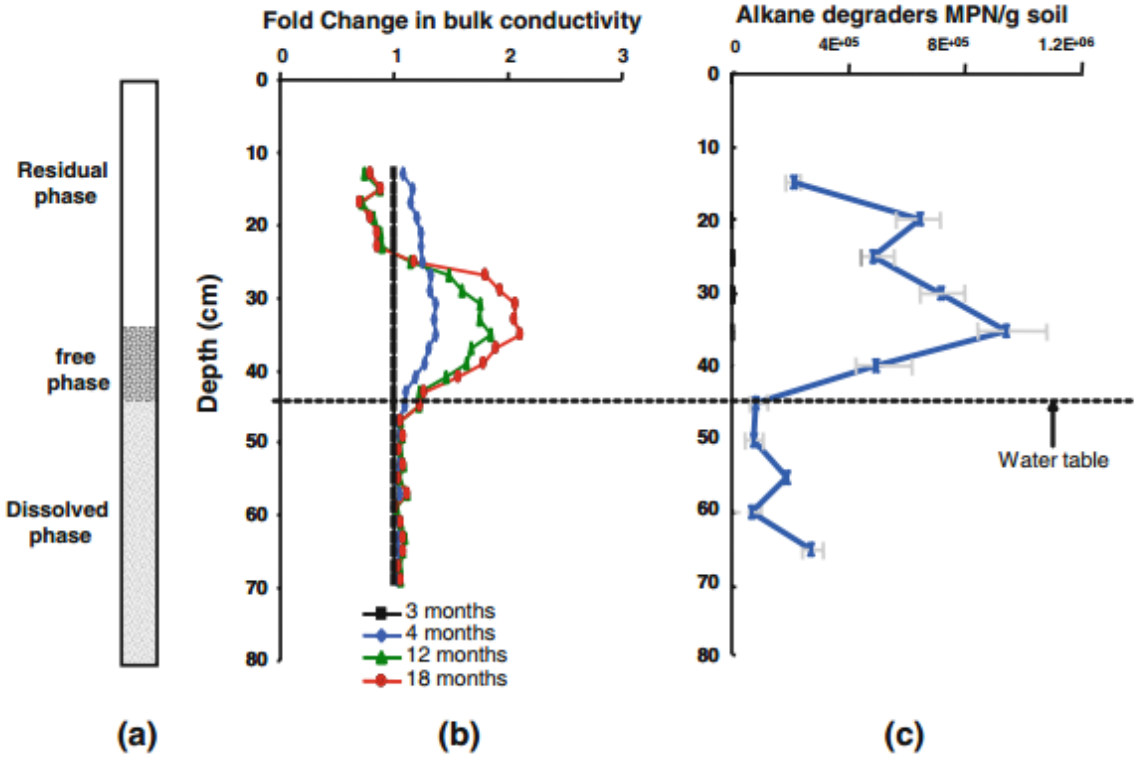

Figure 1.10: Meso-scale laboratory biodegradation experiment showing the fold change of electrical conductivity (b) with respect to the LNAPL distribution (a) and the distribution of Alkane degraders (c) (Atekwana et al., 2004b; Atekwana and Atekwana, 2010).

To further understand the role of bacterial processes, Atekwana et al. (2005) used vertical electrical resistivity probes to investigate the relationship between the bulk electrical conductivity and the different geochemical parameters involved in the biodegradation process (Figures 1.11 and 1.12). The results showed that the increase of bulk electrical conductivity in the aquifer is accompanied by the following: (a) higher concentration of total petroleum hydrocarbons; (b) depletion of electron acceptors such as No_3^- and So_4^{2-} due to their utilization during bacterial degradation; (c) increased dissolved inorganic carbon (DIC) and alkalinity indicating the production of CO_2; (d) higher dissolved Fe (II) and Mn (II) concentrations attributed to the dissolution of Fe (III) and Mn (IV) from aquifer solids; (d) positive $\delta^{13} C_{DIC}$ indicating carbonates dissolution; (e) higher Si concentration indicating enhanced weathering of silicates; (f) enrichment of dominant cations (K^+, Mg^{2+}, Ca^{2+} and NA^+) attributed to minerals weathering by organic acids (g) and higher TDS concentrations. The intervals with the highest bulk electrical conductivity

peaks were observed in the zone below the groundwater table which was the most biologically active as indicated by the depletion of TEAs and the enhanced concentrations of redox species.

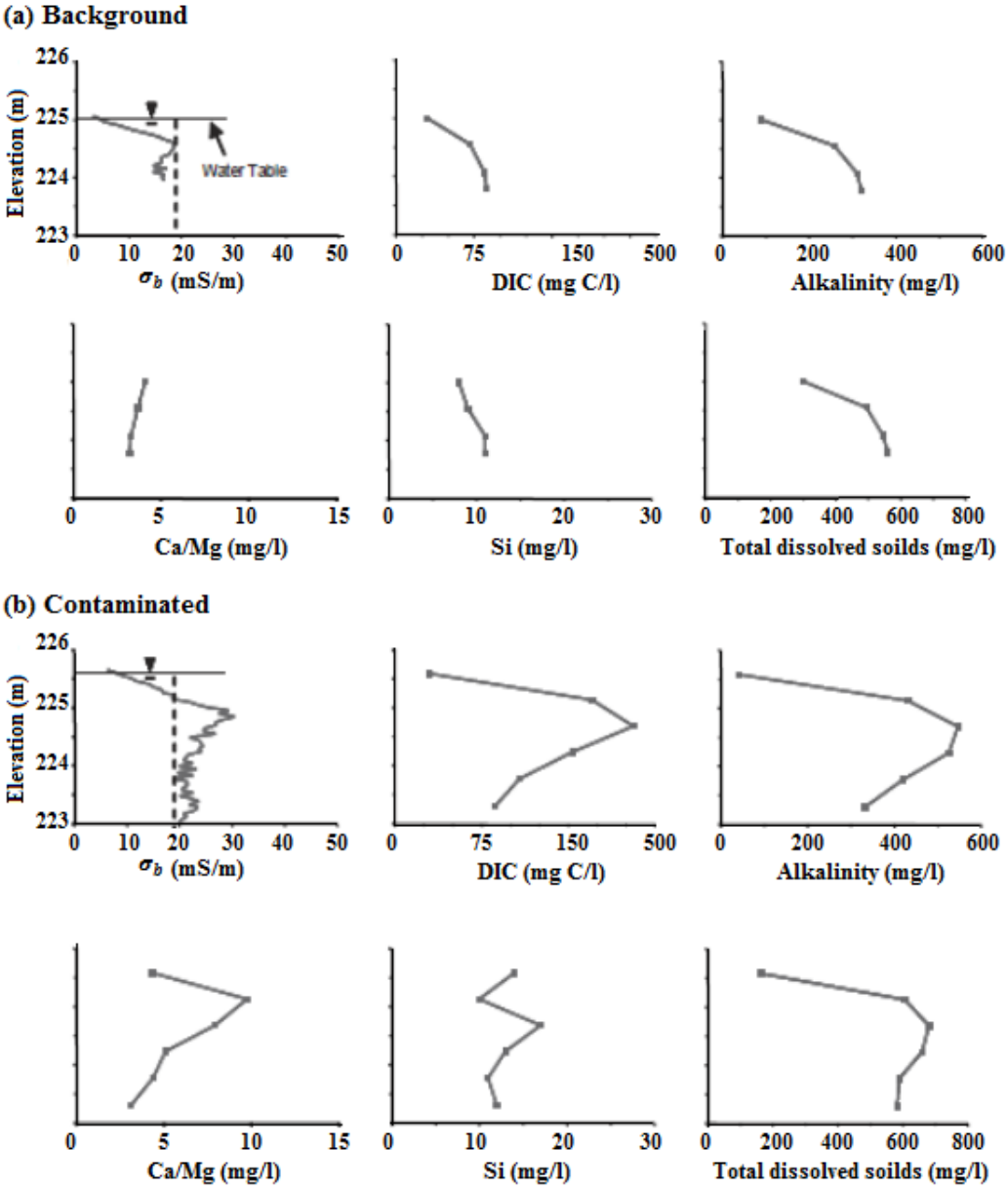

Figure 1.11: Vertical profiles of the bulk electrical conductivity and different geochemical parameters of clean background sediments (a) and hydrocarbon contaminated sediments (b) showing a close correspondence between the chemical and electrical conductivity profiles (modified after Atekwana et al., 2005).

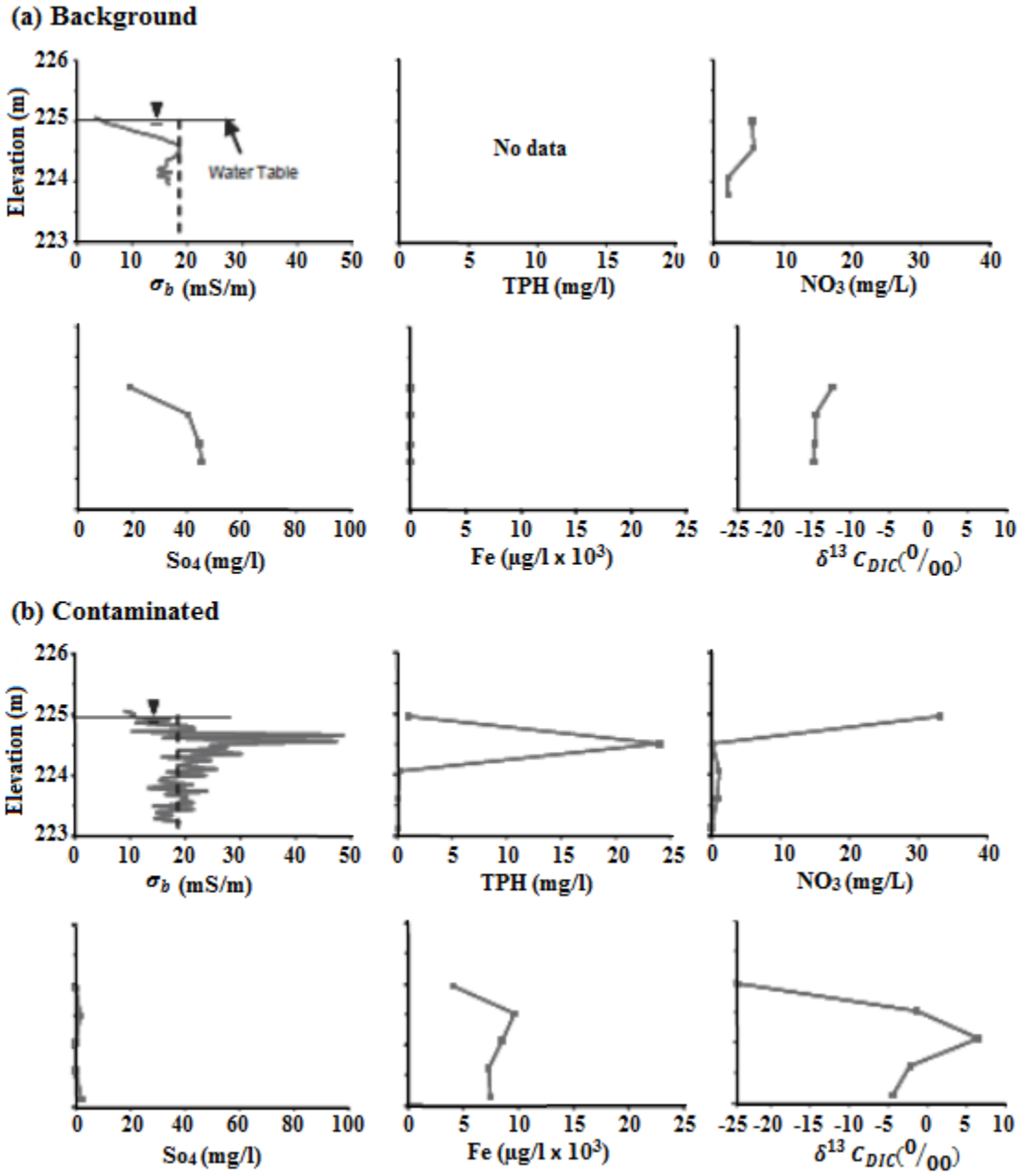

Figure 1.12: Vertical profiles of the bulk electrical conductivity and different geochemical parameters of clean background sediments (a) and hydrocarbon contaminated sediments (b) showing a close correspondence between the chemical and electrical conductivity profiles (modified after Atekwana et al., 2005).

The higher bulk electrical conductivity and higher microbial populations observed in these studies (Atekwana et al., 2004b; Atekwana et al., 2004d; Atekwana et al., 2005) in accordance with higher TDS concentrations overlap with increased calcium and alkalinity and are consistent with weathering of minerals such as carbonates, gypsum and calcium feldspars. Therefore, these results validate the hypothesis which suggested that the increased TDS concentrations due to bacterial mediated mineral weathering increase the bulk electrical conductivity of contaminated

sediments. Moreover, the good correlation between the bulk electrical conductivity and parameters such as DIC and redox species concentrations demonstrates the ability of the electrical conductivity in expressing possible bacterial activity in contaminated sediments.

These investigations illustrated that groundwater and soil electrical resistivity values are generally lower in contaminated sediments undergoing bio-mineralization of hydrocarbons during intrinsic biodegradation. This is attributed to the biogeochemical alterations of hydrocarbons which substantially modified the pore fluid biogeochemistry and induced a temporal shift in the geoelectrical signature from resistive to conductive (Sauck et al., 1998). In the light of the above hypothesis, many field studies recorded low electrical resistivity anomalies at sites impacted by aged hydrocarbon plumes (Atekwana et al., 2000; Shevnin et al., 2005; Werkema et al., 2003). However, the time frame until biological and chemical alterations of hydrocarbons take place is not clearly known and it could be from several weeks to several years, depending on the site biogeochemical conditions. For example, a study done by Yang et al. (2007) reported a high electrical resistivity response over a 10 years old LNAPL spill in Nankan County, Taiwan.

Induced polarization

The sensitivity of the IP phenomena to microbial mediated chemical changes at the mineral-electrolyte interface makes the method ideal for investigating biophysicochemical changes due to hydrocarbon contamination. The accumulation of ions in the pore's fluid enhances the ionic strength and charge build up at the electrical double layer (EDL) which can enhance the membrane polarization mechanism. Additionally, the accumulation of charged bacterial cells with high surface area on mineral surfaces increases the surface roughness and contributes to the enhancement of the polarization magnitude (Abdel Aal et al., 2006; Poortinga et al., 2002).

Sogade et al. (2006) applied the IP method to delineate a contaminant plume in Cape Cod, Massachusetts near Boston, USA. The IP measurements in this study were in great accordance with the plume distribution. This was inferred from the boreholes geochemical data, where the contaminated regions recorded higher chargeability than the clean regions. In a laboratory experiment, Abdel Aal et al. (2003) conducted induced polarization measurements on diesel contaminated sediments in biotic and abiotic columns. The results showed a temporal increase in electrolytic and interfacial conductivities only in the biotic column. This temporal change correlated well with changes in biological and chemical parameters. Therefore, the shift in the sediments electrical properties was attributed to bio-physiochemical changes associated with biodegradation of diesel.

Ground penetrating radar

The increased electrical conductivity of pore fluids due to microbial processes can impact the attenuation constant and the dielectric permittivity of GPR signals (Cassidy et al., 2007). The electrical conductivity controls the attenuation constant of the GPR signal in a way that an increase in the pore fluid conductivity increases the attenuation of GPR reflections. Therefore, the enhanced

conductivities can limit the effective depth of radio waves and result in shadow zones (Sauck, 2000). Atekwana et al. (2000) reported GPR shadow zones coincident with low electrical resistivity anomalies in a hydrocarbon contaminated site in Carson City, Michigan, USA. The study attributed the attenuation of the GPR reflections to enhanced electrical conductivities (corroborated by the electrical resistivity data) resulting from enhanced mineral weathering and increased TDS concentrations. A GPR profile acquired near an LNAPL source plume by Bradford (2007) observed attenuation patterns starting below the water table and extending to deeper depths (Figure 1.13a). Geochemical data from the same study showed that biodegradation is active only in the upper part of the saturated zone, where the LNAPL is in the dissolved phase as indicated by low TEAs concentrations and high ions and TDS concentrations. The GPR results were similar to other GPR profiles conducted at the same source zone, presented by Sauck et al. (1998) and Che-Alota et al. (2009) (Figure 1.13b). Sauck et al. (1998) used the GPR shadow zones to map the transverse extent of the LNAPL contamination in the downgradient locations where the contamination is only in the dissolved phase. The study demonstrated that the GPR higher resolution compared to ERT can provide more information about the small vertical changes in the bulk electrical conductivity which cannot be detected by the ERT technique. Similarly, other studies reported attenuated GPR reflections in the vicinity of gasoline contaminant plumes (e.g., Bermejo et al., 1997; Daniels et al., 1992; Grumman and Daniels, 1995; Maxwel and Schmock, 1995).

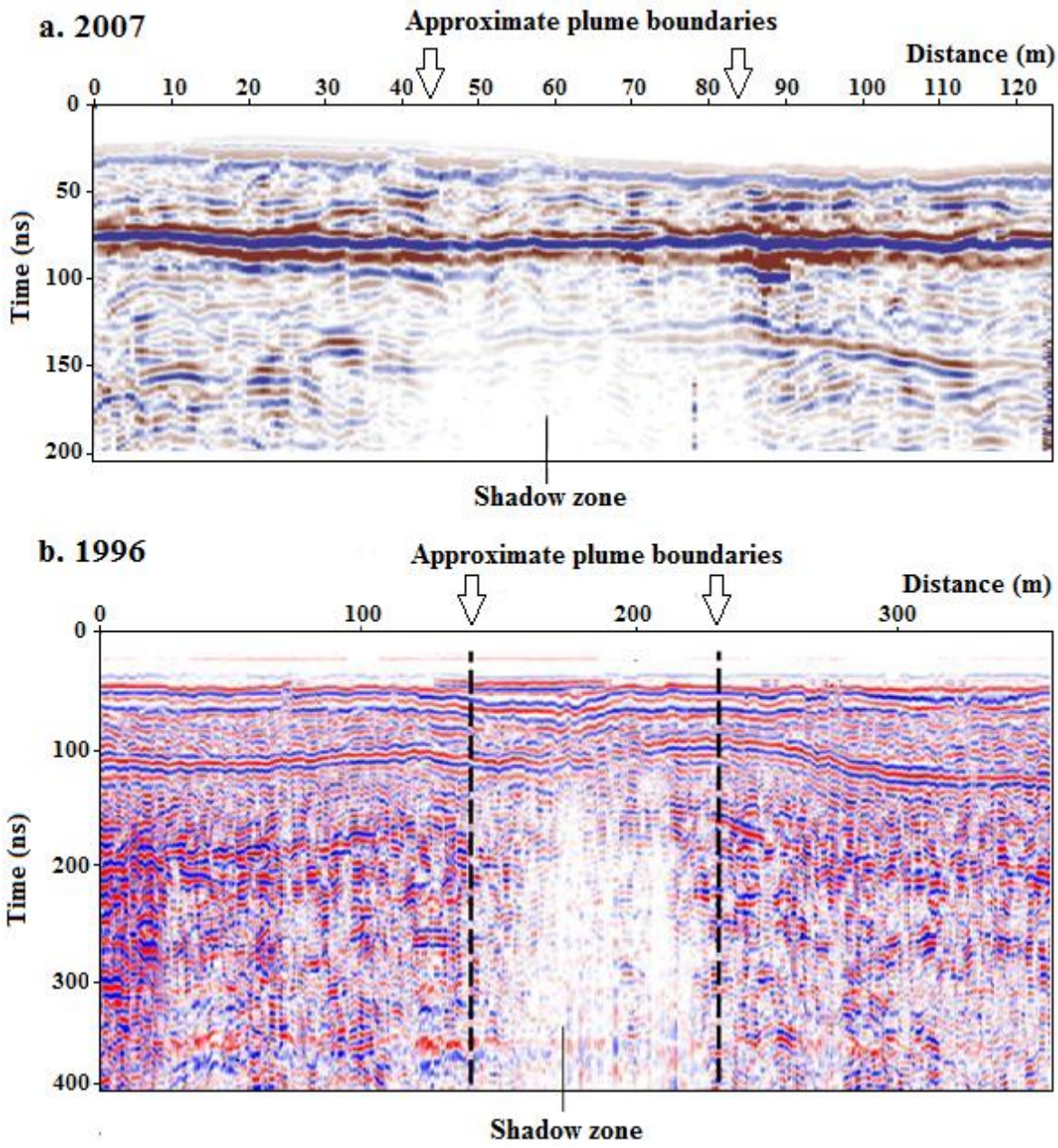

Figure 1.13: GPR profiles done in 2007 (a) and in 1996 (b) on the same site showing attenuated reflections in a hydrocarbon contaminated aquifer (modified after Bradford, 2007 and Che-Alota et al., 2009).

Self Potential

As described previously (section 1.5.2), microbial processes in contaminated aquifers can cause significant changes in the groundwater redox chemistry. These changes can produce different redox conditions which can provide an electrochemical source for the SP signal (Naudet et al., 2004). Sauck et al., (1998) was the first study to relate the SP signal to redox processes in hydrocarbon contaminated aquifers. The study related SP anomalies detected at a hydrocarbon contaminated site to diffusion potentials associated with bacterial mediated redox processes during

the biodegradation of organic carbon. According to Sauck (2000), the driving force of this potential is the mobility of ionic charge carriers which can create chemical concentration gradients in the biologically active zones. The SP survey was repeated in 2007 after the remediation of the contamination source (in 2001). The SP anomalies didn't appear in the new survey, thus suggesting a relationship between the activity of microbial processes and the source mechanism of the SP signal.

According to the geobattery model developed by Sato and Mooney (1960), a mineralization potential can be detected by the SP method due to electron transport through mineral ore deposits during redox reactions. Based on this model, Naudet et al. (2004) devised a biogeobattery model where a redox gradient is created between the highly reduced zone below the water table and the oxidized zone above the water table (Figure 1.14). The electron transport in this model was proposed to be done by bacterial biofilms which form at the water table, where most of the oxygen and organic nutrients are available (Revil et al., 2010). In addition to biofilms, mineral particles precipitating at the water table during the biodegradation process can act as electronic conductors and transport electrons between the distinct redox zones of the biogeobattery (Arora et al., 2007).

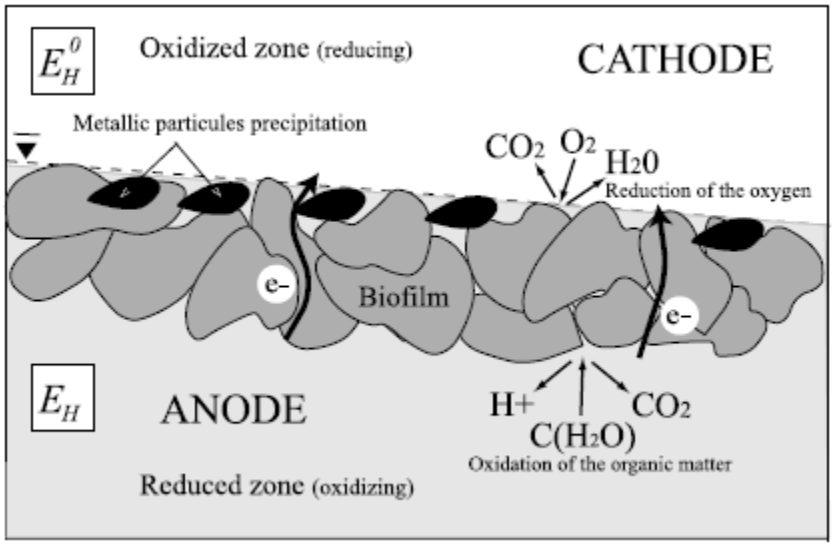

Figure 1.14: Main principles of the biogeobattery model showing the electron transfer between the cathode (oxidized zone above the water table) and the anode (reduced zone in the aquifer) of the geobattery (adapted from Naudet and Revil, 2005).

In the light of the above hypothesis, a linear correlation has been shown between the residual SP signals and redox potential measurements in the field (Naudet et al., 2004) and in a sand box experiment (Naudet and Revil, 2005). Naudet et al. (2004) successfully used the SP method to delineate the redox front of a contaminant plume where an electrochemical cell driven by the oxidation of organic matter and reduction of Fe (III) oxides was considered to be the source of the SP signal. Throughout the study, the electrokinetic component was first removed from the SP field data to produce a map of the residual SP, which represents the electrochemical signal associated with redox processes (Figure 1.15a). The residual SP map showed a good linear correlation

(R=0.85) with the redox potential measured in boreholes (Figure 1.15b). This linear correlation was used to construct a redox potential map and delineate the plume redox front from the residual SP data (Figure 1.16). Minsley et al. (2003) related the electrical current sources and sinks to variations in the redox potential values (high and low). The SP data obtained in this study correlated well with hydrocarbon concentrations and the authors suggested that these current sources can be considered as an indication of contaminated media with active electrochemical source mechanisms.

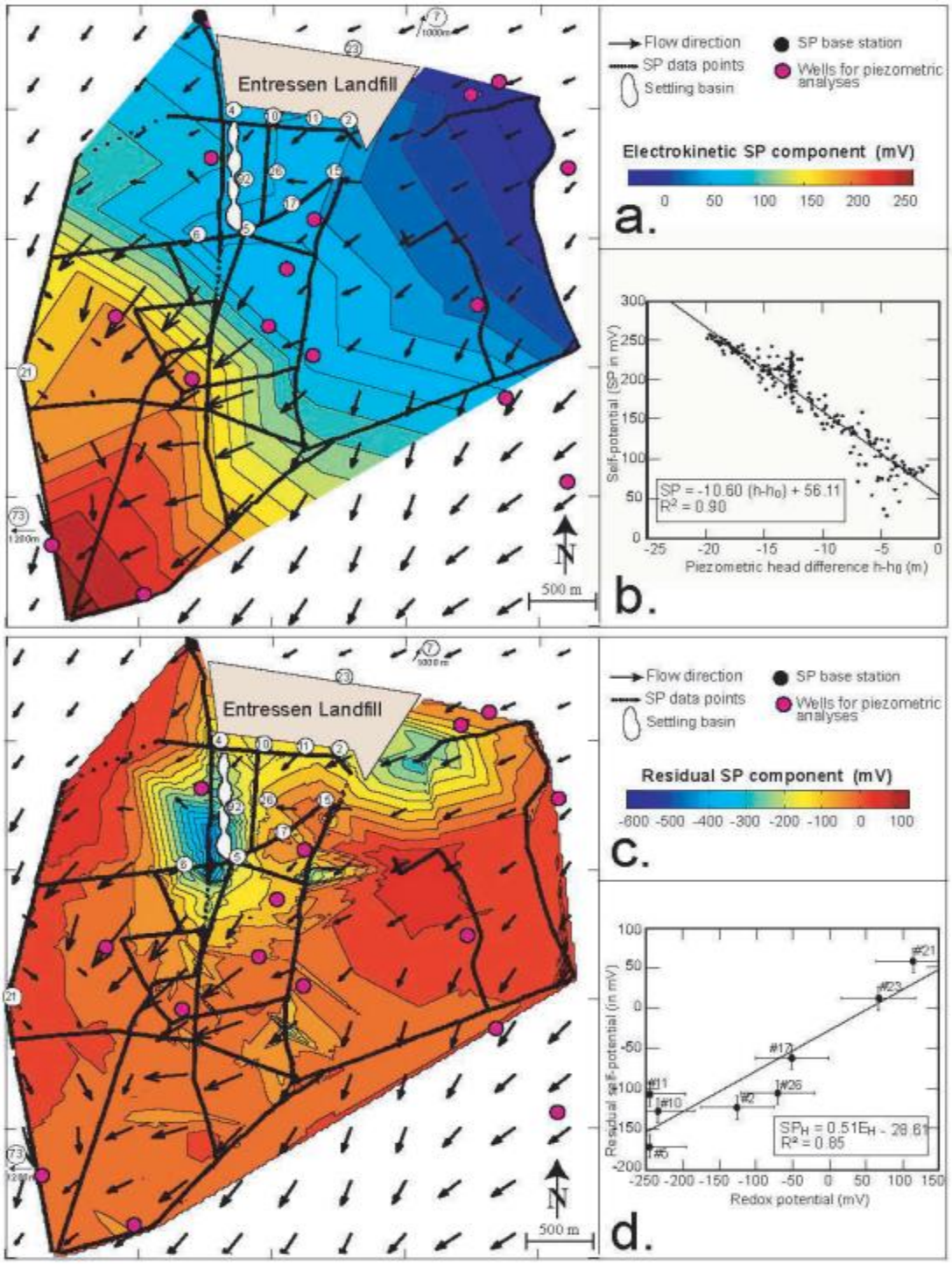

Figure 1.15: The electrokinetic SP component (a) and the residual SP component (c) obtained from the field SP data acquired at the Entressen landfill. The SP map showed a good correlation (d) with the measured redox potential values, with a regression coefficient of 0.85 (Naudet et al., 2004).

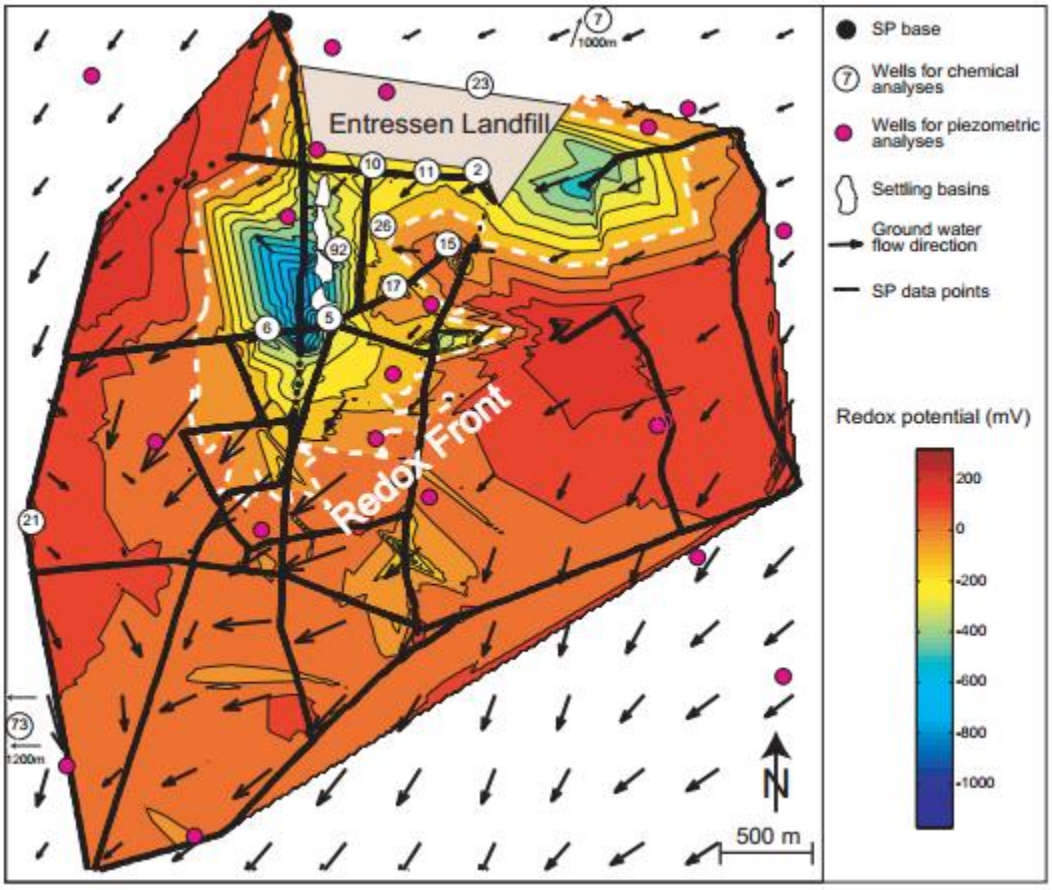

Figure 1.16: The redox potential map constructed by using the linear relationship between the residual SP data and the redox potential measured in boreholes in the Entressen landfill (Naudet et al., 2004).

In a sand box containing a permanganate contaminant plume, Mao et al. (2015) obtained a horizontal dipole source current density from the inversion of self potential data. This source current density remained at the plume front through its transport path across the sand box (Figure 1.17). This was verified by the visual observation of the plume location in the sandbox and by electrical resistivity measurements (Figure 1.18). The self potential data obtained from the predicted source current density had a very good match with the self potential data measured at the field (Figure 1.19). The authors suggested that the strong concentration gradient between the plume and the artificial groundwater of the sand box might be responsible for the obtained source current density.

The above investigations illustrate the ability of the SP method to be used as a proxy of redox potential and to delineate contaminant plumes in shallow aquifers. Nevertheless, Forte and Bentley (2013) did not reveal any high SP signals in a site where the groundwater is contaminated with degraded hydrocarbons. This response is explained by Revil et al. (2010) who stated that a biogeobattery producing large SP anomalies exists only in the presence of electronic conductors such as biofilms and minerals precipitates.

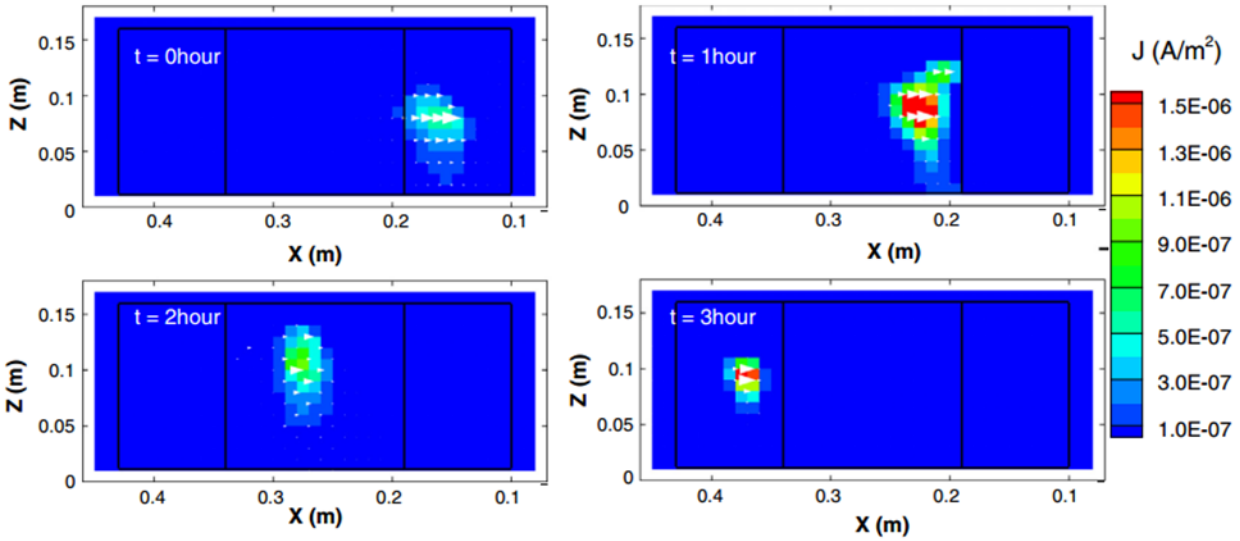

Figure 1.17: Inverted source current density in a sandbox contaminated by a permanganate plume at 4 different time steps (Mao et al., 2015).

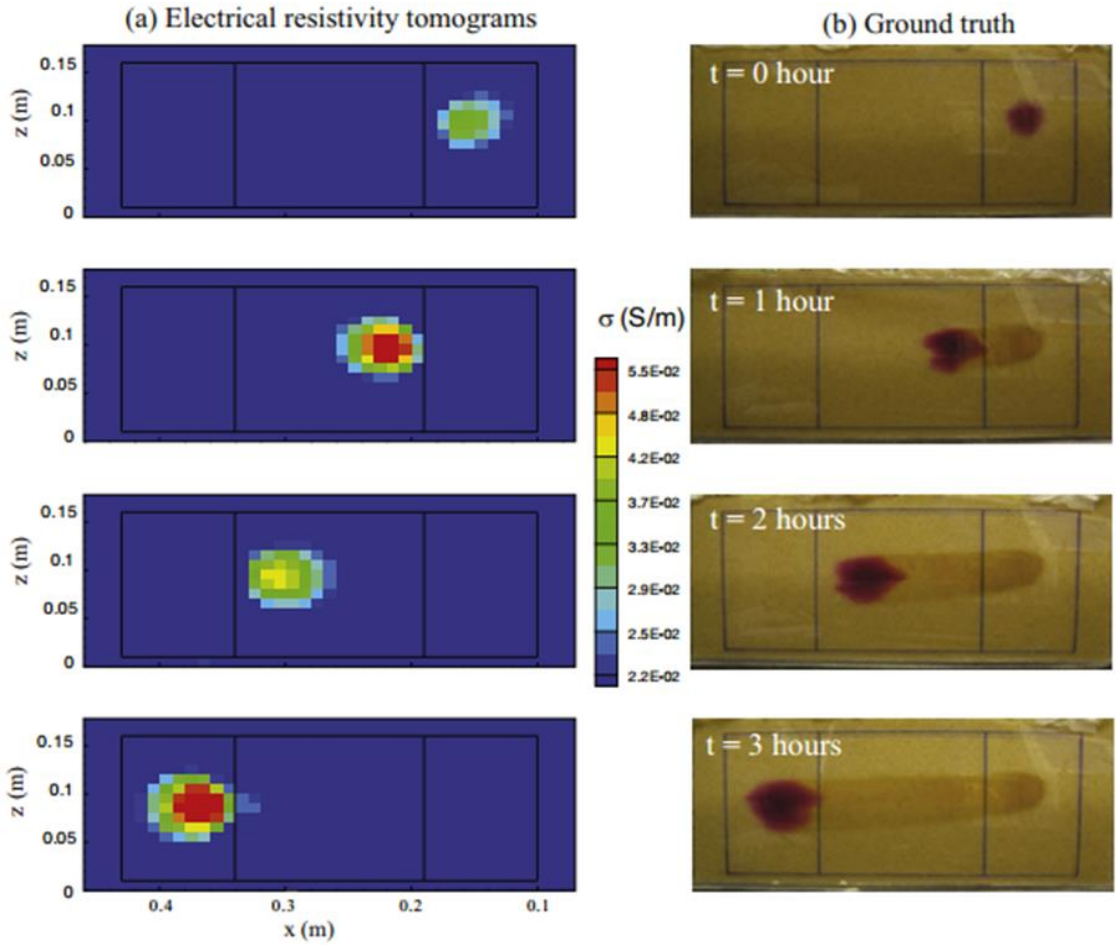

Figure 1.18: Electrical resistivity tomograms (a) and images of the location of the plume in the sandbox (b) (Mao at al., 2015).

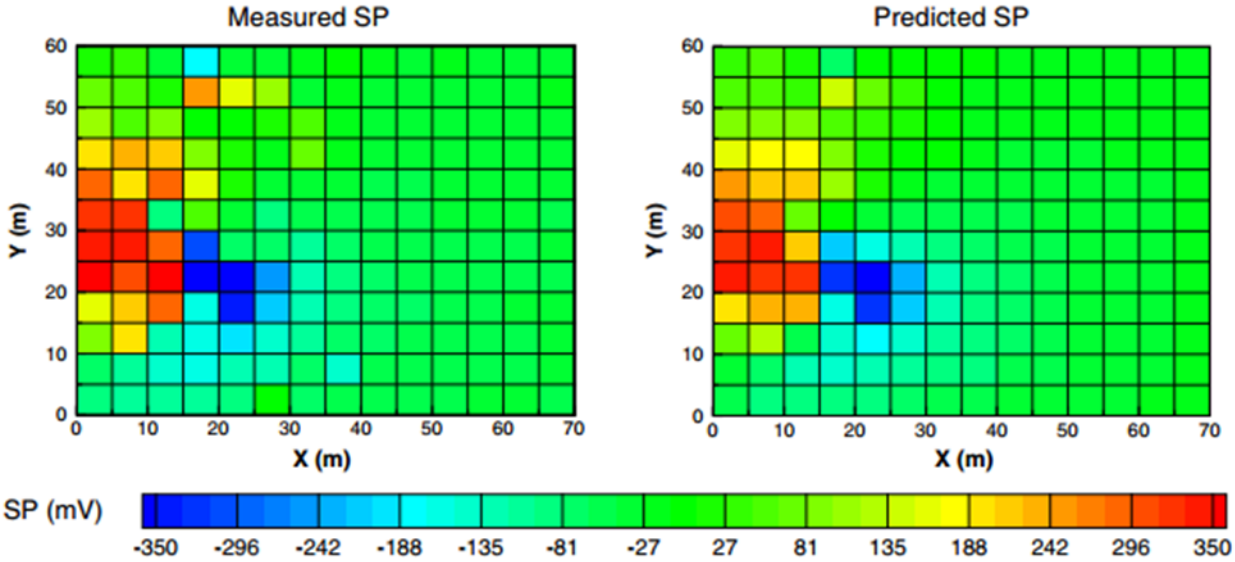

Figure 1.19: The measured self potential data and the self potential data predicted from the inverted source current density (Mao et al., 2015).

Magnetic Susceptibility

The formation of magnetic minerals through biological precipitation and minerals weathering during the hydrocarbon biodegradation process induces changes in the iron mineral content of sediments which can be measured by the MS method. An example would be the utilization of hydrocarbons by anaerobic Fe (III) reducing bacteria to transform iron oxides and hydroxides into crystalline Fe (II) containing different mineral phases such as magnetite, pyrite and siderite (Postma 1981; Fredrickson et al., 1998). Therefore, it was suggested that MS measurements are sensitive to the microbial Fe transformation coupled to the hydrocarbons biodegradation process. Support for this theory came from previous studies such as Hanesch and Scholger (2002) and Martins et al. (2007) that observed a good correlation between the hydrocarbon content and MS values in contaminated soil samples. Rijal (2010) studied the variation of normalized MS with time in soil microcosms amended with different concentrations of gasoline and diesel. The study showed a much higher increase of MS values in microbial active microcosms compared to sterile ones (Figure 1.20).

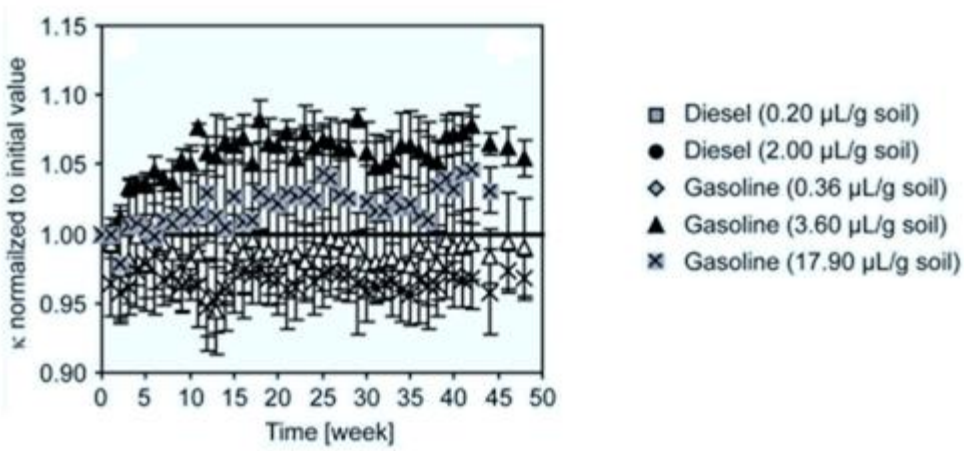

Figure 1.20: Variation of MS with time in soil microcosms amended with different concentrations of diesel and gasoline. The results of the sterile microcosms are represented by the open symbols (Rijal, 2010).

In a microcosm laboratory study, Porsch et al. (2010) investigated the variation of volume specific magnetic susceptibility with respect to the reduction of Ferrihydrite by *Shewanella oneidensis* MR-1 (iron reducing bacteria). The study reported a large initial increase of volume specific MS accompanied by an increase in the reduction of iron and followed by a slight decrease of MS at day 18 (Figure 1.21). The XRD patterns of the minerals formed during the reduction of Ferrihydrite by the MR-1 bacteria showed that the initial increase of MS (days 4 and 8) is associated with the formation of Magnetite (Figure 1.21c). The slight decrease in MS at day 18 was shown to be associated with the further reduction of magnetite to siderite; a paramagnetic mineral with low volume specific magnetic susceptibility which was detected only at the end of the experiment. The increase in MS accompanied by the increase of iron reduction and magnetite formation occurred only in the microbial active microcosms, indicating microbial induced changes in the Fe-mineralogy which impacted the MS results.

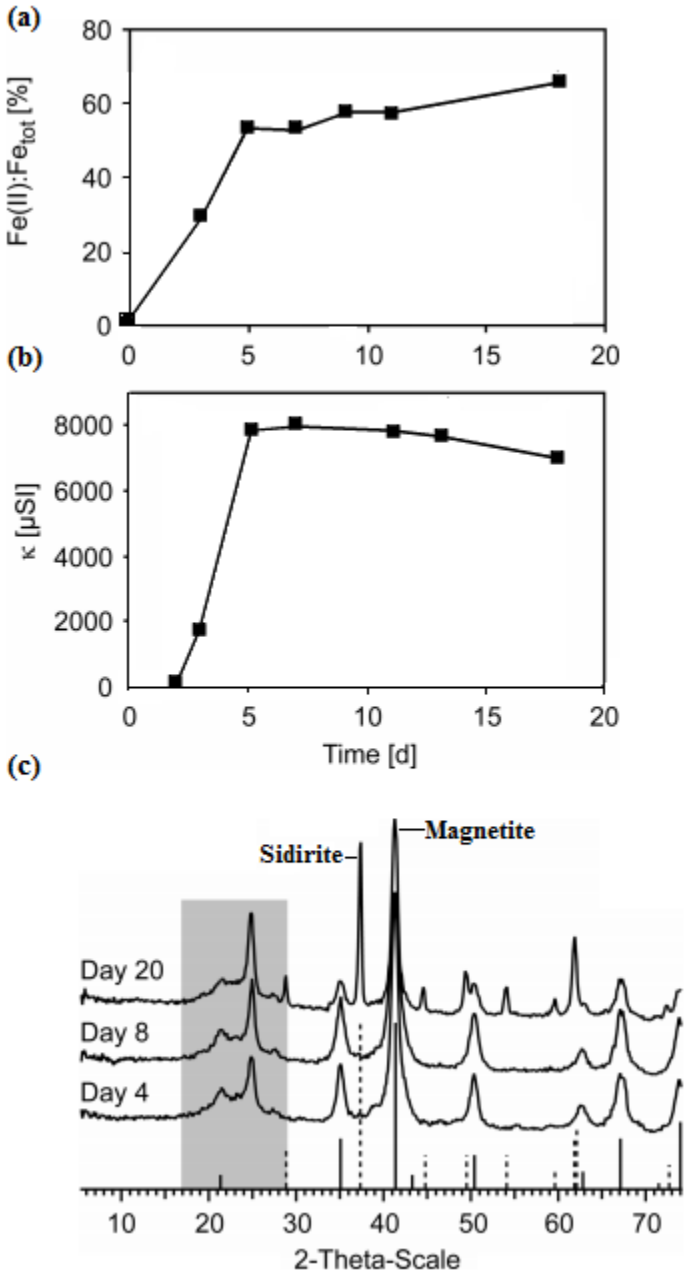

Figure 1.21: Changes of Fe (II) to total Fe ratio during the reduction of Ferrihydrite (a). Variation of the volume specific MS with time (b). XRD pattern of the iron minerals formed during the reduction of Ferrihydrite showing peaks of magnetite and siderite (c) (Modified after Porsch et al., 2010).

Similarly, after analyzing the MS variations in a hydrocarbon contaminated aquifer where iron reduction and methanogenesis are the main TEAPs, Mewafy et al. (2011) documented enhanced values of MS. The authors attributed these enhancements to the precipitation of magnetite coupled to the iron-reduction of anaerobic and aerobic bacteria. The presence of hydrocarbons was essential for magnetite to form in a study done by Rijal et al. (2010). A clear decrease in magnetite formation was observed outside the strongly contaminated zone. The

enhanced magnetite formation in the contaminated zone was attributed to the intensive geo-microbiological activity.

1.7. References

Abdel Aal, G.Z., E.A. Atekwana, L.D. Slater, and C. Ulrich, 2003. Induced polarization (IP) measurements of soils from an aged hydrocarbon contaminated site. Proceedings of the Symposium on the Application of Geophysics to Engineering and Environmental Problems, San Antonio, Texas, April 6–10, pp. 190– 202.

Abdel Aal, G.Z., D. Lee, D. Slater, and E. A. Atekwana 2006. Induced-polarization measurements on unconsolidated sediments from a site of active hydrocarbon biodegradation. Geophysics Vol., 71, No. 2 (March-April 2006); P. H13–H24, 9 FIGS., 3 TABLES. 10.1190/1.2187760

Abdel Aal, G. Z., E. A. Atekwana, and E. A. Atekwana, 2010. Effect of bioclogging in porous media on complex conductivity signatures. J. Geophys. Res. 115, 1–10.

Allen, J.P., E. A. Atekwana, E. A. Atekwana, J.W. Duris, D.D. Werkema, and S. Rossbac, 2007. The microbial community structure in petroleum-contaminated sediments corresponds to geophysical signatures. Appl Environ Microbiol 73:2860–2870

Arora, T., N. Linde, A. Revil, and J. Castermant, 2007. Non-intrusive characterization of the redox potential of landfill leachate plumes from self-potential data. J. Contam. Hydrol. 92, 274–92. doi:10.1016/j.jconhyd.2007.01.018

Atlas, R. and J. Bragg, 2009. "Bioremediation of marine oil spills: when and when not—the Exxon Valdez experience," Microbial Biotechnology, vol. 2, no. 2, pp. 213–221, 2009.

Atekwana, E. A., W. A. Sauk, and D. D. Werkema, 2000. Investigations of geoelectrical signatures at a hydrocarbon contaminated site. Appl. Geophys. 44, 167–180.

Atekwana, E. A., E. A. Atekwana, R. S. Rowe, D. D. Werkema, and F. D. Legall, 2004a. Total dissolved solids in groundwater and its relationship to bulk conductivity of soils contaminated with hydrocarbon: Journal of Applied Geophysics, 56, 281–294.

Atekwana, E. A., E. A. Atekwana, D. D. Werkema, J. P. Allen, L. A. Smart, J. W. Duris, D. P. Cassidy, W. A. Sauck, and S. Rossbach, 2004b. Evidence for microbial enhanced electrical conductivity in hydrocarbon-contaminated sediments: Geophysical Research Letters, 31, L23501, doi: 10.1029/2004GL021359.

Atekwana E.A., E.A. Atekwana , D.D. Werkema, J.P. Allen, L.A. Smart, J. W. Duris, D.P. Cassidy, W.A. Sauck, and S. Rossbach, 2004d. Evidence for microbial enhanced electrical conductivity in hydrocarbon-contaminated sediments. Geophys Res Lett 31:L23501

Atekwana, E. A., E. A. Atekwana, F. D. Legall, and R. V. Krishnamurthy, 2005. Biodegradation and mineral weathering controls on bulk electrical conductivity in a shallow hydrocarbon contaminated aquifer. J. Contam. Hydrol. 80, 149–167.

Atekwana, E. A. and E. A. Atekwana, 2010. Geophysical Signatures of Microbial Activity at Hydrocarbon Contaminated Sites: A Review. Surv Geophys (2010) 31:247–283DOI 10.1007/s10712-009-9089-8.

Bartha R. and I. Bossert, 1984. The treatment and disposal of petroleum wastes, in *Petroleum Microbiology*, R. M. Atlas, Ed., pp. 553–578, Macmillan, New York, NY, USA.

Brusseau M.L., 1998.The impact of physical, chemical and biological factors on biodegradation, in Proceedings of the International Conference on Biotechnology for Soil Remediation: Scientific Bases and Practical Applications, R. Serra, Ed., pp. 81–98, C.I.P.A. S.R.L., Milan, Italy, 1998.

Barathi S. and N. Vasudevan, 2001. Utilization of petroleum hydrocarbons by Pseudomonas fluorescens isolated from a petroleum-contaminated soil, Environment International, vol. 26, no. 5-6, pp. 413–416, 2001

Baedecker M.J., I.M. Cozzarelli, and J.A. Hopple, 1987. The composition and fate of hydrocarbons in a shallow glacial-outwash aquifer. U.S. Geol. Survey Open-File Report, pp. 87–109.

Baedecker, M.J., I.M Cozzarelli, R.P Eganhouse, D.I. Siegel, and P.C. Bennett, 1993. Crude oil in a shallow sand and gravel aquifer: III. Biogeochemical reactions and mass balance modeling in anoxic groundwater. Applied Geochemistry 8, 569–586.

Bermejo, J. L., W. A. Sauck, and E. A. Atekwana, 1997, Geophysical discovery of a new LNAPL plume at the former Wurtsmith AFB, Oscoda, Michigan: Ground Water Monitoring Review, 17, 131– 137.

Bennett, P. C., F. K. Hiebert, and W. J. Choi, 1996. Microbial colonization and weathering of silicates in a petroleum-contaminated groundwater: Chemical Geology, 132, 45–53.

Benson, A. K., 1995. Applications of ground penetrating radar in assessing some geological hazards: examples of groundwater contamination, faults, and cavities. Journal of Applied Geophysics 33, 177–193.

Benson, A. K., K. L. Payne, and M. A. Stubben, 1997. Mapping groundwater contamination using DC resistivity and VLF geophysical methods: a case study. Geo- physics 62, 80–86

Benson, A.K. and N. B. Mutsoe, 1996. DC resistivity, ground penetrating radar, and soil and water quality data combined to assess hydrocarbon contamination: a case study. Environmental Geosciences 3, 165–175.

Bradford J.H., 2007. Frequency-dependent attenuation analysis of ground-penetrating radar data. Geophysics 72:J7–J16. doi:10.1190/1.2710183

Boreden R.C., 1994. Natural bioremediation of hydrocarbon contaminated groundwater.In: Handbook of bioremediation.CRC Press, Boca Raton,F.L. pp 177-199

Che-Alota V, E.A. Atekwana, E.A. Atekwana, W. A. Sauck, and D. D. Werkema, 2009. Temporal geophysical signatures due to contaminant mass reduction. Geophysics 74. doi: 10.1190/1.3139769

Campbell, D. L., J. E. Lucius, K. J. Ellefsen, and M. DeszczPan, 1996. Monitoring of a controlled LNAPL spill using ground penetrating radar. Proceedings of the Symposium on the

Application of Geophysics to Engineering and Environmental Problems (SAGEEP ’96), Keystone, CO, pp. 511–517.

Cozzarelli, I.M., R. P. Eganhouse, and M. J. Baedecker, 1990. Transformation of monoaromatic hydrocarbons to organic acids in anoxic groundwater environment. Envi- ronmental Geology and Water Science 16 _2., 135–141.

Cassidy, D. P., D. D. Werkema, W. A. Sauck, E. A. Atekwana, S. Rossbach, and J. Duris, 2001.The effects of LNAPL biodegradation products on electrical conductivity measurements: Journal of Environmental and Engineering Geophysics, 6, 47–52.

Cassidy, N. J., 2007. Evaluating LNAPL contamination using GPR signal attenuation analysis and dielectric property measurements: Practical implications for hydrological studies. Journal of Contaminant Hydrology, 94, 49-75.

Cooney,J. J., S. A. Silver, and E. A. Beck, 1985. Factors influencing hydrocarbon degradation in three freshwater lakes, Microbial Ecology, vol. 11, no. 2, pp. 127–137, 1985.

Chaillan, F., A. Le Fleche, and E. Bury, 2004. Identification and biodegradation potential of tropical aerobic hydrocarbon degrading microorganisms,” Research in Microbiology, vol. 155, no. 7, pp. 587–595, 2004.

Choi, S.C., K. K. Kwon, J.H. Sohn, and S.-J. Kim, 2002. Evaluation of fertilizer additions to stimulate oil biodegradation in sand seashore mesocosms, Journal of Microbiology and Biotechnology, vol. 12, no. 3, pp. 431–436, 2002.

Cooney, J. J., S. A. Silver, and E. A. Beck, 1985. “Factors influencing hydrocarbon degradation in three freshwater lakes,” Microbial Ecology, vol. 11, no. 2, pp. 127–137, 1985.

Daugulis, A.J. and C.M. McCracken, 2003. “Microbial degradation of high and low molecular weight polyaromatic hydrocarbons in a two-phase partitioning bioreactor by two strains of Sphingomonas sp,” Biotechnology Letters, vol. 25, no. 17, pp. 1441–1444, 2003.

DeRyck, S. M., J. D. Redman, and A. P. Annan, 1993. Geophysical monitoring of a controlled kerosene spill: Symposium on the Application of Geophysics to Engineering and Environmental Problems (SAGEEP), Proceedings, 5–20.

Davis, C.A., E. A. Atekwana, E. A. Atekwana, L. D. Slater, S. Rossbach, and M.R. Mormile, 2006. Microbial growth and biofilm formation in geologic media is detected with complex conductivity measurements. Geophys. Res. Lett. 33:L18403

Daniels, J.J., R. Roberts, and M. Vendl, 1992. Site studies of ground penetrating radar for monitoring petroleum product contaminants. Proceedings of the Symposium on the Application of Geophysics to Engineering and Environmental Problems _SAGEEP ’92. Oakbrook, IL, pp. 597–609.

Endres, A.L. and J. P. Greenhouse, 1996. Detection and monitoring of chlorinated solvent contamination by thermal neutron logging. Ground Water 34, 283–292.

Eganhouse, R. P., M. J. Baedecker, I. M. Cozzarelli, G.R. Aiken, K.A. Thorn, and T.F. Dorsey, 1993. Crude oil in a shallow sand and gravel aquifer: II. Organic geochemistry. Applied Geochemistry 8, 551–567.

Fredrickson, J. K., J. M. Zachara, D. W. Kennedy, H. L. Dong, T. C. Onstott, N. W. Hinman, and S. M. Li, 1998. Biogenic iron mineralization accompanying the dissimilatory reduction of hydrous ferric oxide by a groundwater bacterium, Geochim. Cosmochim. Acta, 62(19 – 20), 3239– 3257, doi:10.1016/ S0016-7037(98)00243-9.

Floodgate, G., 1984. "The fate of petroleum in marine ecosystems," in Petroleum Microbiology, R. M. Atlas, Ed., pp. 355–398, Macmillion, New York, NY, USA, 1984.

Fritsche, M. and M. Hofrichter, 2000. "Aerobic degradation by microorganisms," in Environmental Processes- Soil Decontamination, J. Klein, Ed., pp. 146–155, Wiley-VCH, Weinheim, Germany, 2000.

Grumman, D.L. and J. J. Daniels, 1995. Experiments on the detection of organic contaminants in the vadose zone. Journal of Environmental and Engineering Geophysics, 31–38

Griffith, D. H., J. Turnbull, and A. I. Olayinka, 1990. Two-dimensional resistivity mapping with a computer controlled array. First Break 8, 121-129

Huling SG, B. Pivetz, R. Stransky, 2002. Terminal electron acceptor mass balance: light nonaqueous phase liquids and natural attenuation. J Environ Eng 128:246–252.

Hiebert, F. K., and P. C. Bennett, 1992, Microbial control of silicate weathering in organic rich ground water: Science, 258, 278–281.

Hansel, C. M., S. G. Benner, J. Neiss, A. Dohnalkova, R. K. Kukkadapu, and S. Fendorf , 2003. Secondary mineralization pathways induced by dissimilatory iron reduction of ferrihydrite under advective flow, Geochim. Cosmochim. Acta, 67(16), 2977–2992, doi: 10.1016/S0016-7037(03)00276-X.

Lee, J. Y., J. Y. Cheon, K. K. Lee, S. Y. Lee, and M. H. Lee, 2001. Factors affecting the distribution of hydrocarbon contaminants and hydrogeochemical parameters in a shallow sand aquifer. Contam. Hydrol. 50 (12), 139-158

Mitsch, W.J. and J. G. Gosselink, 1993. Wetlands, John Wiley & Sons, New York, NY, USA, 2nd edition.

Maxwell, M. and J. Schmok, 1995. Detection and mapping of an LNAPL plume using GPR: a case study. Proceedings of the Symposium on the Application of Geophysics to Engineering and Environmental Problems_SAGEEP '95., Orlando, FL, pp. 15–23.

McMahon, P. B., D. A Vroblesky, P. M. Bradley, F. H. Chapelle, and C. D. Guller, 1995. Evidence of enhanced mineral dissolution in organic acid rich shallow ground water. Ground Water 33, 207–216.

McMahon, P. B. and F. H.Chapelle, 1991. Microbial production of organic acids in aquitard sediments and its role in aquifer geochemistry. Nature 349, 233–235.

Mao, D., A. Revil, R. D. Hort, J. Munakata-Marr, E. A. Atekwana, and B. Kulessa 2015. Resistivity and self-potential tomography applied to groundwater remediation and contaminant plumes: Sandbox and field experiments. Journal of Hydrology 530, 1-14.

Nilanjana, D. and P. Chandran, 2011. Microbial Degradation of Petroleum Hydrocarbon Contaminants: An Overview SAGE-Hindawi Access to Research Biotechnology Research International Volume 2011, Article ID 941810, 13 pages doi:10.4061/2011/941810

Naudet, V., A. Revil, J. Y. Bottero, and P. Begassat, 2003. Relationship between self-potential (SP) signals and redox conditions in contaminated groundwater: Geophysical Research Letters, 30, 2091, doi: 10.1029/2003GL018096.

Naudet, V., A. Revil, E. Rizzo, J. Y. Bottero, and P. Bégassat, 2004. Groundwater redox conditions and conductivity in a contaminant plume from geoelectrical investigations. Hydrol. Earth Syst. Sci. 8, 8–22. doi:10.5194/hess-8-8-2004

Naudet, V. and A. Revil, 2005. A sandbox experiment to investigate bacteria-mediated redox processes on self-potential signals. Geophys. Res. Lett. 32.

Osella A, M. de la Vega, and E. Lascano, 2002. Characterization of a contaminant plume due to a hydrocarbon spill using geoelectrical methods. J Environ Eng Geophys 7:78–87

Olhoeft, G.R., 1992. Geophysical detection of hydrocarbon and organic chemical contamination. Proceedings of the Symposium on the Application of Geophysics to Engi- neering and Environmental Problems _SAGEEP '92., Oakbrook, IL, pp. 587–595.

Pinder, G.F. and Gray, W.G., 2008. Essentials of Multiphase Flow and Transport in Porous Media. Published Online: 7 FEB 2008. DOI: 10.1002/9780470380802.ch5

Prommer, H., G. B. Davis, and D. A. Barry, 1999. Geochemical changes during biodegradation of petroleum hydrocarbons: Field investigations and biogeochemical modeling, Org. Geochem., 30(6), 423–435, doi:10.1016/S0146-6380(99)00027-3.

Poortinga, A.T, R. Bos, W. Norde, and H.J. Busscher, 2002. Electric double layer interactions in bacterial adhesion to surfaces. Surf Sci Rep 47:1–32.

Perry, J. J., 1984 "Microbial metabolism of cyclic alkanes," in Petroleum Microbiology, R. M. Atlas, Ed., pp. 61–98,Macmillan, New York, NY, USA.

Rahman, K. S. M., T. J. Rahman, Y. Kourkoutas, I. Petsas, R. Marchant, and I. M. Banat, 2003. Enhanced bioremediation of n-alkane in petroleum sludge using bacterial consortium amended with rhamnolipid and micronutrients, Bioresource Technology, vol. 90, no. 2, pp. 159–168.

Revil, A., C. A. Mendonça, E. A. Atekwana, B. Kulessa, S. S. Hubbard, and K. J. Bohlen, 2010. Understanding biogeobatteries: Where geophysics meets microbiology. J. Geophys. Res. 115, G00G02. doi:10.1029/2009JG001065

Revil, A., V. Naudet, J. Nouzaret, and M. Pessel, 2003. Principles of electrography applied to self-potential electrokinetic sources and hydrogeological applications. Water Resour. Res. 39.1114 doi:10.1029/2001WR000916

Soltani, M., 2004. Distribution lipidique et voies métaboliques chez quatre bactéries Gramnégatives hydrocarbonoclastes. Variation en fonction de la source de carbone. PhD thesis, Université de Pierre et Marie Curie - Paris 6.

Schneider, G.W. and J. P. Greenhouse, 1992. Geophysical detection of perchloroethylene in a sandy aquifer using resistivity and nuclear logging techniques. Proceedings of the Symposium on the Application of Geophysics to Engineering and Environmental Problems _SAGEEP '92., Oakbrook, IL, pp. 619–628.

Schneider, G.W., S. M. de Ryck, and P. A. Ferre, 1993. The application of automated high resolution d.c. resistivity in monitoring hydrogeological field experiments. Proceedings of the Symposium on the Application of Geophysics to Engineering and Environmental Problems _SAGEEP '93., San Diego, CA, pp. 145–162.

Sauck, W. A., E. A. Atekwana, and M. S. Nash, 1998. Elevated conductivities associated with an LNAPL plume imaged by integrated geophysical techniques: Journal of Environmental and Engineering Geophysics, 2, 203–212.

Sauck, W. A., 2000. A conceptual model for the geoelectrical response of LNAPL plumes in granular sediments: Journal of Applied Geo-physics, 44, 151–165.

Semple, K. T., K. J. Doick, L. Y. Wick, and H. Harms, 2007. Microbial interactions with organic contaminants in soil: definitions, processes and measurement. Environ. Pollut. 150, 166–76. doi:10.1016/j.envpol.2007.07.023

Shevnin, V., O. Delgado-Rodriguez, L. Fernandez-Linares, H. Zegarra Martinez, A. Mousatov, and A. Ryjov, 2005. Geoelectrical characterization of an oil-contaminated site in Tabasco, Mexico. Geofis. Int. 44, 251–263.

Slater, L., D. Ntarlagiannis, Y.R. Personna, and S. Hubbard, 2007. Pore-scale spectral induced polarization signatures associated with FeS biomineral transformations. Geophys Res Lett 34:L21404

Tiehm, A., and S. Schulze, 2003. Intrinsic Aromatic Hydrocarbon Biodegradation for Groundwater Remediation. Oil Gas Sci. Technol. 58, 449–462. doi:10.2516/ogst:2003028

Throne-Holst, M., A. Wentzel, T. E. Ellingsen, H.-K. Kotlar, and S. B. Zotchev, 2007. "Identification of novel genes involved in long-chain n-alkane degradation by Acinetobacter sp. Strain DSM 17874," Applied and Environmental Microbiology, vol. 73, no. 10, pp. 3327–3332, 2007.

Werkema, D. D., E. A. Atekwana, A. Enders, W. A. Sauck, and D. P. Cassidy, 2003. Investigating the geoelectrical response of hydrocarbon contamination undergoing biodegradation: Geophysical Research Letters, 30, 1647, doi:10.1029/2003GL017346

Vroblesky, D.A. and F. H. Chapelle, 1994. Temporal and spatial changes of terminal electron-accepting processes in a petroleum hydrocarbon-contaminated aquifer and the significance for contaminant biodegradation. Water Resour Res 30:1561–1570

Venosa A. D. and X. Zhu, 2003. Biodegradation of crude oil contaminating marine shorelines and freshwater wetlands, Spill Science and Technology Bulletin, vol. 8, no. 2, pp. 163–178, 2003.

Ulrici, W. 2000. Contaminant soil areas, different countries and contaminant monitoring of contaminants, in Environmental Process II. Soil Decontamination Biotechnology, H. J. Rehm and G. Reed, Eds., vol. 11, pp. 5–42, 2000.

Yang, C.H., C. Y. Yu, and S. W. Su, 2007. High resistivities associated with a newly formed LNAPL plume imaged by geoelectrical techniques—a case study. J Chin Inst Eng 30:53–6.

Chapter 2

Study Site: Geological and Geochemical Characterization

2.1. Location and history

The study site is an abandoned crude oil refinery located at 130 km North-West to Paris. The refinery extends over an area of 260 hectares along the Seine River in the city of Petit-Couronne (Figure 2.1). The construction of the refinery was launched in 1928 by the Society of Petroleum Jupiter and was set in official service on March 1, 1929. The refinery was considered as a true "stronghold" of the industry in the department of Seine-Maritime, with more than 200 recruited workers. In 1933, the refinery quickly distinguished itself as one of the most modern in Europe, with a high processing rate which achieved an annual refining capacity of about 600,000 tons of crude oil. This crude oil came from the Dutch East Indies and Venezuela and was transported to the refinery by a pipeline system extending from the port of Le Havre to the city of Petit-Couronne.

In 1948, the refinery was taken over by the Shell group. In 1950, extensions and changes in the refinery structures increased the activity of storage, production and processing capacities to 2 million tons of crude oil per year. The refinery was later ranked as the second in France after achieving a distillation capacity of 10 million tons of crude oil per year in 1969. In April 2008, the Swiss group Petroplus invested the site, but due to financial problems, the company decided to sell the refinery on January 20, 2012. By April 16, 2013, the Rouen Commercial court declared permanent site closure ending any activity on it (Antea Group, Rapport A67173/A). Following the site closure, Valgo took over the site in order to study the pollution and remediate it starting from 2014.

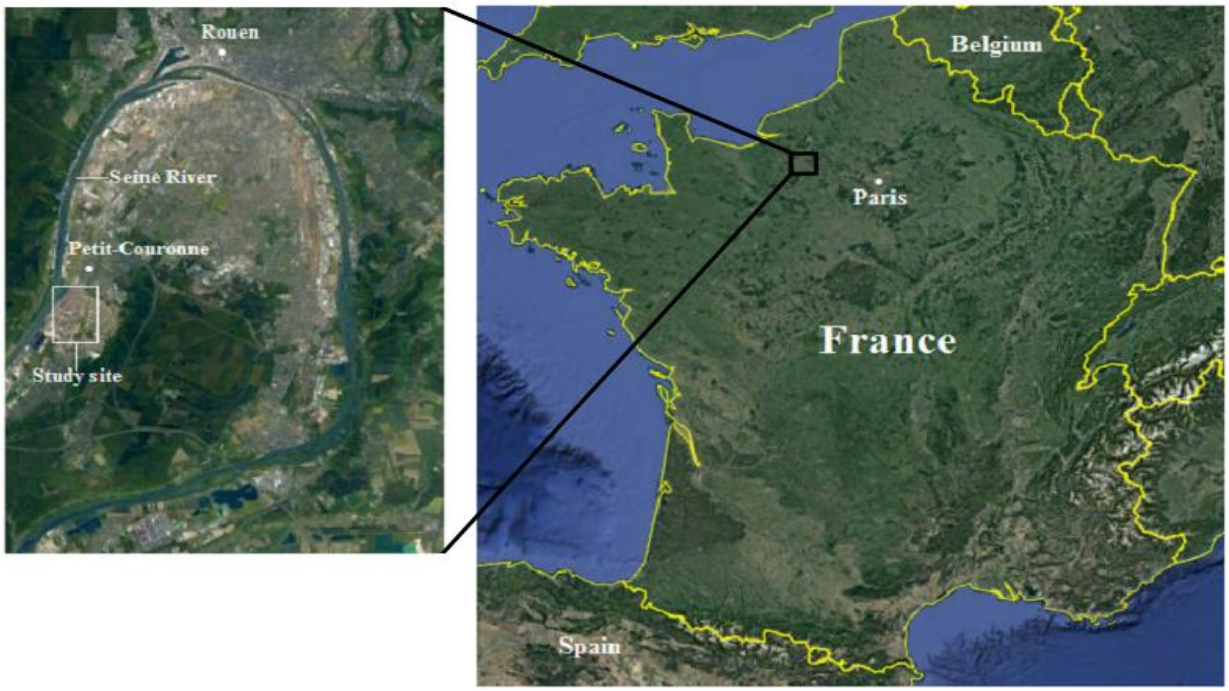

Figure 2.1: The study site location in the city of Petit-Couronne (Google Earth).

2.2. Geological and hydrogeological contexts

The refinery has an elevation ranging between 5 and 15 meters above sea level. East to the refinery, there is a storage zone which reaches an elevation of around 70 meters (Figure 2.2).

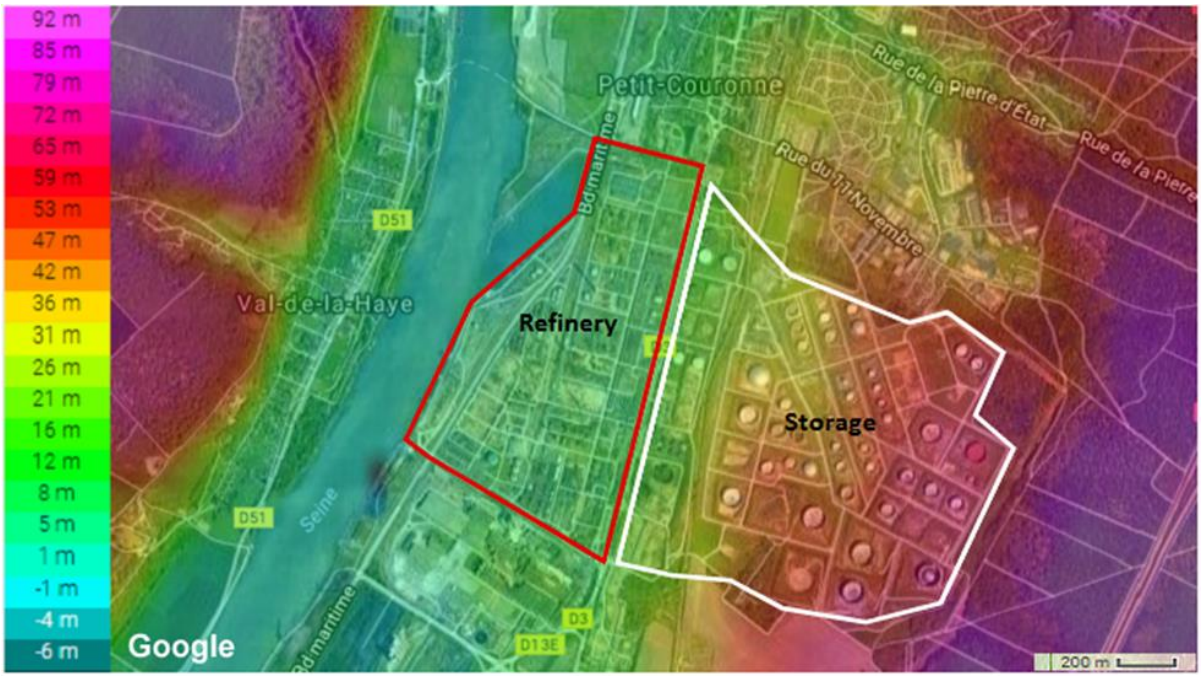

Figure 2.2: Aerial view of the refinery and the storage zone with the elevation (meter NGF) above sea level (http://fr-fr.topographic-map.com).

In terms of geology, the study site is located in the North-West of the Paris basin, on the alluvial plain of the Seine River. The geological map presented in Figure 2.3 shows that the refinery and part of the Petit-Couronne city lay on a plain of ancient alluvial formations containing sand and gravel. East to the refinery, the chalk bedrock formation rises and underlays the storage zone and part of the city.

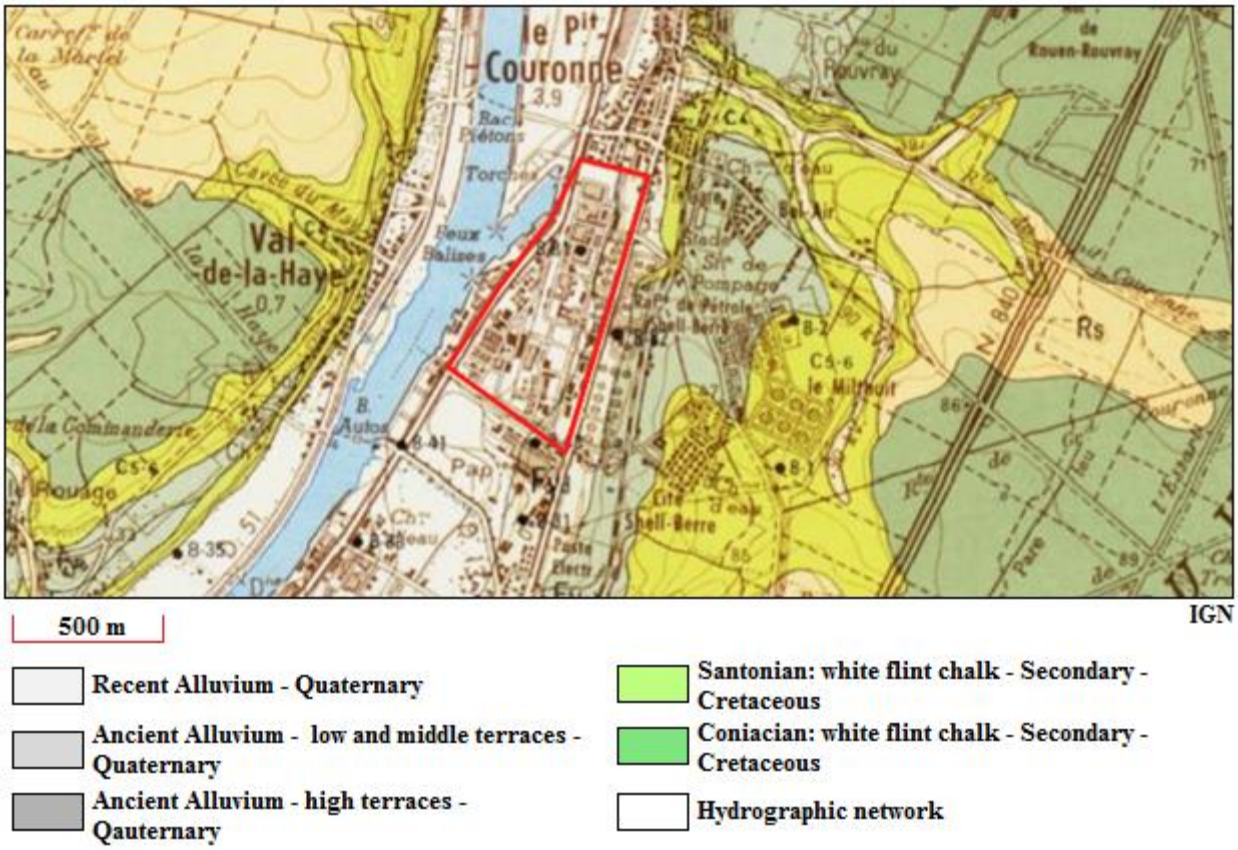

Figure 2.3: Geological map of the study site area (Infoterre, BRGM). The map shows that the study site lays on a plain of ancient alluvial deposits.

Generally, the first encountered geological entity in the site is an anthropogenic layer composed of sand and coarse grain gravel. Below, there is a layer of alluvial sediments coarsening from sand to gravel and followed by a chalk bedrock layer. Figure 2.4 shows a geological profile obtained from a borehole drilled at the South-Western border of the refinery. The profile shows a thin anthropogenic layer (0.3 m thick) overlaying a layer of alluvial deposits which reaches a depth of around 10 m. The alluvial layer is underlain by white and grey layers of chalk reaching a depth of 20 m (maximum depth of investigation of this borehole). The layers encountered during the geological surveys were generally identical on different sampling points.

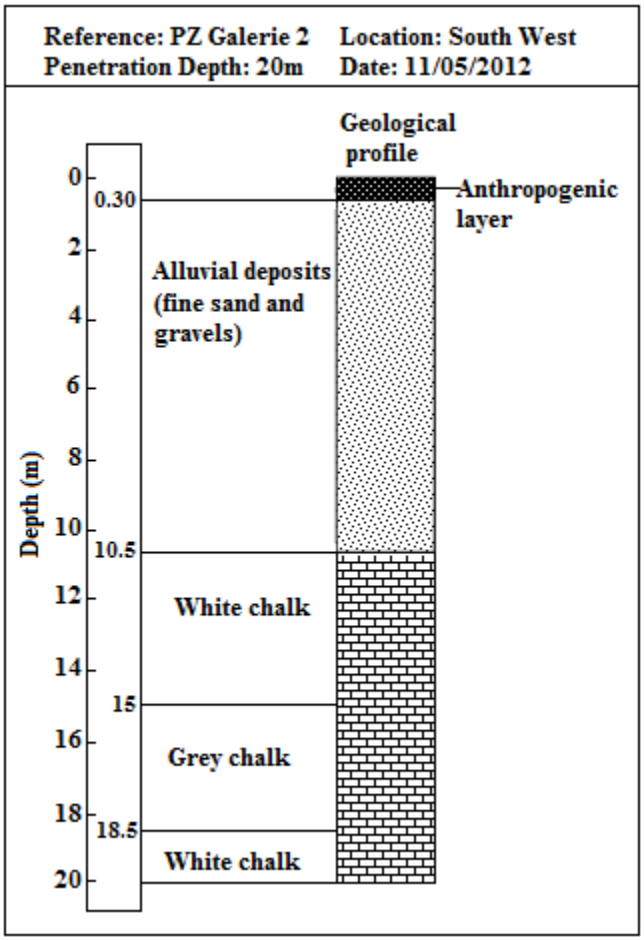

Figure 2.4: Geological profile obtained from a borehole drilled in the South-Western boundary of the site. The profile shows three different layers: an anthropogenic layer, an alluvial deposits layer and a chalk bedrock layer.

The hydrogeological setting of the site is characterized by two aquifers, an alluvial aquifer of the Seine River overlaying a chalk aquifer. The alluvial aquifer is in the layer of sand and gravel, between 4 and 12 m deep. Both aquifers of different hydrodynamic characteristics (porosity, permeability, etc.) are in hydraulic continuity and thus form a bilayer in the absence of a continuous impermeable horizon. The alluvial aquifer is characterized by permeability values ranging between 8.10^{-3} and 5.10^{-5} m/s. The chalk aquifer is characterized by transmissivity values ranging from 8.10^{-2} to 6.10^{-1} m^2 /s and permeability values ranging from $2.5.10^{-3}$ m/s to 2.10^{-2} m/s. This indicates that the geological system in the site is generally permeable with a productive reservoir having a thickness of around 30 m.

The groundwater flows generally from the South-East to the South-West towards the Seine River (Figure 2.5). The groundwater elevation is influenced by the high and low tides of the nearby River. The variations due to the tides can reach +2 m (NGF) at high tides and +1 m (NGF) at low tides. The effect of the tides decreases as the distance from the River bank increases. Along the Seine River and 500 m away from it, the amplitudes of tidal fluctuations may reach meadows of 1

to 2 m. About 700 meters away from the River, the amplitudes vary between 0.15 and 0.20 m. The tidal influence is negligible at a distance larger than 1500 meters.

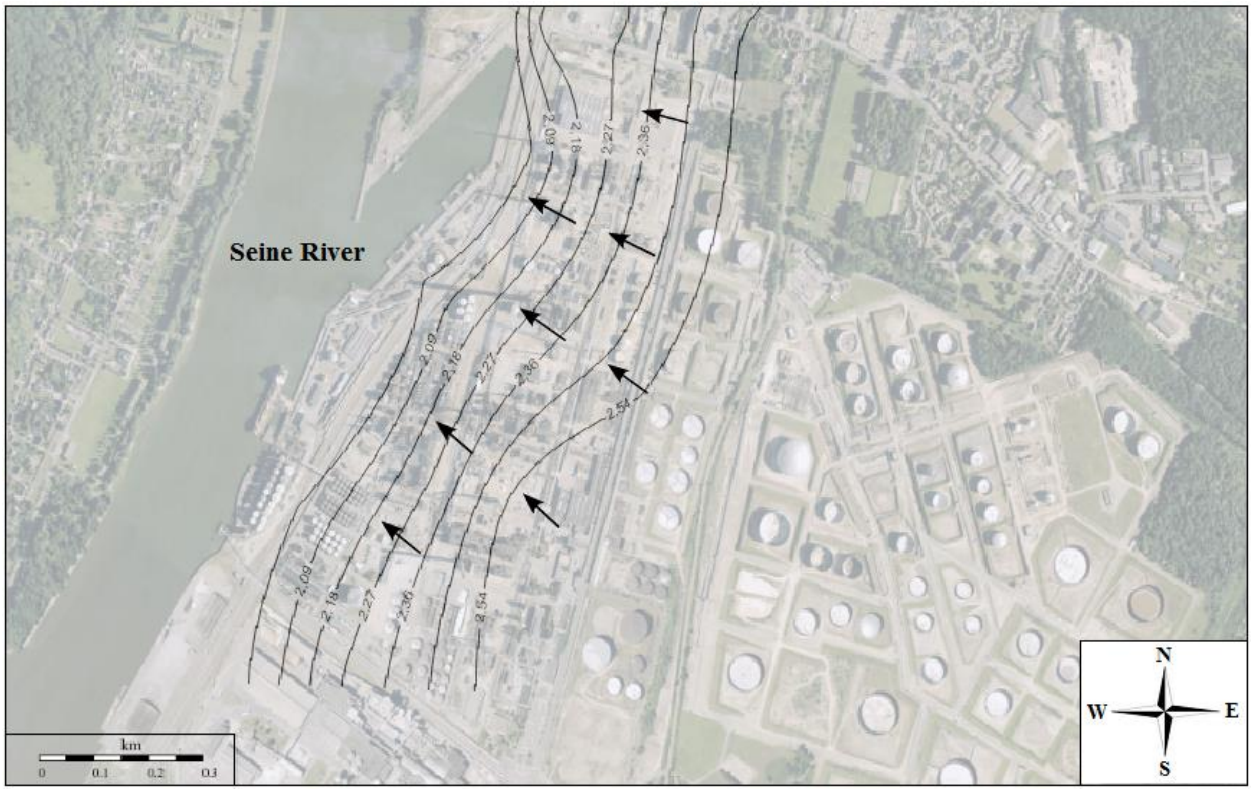

Figure 2.5: Groundwater elevation (NGF) isolines in the study site. The arrows show the direction of groundwater flow (from the South-East to the North-West towards the Seine River).

2.3. Incidents and pollution sources

The Petit Couronne refinery had an average refining activity of 6.5 million tons of crude oil per year, it was supplied with crude oil by pipelines from the port of Le Havre and had numerous distribution channels. The refinery operated various petroleum processing units derived from crude oil. The distribution of the refinery production from 100% crude oil was as follows:

- Intimate fuel 7%
- Bitumen 13%
- Kerosene 9%
- Oil 5%
- Heavy Fuel 5%
- Benzene 22%
- Diesel 17%

The refinery also had a storage zone of liquid hydrocarbons composed of sixty large tanks. Therefore, in the case of an accident or leakage, the soil and groundwater can be contaminated by various types of hydrocarbons including both LNAPL and DNAPL products.

A study which aims to investigate the history of the pollution in the refinery was conducted by ARIA (Analyse, Recherche et Information sur les Accidents), an association which identifies incidents that may affect health safety, agriculture and environment (ARIA report, 2009). The study observed hydrocarbon traces in water samples taken from the drinking water supply catchments of the city of Petit Couronne by the end of 1985. In 1986, the odors of hydrocarbons were increasingly detected in groundwater samples. This led the communities responsible for water supply and distribution to complain against the refinery. Following these complaints, the court released an order to the polluter which includes defining the polluted geographical area and proposing solutions in order to restore the quality of the catchments in the shortest period possible. According to chemical analyses of samples performed between 1986 and 1990, a mixture of 30% light products and 70% heavy products was observed at the end of 1986. On the other hand, 70% of light products and 30% of heavy products were observed in 1990. In the early 90s, hydrocarbon odors were detected again at some neighborhoods of the city. It was in July 1990 that the report of the court against the refinery was published. The court report requested the refinery to undergo a permanent pumping in order to create a drawdown cone which can limit the spreading of the contaminants. Additionally, the request included environmental monitoring of non-contaminated areas by sampling methods.

August 4, 1990, marks a major event of pollution, which was the explosion of a residential pavilion that remained empty for two weeks. The explosion was caused by a water heater installed in a basement where hydrocarbon vapors have accumulated. The study also indicated that a leak was observed in the 23rd of August 1990 in a gasoline transport pipe. This contamination source was both aerial and buried. However, many contamination events have occurred due to the refinery activities throughout its operating years (about 80 years), and not all these events are known or documented. According to the operators archives, the pollution accidents occurred due to events such as buried pipes leaks, disintegrated sewage, accidental oil spills (stripping, purging, overflow, etc.) and defective storage. The block diagram presented in Figure 2.6 shows schematically the LNAPL and DNAPL contamination partitioning scenarios (discussed in chapter 1, section 1.4) with respect to the geological setting of the refinery. It is expected that all the 4 contamination phases are present as the following:

- Free phase of LNAPL products floating on the groundwater table of the alluvial aquifer at a depth ranging between 4 and 12 m.
- Residual phase contamination in the zone above the groundwater table, generally below the contamination source zones and in other locations due to the groundwater tidal fluctuations caused by the Seine River.
- Plumes of dissolved phases of LNAPL and DNAPL products in the alluvial aquifer extending in the groundwater flow direction (towards the Seine River). However, the daily

tidal variations influence the groundwater flow direction by reversing it. This fixes the groundwater pollution and reduces the movement of the hydrocarbon plume in the aquifer.

- Free phase of DNAPL products following the topography of the aquitard at the interface between the alluvial aquifer and the chalk bedrock.

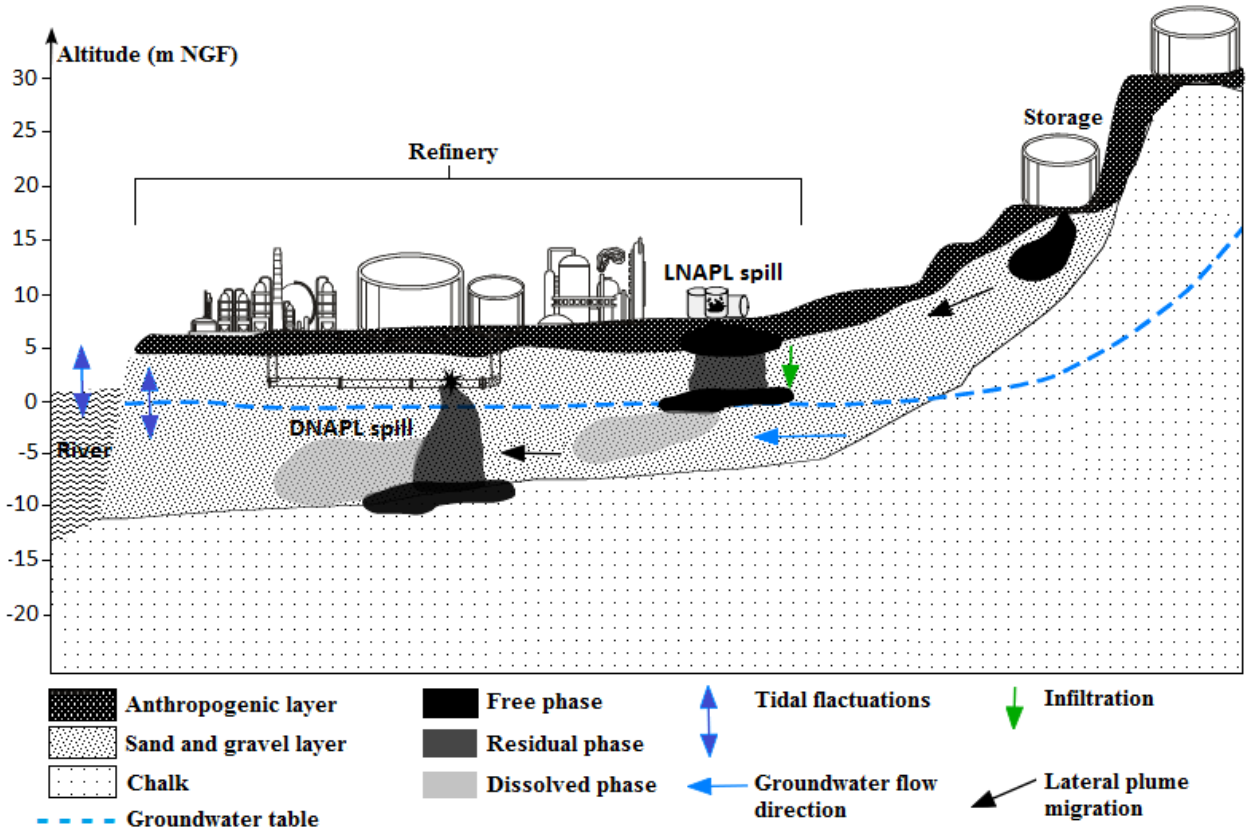

Figure 2.6: Schematic of the refinery geological structures and the partitioning of LNAPL and DNAPL products into dissolved, free and residual phases after the occurrence of oil spills.

2.4. Geochemical characterization

A number of wells divided into two groups have been installed on the site to measure different geochemical parameters of the soil and groundwater. The first group was drilled between 9 and 20 m deep by using tricone rotary drilling with water injection. The second group was drilled between 7 and 10 m deep by using the pipe jacking technique.

2.4.1. Floating phase

The investigations conducted in the wells showed two main plumes floating on the groundwater table as shown by Figure 2.7:

(1) A main plume covering half of the site with a surface area of around 200000 m^2. The plume has 3 parts:

a. A central branch located in the center of the refinery having a variable thickness. The investigations done in this zone showed plume thicknesses of 0.5 cm in B13, 49.5 cm in B19, 63 cm in B14, 67 cm in B16 and 31 cm in B18.

b. A South-Eastern branch located in the Southern boundary of the site reaching a thickness of 122 cm in B25.

c. A South-Western branch located along the South-Western boundary of the refinery. Plume thicknesses of 184 cm in B29, 207 cm in B27 and 33 cm in B26 were observed in this part of the site.

(2) A second plume exists along the North-Western boundary of the site and covers an area of approximately 14,000 m^2. This plume is associated with former oil separators and bus stations, and has a thickness of 124 cm in B32 and 14 cm in B30.

Due to access limitations and difficulties to conduct geophysical measurements, this study is limited to the central branch of the main plume, to the North-Western plume and to the Northern part of the refinery.

2.4.2. Hydrocarbons content in groundwater

A series of analyses have been conducted on groundwater samples collected from the site's boreholes in order to quantify the amount of hydrocarbons present in groundwater. The methods used for analyzing the samples were as follows:

1. Head space gas chromatography/mass spectrometry (GM/MS) to quantify the volatile C5-C10 hydrocarbons.

2. Hexane extraction gas chromatography with flame ionization detector (GC-FID) to quantify the total C10-C40 hydrocarbons.

3. Head space gas chromatography/mass spectrometry (GM/MS) to quantify the BTEX and volatile organic compounds concentrations.

4. Acetone/Hexane extraction and gas chromatography/mass spectrometry (GM/MS) for the quantification of Polycyclic Aromatic Hydrocarbons (PAH).

Results from few representative wells located in the main parts of the site will be discussed in this section. C5-C10 hydrocarbons analyses of groundwater samples indicated that the highest concentrations are found in the periphery of the zones characterized by the presence of a floating plume. Samples taken from boreholes B31 and B12 located in the North-Western part of the site recorded significant concentrations ranging from 98 to 100 mg/L. Lower concentrations ranging between 13 and 27 mg/L have been recorded in B13 and B11, while values ranging between 1.4

and 3.7 mg/L were recorded in B33 and B9 located between the North-West and the center of the site (Figure 2.7). C10-C40 hydrocarbons analyses showed similar results to those of the C5-C10 hydrocarbons, with the highest concentrations at the periphery of the zones impacted by a floating plume (Figure 2.8). Values ranging from 1.2 to 4 mg/L were recorded in B31 and B12, while values ranging from 1.6 to 6.1 mg/L were observed in B13 and B11. Wells B33 and B9 recorded values ranging between 1.3 and 2.6 mg /L.

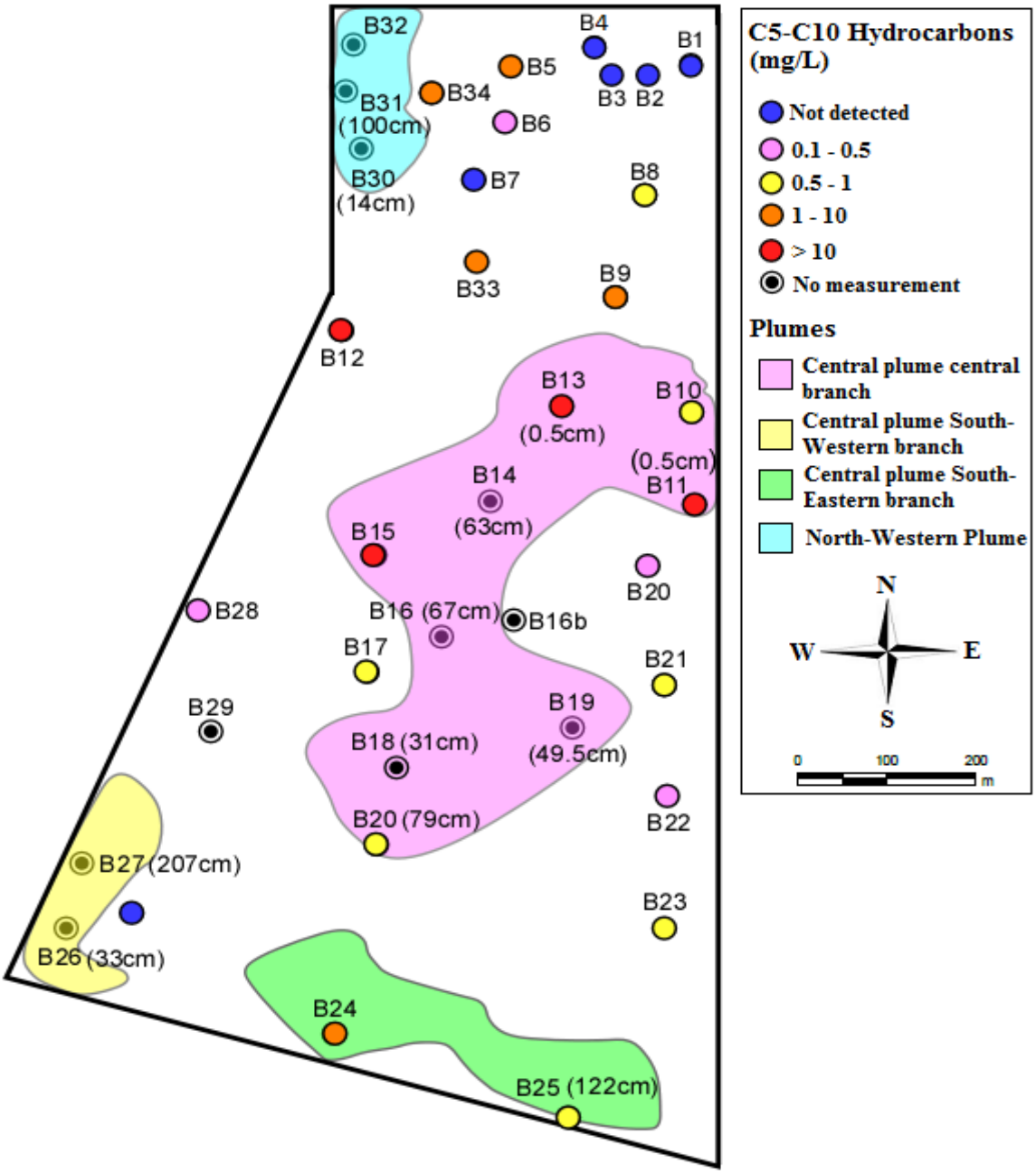

Figure 2.7: Concentration of C5-C10 hydrocarbons in groundwater and the locations of the contamination plumes.

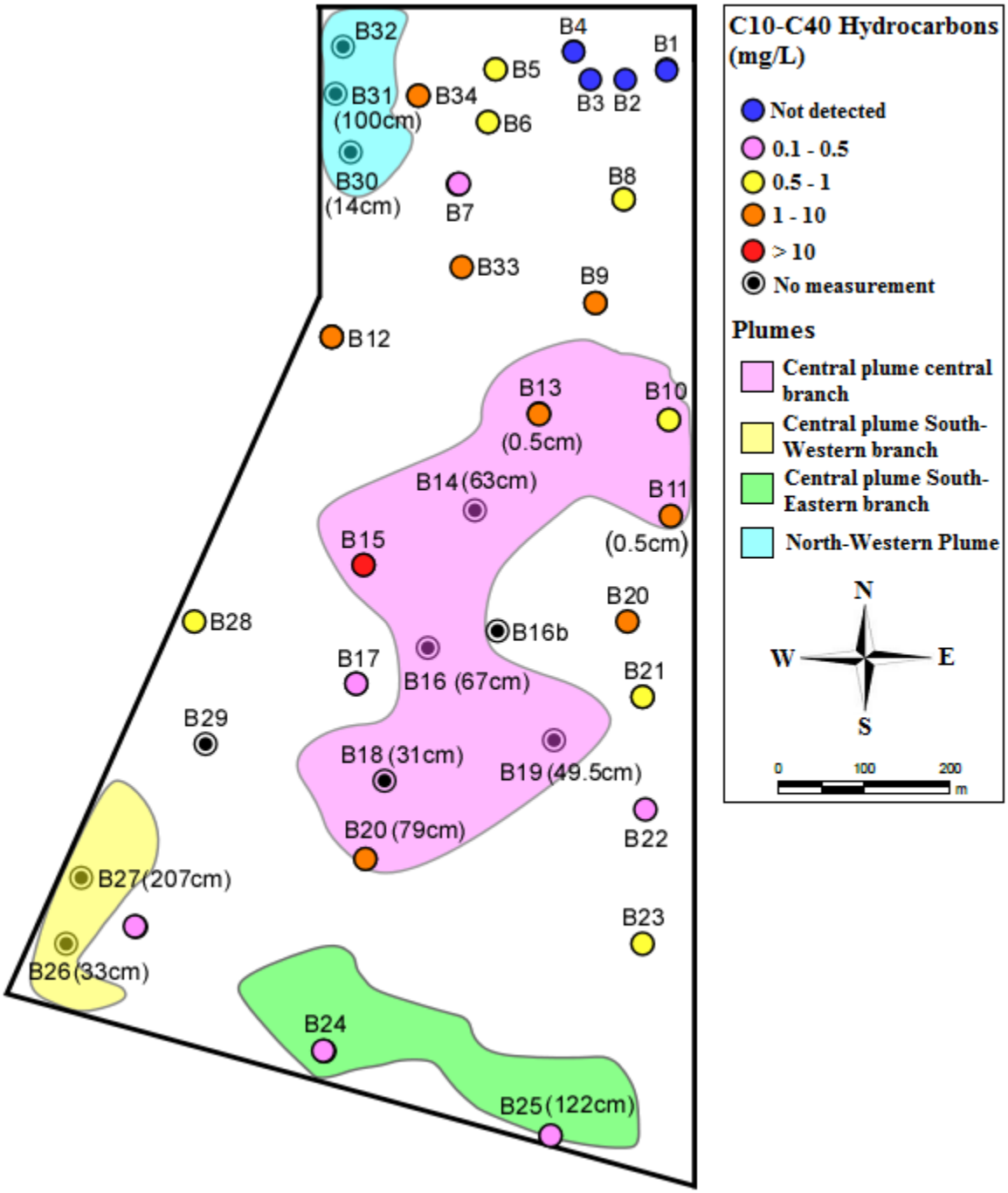

Figure 2.8: Concentration of C10-C40 hydrocarbons in groundwater and the locations of the contamination plumes.

Volatile aromatic hydrocarbons analyses of samples taken from boreholes B31 and B12 showed contents of BTEX ranging between 4.3 and 81 mg/L, with benzene concentrations ranging from 1.9 to 12 mg/L. Borehole B13 located at the North of the site showed a BTEX content of 18 mg/L, with a benzene content of 4.9 mg/L. The other boreholes located between the North-West and the center of the site showed values ranging from tens to hundreds mg/L of BTEX (10 to 20%

benzene). Additionally, PAHs measurements conducted on samples taken from B31, B12 and B13 recorded significant levels of naphthalene with values ranging from 40 to 290 g/L.

Analyses conducted on groundwater samples taken from the boreholes located in the North-Eastern part of the site (B1, B2, B3 and B4) recorded zero concentrations of hydrocarbons. This zone was considered as a groundwater clean zone and has a significant importance in our study because it could be used to determine the impact of the contamination on the groundwater chemical, biological and geophysical properties.

2.4.3. Groundwater geochemical parameters

Investigations of the total dissolved solids, dissolved oxygen and groundwater electrical conductivity (GEC) were accomplished by placing an INW (Instrumentation North West) smart sensor in each of the boreholes (Figure 2.9). Additionally, redox potential measurements were conducted on groundwater samples taken from the boreholes. The geochemical measurements showed the following:

1. Homogeneous temperature values ranging between 12.1 °C and 16.8 °C.

2. Neutral pH values ranging from 6.07 to 7.14.

3. TDS concentrations ranging from 100 to 1100 mg/L (Figure 2.10) and GEC values ranging between 442 and 2251 µS/cm (Figure 2.11). Both parameters showed higher values in the groundwater contaminated zones (e.g., B8, B9, B10, B11, B13, B20, etc.) compared to the groundwater clean zone (B1, B2, B3 and B4).

4. Dissolved oxygen values ranging from 0.18 mg/L to 3.32 mg/L, with lower values occurring in the groundwater contaminated zones (e.g., B8, B9, B10, B11, B13, B20, etc.) compared to the clean groundwater zone (Figure 2.12).

5. Redox potential values ranging between -304 mV and 21.8 mV (Figure 2.13), with positive values mostly occurring in the clean groundwater zone (B1, B2, B3 and B4), and negative values in the contaminated zones (e.g., B8, B9, B10, B11, B13, B20, etc.).

Figure 2.9: The INW smart sensor which was used to measure geochemical parameters such as the concentration of total dissolved solids and groundwater electrical conductivity.

The high values of TDS and GEC are consistent with the presence of large amounts of organic carbon and low dissolved oxygen concentrations. These observations, that showed significant differences in the measured geochemical parameters between the contaminated and clean zones, suggest that biodegradation of hydrocarbons is occurring in the contaminated aquifer. However, borehole B5 showed lower GEC and TDS values compared to other contaminated locations. These lower values are attributed to the constant flushing of clean groundwater at the boundary of the plume, which can replace the high salinity contaminated groundwater in the groundwater flow direction.

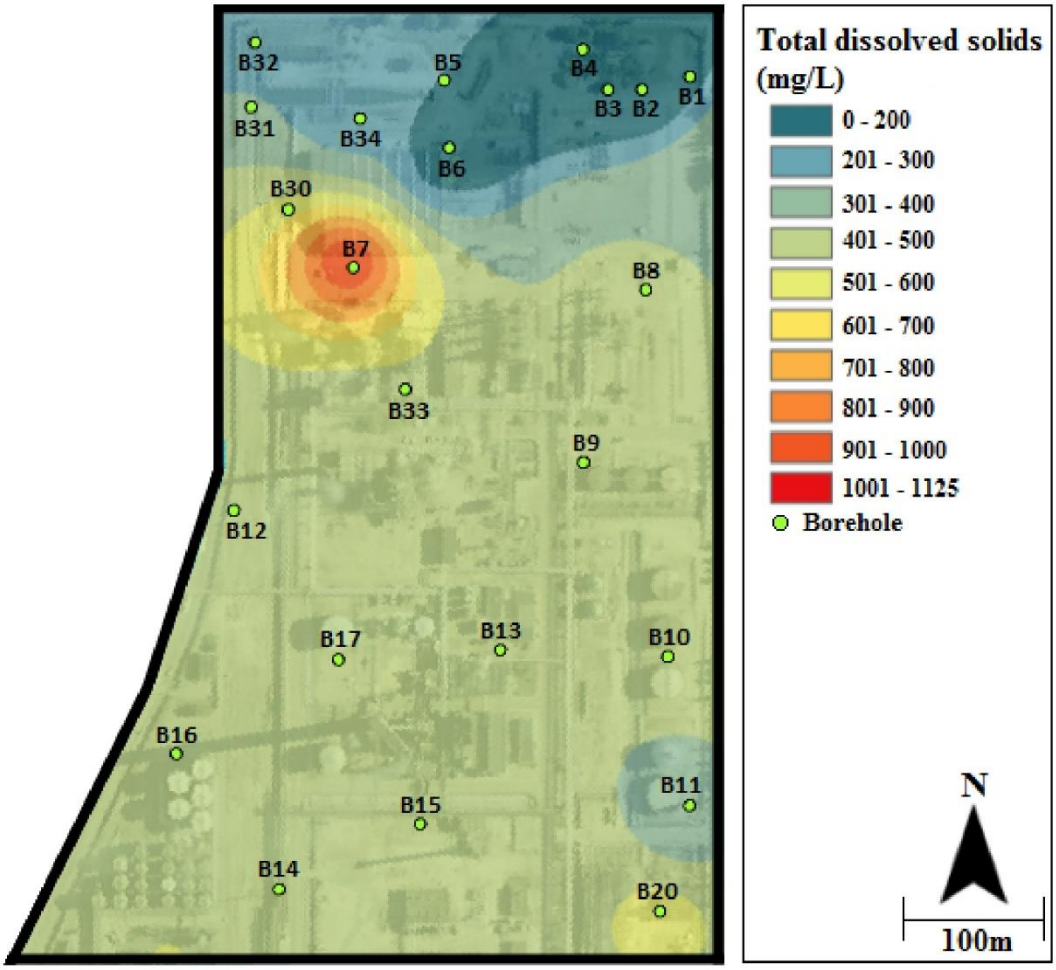

Figure 2.10: The concentrations of total dissolved solids (TDS) measured in the site's boreholes overlaying an aerial photo of the site. The map shows higher TDS concentrations close to the contaminated zone boreholes (e.g., B13, B7, B8, B33, etc.).

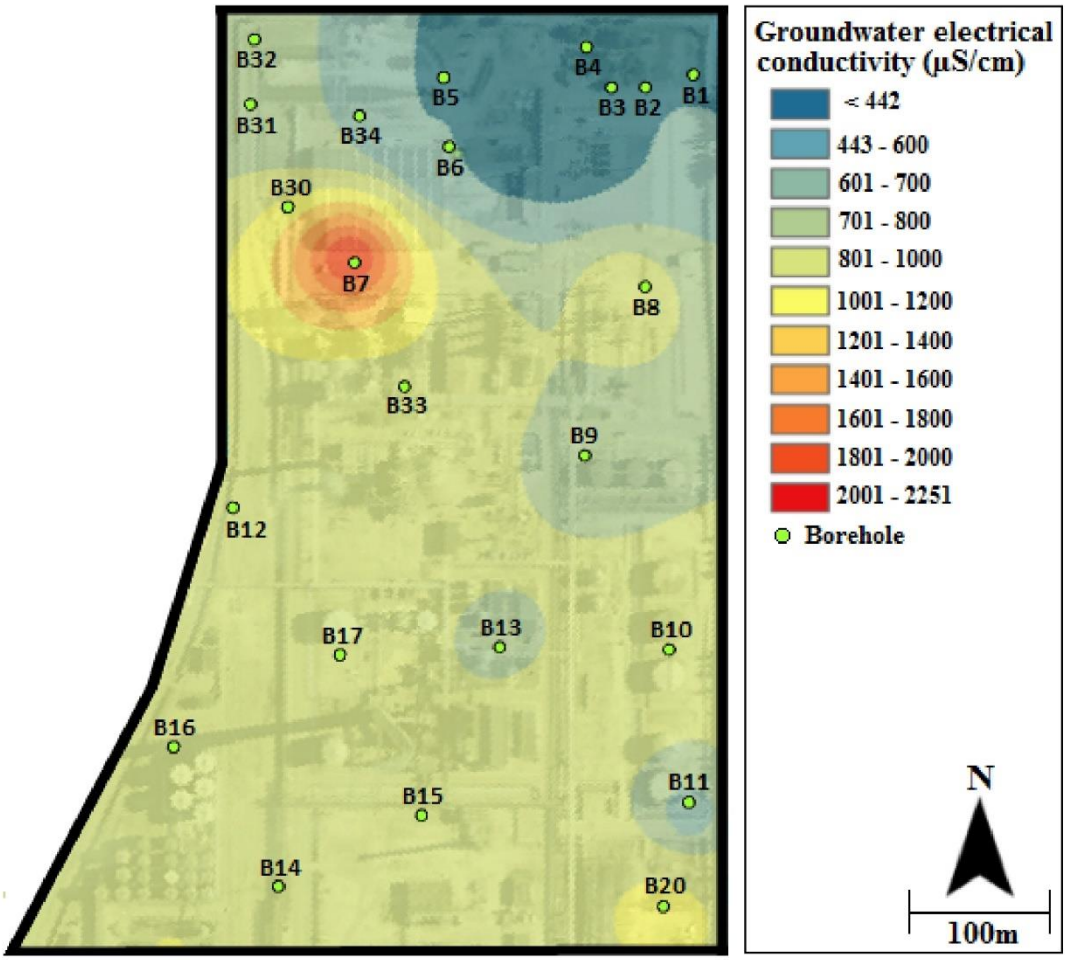

Figure 2.11: The distribution of groundwater electrical conductivity measured in the site's boreholes overlaying an aerial photo of the site. The map shows higher electrical conductivity values close to the contaminated zone boreholes (e.g., B10, B13, B7, B8 and B33).

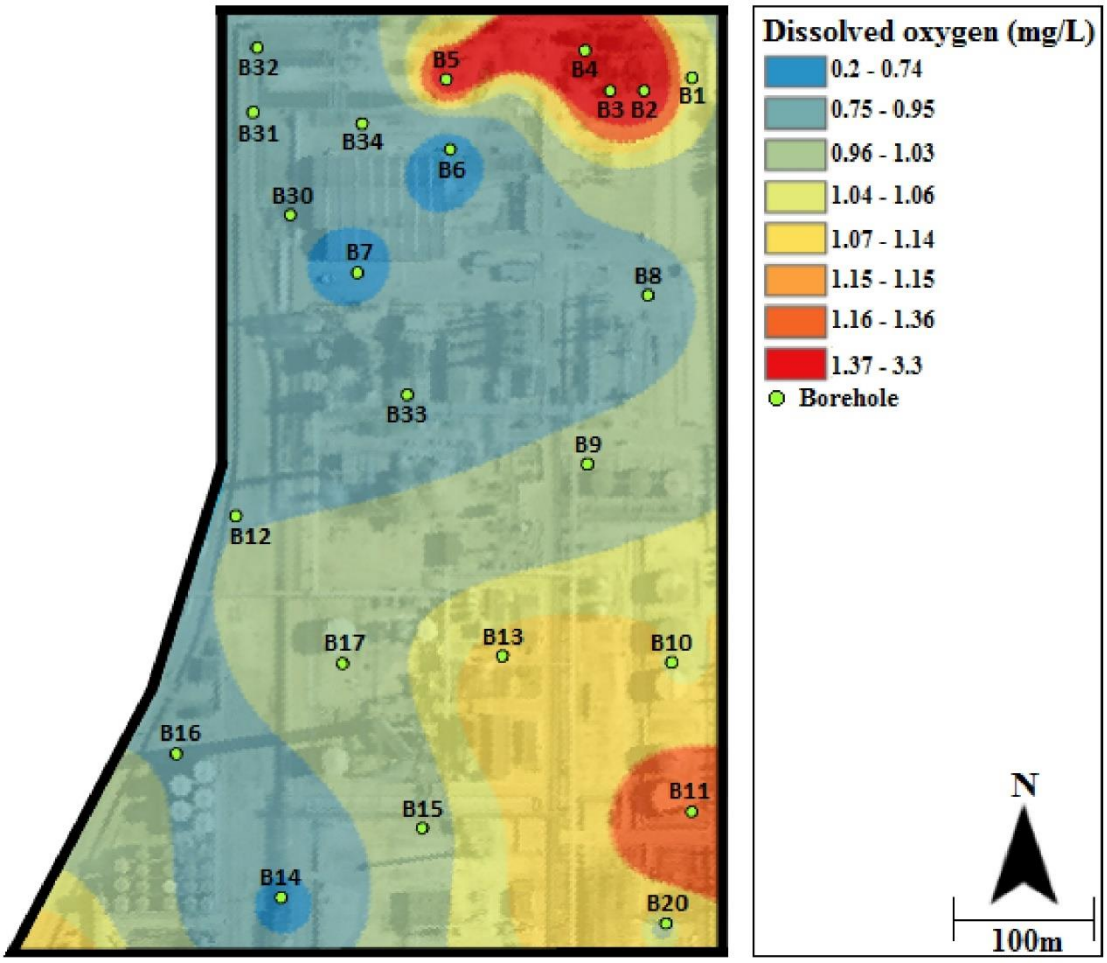

Figure 2.12: The concentrations of dissolved oxygen measured in the site's boreholes overlaying an aerial photo of the site. The map shows low dissolved oxygen concentrations close to the contaminated zone boreholes (e.g., B13, B7, B8, B33, etc.).

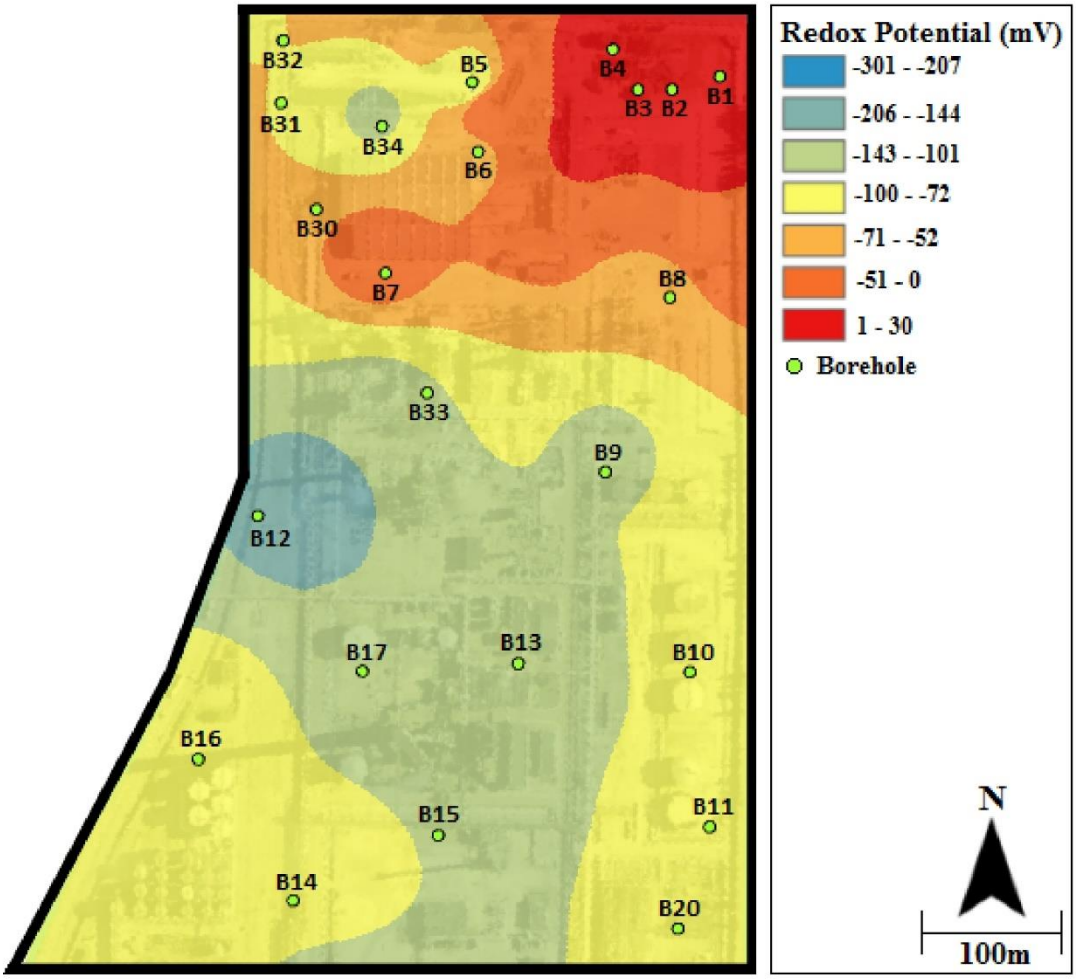

Figure 2.13: The distribution of redox potential measured in the site's boreholes overlaying an aerial photo of the site. The map shows negative redox potential values close to the contaminated zone boreholes (e.g., B10, B13, B7, B8 and B33) and positive redox potential values close to the clean zone boreholes (e.g., B1, B2, B3 and B4).

2.4.4. Scanning electron Microscope

Scanning electron microscope (SEM) Zeiss evo Ep 40 was used to image the soil samples and to perform mineralogical and geochemical characterization of rocks at the micrometer scale. Coating of the soil samples prior to examination by the SEM is required to improve the imaging quality by creating a conductive layer of metal. This layer inhibits charging, reduces thermal damage and improves the secondary electron signal required for topographic examination. We used carbon coating which is mainly used to prepare samples for X-ray microanalysis. When the carbon source is heated to its evaporation temperature, a fine stream of carbon is deposited on the specimens. The coated samples are then passed through the SEM and the data acquisition is done via a computer connected to the microscope. Images with a resolution in the order of 2 to 20 nm were obtained and the chemical elements were mapped via the X-ray microanalysis. SEM images

of contaminated sediments showed that mineral grain surfaces are etched and pitted compared to images of clean soil samples (Figures 2.14 and 2.15). These remarkable dissolution features suggest intense mineral surfaces alterations by microbial processes (McMahon et al., 1995).

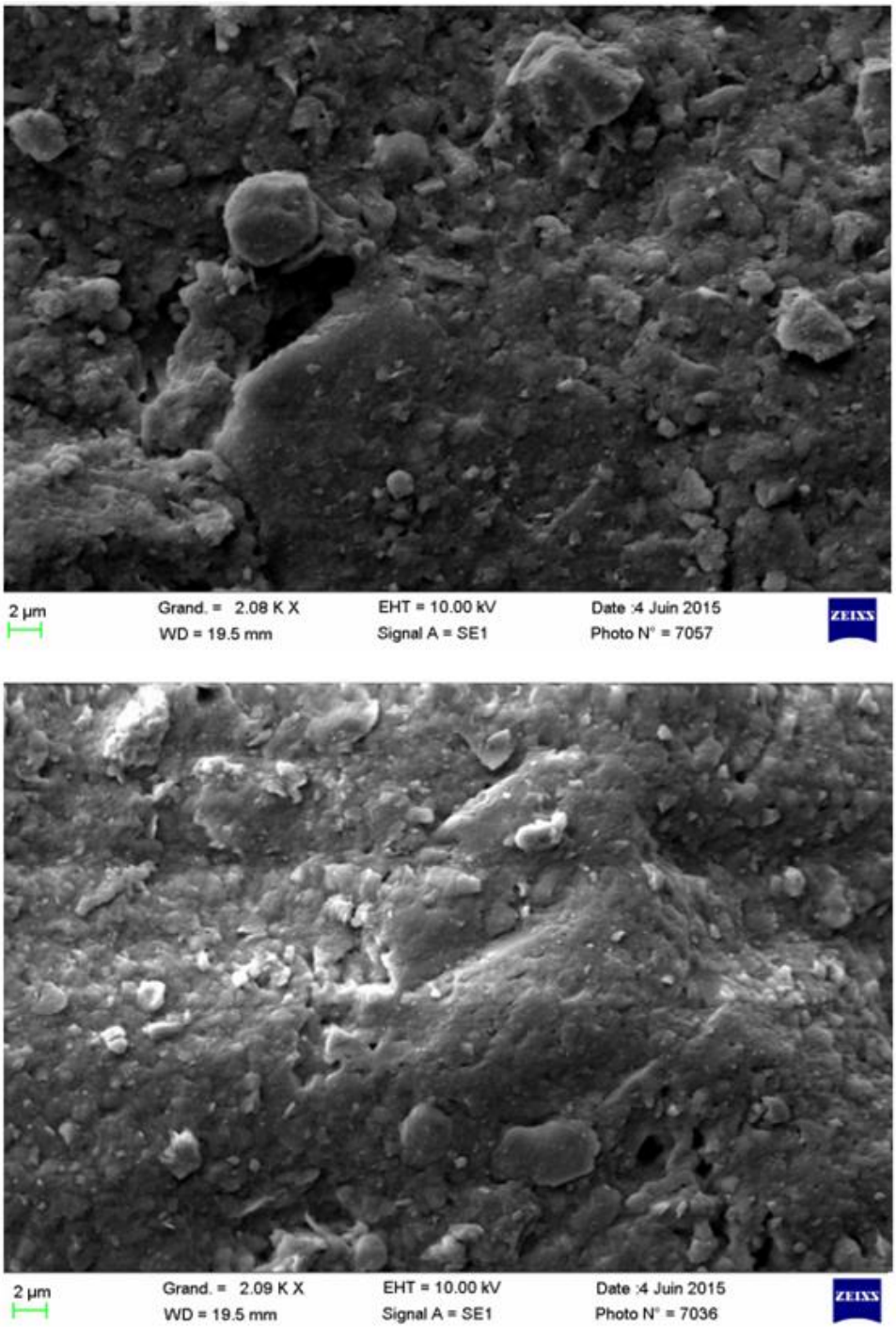

Figure 2.14: SEM images of contaminated soil samples showing etching and pitting patterns caused by bacterial mediated minerals weathering.

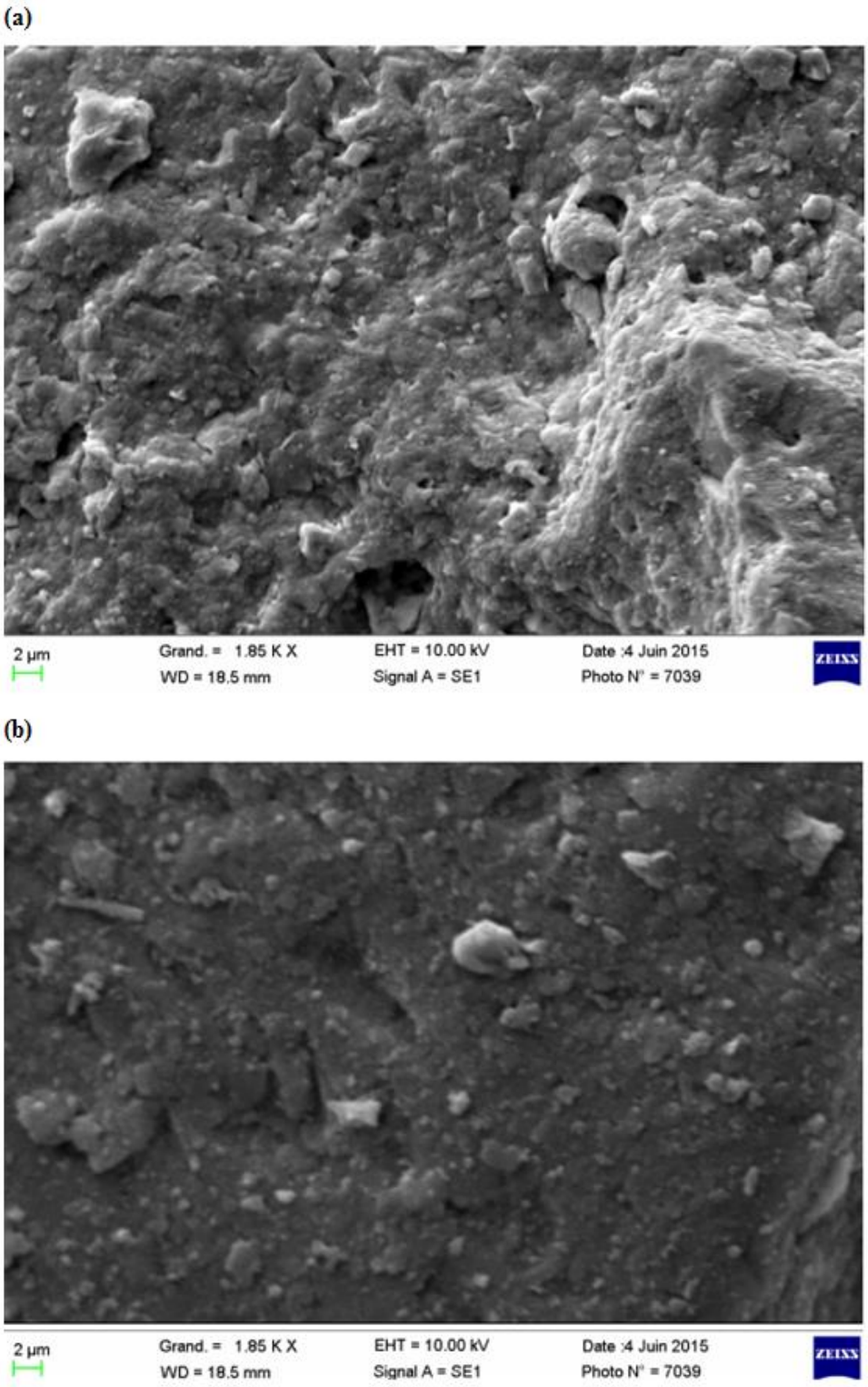

Figure 2.15: SEM images of a contaminated (a) and a clean soil sample (b). The images show minerals weathering features which are present only in the contaminated sample.

2.4.5. Spectrocolorimetry

The sediment color is considered as an important parameter which can be used to describe sedimentary facies in a qualitative way. In this sense, the spectrocolorimetric analysis has been always considered as an environmental proxy, which permits the precise identification of sediments constituents such as iron, carbonates and clays. First derivative reflectance spectra (FDS) method was proposed as a tool to determine sediment's mineralogical composition (Barranco et al., 1989; Balsam and Deaton, 1991; Deaton and Balsam, 1991). According to the FDS method, the sedimentary components can be identified according to the position of the first derivative peak, in a way that each component has its distinctive spectral signature. For example, different studies have documented spectral signatures between 445 and 575 nm for iron oxides, and between 605 and 695 nm for organic compounds.

Spectrocolorimetric analyses were conducted on soil cores by using a Minolta CM 2600d spectrocolorimeter. Throughout the measurement, the surficial layer of sediments was removed, after which a polyethylene film was placed on each soil core with caution taken to avoid the formation of air bubbles and folds. The measurements were then performed with a 1 cm sampling interval. We used the protocol of Balsam et al. (1997) and calibrated the device without the film since it is programmed to receive a given reflectance value for standard white. According to international standards and to published measurements done on iron-rich deposits (Balsam and Beeson, 2003; Damuth and Balsam, 2003), the signature of the first derivative spectrum shows a clear presence of iron deposits in the contaminated soil samples, indicated by the peaks between 545 and 575 nm (Figure 2.16). The peaks identified in the organic matter domain ranging from 600 to 700 nm indicate the presence of altered organic matter. In terms of sediments composition, this means that the contaminated sediments contain iron-rich deposits and altered organic matter.

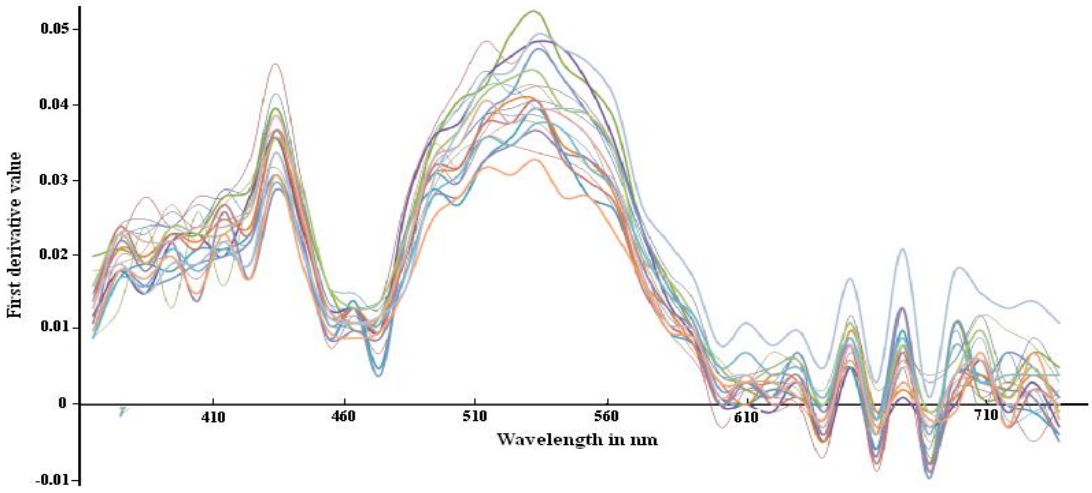

Figure 2.16: The Spectrocolorimetry results showing peaks related to iron deposits (545-575 nm) and altered organic matter (600-700 nm).

Chapter 3

Geophysical Methods

3.1. Electrical resistivity

Electrical resistivity tomography is one of the most commonly used geophysical techniques which can provide 1D, 2D, 3D and 4D images that describe the distribution of electrical resistivity in the subsurface. Significant advancements over the past two decades demonstrated the electrical resistivity method as an efficient tool which can be used in various environmental applications, including contaminated land investigations (Loke, 1991; Atekwana and Atekwana, 2010). The electrical resistivity determines the capacity of a material to allow charges to flow freely through it. Therefore a high resistivity structure is a structure which readily allows the movement of electrical current. The electrical resistivity $\boldsymbol{\rho}$ is the inverse of the electrical conductivity $\boldsymbol{\sigma}$:

$$\sigma = \frac{1}{\rho} . \quad (1)$$

3.1.1. Electrical Conduction and Resistivity (Theory)

The electrical conductivity/resistivity depends on the conduction phenomena and the circulation of free charges under the effect of an electrical field. The subsurface is considered as a complex system consisting of solid grains with pore spaces which could be partially or totally filled with various fluids having various chemical properties (e.g., salinity). The different phases present in the soil system contribute differently to the bulk electrical resistivity measured in the field and influence the resistivity response according to the different conduction processes:

1. Surface conduction which is controlled by the physical and electrical properties of the electrical double layer (EDL) located at the interface between the solid grains and the pores electrolytic solution.
2. Electronic conduction which is linked to the movement of electrons through metallic conductors such as disseminated minerals (e.g., sulfides and oxides).
3. Electrolytic conduction which is linked to the movement of ions dissolved in the pore fluid. This phenomenon depends on the electrical conductivity of the pore fluid solution, the porosity and the fluid saturation degree.

According to experiments done by Archie between the late 1920s and the early 1930s, the bulk electrical resistivity $\boldsymbol{\rho_0}$ of a rock material is directly proportional to the pore fluid electrical resistivity $\boldsymbol{\rho_w}$. In the case of fully saturated rocks:

$$\rho_0 = F.\rho_w , \quad (2)$$

where $\boldsymbol{F}$ is the formation factor which is related to the rock matrix. The formation factor is influenced by the variability of porosity in rocks and by the connectivity of its corresponding pore spaces:

$$F = \theta^{-m} , \quad (3)$$

where $\boldsymbol{\theta}$ is the porosity and $\boldsymbol{m}$ is the cementation index which is related to changes in the pore space pathways referred to as the tortuosity (Ellis and Singer, 2007).

The combination of equations (2) and (3) results in what is known as Archie's first law:

$$\rho_0 = \rho_w \theta^{-m}. \quad (4)$$

Therefore, the bulk electrical resistivity of a rock material can vary according to: (i) changes in the rocks properties (lithology, porosity, etc.) which can influence the formation factor and cementation index and (ii) changes in the pore fluid properties (e.g., water content, chemical composition, temperature, etc.) which can influence the pore fluid electrical resistivity (Palacky, 1987; Breede et al., 2012; Slater et Lesmes, 2002; Revil et al., 2011).

The electrical resistivity theory is based on Ohm's law that describes the flow of electrical current in a material by relating the current density $\boldsymbol{J}$ (in A m^{-2}) to the electrical field intensity $\boldsymbol{E}$ (in V m^{-1}) and the electrical conductivity $\boldsymbol{\sigma}$ by the equation of Tsourlos (1995):

$$J = \sigma . E \ . \quad (5)$$

The relationship between the electrical potential $\boldsymbol{\varphi}$ which is measured in practice and the electrical field intensity $\boldsymbol{E}$ is given by:

$$E = -\nabla\varphi \ . \quad (6)$$

Combining equations (5) and (6), we get:

$$J = -\sigma\nabla\varphi \ , \quad (7)$$

Therefore, the current density is dependent upon the distribution of the electrical potential in the subsurface and the electrical conductivity of the medium. The distribution of the electrical potential in the subsurface (in an inhomogeneous anisotropic medium) is given by the following *Laplace* equation:

$$\nabla . (\sigma\nabla\varphi) = 0 \ . \quad (8)$$

In practice, the electrical resistivity method comprises injecting direct current into the subsurface by using current electrodes, and then, determining the distribution of the apparent electrical resistivity by measuring the electrical potential difference between two potential electrodes (Loke, 1991). The electrical resistance of an electrical conductor is given by the simplified form of Ohm's law as:

$$R = \frac{\Delta v}{I} \ , \quad (9)$$

where $\Delta\boldsymbol{v}$ is the electrical potential and $\mathbf{I}$ is the electrical current intensity. The resistivity measured at the field is multiplied by a geometric factor $\boldsymbol{K}$ to obtain the apparent electrical resistivity in a homogenous half space:

$$K = \frac{2\pi}{\left(\frac{1}{r_{AM}} - \frac{1}{r_{BM}}\right) - \left(\frac{1}{r_{AN}} - \frac{1}{r_{BN}}\right)}, \quad (10)$$

where ***r*** is the distance between the potential electrodes (M and N) and the current electrodes (A and B). ***K*** is the configuration (geometric) factor which describes the arrangement of the electrodes and is different for each configuration array. Combining equations (9) and (10), the apparent electrical resistivity can be written as:

$$\rho_a = \frac{\Delta V}{I} K, \quad (11)$$

and

$$\rho_a = \frac{2\pi\Delta v}{I \times \left[\left(\frac{1}{r_{AM}} - \frac{1}{r_{BM}}\right) - \left(\frac{1}{r_{AN}} - \frac{1}{r_{BN}}\right)\right]}. \quad (12)$$

3.1.2. Induced polarization effect

Upon applying an electrical current, the subsurface constituents become polarized and form a natural battery. After switching off the current source, the study of the decaying potential as a function of time is known as the induced polarization (IP) technique (Bleil, 1953; Hallof, 1957; Madden and Neves, 1957; Telford et al., 1997; Vacquier et al., 1957). This method is sensitive to the capacitive properties of rocks and sediments which are influenced by lithology and changes in the pore fluid chemistry (Atekwana and Atekwana, 2010). The induced polarization effect is similar in principle to charging a capacitor or a battery, and is observed as a delay of the voltage response (Naudet, 2004). The polarizability describes the capacity of the subsurface materials to store electrical charges and is influenced by parameters such as the electrical conductivity and the dielectric permittivity, which define how easily a material can become electrically charged.

The induced polarization phenomena is a current induced effect which takes place at the interface between the mineral grains and the pore fluid electrolyte (Allaud and Martin, 1977). The impedance of the mineral electrolyte interface has been a subject for many laboratory studies which aimed to understand its associated physio-chemical mechanisms (Angoran and Madden, 1977; Klein et al., 1984; Lesmes and Morgan, 2001; Lesmes and Frye, 2001; Olhoeft, 1985; Ward and Frazer, 1967). These studies showed that the capacitive impedance of the current passage is linked to an electrical double layer forming at the mineral-fluid interface. The EDL forms as a result of the attraction between the negative ions adsorbed on the solid grain surface and the opposite polarity ions in the electrolyte. The EDL constitutes of 2 layers: a fixed layer resulting from the attraction between the negative ions at the mineral surface and the cations of the pore fluid (referred to as the stern layer); and a layer of the electrolyte mobile cations referred to as the diffuse layer (Figure 3.1).

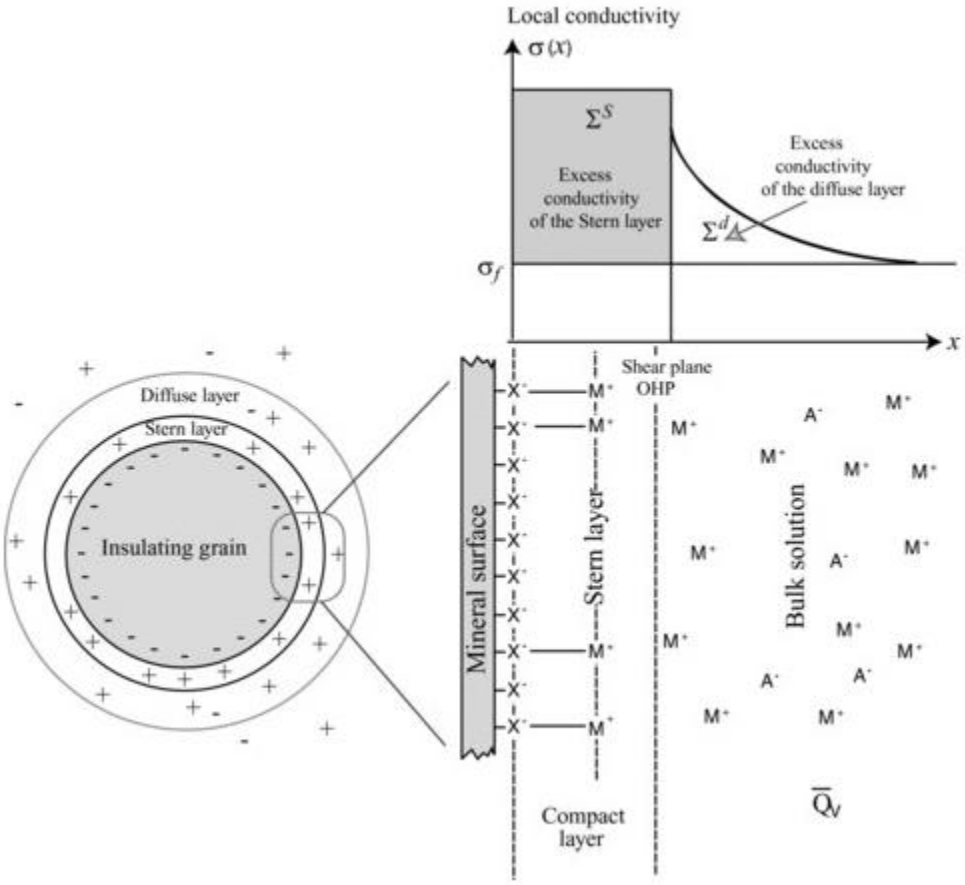

Figure 3.1: Illustration of the electrical double layer which forms at the mineral-electrolyte interface (Schmutz et al., 2010).

The IP effect is associated with excess charge build-up in the pore fluid electrolyte which is considered as the current conduction path. The excess charge build-up may result from decreased mobility of the ionic charge carriers or from blockage of the pore current conduction path (Sogade et al., 2006). The process by which the conduction path is blocked defines two types of polarization mechanisms. The first is the electrode polarization which includes the blockage of the conduction path by conductive mineral grains such as disseminated minerals (e.g., pyrite and graphite) (Telford et al., 1990). The charges present at the mineral surface attract the charges of the pore fluid and form an EDL at the interface between the grain surface and the pore fluid (Figure 3.2). In this case, the current conduction mechanism changes from ionic to electronic.

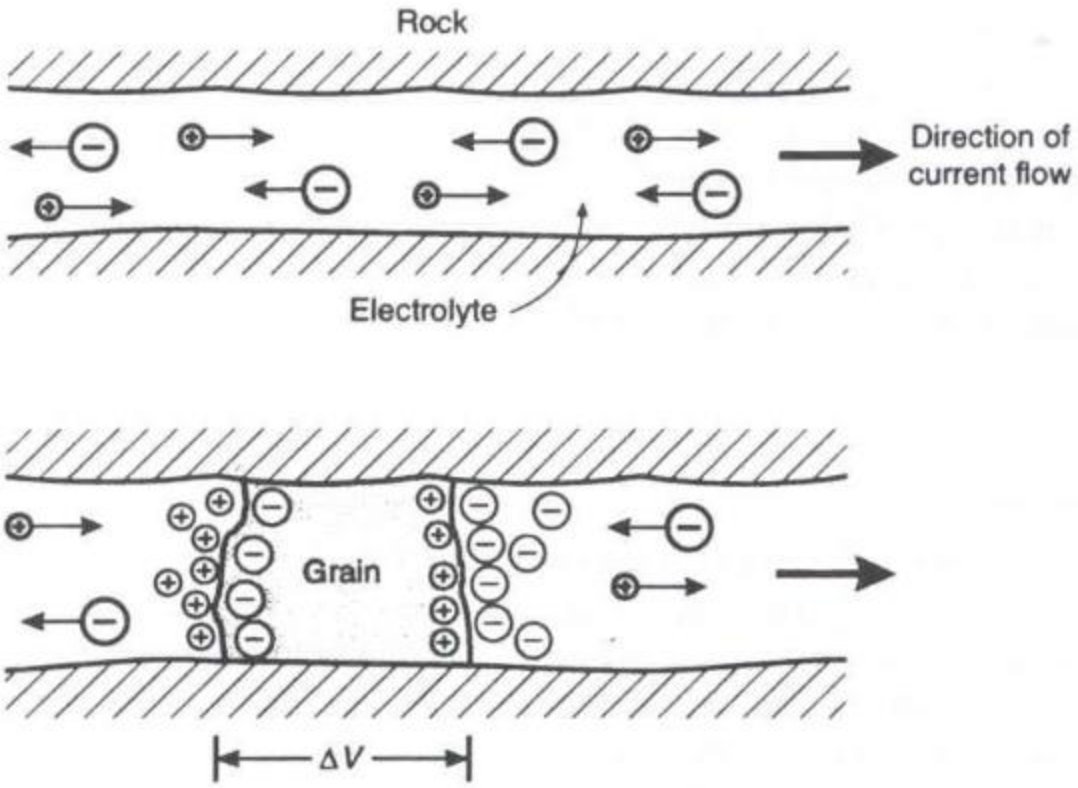

Figure 3.2: The electrode polarization mechanism. The current conduction path is blocked by a conductive mineral grain (Reynolds, 1997).

The second polarization mechanism is the membrane polarization which includes the blockage of the conduction path by a thick diffuse layer. This thick diffuse layer reduces the mobility of ion charge carriers by acting as a selective membrane which allows the passage of ions with certain size and polarity (Kemna, 2000; Slater et al, 2005; Ward, 1990). This kind of polarization referred also to as membrane electrolytic polarization can be caused by two different processes. The first one is due to constrictions within the pores channels, where the positive charges of the pore fluid build a layer with a thickness up to 100 µm. When a voltage is applied, the thick positively charged layer blocks the flow of ions and produces a potential difference across the constriction zone (Figure 3.3). The second process is due to the presence of negatively charged clay particles which attract the positive ions of the pore fluid and form an electrical double layer. This layer acts as an impervious membrane which blocks the flow of other ions and causes the polarization of the medium (Figure 3.4).

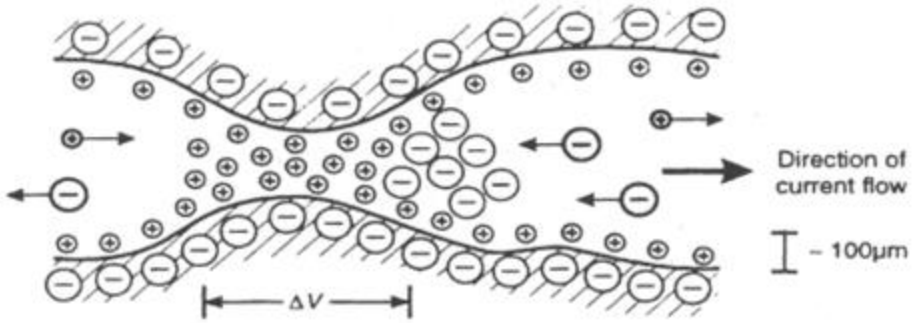

Figure 3.3: Membrane polarization due to a constriction in the pore channel (Reynolds, 1997).

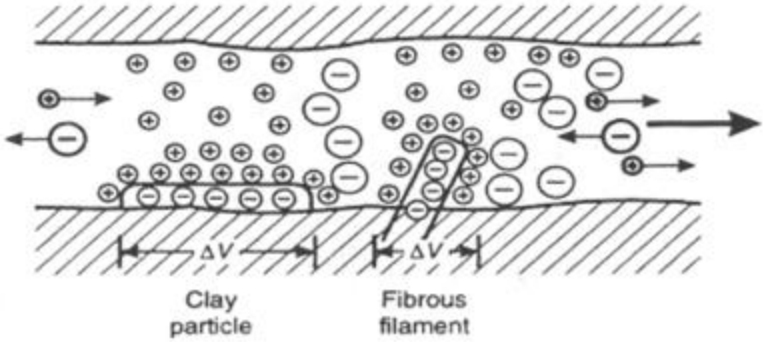

Figure 3.4: Membrane polarization caused by the presence of negatively charged clay minerals (Reynolds, 1997).

The IP can be measured in both time and frequency domains. The frequency domain IP investigates the influence of soil polarization on the phase shift between the current signal and the voltage. The time domain IP measurement is acquired by injecting current and then measuring the decay of the primary voltage $\boldsymbol{V_p}$ (with time) after switching off the current source. The observed voltage doesn't drop off to zero directly after switching off the source, but instead, it drops to a secondary voltage $\boldsymbol{V_s}$ which is lower than $\boldsymbol{V_p}$. The secondary voltage diminishes with time in a rate which depends on the polarization of the medium (Figure 3.5).

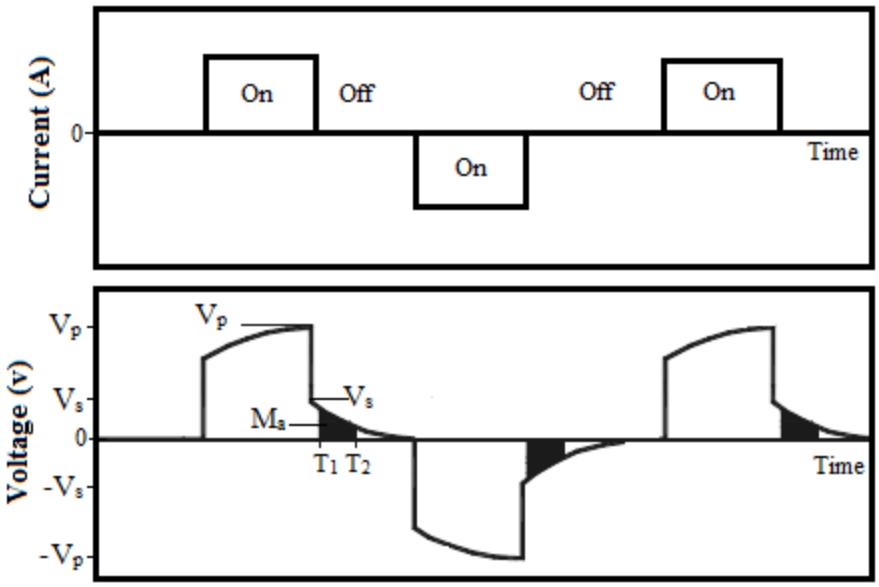

Figure 3.5: The voltage decay mechanism after turning off the current injection source. The measured apparent chargeability is the area below the secondary voltage decay curve.

The IP effect in the time domain is measured by the chargeability ***m*** which is defined as the ratio between the secondary and the primary voltages $\boldsymbol{V_s}$ and $\boldsymbol{V_p}$:

$$m = \frac{Vs}{Vp} . \tag{13}$$

The value of $\boldsymbol{V_p}$ depends on the selected time on the potential decay curve (t). Therefore, in the field, ***m*** is measured as the integrated apparent chargeability ($\mathbf{M_a}$). $\mathbf{M_a}$ is defined as the area under the decay potential curve and is obtained from the integral of the decaying secondary voltage $\boldsymbol{V_s}$ (t) over a time interval on the discharge curve (T_1 to T_2), divided by the primary voltage $\boldsymbol{V_p}$:

$$M_a = \frac{1}{V_p} \int_{T1}^{T2} V_t(dt) . \tag{14}$$

Dividing the integrated apparent chargeability $\boldsymbol{M_a}$ by the electrical resistivity $\boldsymbol{\rho}$ gives the normalized chargeability $\boldsymbol{M_N}$ which quantifies the amplitude of polarization:

$$M_N = \frac{M}{\rho} . \tag{15}$$

$\boldsymbol{M_N}$ is independent of the bulk electrical resistivity and more sensitive to geochemical conditions such as the groundwater electrical conductivity (Slater and Lesmes, 2002).

3.1.3. Measurement Principles

Several types of investigations that aim to obtain the distribution of electrical resistivity and chargeability of the subsurface can be conducted by using the electrical resistivity method. The method employs a certain number of quadripoles to inject the current and then measure its

corresponding potential difference. The obtained potential difference is then used to calculate the electrical resistivity which is sensitive to different chemical and physical parameters of the subsurface (as described earlier in the theory section). Induced polarization measurements are also done by measuring the decaying potential as a function of time after turning off the electrical current source. In the one-dimensional approach, two potential electrodes are fixed at a defined distance, whereas the distance between two current electrodes is gradually increased. The apparent electrical resistivity is then obtained and plotted against the electrodes spacing on a log-log plot. This will result in 1-D vertical information at the midpoint between the potential electrodes.

To get information about the horizontal and lateral apparent resistivity distributions, one should conduct 2-D studies referred to as electrical resistivity tomography (ERT). The ERT approach works in a similar manner to the 1-D approach with the difference that the electrodes are moved across a profile line (Figure 3.6). The distance between the current and potential electrodes is fixed and the electrodes are moved progressively along a profile line where measurements are recorded at each position. This is repeated again for different electrodes spacings until the maximum electrodes spacing is reached. For research purposes, this mechanism is done automatically by the field electrical resistivity meter (e.g., Syscal Pro) and the output will be a cross-sectional 2-D profile showing the lateral and vertical changes of electrical resistivity in the subsurface (Samouëlian et al., 2005).

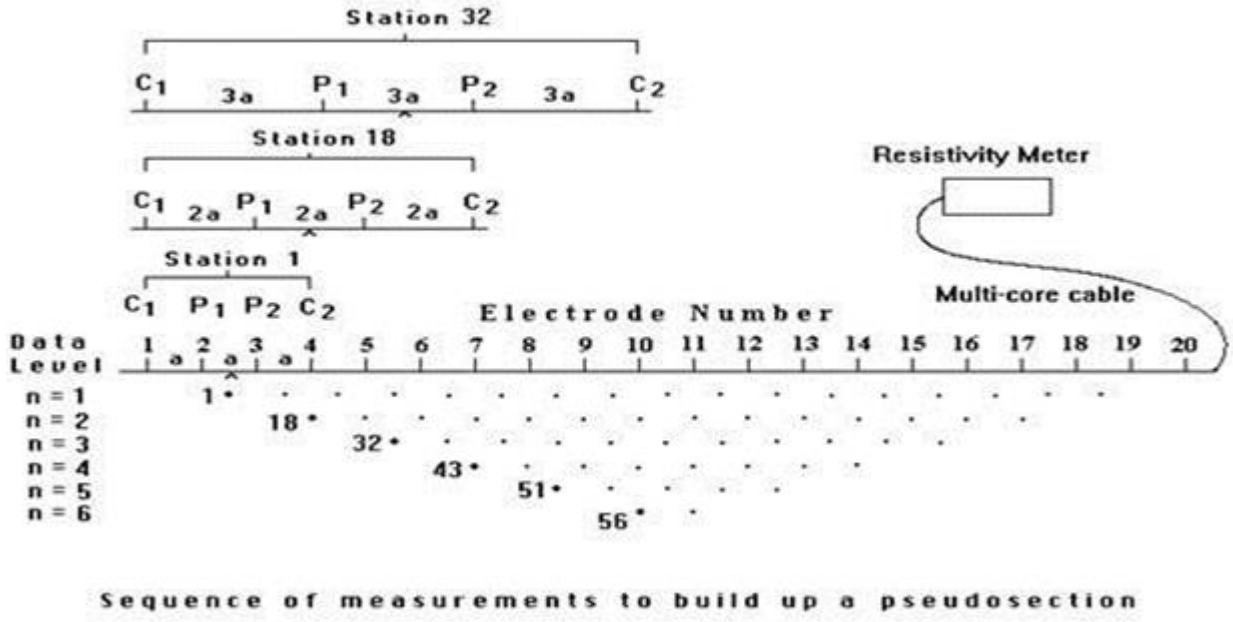

Figure 3.6: Principles of the electrical resistivity tomography measurement (adapted from Loke, 1991).

Before a field survey is conducted, it is important to define measurement settings, particularly the type of the configuration array which determines the geometry of the current and potential electrodes. The choice of an array depends on the type of the desired information such as the depth of investigation and the spatial and lateral resolutions. Different configuration arrays are available and are described in many previous studies (e.g., Loke et al., 2013). The data acquired

by the different arrays differ in parameters such as the depth of investigation, signal strength and horizontal and vertical data coverage. The parameter that defines a configuration array is the geometric factor **K**, which is defined by the electrodes spacing **a** and the number of data levels **n**. The different arrays and their corresponding **K** factors are depicted in Figure 3.7.

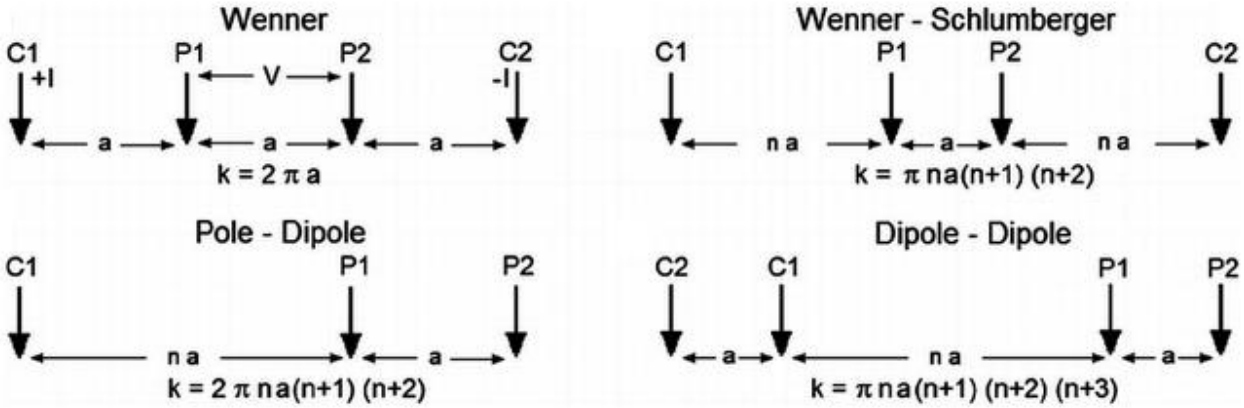

Figure 3.7: The different configuration arrays (wenner, wenner-schlumberger, pole-dipole and dipole-dipole). C1 and C2 are the current electrodes, P1 and P2 are the potential electrodes and K is the configuration factor which depends on the electrodes spacing (modified after Loke et al., 2013).

In the dipole-dipole array, the dipole of the injection electrodes is placed on one side and the dipole of the measurement electrodes on the other side. The distance between the electrodes of each dipole is **a** and the distance between the two dipoles is "**n.a**". For a wenner array, the electrodes are asymmetrically arranged, with the potential electrodes between the current electrodes with an equal distance **a** between the four electrodes.

Figure 3.8 shows the sensitivities of both the wenner and dipole-dipole arrays. The sensitivity describes the degree at which a change in the subsurface resistivity at a certain location with respect to the quadripole can be detected by the measurement. The wenner array has horizontal high sensitivity contours directly beneath the quadripole center (between C1 and P1). Therefore, it is more sensitive to horizontal changes in resistivity values. On the contrary, the dipole-dipole array shows high sensitivity values in the vertical direction and on the sides below the two dipoles (C1-C2 and P1-P2). Therefore, it is more sensitive to resistivity changes in the vertical direction. The dipole-dipole array has a higher depth of investigation compared to the wenner array, whereas the wenner array has a lower signal to noise ratio and provides a better resolution at shallow depths (Figure 3.9).

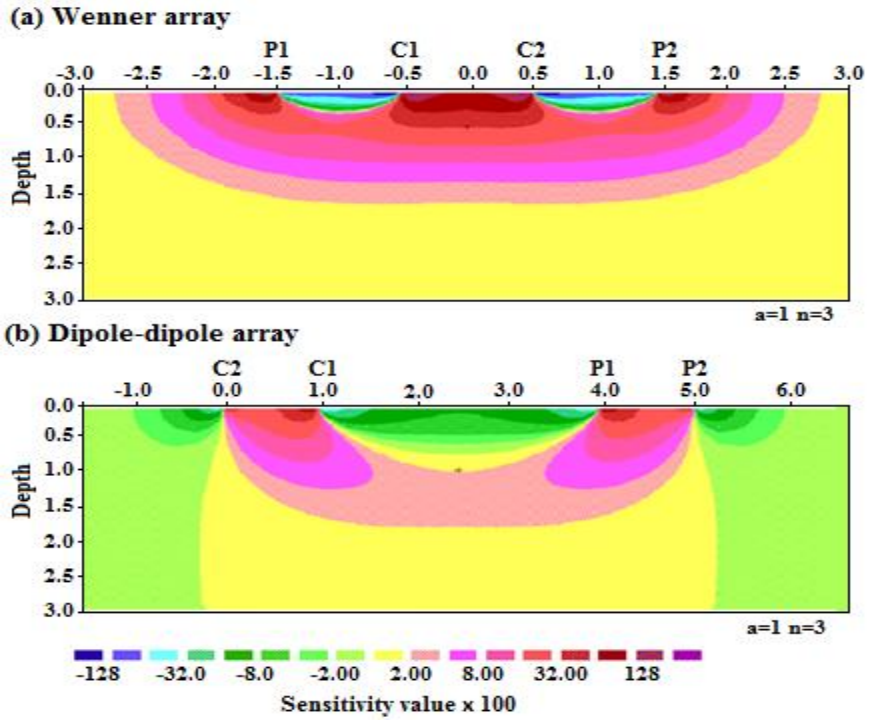

Figure 3.8: Sensitivity of the wenner (a) and dipole-dipole (b) arrays (modified after Loke, 1991).

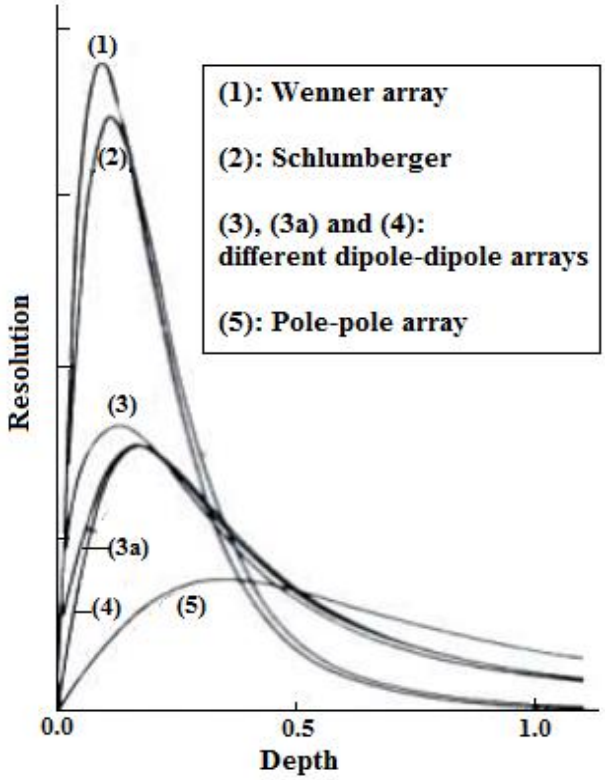

Figure 3.9: The resolution of the different configuration arrays with respect to depth (Geophysics 1, E., Appel, 2011).

To get the desired information about the apparent resistivity and chargeability distributions in the subsurface, a Syscal Pro resistivity meter from IRIS instruments was used. The Syscal Pro is an automated resistivity meter for dc electrical surveys and is commonly used in surveys dealing with groundwater exploration and structural geology investigation (www.iris-instruments.com). The following equipment was used during the ERT surveys:

- Syscal Pro resistivity meter
- Multi-core cables
- Connection cables
- Crocodile clips
- Steel electrodes
- Small hammer
- Laptop
- Connection boxes

After mapping out the profiles by using a measuring tape, a number of steel electrodes were planted in the ground with a constant electrodes spacing (Figure 3.10). Multi-core cables were then laid down parallel to the electrodes in a way that each node is facing one of the electrodes. Crocodile clips were then used to connect the electrodes to the cable nodes, taking into account that each cable takes up to 18 electrodes. The cables were then connected to the Syscal Pro resistivity meter channels after taking the electrodes order into consideration. The field measurement configuration was done by the software Electre Pro which allows adjusting parameters such as the number of electrodes, electrodes spacing, type of configuration array, injected current intensity, number of data levels, number of stacks per measurement and time of data acquisition. The number of electrodes and the electrodes spacing used were chosen according to the required resolution and penetration depth, taking into consideration that the depth of investigation increases as the size of the profile increases.

A field laptop was used to upload the measurement setup file done by Electre Pro into the resistivity meter system. Prior to starting the data acquisition, the electrical contact between each electrode and the ground was checked by using an option available in the Syscal Pro system. Water and salt were added in cases of poor electrical contact and small holes were drilled in the areas were asphaltic layers were encountered. In this case, bentonite mud was added to the holes before placing the electrodes in order to improve the electrical contact. Areas where pipes are present in the subsurface were avoided as much as possible to avoid the effect of the pipes on the geophysical data acquisition and interpretation processes.

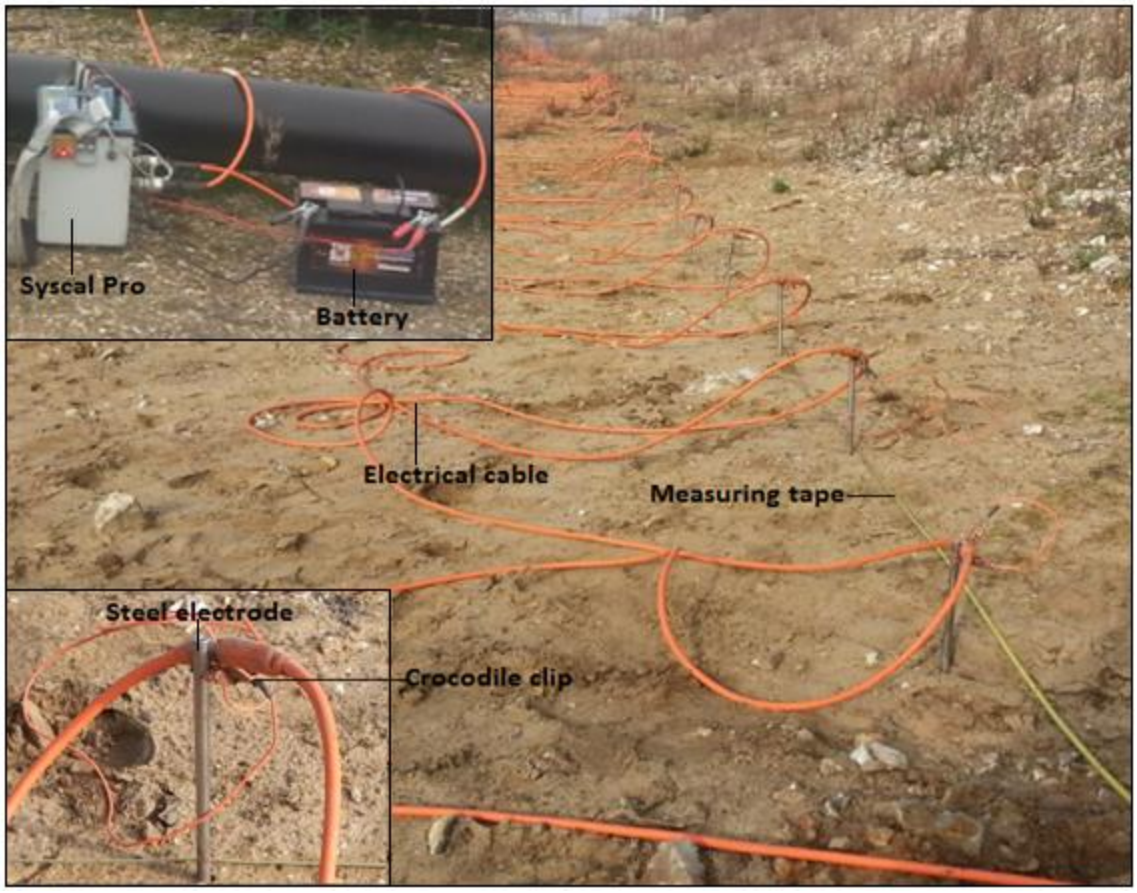

Figure 3.10: The field setup and the equipment used in the electrical resistivity tomography survey.

3.1.4. Data processing

a. Filtering

The ERT profiles collected in the field were first filtered by the software Prosys 2, where bad and negative data points were manually removed before saving the file in the Res2Dinv format. The second filtering step was done by using the option "exterminate bad data points" in the inversion software Res2Dinv (Figure 3.11). This step allows the removal of points which have apparent resistivities much higher or lower than points which are at the same data level. These bad data points could result from poor electrical contact between the electrodes and the ground surface, or due to system failure and very humid conditions. For filtering the IP data, the potential decay curves were analyzed and those with anomalous behaviors were removed.

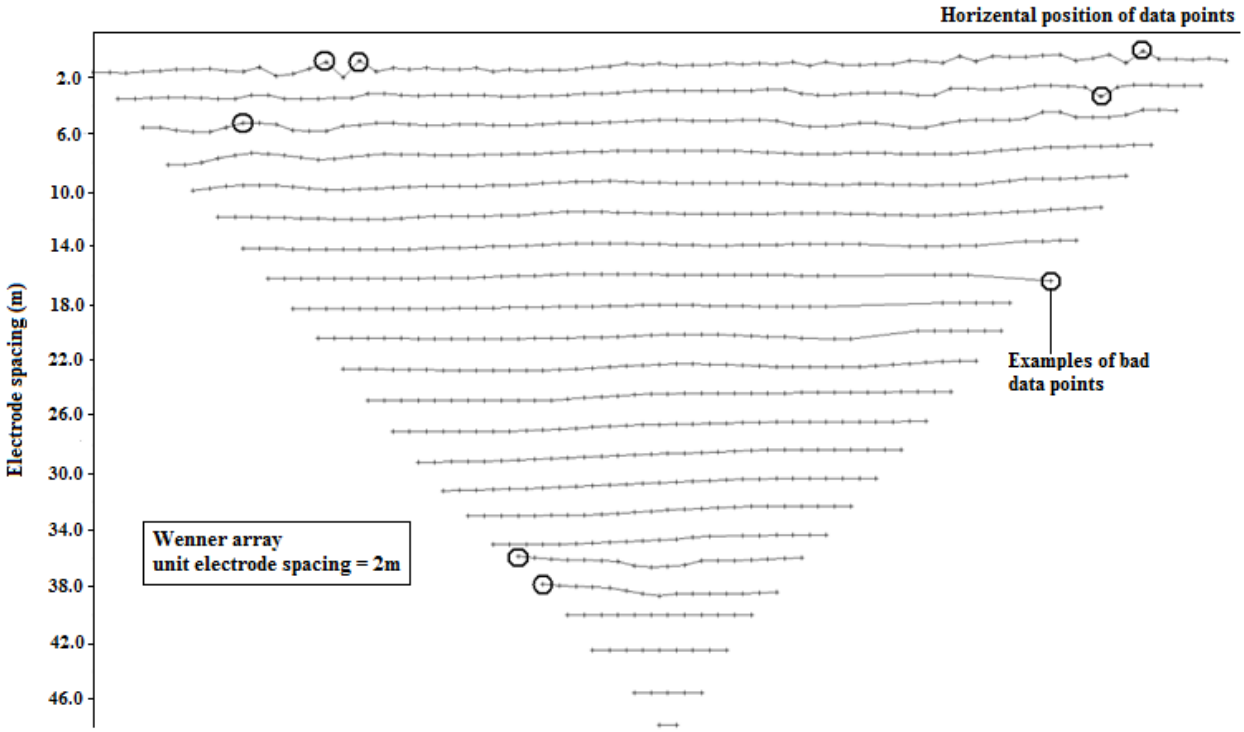

Figure 3.11: Data filtering by using the "exterminate bad data points" option in Res2Dinv. The circles represent examples of bad data points.

b. Inversion

The ERT profiles acquired in the field constitute of the distribution of apparent electrical resistivity. This is not an explicit measurement of the electrical resistivity due to contributions from the heterogeneous transmitting medium and from the electrodes geometry and positions. Therefore, an inversion algorithm is needed to calculate the distribution of the real electrical resistivity.

There exist several available softwares which can perform this inverse problem. One of these is Res2Dinv, a commercially available software (Loke and Barker, 1996). Res2Dinv creates a 2-D model of rectangular blocks by using the field data. The arrangement and size of the blocks are generated according to the distribution of the field data points. The maximum depth of the model is set approximately to the maximum measurement depth according to the largest electrodes spacing used. The forward modeling relies on the use of the finite difference or finite element method for the numerical computation of the electrical resistivity. A nonlinear least squares optimization technique with a smoothing constraint is used to invert the apparent resistivity section into a real resistivity section showing the lateral and vertical distributions of electrical resistivity in the subsurface (Figure 3.12). The inversion algorithm tries to minimize the cost function between the calculated apparent resistivity distribution and the resistivity measured at the field by using several iteration steps until it gets the best fit. The error of the inverted resistivity model is given as a root main square error (RMS):

$$RMS = \sqrt{\frac{1}{n}\sum_{i=1}^{n}(r_i^{mes} - r_i^{mod})^2}, \quad (16)$$

where $\boldsymbol{n}$ is the number of data points, $\boldsymbol{r_i^{mes}}$ is the apparent resistivity data measured at the field and $\boldsymbol{r_i^{mod}}$ is the apparent resistivity data calculated by the model. An RMS error below 10 % is considered to be acceptable.

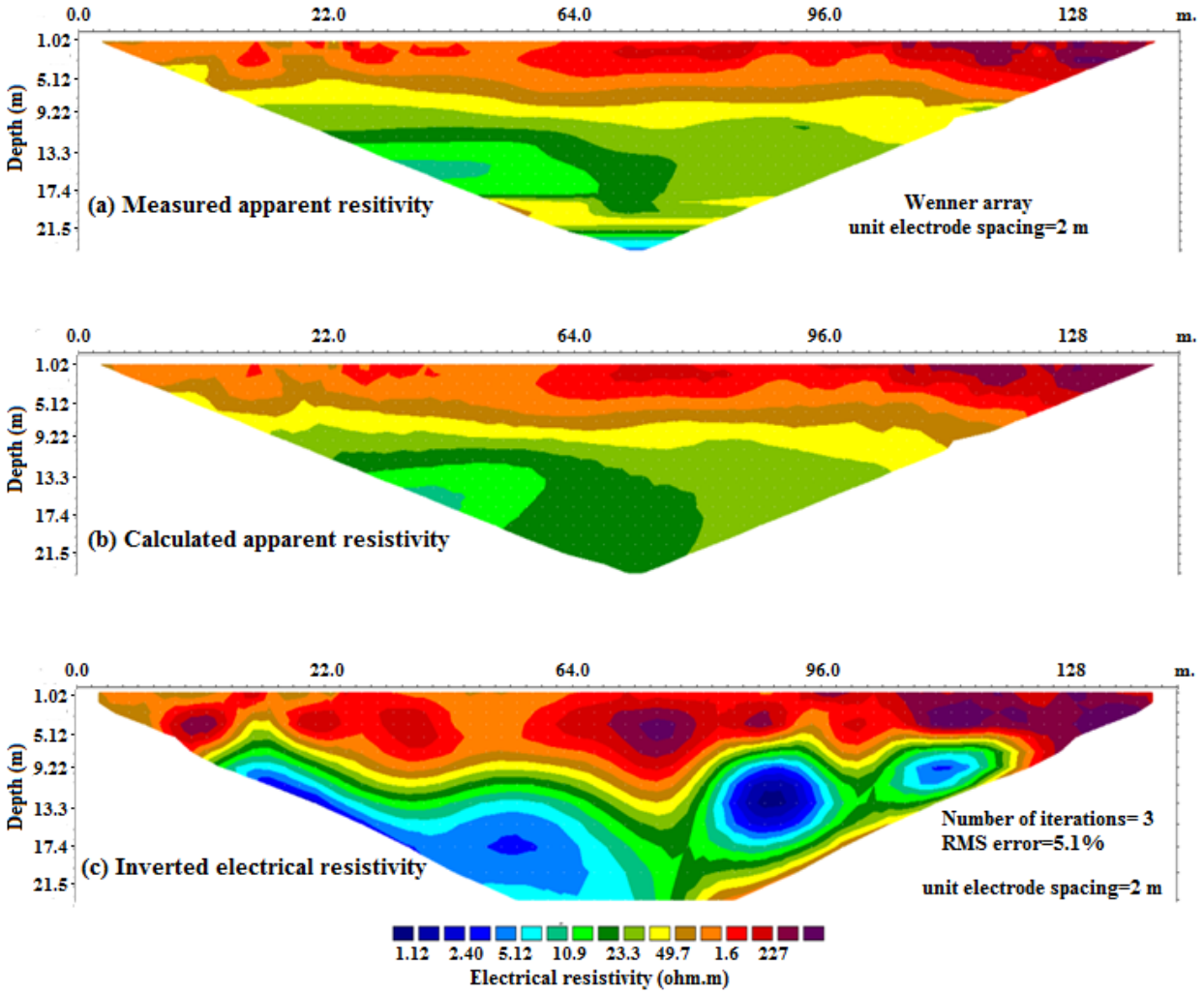

Figure 3.12: Results of the mathematical inversion used to calculate the distribution of the real electrical resistivity from the distribution of the apparent electrical resistivity by Res2Dinv. The figure shows: a model of the measured resistivity values (a); a model of the calculated resistivity values (b) and a model of the inverted resistivity values after 3 iterations (c).

During the inversion, the first adjusted parameter was the damping factor which should be higher for noisy data sets. The initial damping factor was set to 0.160 while the minimum damping factor was set to 0.015. For more noisy data, particularly those of the dipole-dipole array the initial damping factor used was 0.25 and the minimum factor used was 0.1. The second parameter was the mesh grid size. For noisy data sets, it was better to use 4 nodes per unit electrodes spacing.

This renders the inversion slower but produces more accurate values. For this reason, a number of 4 nodes per unit electrodes spacing was set for the dipole-dipole data, while 2 nodes per unit electrode spacing was set for the wenner array data. For more accurate results and because the smallest values were 10 times smaller than the largest apparent resistivity values in some cases, the Jacobian matrix was set to be calculated for all the iteration steps during the inversion process. Two inversion methods were used, these are the robust constrained and the conventional least square inversion methods. The robust constrained inversion produced results with lower RMS errors compared to the conventional least square inversion method.

3.2. Ground penetrating radar

Ground penetrating radar (GPR) is another geophysical method which is commonly used in various environmental domains such as hydrogeology, geology and archaeology (Bristow and Jol, 2003; Rubin and Hubbard, 2005). The GPR is a high frequency electromagnetic method which scans the earth's interior by sending pulses of electromagnetic waves into the subsurface (Annan, 2002, 2003; Neal, 2004). These waves encounter changes in the subsurface dielectric properties before they are reflected back to the surface and captured by a receiver. Recent developments demonstrated the GPR method as an efficient tool which can be used to study hydrocarbon contamination in soil systems (e.g., Atekwana et al., 2000; Cassidy, 2007).

3.2.1. Theory

The radar wave velocity $\boldsymbol{v}$ in different materials is determined by the dielectric permittivity $\boldsymbol{\varepsilon}$, which is the measure of electric charge polarization triggered by the application of an electrical field on a medium:

$$v = \frac{1}{\sqrt{\mu\varepsilon}}\,, \tag{17}$$

where $\boldsymbol{\mu}$ is the magnetic permeability. The dielectric constant $\boldsymbol{k}$ (also called relative dielectric permittivity) is commonly used to describe the dielectric behavior in geological materials and increases as the water content increases. $\boldsymbol{k}$ is obtained by dividing the dielectric permittivity $\boldsymbol{\varepsilon}$ by the permittivity of vacuum $\boldsymbol{\varepsilon_0}$:

$$k = \frac{\varepsilon}{\varepsilon_0}\,. \tag{18}$$

As the near surface sediments are considered to be nonmagnetic, the magnetic permeability $\boldsymbol{\mu}$ is assumed to be constant. Therefore, the radar electromagnetic wave velocity can be written as:

$$v = \frac{c}{\sqrt{k}}\,, \tag{19}$$

where $\boldsymbol{c}$ is the velocity of light in vacuum (0.3 m/ns). The GPR provides better spatial resolution in comparison to the electrical resistivity method, but it has a limited depth of penetration

depending on the lithology and sediments composition. The penetration depth of the GPR wave is controlled by the electrical conductivity $\boldsymbol{\sigma}$ which contributes strongly to the attenuation constant $\boldsymbol{\alpha}$ (m) of the radar signal by the following equation:

$$\alpha \approx \frac{\sigma}{2}\sqrt{\frac{\mu}{\varepsilon}}. \tag{20}$$

Soil systems with high clay content have a high electrical conductivity which can produce a high attenuation constant. Therefore the GPR has a limited depth of penetration in clayey soils in comparison to clay-free soils such as those consisting of sand and gravel.

3.2.2. Measurement principles

GPR surveys can be conducted in two different modes, the transillumination mode and the reflection mode (Annan and Cosway, 1992). Reflection surveys are the most commonly used in geological applications and can be employed in two modes, the common-offset mode and the multi-offset common midpoint (CMP) mode. In the common-offset mode, the GPR system consists of a transmitter and a receiver having fixed separation (offset) and orientation at each measurement point (Figure 3.13a).

The measurements are taken at regular station intervals $\Delta(x)$ as the GPR system is moved over the surface. The transmitter antenna generates an electromagnetic pulse into the ground, while the receiver antenna captures the reflected, diffracted and direct waves which are transmitted back to the surface. The movement of the device from one measurement point to another provides many traces on a profile line referred to as the radargram (Figure 3.13b). The radargram represents the amplitude and time of arrival of each wave (two way travel time) as a function of distance. Therefore, the subsurface reflectivity is mapped versus the spatial position, where variations in reflections amplitudes and time delay reflect variations in velocity, attenuation and electromagnetic impedance. The GPR records reflections from subsurface features which could be stratigraphic (e.g., geological interfaces, groundwater table, etc.) or buried structures (tunnels, pipes, concrete slabs, etc.) on a 2D profile. The shape of the obtained reflections can give information about the detected structure. For example, as shown in the radargram of Figure 3.13, a point reflector (e.g., buried pipe) will produce a hyperbolic reflection, while a plane reflector (e.g., geological interface, groundwater table, etc.) will produce a continuous reflection having a shape that reflects the topography of the detected interface.

The parameters which control the common offset mode measurement are the time window, the fixed antenna spacing, the antenna orientation, the time sampling interval and the system central frequency. The CMP mode is similar to the seismic refraction method and differs from the common-offset mode by that the antenna spacing is varied. The CMP measures the change in the two way travel time to estimate the radar signal velocity versus depth.

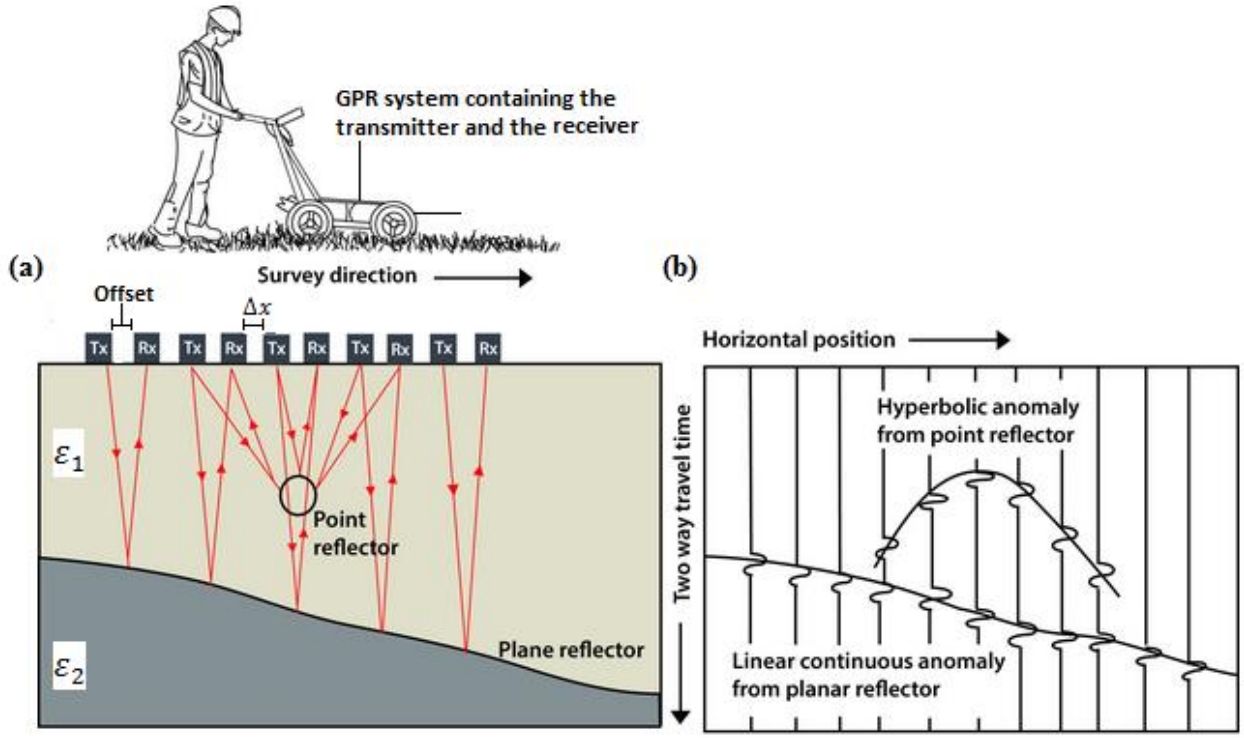

Figure 3.13: GPR common-offset mode working principles (a) and the radargram which shows the two way travel time of the radar wave with respect to the horizontal position on a profile line (b) (modified after scantech.ie).

The GPR profiles acquired in this project were carried out by using the common-offset mode. A Mala Geosciences GPR system composed of a shielded antenna comprising the transmitter and the receiver in a single housing was used (Figure 3.14). The design of the shield ensures receiving and emitting signals only from the bottom of the housing which is in contact with the ground surface. This protects the receiver from external noise signals, especially in industrial sites where electromagnetic signals sources could be encountered frequently. A Mala X3M integrated control unit is attached to the antenna, in addition to a 300 mm distance measuring wheel that controls the data collection at user's defined distance intervals. 100 MHz and 250 MHz antennas were used and the measurements were done by using a wheel mode with a recording interval of 0.10 meters, a time window ranging between 200 and 600 ns and a number of 512 stacks per trace. Prior to data acquisition, each profile line was marked by a rope and a measuring tape to ensure straight profiles with precise lengths. The ground surface was cleaned from rocks and metals which could perturb the radar signal. The ground surface was also insured to be as flat as possible to avoid effects of the topography variation in the radar measurements.

Figure 3.14: The Mala Geoscience GPR system used to acquire the GPR data. The system contains a shielded antenna, a control unit (X3M), a distance measuring wheel and a field laptop.

3.2.3. Data Processing

The data acquisition was followed by the following processing steps: (i) dewow filtering to remove the initial direct current signal component and its subsequent low frequency trend present in the data; (ii) background removal; (iii) time-zero correction to overcome the time zero point jump caused by equipment instability and to find the true ground surface reflection; (iv) band-pass filtering to remove the low and high frequency components and (v) to improve the visual quality of the data, it was necessary to multiply the traces by a gain function that overcomes the effects of geometrical spreading losses (Figure 3.15).

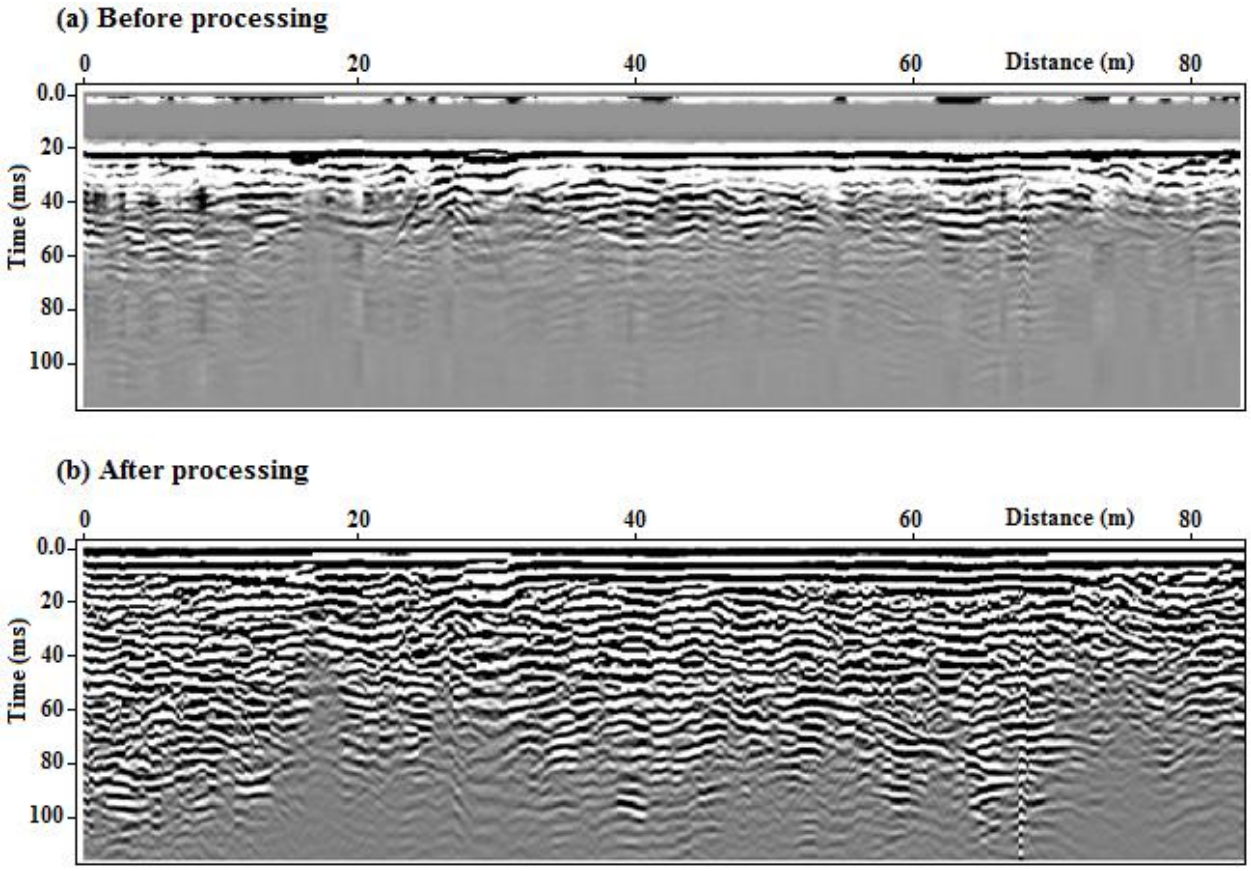

Figure 3.15: A GPR profile before (a) and after processing (b). The processing steps applied were: dewow filtering, time zero correction, background removal, band pass filtering and multiplication by a gain function.

3.3. Self-potential

The self-potential (SP) method is a passive geoelectrical technique which differs from the electrical resistivity method by that it doesn't require injecting electrical current into the subsurface. The method detects naturally occurring electrical currents by measuring the electrical potential difference between a reference electrode and a measurement electrode at the ground surface. These natural currents which could be generated by different internal current sources can produce several types of self-potential signals such as the streaming potential, the thermoelectric potential, the electrochemical potential and the mineralization potential.

3.3.1. Theory

The self-potential signal is related to electrical charges polarization which is generated by non-equilibrium thermodynamic processes in a porous medium. The source current density which produces the SP signal could be generated through: (1) groundwater flow processes (electrokinetic component, e.g., Jardani et al., 2006) or by electrochemical processes such as oxidoreduction

reactions (Nyquist and Corry 2002; Naudet et. al., 2003) and temperature gradients (Revil et al., 2013). In the subsurface, the self-potential anomaly is based on the total current density $\boldsymbol{J}$ which is the sum of the conductive current term $\boldsymbol{\sigma\nabla\varphi}$ and the net source current density $\boldsymbol{J_s}$:

$$J = -\sigma\nabla\varphi + J_s \,, \tag{21}$$

where the conductive current term is described by Ohm's law and is the product of the natural electrical potential $\boldsymbol{\varphi}$ (referred to as the self-potential) and the medium electrical conductivity $\boldsymbol{\sigma}$. The term $\boldsymbol{J_s}$ represents the total source current density described as the sum of the electrokinetic and redox components:

$$J_s = \sigma(-\nabla E_H + C\nabla h) \,, \tag{22}$$

where $\boldsymbol{C}$ is the electrokinetic coupling coefficient and $\boldsymbol{h}$ is the hydraulic head (in m). The electrokinetic contribution or the streaming potential is associated with the flow of water in porous media. The electrical signal is generated as the water current drags the excess electrical charges coating the mineral surfaces in the electrical diffuse layer (at the fluid-mineral interface) (Revil et al., 2003; Jardani et al., 2006). $\boldsymbol{E_H}$ is the redox potential (in mV) which constitutes the electrochemical potential part of the signal. According to the charge conversion law the equation of the current density can be written as:

$$\nabla . J = 0 \,. \tag{23}$$

The electrical field is the solution of the following Poisson's equation,

$$\nabla . (\sigma\nabla\varphi) = \nabla . J_s \,. \tag{24}$$

A first order approximation of the Fournier equation (Fournier, 1989) which relates the self-potential signal to the variation of hydraulic heads has been expressed by Revil et al. (2003):

$$\varphi - \varphi_0 = C'(h - h_0) \,, \tag{25}$$

where $\boldsymbol{\varphi}$ and $\boldsymbol{\varphi_0}$ are the electrical potentials at the measurement and base stations respectively. $\boldsymbol{h}$ and $\boldsymbol{h_0}$ are the hydraulic heads at the measurement and base stations respectively and $\boldsymbol{C'}$ is the electrokinetic coupling coefficient. The removal of the electrokinetic component from the electrical potential $\boldsymbol{\varphi}$ will result in the residual potential $\boldsymbol{\varphi_H}$ which can be related to the redox potential by the following linear approximation:

$$\varphi_H - \varphi_0 = C_H(E_H - E_0) \,, \tag{26}$$

where $\boldsymbol{C_H}$ is the redox coupling coefficient and $\boldsymbol{E_H}$ and $\boldsymbol{E_0}$ are the redox potential measurements at the measurement and base stations respectively.

3.3.2. Measurement principles

In this study**,** the self-potential measurements were done by using two non-polarizable (Pb-$PbCl_2$) Petiau electrodes. The first electrode is fixed and referred to as the reference electrode,

whereas the second electrode can move into different measurement points with a rolling wire (Figure 3.16). The used electrodes are rods of lead suspended in porous containers supersaturated with KCL/$PbCl_2$ solutions. The electrodes were placed in small holes filled with bentonite mud during the measurements. This ensures good electrical contact between the soil and the non-polarizable electrodes (Jardani et al., 2006). The potential difference at each point was measured by using a high input impedance (10 MΩ) voltmeter (MX20) which was connected to the electrodes through the rolling wire. Each measurement was repeated several times at each point until a stable value was reached.

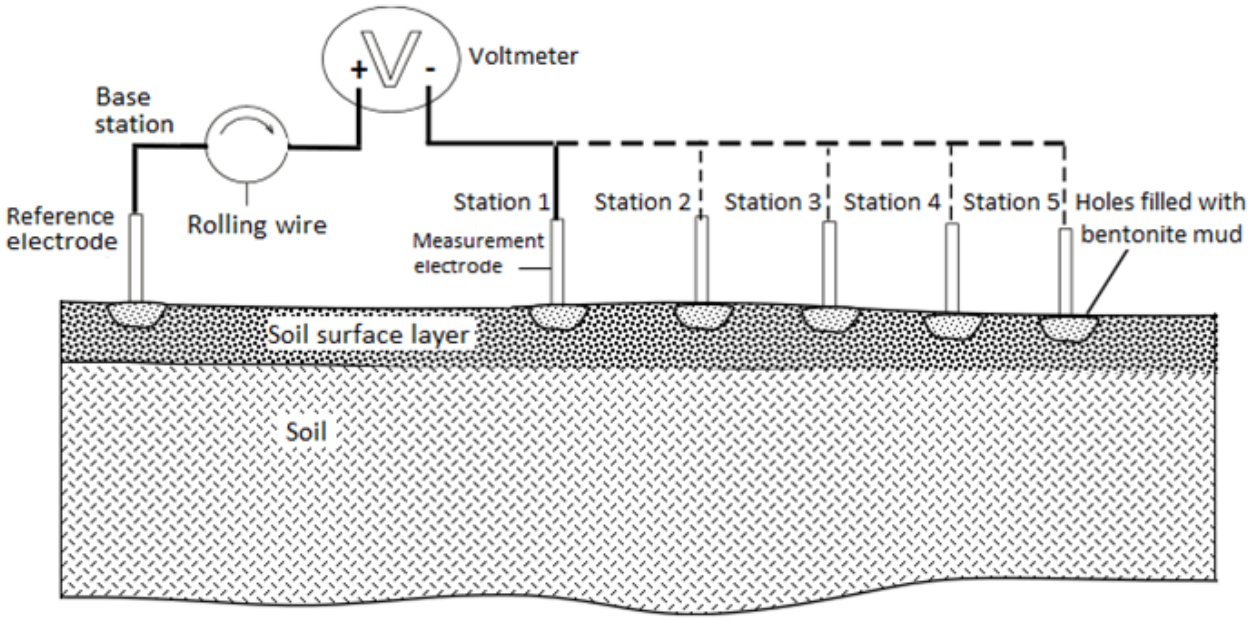

Figure 3.16: The self-potential method measurement principles. Two electrodes are used, the first one is the measurement electrode and has a fixed location, whereas the second one is the measurement electrode and is moved to different measurement points by using a rolling wire.

3.4. Magnetic Susceptibility

Magnetic susceptibility (MS) of a natural material is a measure of its degree of magnetization in the presence of a magnetic field (Morris et al., 1994). All natural substances are considered magnetic, with various degrees of magnetic strength. Magnetic materials are divided into three categories according to their degree of magnetization: diamagnetic, ferromagnetic and paramagnetic. Ferromagnetic substances have the strongest magnetism of all and are considered true magnetic materials. Ferromagnetism is a result of the magnetic moments alignment of all the atoms in the crystal lattice through interactions of electron orbitals. Iron is among the most abundant ferromagnetic materials, as it occurs in many oxides such as magnetite and hematite, and in some sulfides such as greigite and pyrrhotite (Mullins, 1977; Thompson and Morton, 1979). Therefore, the magnetic susceptibility method is sensitive to changes in the iron-mineral content of sediments (Thompson and Oldfield, 1986). As mentioned before in section 1.6.2,

biophysicochemical processes associated with the biodegradation of hydrocarbons may induce changes in the iron mineral content of sediments, which can be displayed as changes in the magnetic susceptibility signatures (Kappler and Straub, 2005; Lovley and Anderson, 2000; Weber et al., 2006). Therefore, the MS method can be used as a fast and cost-effective indicator of biodegradation in hydrocarbon contaminated sediments (Mewafy et al., 2011; Rijal et al., 2010, 2012).

3.4.1. Theory

The MS can be determined as volume magnetic susceptibility, defined as the ratio between the induced magnetization per unit volume and the applied magnetic intensity. The MS can also be displayed as mass specific magnetic susceptibility obtained by dividing the volume magnetic susceptibility by the density of the material (Thompson and Morton, 1979). The magnetic state of a soil sample is generally described by the following equation:

$$B = \mu_0 (H + M) , \tag{27}$$

where $\boldsymbol{B}$ is the sample flux density in Tesla (T), $\boldsymbol{\mu_0}$ is the permeability of free space ($4\pi \times 10^{-7}$), $\boldsymbol{H}$ is the intensity of the applied electrical field (in Am^{-1}) and $\boldsymbol{M}$ is the sample magnetization (in Am^{-1}). Dividing by $\boldsymbol{H}$, we get:

$$\mu = \mu_0 + \mu_0 K , \tag{28}$$

where $\boldsymbol{\mu}$ is the permeability of the sample (in Am^{-1}) and $\boldsymbol{K}$ is the magnetic susceptibility of the sample volume (dimensionless). Therefore, the equation can be written as:

$$\mu_0 K = \mu - \mu_0 . \tag{29}$$

Having the relative permeability $\boldsymbol{\mu_r}$ defined as the ratio between the permeability of a material and the permeability of vacuum:

$$\mu_r = \frac{\mu}{\mu_0} , \tag{30}$$

the bulk volume magnetic susceptibility can be directly related to the relative permeability through the following equation:

$$K = \mu_r - 1 . \tag{31}$$

3.4.2. Measurement principles

The MS sensor consists of an oscillator having very high thermal stability, with an inductor which determines the oscillation frequency according to changes in the permeability. When the inductor contains only air, $\boldsymbol{\mu_0}$ value determines the oscillation frequency. When the inductor is in contact with a soil sample, the $\boldsymbol{\mu}$ value determines the oscillation frequency. The values of $\boldsymbol{\mu_0}$ and $\boldsymbol{\mu}$ are recorded and then the value of magnetic susceptibility is calculated. Soil samples and soil

cores mainly composed of sand were collected by advancing a core barrel with a PVC liner ahead of a drilling stem. The cores were preserved in coolers and transported to the lab, oven dried, sieved and analyzed for MS by using a Bartington MS2 magnetic susceptibility meter (Figure 3.17). We conducted the measurements by using an interval of 0.5 cm and the device was calibrated after each measurement to minimize the drift and maintain a valid measurement. To get high accuracy measurements, the sensor was kept 10 secs at each point and each measurement was repeated several times.

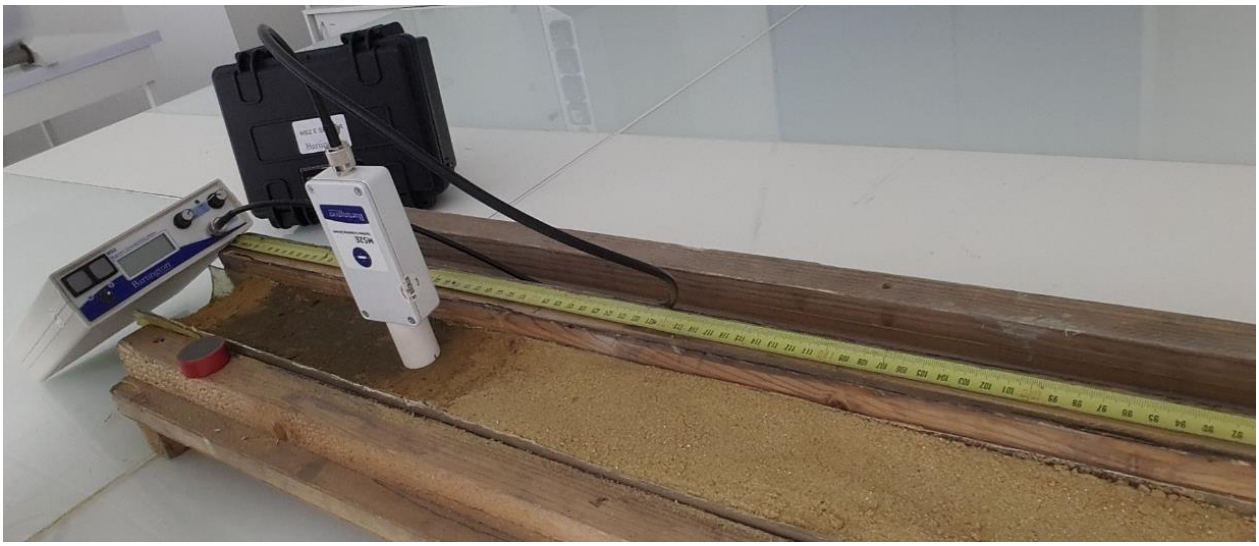

Figure 3.17: The MS2 Bartington equipment used to conduct the magnetic susceptibility measurements on a soil core.

3.5. References

Annan, A.P. and Cosway, S.W., 1992. Ground penetrating radar survey design. Proceedings of the Symposium on the Application of Geophysics to Engineering and Environmental Problems, SAGEEP'92, Oakbrook, IL, April 26–29, pp. 329–351.

Annan, A.P., 2002. The history of ground penetrating radar. Subsurface Sensing Technologies and Applications, Vol. 3, No. 4, October 2002, pp. 303–320.

Annan, A.P., 2003. Ground penetrating radar: Principles, procedures & applications. Sensors and Software Inc. Technical Paper.

Allaud, L. A., and M. H. Martin, 1977. Schlumberger, the history of a technique: John Wiley & Sons, Inc Angoran, Y., and T. R. Madden, 1977. Induced polarization: A preliminary study of its chemical basis: Geophysics, 42, 788–803.

Atekwana, E. A. and E. A. Atekwana, 2010. Geophysical Signatures of Microbial Activity at Hydrocarbon Contaminated Sites: A Review. Surv Geophys (2010) 31:247–283DOI 10.1007/s10712-009-9089-8.

Atekwana E. A., W. A. Sauck, and D. D. Werkema, 2000. Investigations of geoelectrical signatures at a hydrocarbon contaminated site. Journal of Applied Geophysics, 44 (2-3), 167–180.

Bleil, D. F., 1953. Induced polarization: a method of geophysical prospecting: Geophysics, 18, 636-661. Bristow, C.S. and Jol, H.M., 2003, Ground Penetrating Radar in Sediments, Geological Society, London, Special Publications, 211.

Cassidy, N. J., 2007. Evaluating LNAPL contamination using gpr signal attenuation analysis and dielectric property measurements: Practical implications for hydrological studies. Journal of Contaminant Hydrology, 94, 49–75.

Daily, W., A. Ramirez, A. Binley and D. LaBrecque, 2005. Electrical Resistance Tomography—Practice and Theory, Soc. Exploration Geophysics: Near Surface Geophysics (Investigations in Geophysics No. 13), ed. Dwaine Butler, ISBN-13: 978-1560801306.

Hallof, P. G., 1957. On the interpretation of resistivity and induced polarization results: Ph.D. thesis, Massachusetts Institute of Technology.

Jardani, A., J. P. Dupont, and A. Revil, 2006. Self-potential signals associated with preferential groundwater flow pathways in sinkholes. J. Geophys. Res. 111.

Kappler, A., K. L. Straub, 2005. Geomicrobiological cycling of iron. In Molecular Geomicrobiology, 59 (eds. J. F. Banfield, J. Cervini-Silva, and K. M. Nealson), The Mineralogical Society of America, 85-108pp.

Klein, J. D., T. Biegler, and M. D. Horne, 1984. Mineral interfacial processes in the method of induced polarization: Geophysics, 49, 1105–1114.

Lesmes, D. P., and K. F. Frye, 2001. The influence of pore fluid chemistry on the complex conductivity and induced polarization responses of Berea. sandstone: Journal of Geophysical Research, 106, 4079–4090.

Lesmes, D. P., and F. D. Morgan, 2001. Dielectric spectroscopy of sedimentary rocks: Journal of Geophysical Research, 106, 13392–13346.

Loke M.H., 1991. Electrical imaging surveys for environmental and engineering studies A practical guide to 2-D and 3-D surveys.

Loke M., J. Chambers, D. Rucker, O. Kuras, and P. Wilkinson, 2013. Recent developments in the direct-current geoelectrical imaging method. Journal of Applied Geophysics, 95 (0), 135–156.

Lovley, D. R., and R. T. Anderson, 2000. The influence of dissimilatory metal reduction on the fate of organic and metal contaminants in the subsurface. J Hydrol, 238, 77-88.

Loke, M.H., and R. D. Barker, 1996. Rapid lEast-squares inversion of apparent resistivity pseudosections by a quasi- Newton method. Geophysical Prospecting 44, 131–152.

Madden, T. R., and A. S. Neves, 1957. Background effects in the induced polarization method of geophysical exploration: Annual progress report for 1956–57, U. S. Atomic Energy Commission.

Mewafy, F. M., E. A. Atekwana, D. D. Werkema Jr., L. D. Slater, D. Ntarlagiannis, A. Revil, M. Skold, and G. N. Delin, 2011. Magnetic susceptibility as a proxy for investigating microbially mediated iron reduction, Geophys. Res. Lett., 38, L21402, doi: 10.1029/2011GL049271.

Morris, W.A., J. K. Versteeg, C. H. Marvin, B. E. McCarry, and N. A. Rukavina, 1994. Preliminary comparisons between magnetic susceptibility and polycyclic aromatic hydrocarbon content in sediments from Hamilton Harbour, Western Lake Ontario. Sci Total Environ, 152, 153-160.

Mullins, C. E., 1977. Magnetic susceptibility of soil and its significance in soil science - a review. J Soil Sci, 28, 2, 223-246.

Naudet, V. ,2004. Les méthodes de résistivité électrique et de potentiel spontané appliquées aux sites contaminés. PhD thesis, University Paul Cézanne.

Neal, A., 2004. Ground penetrating radar and its use in sedimentology: principles, problems and progress. “Earth-Science Reviews”, 66(3-4): 261-+.

Olhoeft, G. R., 1985. Low-frequency electrical properties: Geophysics, 50, 2492–2503.

Rijal M. L., E. Appel, E. Petrovský , and U. Blaha, 2010. Change of magnetic properties due to fluctuations of hydrocarbon contaminated groundwater in unconsolidated sediments. Environ. Pollut., 158, 1756□1762

Revil, A., V. Naudet, J. Nouzaret, and M. Pessel, 2003. Principles of electrography applied to self-potential electrokinetic sources and hydrogeological applications. Water Resour. Res. 39.1114 doi: 10.1029/2001WR000916

Rubin Y., and S. S. Hubbard S, 2005. Hydrogeophysics. Water Science and Technology.

Santamarina, J.C., K. A. Klein, and M. A. Fam, 2001. Soils and Waves: Particulate Materials Behavior, Characterization and Process Monitoring, John Wiley & Sons, Sussex, England, 508 pp.

Samouëlian, A., I. Cousin, A. Tabbagh, A. Bruand, and G. Richard, 2005. Electrical resistivity survey in soil science: a review. Soil and Tillage Research. Volume 83, Issue 2, September 2005, Pages 173–193.

Schmutz M., A. Revil, P. Vaudelet, M. Batzle, E. Vinao, and A. W., 2010. Influence of oil saturation upon spectral induced polarization of oil-bearing sands. Geophysical Journal International, 183, 211–224.

Sogade J.A., F. Scira-Scappuzzo, Y. Vichabian, W.Q. Shi, W. Rodi, D.P. Lesmes , and F.D. Morgan, 2006. Induced polarization detection and mapping of contaminant plumes. Geophysics 71:B75–B84

Telford, W., Geldart, L., and Sheriff, R. (1990). Applied Geophysics Cambridge University Press, 1st edition.

Thompson, R. and F. Oldfield, 1986. Environmental magnetism. Allen and Unwin, 227 pp.

Vaquier, V., C. R. Holmes, P. R. Kintzinger, and M. Lavergne, 1957. Prospecting for ground water by induced polarization: Geophysics, 22, 660–687.

Ward, S. H. and D. C. Fraser, 1967. Conduction of electricity in rocks, in S. H. Ward, ed., Mining geophysics: SEG, 197–223.

Weber, K. A., L. A. Achenbach, and J. D. Coates, 2006. Microorganisms pumping iron: anaerobic microbial iron oxidation and reduction. Nature reviews. Microbiology, 4(10), pp.752–764.

Chapter 4

Geophysical and Geochemical Characterization of a Site Impacted by Hydrocarbon Contamination Undergoing Biodegradation

Paper 1 (Journal of Near Surface Geophysics)

Geophysical and geochemical characterization of a site impacted by hydrocarbon contamination undergoing biodegradation

M. Abbas[1], A. Jardani[1], N. Machour[2], and J.P. Dupont[1]

(1) Université de Rouen, M2C, UMR 6143, CNRS, Morphodynamique Continentale et Côtière, Mont Saint Aignan, France.

(2) Université de Rouen, UMR 6014 CNRS COBRA SIMA-IUT Evreux 55 rue Saint Germain, Evreux, France.

Corresponding author: abbas_mohammad@live.com

Emails: abbas_mohammad@live.com; abderrahim.jardani@univ-rouen.fr; nadine.merlet@univ-rouen.fr; jean-paul.dupont@univ-rouen.fr

Journal of Near Surface Geophysics (Accepted 01, October 2017)

Abstract

The hydrocarbon contamination, which can alter the physiochemical and biological properties of the subsurface, can be monitored by using geochemical analyses and integrated geophysical techniques. Electrical resistivity tomography, induced polarization, ground penetrating radar and self-potential methods were used in this work to characterize the hydrocarbon contamination and investigate the geoelectrical properties of a site impacted by an aged hydrocarbon plume. Throughout the investigation, the geoelectrical measurements supported the conductive plume model and consistently recorded low resistivity anomalies and high chargeability values in the contaminated aquifer. Furthermore, the low resistivity anomalies were found to be coincident with regions of GPR attenuated reflections and significant negative self-potential anomalies associated with oxidation-reduction processes. These findings were supported by the geochemical measurements which revealed depleted concentrations of terminal electron acceptors and elevated amounts of ions and total dissolved solids, which could be attributed to bacterial biodegradation of hydrocarbons. The study showed that biological alterations of hydrocarbons induced subtle changes in the pore water biogeochemistry, which consequently modified the geophysical properties of contaminated sediments. Based on these observations, the extent of groundwater contamination was delineated according to the geophysical contrast between the contaminated and clean zones. The combination of the different geophysical methods constrained by geochemical point measurements provided insight on the different processes which might have modified the soil and groundwater biogeochemical properties.

4.1. Introduction

Hydrocarbon contamination of the shallow subsurface remains a major environmental concern. The task of delineating contamination plumes as well as studying their impact on the soil and groundwater biogeochemical properties is needed to support the remediation efforts and plans. Often, the characterization of hydrocarbon contamination is performed by chemical analysis of soil and groundwater samples. This invasive technique leads to a limited number of investigations and involves a high cost. Geophysical methods hold great promise as cost-effective and non-invasive tools, which can be used in hydrocarbon contamination studies. As such, geophysical methods, including electrical resistivity tomography (ERT), induced polarization (IP), ground penetrating radar (GPR) and self-potential (SP) have been successfully used to characterize contaminant plumes and investigate their impact on soil and groundwater properties (Arora et al., 2007; Atekwana et al., 2000, 2002, 2004b; Benson et al., 1997; Campbell et al., 1996; Glaser et al., 2013; Werkema et al., 2003).

At the initial stage of contamination, fresh spills are suggested to be associated with an increase of the bulk electrical resistivity and GPR wave velocities in contaminated sediments. This assumption is based on the partial replacement of water in the pores by petroleum hydrocarbons, which exhibit higher electrical resistivity and lower relative permittivity (2–3) compared to water saturated sediments (20–30 for sand) and clean water (80) (Atekwana and Atekwana, 2010; Mazac et al., 1990; DeRyck et al., 1993). Such assumption received wide support from field studies and controlled spills laboratory experiments that reported enhanced GPR reflections (e.g., Campbell et al., 1996; Benson, 1995) and high electrical resistivity anomalies (e.g., DeRyck et al., 1993; Schneider and Greenhouse, 1992) at hydrocarbon contaminated sites. Conversely, Sauck et al. (1998) suggested a change in the electrical response from resistive to conductive due to a variety of biogeochemical processes associated with aged hydrocarbon contamination. This temporal change in the resistivity response was mainly attributed to the increase in the concentration of total dissolved solids (TDS) in pore fluids. The increase in TDS concentrations was related to enhanced mineral dissolution by biodegradation byproducts during the bacterial degradation of hydrocarbons (McMahon et al., 1995). This hypothesis was supported by geochemical studies that reported highly conductive groundwater below hydrocarbon plumes (Baedecker et al., 1987; Baedecker et al., 1993; Eganhouse et al., 1993), as well as by geophysical studies that showed low electrical resistivity anomalies (e.g., Atekwana et al., 2000; Atekwana et al., 2005; Sauck et al., 1998, Sauck, 2000; Shevnin et al., 2005) and attenuated GPR reflections (Atekwana et al., 2000; Bermejo et al., 1997) at hydrocarbon contaminated sites.

However, the high resistivity response associated with the presence of hydrocarbons can last after decades of the contamination event (e.g., Benson et al., 1997; Petterssen and Nobes, 2003; Tezkan et al., 2005). Petterssen and Nobes (2003) attributed the resistive response of an aged contaminant plume (46 years old) to the extreme cold weather which could have inhibited the bacterial activity at the site. Even if the contamination is aged, biodegradation occurs only when appropriate moisture and nutrient conditions are available for the bacterial populations that are

capable of degrading hydrocarbons (Haack and Bekins, 2000). The application of geophysical techniques at hydrocarbon sites over the last two decades has yielded dramatically variable results. This is due to the fact that geophysical attributes are affected by factors related to the contaminant (e.g., type of hydrocarbons and their distribution relative to air and water) and by factors related to the contaminated environment (e.g., geological and biological conditions). Therefore, testing the ability of geophysical methods to characterize the contamination is a crucial task before their use in a remediation plan.

The electrical resistivity method is sensitive to changes in both the pore-fluid and mineral-fluid interface chemistry, but it is not able to differentiate between the relative contributions of these two mechanisms to the bulk electrical resistivity (Atekwana and Atekwana, 2010). The diffusion controlled polarization processes which occur at the mineral-fluid interface, induce significant changes in the low frequency capacitive properties of sediments which could be measured by the IP method (Allaud and Martin, 1977). The sensitivity of the IP phenomena to microbial mediated chemical changes at the mineral-electrolyte interface makes the method ideal for investigating bio-physico-chemical changes due to hydrocarbon contamination (Slater and Lesmes, 2002; Sogade et al., 2006; Abdel Aal et al., 2010).

The self-potential (SP) method is another geophysical technique, which can be used to monitor hydrocarbon plumes undergoing biodegradation of the contaminant mass (e.g., Minsley et al., 2007). Bacterial biodegradation of hydrocarbons induces changes in the groundwater redox conditions which result in the creation of zones with different redox potentials. This leads to the establishment of redox gradients that produce an electrochemical source for the SP signal through natural geobattery processes (Béhaegel et al., 2004; Naudet et al., 2003, 2004; Naudet and Revil, 2005; Timm and Möller, 2001). In the light of the above hypothesis, significant negative SP anomalies have been observed at hydrocarbon contaminated sites and a linear correlation was established between self-potential signals and redox potential measurements (Hämmann et al., 1997; Nyquist and Corry, 2002; Naudet et al., 2003; Arora et al., 2007; Rittgers et al., 2013).

The impact of the contamination on each geophysical signal depends on the biological and chemical processes occurring at the site. For example, a study performed by Blondel et al. (2014) did not observe any modifications between the contaminated and clean areas for normalized chargeability. The contamination did not influence the capacitive part of the conduction, which is controlled by chemical changes at the mineral-fluid interface. In contrast, the contamination influenced the ohmic part of the conduction, which is controlled by changes in the pore fluid chemistry. This was inferred by observing low resistivity anomalies in the impacted zones. Naudet et al. (2004) applied the combination of SP and ERT and successfully delineated the extent of a contaminant plume in the Entressen landfill (France). The authors used electrical conductivity values from a 2D-electrical resistivity survey to produce a map of fluid conductivity showing the position of the contaminant plume. Successively, they used the obtained residual SP distribution to produce a map of redox potential which was able to delineate the redox front of the plume. The groundwater electrical conductivity changes were attributed to bacterial processes that were

evidenced by the recorded SP anomalies, which were considered to be driven by redox gradients established during the biodegradation process. Additionally, the vertical and horizontal resolutions of each geophysical method play an important role in the detection of changes induced by the presence of hydrocarbon contamination. Sauck et al. (1998) used the GPR shadow zones to map the transverse extent of a hydrocarbon plume in the downgradient locations where the contamination is only in the dissolved phase. The study concluded that the GPR higher resolution compared to ERT can provide more information about the small vertical heterogeneities, which were not detected by the ERT technique.

These investigations illustrate that each geophysical method is sensitive to a certain geochemical parameter and has a different resolution. Therefore, the combination of different geophysical techniques would be the best way to obtain complementary data sets that can reduce the ambiguities in the geophysical interpretations and constrain the solution by providing insight on the different mechanisms that might modify the subsurface biogeochemical properties. Furthermore, the man-made structures which are commonly encountered at industrial sites introduce limitations to the use of certain geophysical methods. For example, ERT surveys cannot be easily conducted in areas with an asphaltic layer, while GPR surveys can. Thus, the use of different methods can cover larger areas in industrial sites.

To the best of our knowledge, there are only few studies that have investigated the geophysical response or recorded consistent results from the four different geophysical methods for the same site and field conditions. In this study, four geophysical methods including ERT, IP, GPR and SP were combined to define the type of geophysical response of a hydrocarbon impacted site with at least 80 years of spillage history. The geophysical data were compared by geochemical point measurements to evaluate the relationship between the distribution of geochemical parameters and the observed geophysical signatures. In addition, the study investigates the adverse effects of the contamination on the soil and groundwater biogeochemical conditions. As discussed earlier, the geophysical response can vary dramatically depending on each site environmental conditions. Therefore, this study is designed to evaluate the ability of the geophysical methods to characterize the contamination at a part of the contaminated site. This aims to find a good combination of non-intrusive and low cost methods which can be used to follow the remediation process on the whole site by providing large scale information in a fast way.

4.2. Study site

The study site was an abandoned petroleum refinery located North-West to Paris (France) and situated on an alluvial plain of the Seine River. The site was contaminated by diverse hydrocarbon products, including light non-aqueous phase liquid (LNAPL) and dense non-aqueous phase liquid (DNAPL) through leakage from tanks and pipelines over the refinery operating years (Figure 4.1). The activities of the refinery started at the beginning of the 20’s century and dealt with various petroleum products such as bitumen, kerosene, oil, heavy fuel and benzene. The

seepage of LNAPL and DNAPL products into the subsurface resulted in three contamination phases: a dissolved phase, a free phase and a residual phase. The dissolved phase was detected deep in the aquifer and spreads down to a depth of approximately 25 m. The free phase has a thickness varying from 1 to 100 cm and the residual phase is present mainly at the source zones. However, the groundwater table fluctuations resulted in the presence of the residual phase away from the source zones as the groundwater table and the extended free phase plume rise and drop due to the river high and low tides. It is important to note that not all the contamination source zones are known due to the long history of contamination and due to changes in the refinery structures (i.e., tanks and pipelines) locations associated with almost 85 years of refining activity.

In terms of geology, the first 2 m constitutes an anthropogenic layer composed of sand and coarse grain diameter gravel. A layer of fine to medium sand coarsening to gravel underlays the anthropogenic layer. This layer has an average thickness ranging between 8 and 25 m. An alluvial unconfined aquifer exists in the sand and gravel layer at a depth ranging from 4 to 11 m. The alluvial aquifer is underlain by a chalk aquifer which starts at a depth ranging between 11 and 25m. The groundwater flow direction is from the South-East to the North-West towards the River.

4.3. Methods

4.3.1. Geochemistry

A series of analyses have been conducted on groundwater samples including: head space gas chromatography/mass spectrometry (GM/MS) to quantify the volatile C5-C10 hydrocarbons, the BTEX (benzene, toluene, ethylbenzene and xylene) and the halogenated volatile organic compounds; hexane extraction and gas chromatography/flame ionization detector (GC-FID) to quantify the total C10-C40 hydrocarbons and the standard method (ASTMD6209-13) to quantify the polycyclic aromatic hydrocarbons (PAH). Investigations of the TDS, dissolved oxygen and groundwater electrical conductivity (GEC) were accomplished by placing INW (Instrumentation NorthWest) smart sensors in the site boreholes. Additionally, *in-situ* redox potential measurements were conducted on groundwater samples taken from the boreholes.

4.3.2. Geophysics

a. Electrical resistivity tomography and induced polarization

The ERT method comprises injecting direct current into the subsurface by using current electrodes, and then, determining the spatial distribution of apparent electrical resistivity by measuring the electrical potential difference between potential electrodes (Loke and Barker, 1996). A Syscal Pro system was used to obtain six two-dimensional (2D) ERT and IP profiles. These profiles were acquired according to the contaminants distribution in groundwater (Figure 4.2), where one profile was conducted in the clean zone (P6), two profiles were conducted in the

contaminated zone (P1 and P4) and three profiles extended from the clean to the contaminated zone (P5, P8 and P9). An additional profile was conducted in a clean area outside the contaminated site and will be considered as a background profile.

The measurements were performed by using wenner and dipole-dipole arrays and with an electrode spacing of 2 m. The data collected in the field were filtered and processed using the computer software Res2Dinv (Loke and Barker, 1996). This program uses the field data to determine 2D models of electrical resistivity and chargeability in the subsurface (Griffiths and Baker, 1993). These models are subdivided into several small blocks and a least-square inversion technique is used to retrieve the resistivity and chargeability values of each block with a smoothness constraint. Additionally, the obtained IP data were normalized by the inverted electrical resistivity data to get profiles of the normalized chargeability.

b. Ground penetrating radar

Ground penetrating radar (GPR) is a high frequency electromagnetic method which operates by sending pulses of electromagnetic waves into the subsurface. These waves encounter changes in the subsurface dielectric properties and, afterward, they are reflected back to the surface, where they are captured by a receiver (Neal, 2004). The GPR survey, discussed in this paper, was carried out by using a Mala Geosciences GPR system consisting of a shielded antenna, a Mala X3M integrated control unit and a 300 mm distance measuring wheel that controls the data collection at user's defined distance intervals. The 250 MHz antenna was chosen after field testing with both 100 MHz and 250 MHz antennas, where the 250 MHz antenna provided the best image quality with the required penetration depth.

Four 2D GPR profiles were acquired by using a wheel mode with a recording interval of 0.10 meters, a time window of 450 ns and a number of 512 stacks per trace. The 4 GPR profiles (P1, P4, P6 and P8) were acquired along the ERT profiles to provide a joint interpretation of the data produced by the two geophysical methods. The data acquisition was followed by the following processing steps: (i) dewow filtering to remove the initial direct current signal component and its subsequent low frequency trend; (ii) background removal; (iii) time-zero correction to overcome the time zero point jump (caused by equipment instability) and find the true ground surface reflection; (iv) band-pass filtering to remove the low and high frequency components, where the pass region used was between 50 and 350 MHz and (v) to improve the visual quality of the data, it was necessary to multiply the traces by a gain function that overcomes the effects of geometrical spreading losses.

c. Self potential

Two non-polarizable (Pb-$PbCl_2$) Petiau lead electrodes suspended in porous containers and supersaturated with lead chloride solutions were used to collect the self potential data. The first electrode is the reference electrode which has a fixed location. The second electrode is the measurement electrode which is moved across different locations by a rolling wire. The location of the reference electrode was chosen in the clean zone and was common for all the measurement stations. To ensure a good electrical contact between the electrodes and the resistive surface

sediments, small holes were dug and filled with bentonite mud at the measurements and reference stations (Jardani et al., 2006). The potential difference between the two electrodes was measured by using a high input impedance (10 MΩ) voltmeter (MX20).

A self potential map was acquired in February 2015, by doing the measurements at all possible locations with a random spacing. The zones with no SP measurements correspond to areas where we had no access to, and to areas where buildings and thick asphaltic layers were encountered. Zones where pipelines are present in the subsurface were avoided and anomalies corresponding to such installations were filtered out from the data. The removal of the self-potential electrokinetic component from the SP field data is important for isolating the SP signal produced by redox processes. This was carried out by computing the electro-kinetic component from the following first order approximation of Fournier's equation expressed by Revil et al. (2003):

$$\Delta\varphi_{redox} = \Delta\varphi_{obs} - \Delta\varphi_{EK}, \quad (1)$$

$$\Delta\varphi_{EK} = C'\left(h - h_0\right), \quad (2)$$

where $\Delta\varphi_{redox}$ (mV) is the SP signal due to the redox effect; $\Delta\varphi_{EK}$ (mV) denotes the SP signal related to the electrokinetic effect; C'(mV/m) denotes the electrokinetic coupling coefficient; h (m) is the piezometric head recorded in the different wells and h_0 (m) is the piezometric head at the reference station (Atangana et al., 2015). To determine the electrokinetic coupling coefficient, a simple laboratory experiment was performed by using a 50 cm long and 10 cm in diameter graduated plastic tube (Revil and Jardani, 2013). The bottom of the tube was filled with a representative soil sample extracted from borehole B8 (Figure 4.2). Then, contaminated groundwater having an electrical conductivity of approximately 1000 $\mu S/cm$ was extracted from borehole B8 and injected from the top of the tube. The self potential difference between two non-polarizable electrodes placed at the bottom and the top of the soil sample was measured at different water head levels with an interval of 5 cm. The output of this experiment was a plot of the potential difference against the water head levels from which the electrokinetic coupling coefficient C' (represented in mV per meter of water head variation) was computed. The results showed a C' value of -4.0±1 mV/m. The C' value was then used to calculate the electrokinetic SP contribution associated with groundwater flow, which was then subtracted from the SP data to produce a map of residual SP. We note that the obtained electrokinetic contribution was determined to be very small in comparison to the self-potential signature associated with redox effects.

4.4. Results

4.4.1. Geochemistry

Figure 4.2, shows the results of the C10-C40 and C5-C10 hydrocarbons measurements conducted on groundwater samples. The boreholes located in the North-Western part of the site

(B34 and B12) showed concentrations ranging from 1.2 to 4 mg/L. B13 and B11 recorded higher concentrations ranging between 1.6 and 6.1 mg/L. The boreholes located between the North-West and the center of the site (B33 and B9) showed values ranging between 1.3 and 2.6 mg/L. The measurements of C5-C10 hydrocarbons recorded values ranging from 98 to 100 mg/L in B34 and B12. These measurements also recorded values ranging from 13 to 27 mg/L in B13 and B11, whereas it recorded values ranging from 1.4 to 3.7 mg/L in B33 and B9. Zero concentrations of all the measured types of hydrocarbons were recorded in groundwater samples taken from the North-Eastern part of the site (B1, B2, B3 and B4). Therefore, this zone was considered as a groundwater clean zone.

Figures 4.3, 4.4 and 4.5 and Table 1, show the measured groundwater geochemical parameters. The analyses done on groundwater samples taken from the contaminated aquifer boreholes (e.g., B7, B8, B9, B10, B11, etc.) show: TDS concentrations ranging from 300 to 1000 mg/L (Figure 4.3); GEC values ranging from 500 to 2000 $\mu S/cm$ (Figure 4.4) and low electron acceptors (TEAs) concentrations such as dissolved oxygen (Figure 4.5), sulfate and nitrate (Table 1). In contrast, the analyses done on groundwater samples taken from the clean groundwater zone boreholes (B1, B2, B3 and B4) show: lower TDS concentrations ranging from 50 to 200 mg/L, lower GEC values ranging from 200 to 400 $\mu S/cm$ and higher concentrations of TEAs. However, boreholes B5, B6 and B34 show lower GEC and TDS values compared to the other contaminated locations. This is attributed to the constant flushing of clean groundwater at the boundary of the plume, which can replace the high salinity contaminated groundwater in the flow direction.

The redox potential measurements showed negative redox potential values ranging from -10 to -300 mV in the contaminated groundwater boreholes (e.g., -120 mV in B9, -89.4 mV in B10) and positive redox potential values ranging from 1 to 30 mV in the clean groundwater boreholes (e.g., 30 mV in B3 and 18 mV in B1). Temperature values ranging from 12.1 °C to 16.8 °C and pH values ranging from 6.07 to 7.14 were recorded at the whole site. Based on the contamination history (at least 80 years) and on the observed difference in geochemical parameters between the contaminated and the clean samples, it is assumed that sufficient time has elapsed to modify the biogeochemical properties of the subsurface through alteration of hydrocarbon products by bacterial processes.

4.4.2. Geophysics

This section presents the geophysical results and derives primary interpretations by correlating the geophysical data with soil boring profiles. Figure 4.6a, shows an ERT profile conducted in a clean area located outside the contaminated site. This is considered as the electrical resistivity background profile because the area has similar hydrogeological context to that of the contaminated site. The profile shows a high resistivity zone that extends from a depth of 7 m down to a depth of 23 m. This zone has resistivity values ranging from 200 to 300 Ω.m representing the clean aquifer. The high resistivity zone is overlain by a zone of lower resistivity (5 to 50 Ω.m)

corresponding to clayey sand sediments dominating the unsaturated zone. The IP background profile shows low normalized chargeability values ranging from 0.01 to 0.1 mS/m in the aquifer (Figure 4.6b).

Profile P6, which is located in the clean groundwater zone, shows a high resistivity region extending from near surface into the aquifer, with values ranging from 250 to 500 Ω.m and reflecting background values (Figure 4.7a). This profile was affected by the presence of a metallic pipe which appears as a small low resistivity anomaly located between surface points x=85 m and x=96 m and at a depth of around 2 m. The IP profile P6 shows low normalized chargeability in the aquifer with values ranging from 0.3 to 0.5 mS/m (Figure 4.7b). The high chargeability anomaly located between surface points x=85 m and x=96 m represents the metallic pipe. The GPR profile P6 shows a good reflection pattern reaching a depth of around 8 m, where a fairly continuous reflector representing the water table appears (Figure 4.7c). This reflector is a result of the large change of the relative permittivity from dry sand to saturated sand (Sauck et al., 1998). The GPR profile did not show a reflection from the buried pipe because it was done parallel to the ERT profile and 1 meter away from it due to the presence of dense vegetation.

The geophysical profiles P1 and P4, shown in Figures 4.8 and 4.9, are located within the contaminated area. P1 shows a high resistivity region extending from near surface to a depth of approximately 6 m with resistivity values ranging from 150 to 300 Ω.m (Figure 4.8a). This high resistivity region represents the anthropogenic layer and the sand and gravel vadose zone. Below this zone, the resistivity values decrease to reach approximately 5-30 Ω.m in the aquifer which has a depth of approximately 9 m. The IP profile P1 shows higher normalized chargeability values (1.5 to 5 mS/m) in the aquifer, in comparison to the clean zones' profiles (Figure 4.8b). The most prominent feature in the GPR profile P1 is the region of attenuated reflections (shadow zones) appearing at a depth of 4 m and extending to the bottom of the profile (Figure 4.8c). P4 shows a zone of low resistivity (5 to 30 Ω.m) and high chargeability (1 to 5 mS/m) rising from the aquifer to a very shallow depth and coincident with a region of GPR shadow zones (Figure 4.9). This indicates that the attenuation of GPR reflections may be attributed to the soil enhanced electrical conductivity which can limit the penetration depth of GPR waves (Sauck, 2000). Furthermore, the examination of soil boring data revealed that these attenuation regions in both profiles are coincident with moist and glistening sediments having a darker color and strong gasoline odor. The gradual increase of resistivity values at a depth of approximately 21 m in profile P4 is related to the top of the chalk aquifer which has a depth of around 23 m in this zone (Figure 4.9).

Two resistivity zones are clearly delineated in the aquifer of profile P8 which has both clean and contaminated parts (Figure 4.10b). The first zone, associated with the clean part of the profile, has resistivity values within the range of 150 to 300 Ω.m. This zone, located between x=0 m and x=80 m surface points, extends from a depth of 8 m down to a depth of 23 m and recorded a groundwater electrical conductivity of approximately 1000 $\mu S/cm$. The resistivity response changes to lower values (15-50 Ω.m) in the contaminated part of the aquifer located between x=80 m and x=140 m surface points. The groundwater electrical conductivity in this part recorded a

value of 400 µS/cm. The low resistivity zone, appearing above the high resistivity one, corresponds to clayey sediments which are present exceptionally in this part of the site. The GPR profile P8 shows a strong reflection pattern with the groundwater table reflector appearing at a depth of approximately 8 m in the clean part of the profile (Figure 4.10c). This reflector disappears in the contaminated part of the profile and the shadow zones appear again starting from a depth of 4 m, and between surface points x=75 m and x=120 m. The shadow zones, which appear above the water table in the clean part of profile P8 and in profile P6, are related to the conductive clayey sediments present in this part of the site. Additionally, profile P8 shows a change of SP values from positive in its clean part, to negative in its contaminated part (Figure 4.10a).

To validate the electrical resistivity shift observed in P8, two more profiles extending from the clean to the contaminated zone were conducted (Figure 4.11). These profiles show a sharp shift from high electrical resistivity values (150-300 Ω.m) close to the clean aquifer boreholes, to lower values close to the contaminated aquifer boreholes (5-30 Ω.m). The shift is identified at x=80 m in P8, at x= 76 m in P5 and at x=52 m in P9.

The residual SP map acquired at the site shows negative values ranging from -234 to -10 mV in the regions of contaminated groundwater (Figure 4.12a). Conversely, the map shows positive values ranging from 8 to 80 mV in the region of clean groundwater. Furthermore, the SP data show a good correlation (R^2=0.81) with the redox potential data (Figure 4.12b), with positive redox potential values within the clean groundwater region coincident with positive SP values, and negative redox potential values in the contaminated groundwater region coincident with negative SP values. It is important to note that there is no significant change in the lithology between the clean and contaminated zones. Hence, the observed changes in the self-potential, electrical resistivity, normalized chargeability and GPR signals are significant and suggest that the contaminated media geophysical properties have been modified due to hydrocarbon contamination.

4.5. Discussion

The geophysical results obtained in this study demonstrated the following: (1) regions of low resistivity and high chargeability values starting above the groundwater table and extending into the contaminated aquifers down to a depth of around 23 m; (2) regions of attenuated GPR reflections starting at a shallow depth and (3) a sharp shift in the self-potential signatures from negative values in the contaminated zone to positive values in the clean zone. The shift in the geoelectrical signature, from resistive in the clean zone to conductive in the contaminated zone, indicates that significant alterations of the hydrocarbon contaminants and host media have occurred.

The source of the conductive response is thought to be a leachate produced by bacterial action on hydrocarbons during the biodegradation of the contaminant mass (Atekwana and

Atekwana, 2010). Bacteria obtain their energy through biodegradation of hydrocarbons, as these microorganisms oxidize organic matter for their growth and reduce TEAs for their respiration (Semple et al., 2007; Tiehm and Schulze, 2003). The reduction of TEAs such as oxygen, nitrate, manganese, iron, sulfate and carbon dioxide leads to their depletion. This was shown in the geochemical data, where lower concentrations of oxygen, nitrate and sulfate were observed in the contaminated zone (Figure 4.5 and Table 1). The reduction of TEAs produces metabolic byproducts such as CO_2 and H_2O, which in turn undergo chemical reactions and form organic and carbonic acids (Sauck, 2000). An example would be the reaction of the metabolic byproduct CO_2 with water which produces carbonic acids that reduce the pH of the medium (Martinho et al., 2009). Apparently, organic and carbonic acids cause etching and dissolution of minerals surfaces and the reduction of the pH causes the leaching of soluble salts present at the grains coating (McMahon et al., 1995). These processes lead to an increase in the concentrations of TDS and enhance the ionic strength and electrolytic conductivity of pore fluids (Atekwana et al., 2004a). This explanation is corroborated by our geochemical data which recorded elevated TDS concentrations which are two to three times greater than background values (Figure 4.3). Further support for this explanation was provided by the scanning electron microscope (SEM) images of contaminated samples that showed etched pits and dissolution patterns which could be attributed to microbial alterations of mineral grains (Figure 4.13a). Additionally, higher concentrations of ions were observed in the impacted zones, with the highest concentrations for Pb^{2+}, Zn^{2+}, Mg^{2+} and Ca^{2+} (Table 1). The increase in the TDS concentrations and electrolytic conductivity is reflected in the elevated GEC measurements that showed values ranging between 600 and 2000 $\mu S/cm$ in contaminated samples, whereas the values were in between 200 and 400 $\mu S/cm$ in clean samples (Figure 4.4).

The observed elevated concentrations of TDS and the consequent increase of pore water electrical conductivity can increase the bulk electrical conductivity, and as a result, can produce low electrical resistivity values in the contaminated zones (Atekwana et al., 2004a; Sauck, 2000). The increase in the bulk electrical conductivity was evident in profiles P1, P4 and P8 that showed resistivity values ranging from 5 to 50 Ω.m in the contaminated aquifer. Previous studies also reported low electrical resistivity anomalies, associated with a leachate plume of enhanced TDS concentrations below LNAPL impacted zones (e.g., Atekwana et al., 2005; Sauck et al., 1998). These studies attributed these observations to minerals dissolution processes coupled to the biodegradation of hydrocarbons.

The low electrical resistivity anomaly was coincident with GPR shadow zones that followed the same pattern of the anomaly in profile P4 (Figure 4.9). This indicates that the increased soil electrical conductivity played a key role in the attenuation of GPR signal amplitudes, leading to shadow zones in profiles P1 and P4. This assumption was also validated by profile P8, where the shadow zones appeared and the reflection from the water table disappeared in its contaminated part, which was associated with low resistivity values (Figure 4.10). The increased electrical conductivity of pore fluids introduces significant absorptive losses, which are primarily dependent

upon the pores chemical and physical properties (Cassidy, 2007). The attenuation of the GPR signal depends on the electrical conductivity of the medium as shown in the following equation:

$$\alpha \approx \frac{\sigma}{2}\sqrt{\frac{\mu}{\varepsilon}}\ , \tag{3}$$

where α is the attenuation constant, σ is the electrical conductivity, μ is the magnetic permeability and ε is the dielectric permittivity. Apparently, changes in the pore fluid conductivity impacted the attenuation constant and thus produced attenuated reflections zones (shadow zones) in the GPR profiles. The signal attenuation in the GPR profiles P1 and P4 started at depths of around 4 m and 3 m respectively (Figures 4.8 and 4.9). These shallow shadow zones correspond to the residual phase of the contamination. This was validated by the soil boring data which showed a marked change in the color of sediments with a strong gasoline odor starting at the depths where the shadow zones were encountered. The residual phase was not well detected by the ERT method due to the method's lower resolution compared to the GPR and due to the high resistivity of the vadose zone. As a conclusion, the observed elevated concentrations of TDS are believed to be responsible for the soil increased electrical conductivity which starts at the residual phase expressed by the shadow zones in the GPR profiles, and extends into the aquifer down to a depth of 23 m as a dissolved phase expressed by the low resistivity values in the ERT profiles.

The accumulation of ions in the pore fluids and the associated electrochemical reactions enhance the ionic strength and charge build up at the electrical double layer (EDL) which forms at the electrolyte-mineral interface (Slater et al., 2005; Ward, 1990). This can enhance the membrane polarization of the EDL as a result of decreased mobility of the ionic charge carriers or blockage of the pore current conduction path (Sogade et al., 2006). Besides, Abdel Aal et al. (2014) showed that iron mineral precipitates such as magnetite and pyrite have high interfacial polarizability due to the high population of conduction electrons in the mineral structure. Microbial mineral interactions can lead to the precipitation of different iron phase minerals. For example, the iron reduction by anaerobic Fe (III) reducing bacteria may enhance the production of Fe (II), which can react with Fe (III) and HS^- in solution to form magnetite and pyrite respectively (Abdel Aal et al., 2014). The energy dispersive X-ray spectroscopy (EDX) measurements of contaminated samples showed iron peaks that can contribute to the polarization of the contaminated sediments (Figure 4.14a). The obtained normalized chargeability, defined as the specific capacity, is independent of the conduction magnitude (electrical resistivity) and is sensitive to the geochemical modifications at the mineral-fluid interface (Lesmes and Frey, 2001; Slater and Lesmes, 2002). Therefore, the production of ions that enhanced the solution's ionic strength, in addition to the presence of iron mineral precipitates, are probably responsible for the higher normalized chargeability responses in the contaminated zone profiles (Figures 4.8b and 4.9b).

The leachate plume resulting from the hydrocarbon contamination is rich in organic matter with a great capacity to donate electrons during redox reactions. The consumption of TEAs through microbial respiration in the vicinity of the plume causes a change in the redox chemistry of pore fluids. Baedecker et al. (1993) showed that the plume is more reducing than the surrounding media.

Therefore, the zone within the plume is anoxic and reducing, while the zone outside the plume is oxic and oxidizing. As microorganisms play a key role because they derive their energy from oxidation-reduction reactions to maintain life-sustaining processes (Semple et al., 2007; Tiehm and Schulze, 2003), different microbial communities can be present as continuous biofilms at the water table, where most of the oxygen and organic nutrients are available (Naudet and Revil, 2005). According to the biogeobattery model, bacterial biofilms or mineral precipitates accumulating below the water table separate the reduced zone from the oxidized zone and act as electronic conductors (Delong, 2002; Naudet et al., 2004; Tender et al., 2002). The presence of an electrical conductor allows electron transfer between the distinct redox zones and produces a natural electrical current which can be measured at the surface as an electrical self-potential signal (Naudet et al., 2004; Revil et al., 2010). While the reduction of TEAs during the biodegradation process is limited to a negative range of redox potential (Tiehm and Schulze, 2003), the redox potential measurements showed negative values within the contaminated aquifer in accordance with the negative SP values, and positive values within the clean aquifer in accordance with the positive SP values. The obtained good correlation ($R^2 = 0.81$) between the SP and redox potential values indicates that electron transfer processes driven by redox gradients are occurring at the contaminated site. However, the study does not provide any evidence on the presence of bacterial biofilms due to the destructive sampling procedure, which was done during the drilling process. Nevertheless, the iron peaks observed in the EDX data (only in contaminated samples) indicate that mineral precipitates may have played an important role in the current conduction process (Figure 4.14).

By using the SP data, the clean zone borders were delineated according to the zone of positive SP values (Figure 4.15). The borders of the clean zone were also roughly estimated through remarking the points at which the aquifer resistivity values started to change from high to low in profiles P8, P9 and P5 (Figure 4.15). Both estimations were in great agreement and detected the borders of the clean zone at approximately the same locations in between the contaminated and clean boreholes. The change of the geophysical response in profile P8 occurred at x=80 m in the ERT profile, at x= 75 m in the GPR profile and at x= 88 m in the SP profile (Figure 4.10). This demonstrates the success of the three methods in detecting a geophysical contrast between the contaminated and clean zones at close proximity depending on the horizontal resolution of each method.

The geophysical response in this study supports the findings of Sauck (2000), who suggested that biological alterations of hydrocarbons can substantially modify the pore water biogeochemistry, producing a temporal shift in the geoelectrical signature from resistive to conductive. However, most of the previous studies observed the low resistivity anomalies mostly within the groundwater fluctuation zone and directly below the groundwater table, whereas this study suggests that after sufficient time, a massive contamination of LNAPL and DNAPL products can be observed as a low resistivity anomaly down to several meters in the aquifer due to the contamination dissolved phase.

4.6. Conclusion

The study provides a successful application where the most frequently used geophysical methods in hydrocarbon contamination investigations were combined on the same profile lines. The geochemical data provided evidence of bacterial biodegradation processes and the hydrocarbon contaminated aquifers were localized as low resistivity zones. The combination of the four methods reduced the ambiguity in the interpretations by recording the change in the geophysical signatures at similar locations. Additionally, this combination provided insight on the different processes that might have modified the contaminated sediments chemical and biological properties. The ERT and IP results indicated that the contamination modified the capacitive and ohmic parts of the electrical conduction in contaminated sediments. The GPR was able to give information about the depth to the residual zone and can be used in further investigations to detect the residual phases and locate unknown source zones. The ERT and IP methods provided information about the extent of the contamination in the aquifer due to the dissolved phase and can be used to obtain spatial information on the groundwater quality and chemical conditions. Furthermore, the SP method provided an indirect indication of bacterial activity and possible presence of biofilms and mineral precipitates that are suggested to have played a key role in the electrical current conduction. The observed good correlation between the SP data and the redox potential distribution can be used for the fast monitoring of the plume evolution over time during the remediation process.

The study was able to roughly delineate the clean zone borders and demonstrated a good relationship between the geophysical and the geochemical data. Therefore, this approach can be used to monitor the remediation process according to the observed geophysical contrast between the clean and contaminated zones. The successful detection of the contamination by the four methods provides a methodology which has the ability to provide large area coverage, in a way that a certain geophysical method can be used when another cannot be conducted. The next stage of the research will include time lapse 3D geophysical measurements to monitor the remediation process. A proper understanding of the biological and chemical factors that govern the geophysical responses, and which of these factors are likely to mostly affect the geophysical signal is important. Therefore, the geophysical surveys will be guided by biological and chemical surface phase experiments to get a better understanding of the processes involved in changing the geophysical response of contaminated sediments.

4.7. References

Abdel Aal, G.Z., E.A. Atekwana, and A. Revil, 2014. Geophysical signatures of disseminated iron minerals: A proxy for understanding subsurface biophysicochemical processes. J. Geophys. Res. Biogeosciences 119, 1831–1849. doi: 10.1002/2013JG002492.

Abdel Aal, G.Z., E.A. Atekwana, and E.A. Atekwana, 2010. Effect of bioclogging in porous media on complex conductivity signatures. J. Geophys. Res. 115, 1–10.

Allaud, L. A., and M. H. Martin, 1977. Schlumberger, The history of a technique. John Wiley & Sons, Inc.

Arora, T., N. Linde, A. Revil, and J. Castermant, 2007. Non-intrusive characterization of the redox potential of landfill leachate plumes from self-potential data. J. Contam. Hydrol. 92, 274–92. doi:10.1016/j.jconhyd.2007.01.018.

Atangana, J.Q.Y., M.A Angue, B. Nyeck, C. Ndongue, and J.T. Tchatat, 2015. Electrical Characterization and Mineralogical Differentiation of a Weathering Cover in the South Cameroon Humid Intertropical Zone using the Self-potential Method. Journal of Environmental and Engineering Geophysics 20(1), pp.57-70.

Atekwana, E.A., W.A. Sauk, and D. D. Werkema, 2000. Investigations of geoelectrical signatures at a hydrocarbon contaminated site. Appl. Geophys. 44, 167–180.

Atekwana, E.A., W.A. Sauk, and G.Z. Abdel Aal, 2002. Geophysical investigation of vadose zone conductivity anomalies at a hydrocarbon contaminated site: Implications for the assessment of intrinsic bioremediation. Environ. Eng. Geophys. 7, 103–110.

Atekwana, E.A., E.A. Atekwana, R.S. Rowe, D.D. Werkema, and F.D. Legall, 2004a. Total dissolved solids in groundwater and its relationship to bulk conductivity of soils contaminated with hydrocarbon. Journal of Applied Geophysics 56, 281–294.

Atekwana, E.A., E.A. Atekwana, D.D. Werkema, J.P. Allen, L.A. Smart, J.W. Duris, D. P. Cassidy, W.A. Sauck, and S. Rossbach, 2004b. Evidence for microbial enhanced electrical conductivity in hydrocarbon-contaminated sediments. Geophysical Research Letters 31, L23501. doi:10.1029/2004GL021359.

Atekwana, E.A., E.A. Atekwana, F.D. Legall, and R.V. Krishnamurthy, 2005. Biodegradation and mineral weathering controls on bulk electrical conductivity in a shallow hydrocarbon contaminated aquifer. J. Contam. Hydrol. 80, 149–167.

Atekwana, E.A. and E.A. Atekwana, 2010. Geophysical Signatures of Microbial Activity: A Review. Surv. Geophys. 31, 247–283. doi: 10.1007/s10712- 009 -9089 -8.

Baedecker, M.J., I.M. Cozzarelli, and J.A. Hopple, 1987. The composition and fate of hydrocarbons in a shallow glacial-outwash aquifer. U.S. Geol. Survey Open-File Report, pp. 87–109.

Baedecker, M. J., I.M. Cozzarelli, R.P. Eganhouse, D.I. Siegel, and P.C. Bennett, 1993. Crude oil in a shallow sand and gravel aquifer: III. Biogeochemical reactions and mass balance modeling in anoxic groundwater. Applied Geochemistry 8, 569–586.

Bennett, P.C., F.K. Hiebert, and W.J. Choi, 1996. Microbial colonization and weathering of silicates in a petroleum-contaminated groundwater. Chemical Geology 132, 45–53.

Benson, A.K., 1995. Applications of ground penetrating radar in assessing some geological hazards: examples of groundwater contamination, faults, and cavities. Journal of Applied Geophysics 33, 177–193.

Benson, A.K., K.L. Payne, and M.A. Stubben, 1997. Map- ping groundwater contamination using DC resistivity and VLF geophysical methods: a case study. Geophysics 62, 80–86.

Bermejo, J.L., W.A. Sauck, and E.A. Atekwana, 1997. Geophysical discovery of a new LNAPL plume at the former Wurtsmith AFB, Oscoda, Michigan. Ground Water Monitoring Review 17, 131– 137.

Blondel, A., M. Schmutz, M. Franceschi, M. Carles, and F. Tichane, 2014. Case study of a hydrocarbon contaminated site using the spectral induced polarization method: contribution of laboratory measurements for the interpretation of field results. 3rd International Workshop on Induced Polarization, 6 – 9 April 2014 (Oléron Island, France).

Béhaegel, M., J.C. Gourry, and J. F. Girard, 2004. Geophysical measurements on an ancient coking plant contaminated by tar. EGU 1st General Assembly, Nice, 25–30 April, Poster HS17-1FR2P-0110 (EGU04-A-01783).

Campbell, D.L., J.E. Lucius, K.J. Ellefsen, and M. DeszczPan, 1996. Monitoring of a controlled LNAPL spill using ground penetrating radar. Proceedings of the Symposium on the Application of Geophysics to Engineering and Environmental Problems (SAGEEP ’96), Keystone, CO, pp. 511–517.

Cassidy, D.P., D.D. Werkema, W.A. Sauck, E.A. Atekwana, S. Rossbach, and J. Duris, 2001. The effects of LNAPL biodegradation products on electrical conductivity measurements. Journal of Environmental and Engineering Geophysics 6, 47–52.

Cassidy, N.J., 2007. Evaluating LNAPL contamination using GPR signal attenuation analysis and dielectric property measurements: Practical implications for hydrological studies. Journal of Contaminant Hydrology 94, 49-75.

DeRyck, S.M., J.D. Redman, and A.P. Annan, 1993. Geophysical monitoring of a controlled kerosene spill: Symposium on the Application of Geophysics to Engineering and Environmental Problems (SAGEEP), Proceedings, 5–20.

Delong, E., 2002. L'électricité bactérienne, plus qu’une curiosité. La Recherché, 358, 17.

Eganhouse, R.P., M.J. Baedecker, I.M. Cozzarelli, G.R. Aiken, K.A. Thorn, and T.F. Dorsey, 1993. Crude oil in a shallow sand and gravel aquifer: II. Organic geochemistry. Applied Geochemistry 8, 551–567.

Glaser, D.R., D.D. Werkema, R.J. Versteeg, R.D. Henderson, and D.F. Rucker, 2012. Temporal GPR imaging of an ethanol release within a laboratory-scaled sand tank. Journal of Applied Geophysics 86, 133-145.

Griffith, D. H., J. Turnbull, and A.I. Olayinka, 1990. Two-dimensional resistivity mapping with a computer controlled array. First Break 8, 121-129.

Griffiths, D.H., and R.D. Barker, 1993. Two-dimensional resistivity imaging and modeling in areas of complex geology. Journal of Applied Geophysics 29, 211-226.

Grumman, D.L., and J.J. Daniels, 1995. Experiments on the detection of organic contaminants in the vadose zone. Journal of Environmental and Engineering Geophysics, 31–38.

Hämmann, M., H.R. Maurer, A.G. Green, and H. Horstmeyer, 1997. Self-Potential Image Reconstruction: Capabilities and Limitations. Eng. Geophys., 2, 21–35.

Haack, S.K., and B.A. Bekins, 2000. Microbial populations in contaminant plumes. Hydrogeol. J. 8, 63–76.

Hiebert, F.K., and P.C. Bennett, 1992. Microbial control of silicate weathering in organic rich ground water. Science 258, 278–281.

Jardani, A., J.P. Dupont, and A. Revil, 2006. Self-potential signals associated with preferential groundwater flow pathways in sinkholes. J. Geophys. Res. 111.

Lee, J.Y., J.Y. Cheon, K.K. Lee, S.Y. Lee, and M.H. Lee, 2001. Factors affecting the distribution of hydrocarbon contaminants and hydrogeochemical parameters in a shallow sand aquifer. Contam. Hydrol. 50 (12), 139-158.

Lesmes D., and K. Frey, 2001. The influence of pore fluid chemistry on the complex conductivity and induced-polarization responses of Berea sandstone. J. Geophys. Res., 106, 4079.

Loke, M.H., and R.D. Barker, 1996. Rapid lEast-squares inversion of apparent resistivity pseudosections by a quasi-Newton method. Geophysical Prospecting 44, 131–152.

Mazac, O., L. Benes, I. Landa, and A. Maskova, 1990. Determination of the extent of oil contamination in groundwater by geoelectrical methods. In: Ward SH (ed) Geotechnical and environmental geophysics 2, 107–112.

Martinho, E., M.M. Abreu., M.E. Pampulha, F. Alegria, A. Oliveira, and F. Almeida, 2009. An experimental study of the diesel biodegradation effects on soil biogeophysical parameters. Water Air soil Pollut. 206 (1), 139-154.

McMahon, P.B., D.A. Vroblesky, P.M. Bradley, F.H. Chapelle, and C.D. Guller, 1995. Evidence of enhanced mineral dissolution in organic acid rich shallow ground water. Ground Water 33, 207–216.

Minsley, B.J., J. Sogade and F.D., Morgan, 2007. Three-dimensional self-potential inversion for subsurface DNAPL contaminant detection at the Savannah River Site, South Carolina. Water Resources Research, Vol. 43, W04429, doi:10.1029/2005WR003996, 2007.

Neal, A., 2004. Ground penetrating radar and its use in sedimentology: principles, problems and progress. Earth-Science Reviews 66 (3-4): 261-+.

Naudet, V., A. Revil, J.Y. Bottero, and P. Begassat, 2003. Relationship between self-potential (SP) signals and redox conditions in contaminated groundwater: Geophysical Research Letters 30, 2091. doi: 10.1029/2003GL018096.

Naudet, V., A. Revil, E. Rizzo, J.Y. Bottero, and P. Bégassat, 2004. Groundwater redox conditions and conductivity in a contaminant plume from geoelectrical investigations. Hydrol. Earth Syst. Sci. 8, 8–22. doi: 10.5194/hess-8-8-2004.

Naudet, V., and A. Revil, 2005. A sandbox experiment to investigate bacteria-mediated redox processes on self-potential signals. Geophys. Res. Lett. 32.

Nyquist, J.E., and C.E. Corry, 2002. Self-potential: the ugly duckling of environmental geophysics. The Leading Edge, 21, 446-451. doi:10.1190/1.1481251.

Petterssen, J.K., and D.C. Nobes, 2003. Environmental geophysics at Scott Base: ground penetrating radar and electromagnetic induction as tools for mapping contaminated ground at Antarctic research bases. Cold Reg Sci. Technol 37, 187–195.

Revil, A., V. Naudet, J. Nouzaret, and M. Pessel, 2003. Principles of electrography applied to self-potential electrokinetic sources and hydrogeological applications. Water Resour. Res. 39.1114. doi: 10.1029/2001WR000916.

Revil, A., C.A. Mendonça, E.A. Atekwana, B. Kulessa, S.S. Hubbard, and K.J. Bohlen, 2010. Understanding biogeobatteries: Where geophysics meets microbiology. J. Geophys. Res. 115, G00G02. Doi: 10.1029/2009JG001065.

Rittgers J. B., A. Revil, M. Karaoulis, M.A. Mooney, L.D. Slater, and E.A. Atekwana, 2013. Self-potential signals generated by the corrosion of buried metallic objects with application to contaminant plumes. Geophysics, 78(5), EN65-EN82, doi: 10.1190/GEO2013-0033.1.

Revil, A., and A. Jardani, 2013. The Self-Potential Method, Theory and Applications in Environmental Geosciences, Cambridge University Press, Canbridge.

Samouëlian, A., I. Cousin, A. Tabbagh, A. Bruand, and G. Richard, 2005. Electrical resistivity survey in soil science: a review. Soil and Tillage Research. 83 (2), 173–193.

Sauck, W.A., E.A. Atekwana, and M.S. Nash, 1998. Elevated conductivities associated with an LNAPL plume imaged by integrated geophysical techniques. Journal of Environmental and Engineering Geophysics 2, 203–212.

Sauck, W.A., 2000. A conceptual model for the geoelectrical response of LNAPL plumes in granular sediments. Journal of Applied Geophysics 44, 151–165.

Schneider, G.W., and J.P. Greenhouse, 1992. Geophysical detection of perchloroethylene in a sandy aquifer using resistivity and nuclear logging techniques. Proceedings of the Symposium on the Application of Geophysics to Engineering and Environmental Problems, EEGS, pp. 619-628.

Semple, K.T., K.J. Doick, L.Y. Wick, and H. Harms, 2007. Microbial interactions with organic contaminants in soil: definitions, processes and measurement. Environ. Pollut. 150, 166–76. doi:10.1016/j.envpol.2007.07.023.

Shevnin, V., O. Delgado-Rodriguez, L. Fernandez-Linares, H. Zegarra Martinez, A. Mousatov, and A. Ryjov, 2005. Geoelectrical characterization of an oil-contaminated site in Tabasco, Mexico. Geofis. Int. 44, 251–263.

Slater, L.D., and D. Lesmes, 2002. IP interpretation in environmental Investigations. Geophysics, 67, 77.

Slater, L.D., J. Choi, and Y. Wu, 2005. Electrical properties of iron–sand columns: implications for induced polarization investigation and performance monitoring of iron-wall barriers. Geophysics 70 (4), G87–G94.

Sogade J.A., F. Scira-Scappuzzo, Y. Vichabian, W.Q. Shi, W. Rodi, D.P. Lesmes, and F.D. Morgan, 2006. Induced polarization detection and mapping of contaminant plumes. Geophysics 71, B75–B84.

Tender, L.M., C.E. Reimers, H.A. Stecher, D.E. Holmes, D.R. Bond, D.A. Lowy, K. Pilobello, S.J. Fertig, and D. Lovley, 2002. Harnessing microbially generated power on the seafloor. Nature Biotechnology, 20, 821-825.

Tezkan, B., P. Georgescu, and U. Fauzi, 2005. A radiomagnetotelluric survey on an oil-contaminated area near the Brazi Refinery, Romania. Geophys. Prospect. 53, 311–323.

Timm, F., and P. Möller, 2001. The relation between electrical and redox potential: an evidence from laboratory to field experiments. J. Geochem. Explor., 72, 115-127.

Tiehm, A., and S. Schulze, 2003. Intrinsic Aromatic Hydrocarbon Biodegradation for Groundwater Remediation. Oil Gas Sci. Technol. 58, 449–462. doi: 10.2516/ogst: 2003028.

Werkema, D.D., E.A. Atekwana, W.A. Sauck, S. Rossbach, and J. Duris, 2000. Vertical Distribution of Microbial Abundances and Apparent Resistivity at a LNAPL Spill Site. Proc. Symp. Appl. Geophys. to Eng. Environ. Probl. 669–678.

Werkema, D.D., E.A. Atekwana, A. Enders, W.A. Sauck, and D.P. Cassidy, 2003. Investigating the geoelectrical response of hydrocarbon contamination undergoing biodegradation. Geophysical Research Letters 30, 1647, doi: 10.1029/2003GL017346.

Ward, S.H., 1990. Resistivity and induced polarization methods. In: Ward, S.H. (Ed.), Geotechnical and Environmental Geophysics. SEG, pp. 169–189.

Figures

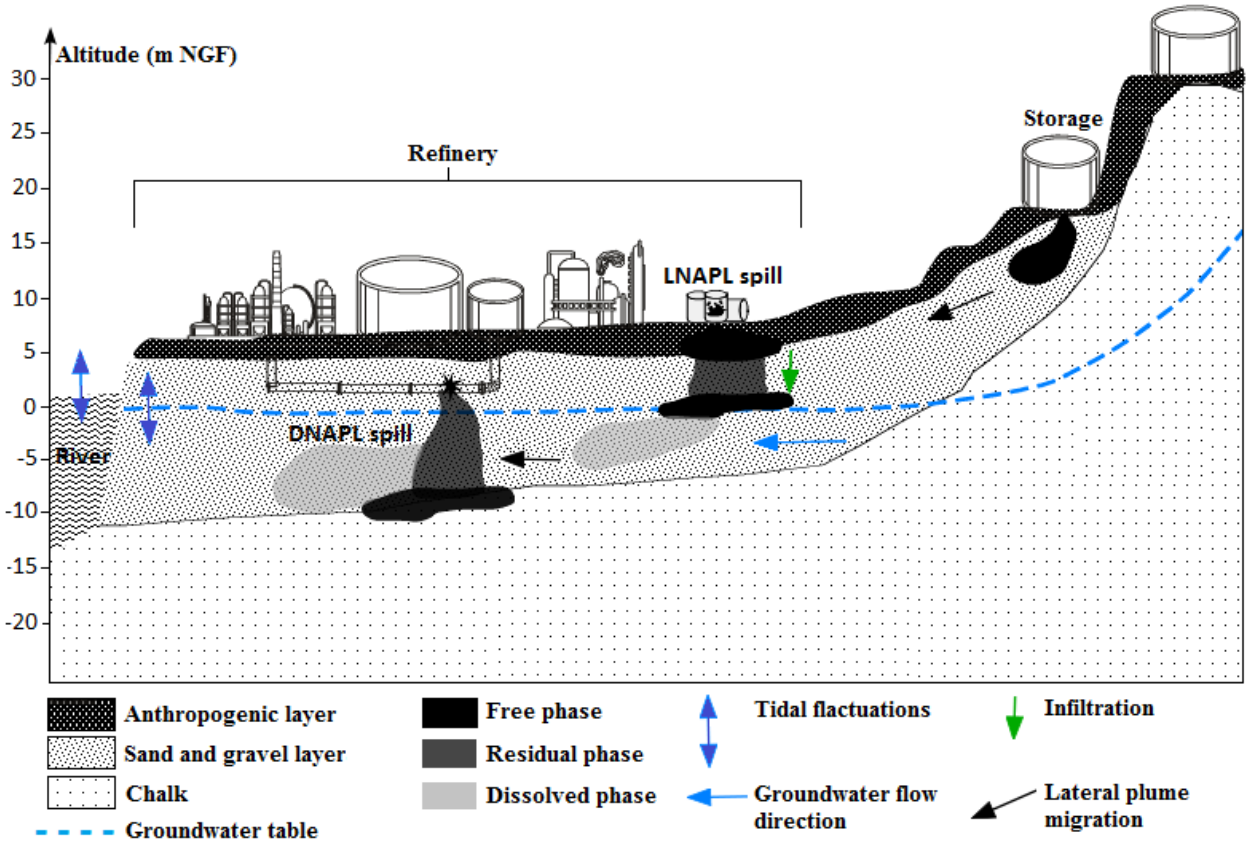

Figure 4.1: Schematic of the refinery geological structures and the partitioning of LNAPL and DNAPL products into dissolved, free and residual phases.

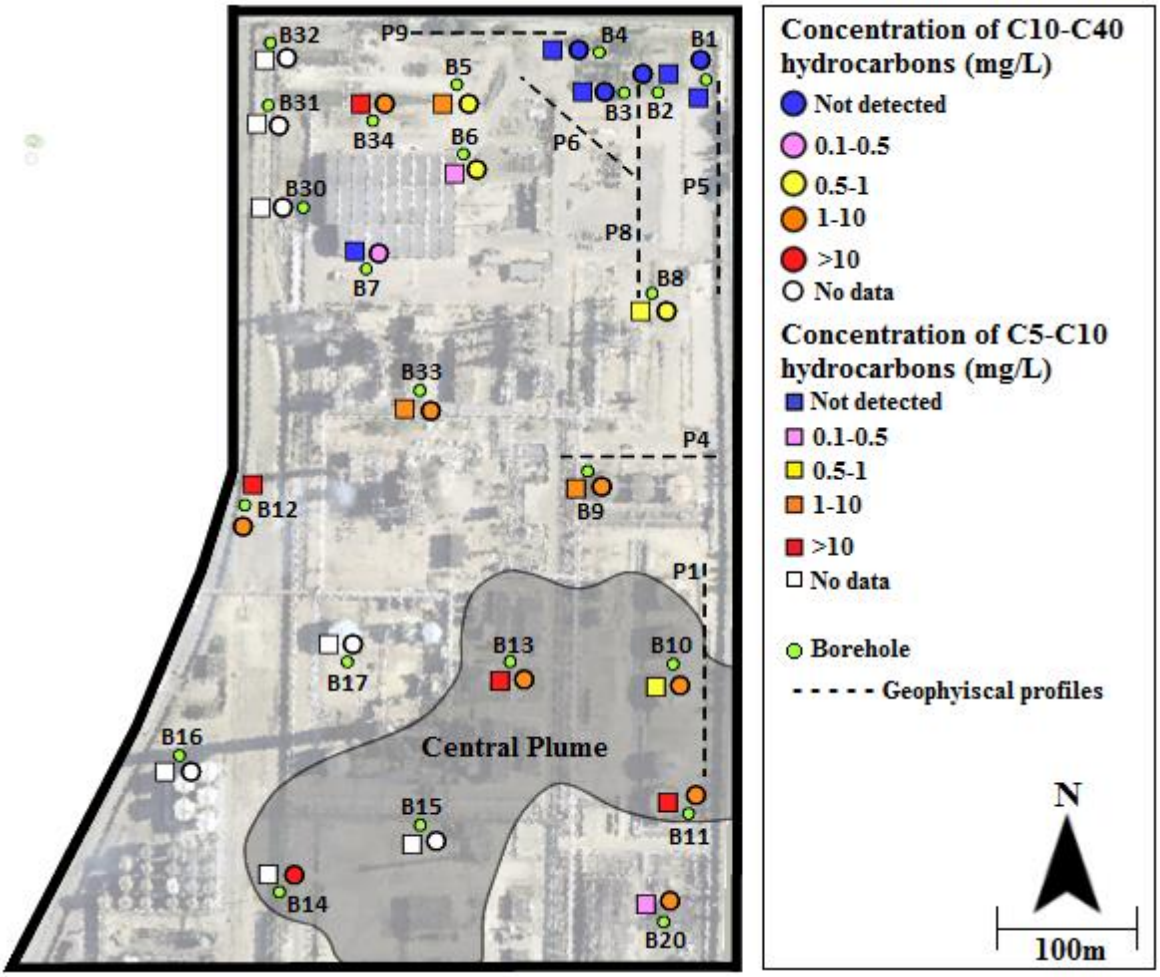

Figure 4.2: The distribution of C10-C40 and C5-C10 hydrocarbons in groundwater and the free phase plume with respect to the conducted geophysical profiles. The longer geophysical profiles are those having a length of 140 m, whereas the shorter profiles are those having a length of 104 m.

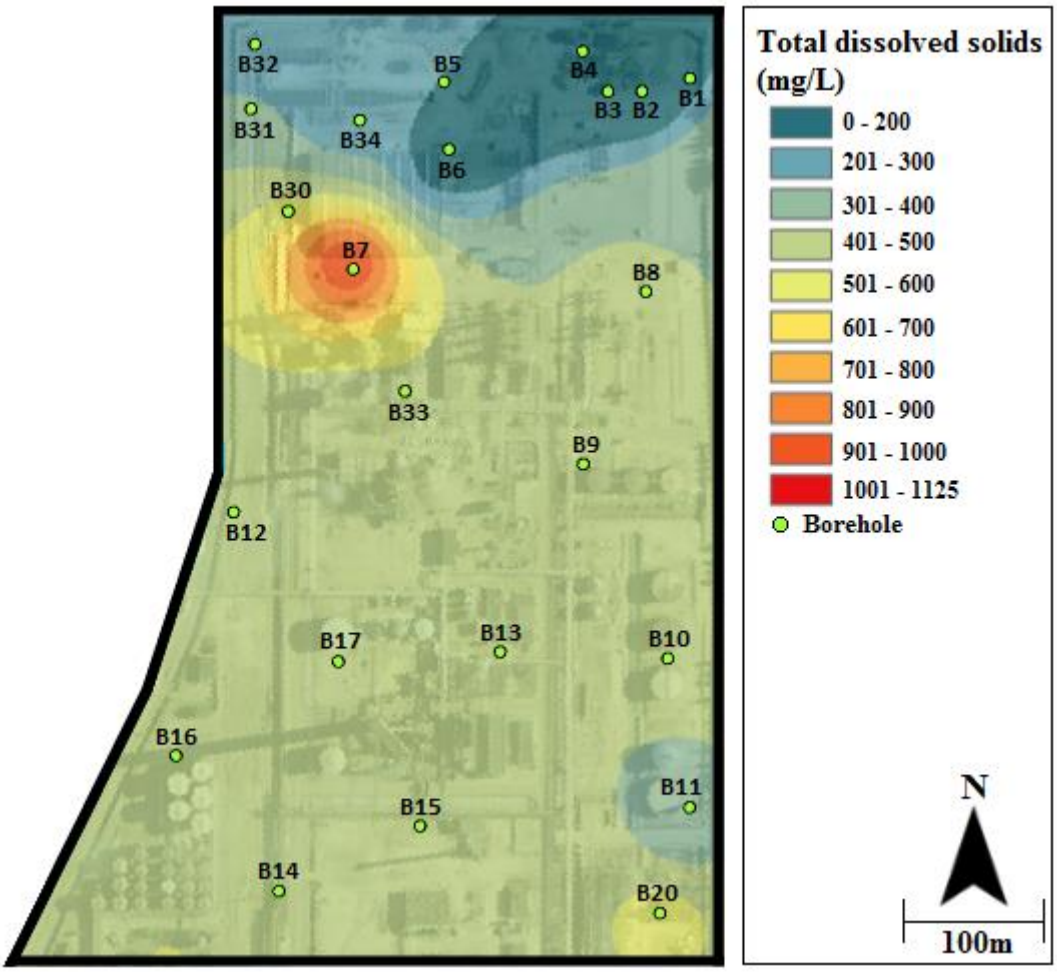

Figure 4.3: The concentrations of total dissolved solids (TDS) measured in the site's boreholes. The map shows higher TDS concentrations close to the contaminated zone boreholes (e.g., b13, b7, b8, b33, etc.).

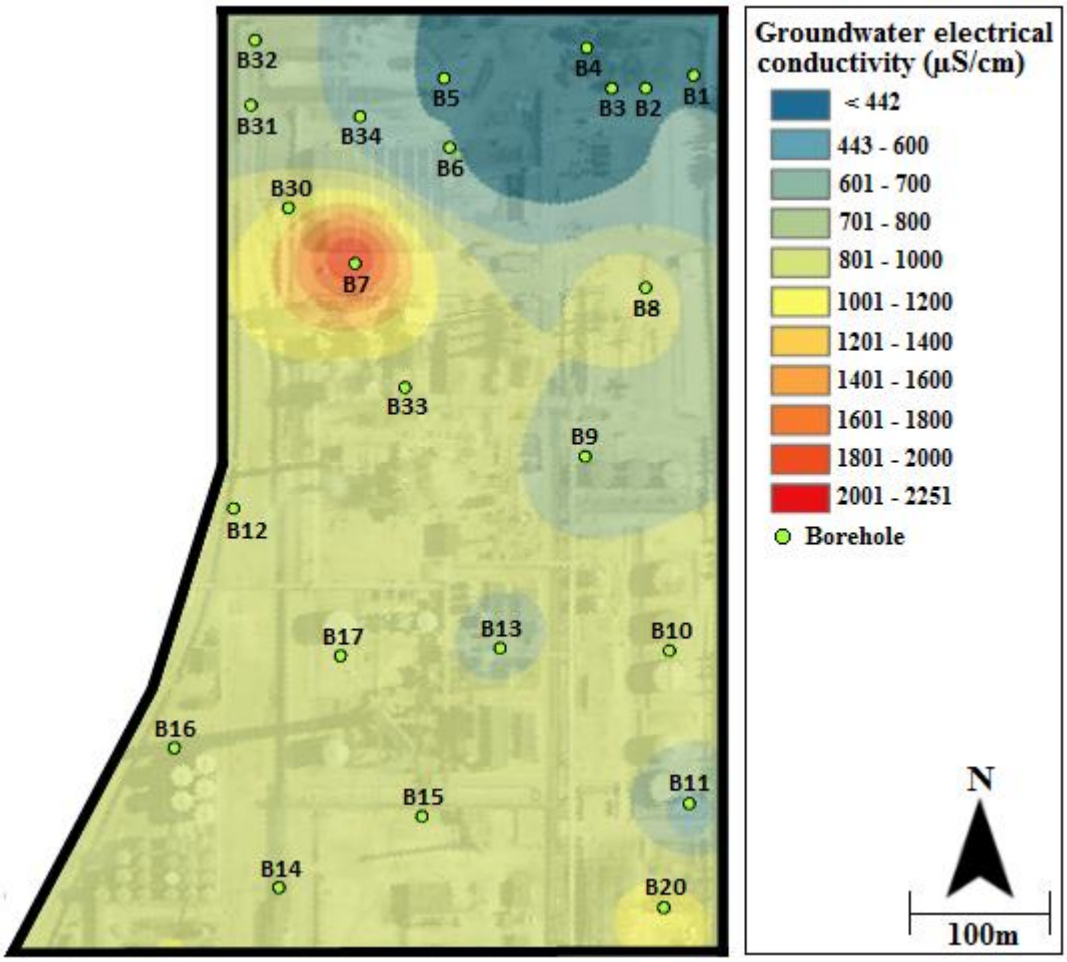

Figure 4.4: The distribution of groundwater electrical conductivity values measured in the site's boreholes. The map shows higher electrical conductivity values close to the contaminated zone boreholes (e.g., B13, B7, B8, B33, etc.).

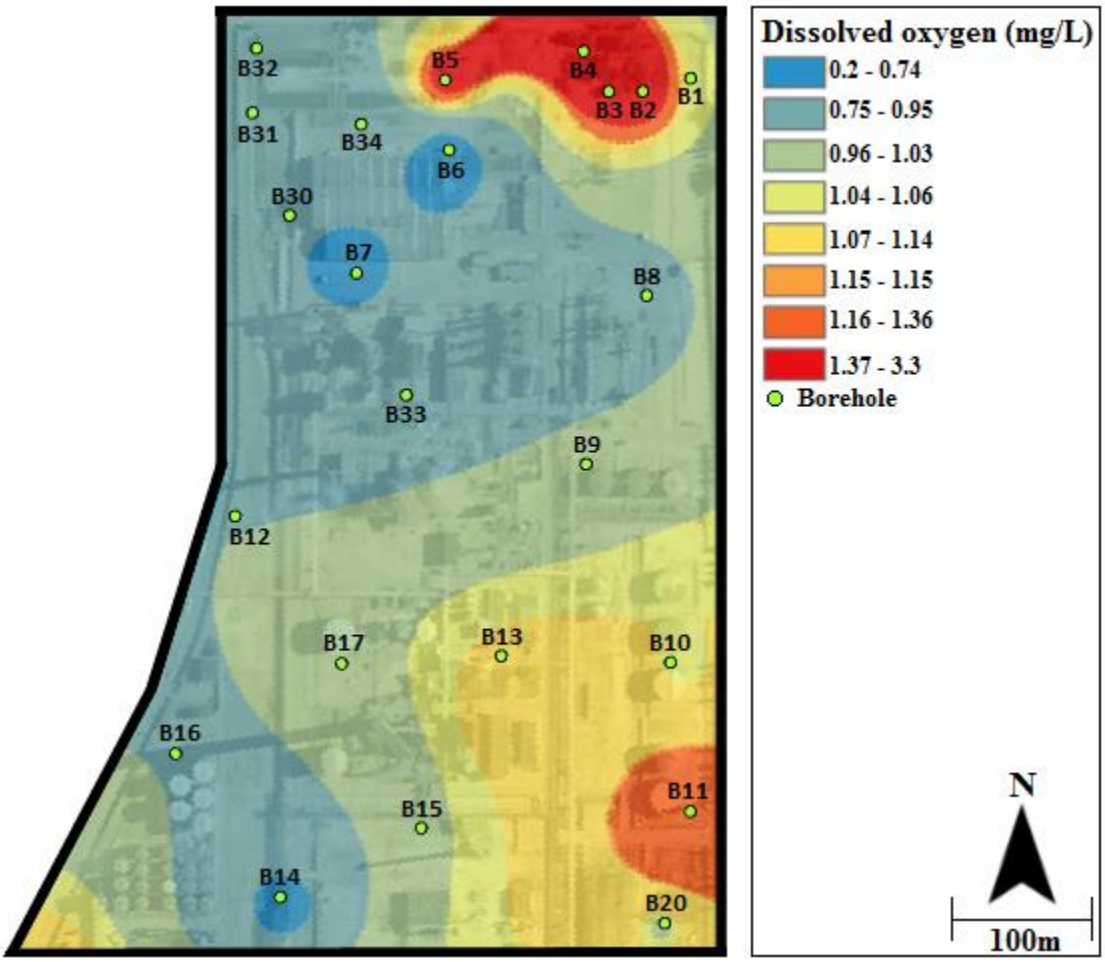

Figure 4.5: The concentrations of dissolved oxygen measured in the site's boreholes. The map shows low dissolved oxygen concentrations close to the contaminated zone boreholes (e.g., b13, b7, b8, b33, etc.).

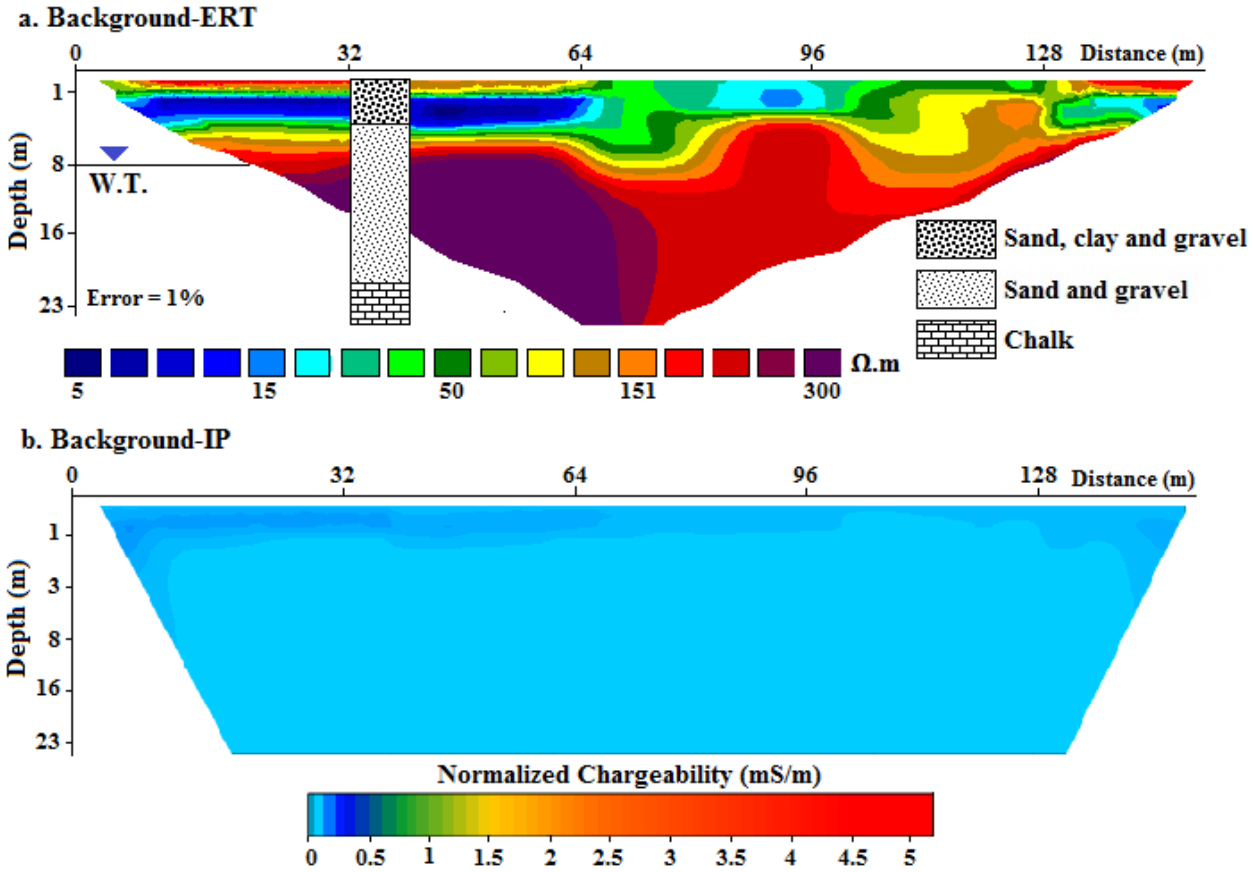

Figure 4.6: The ERT (a) and IP (b) background profiles showing high resistivity and low chargeability values in the clean background aquifer.

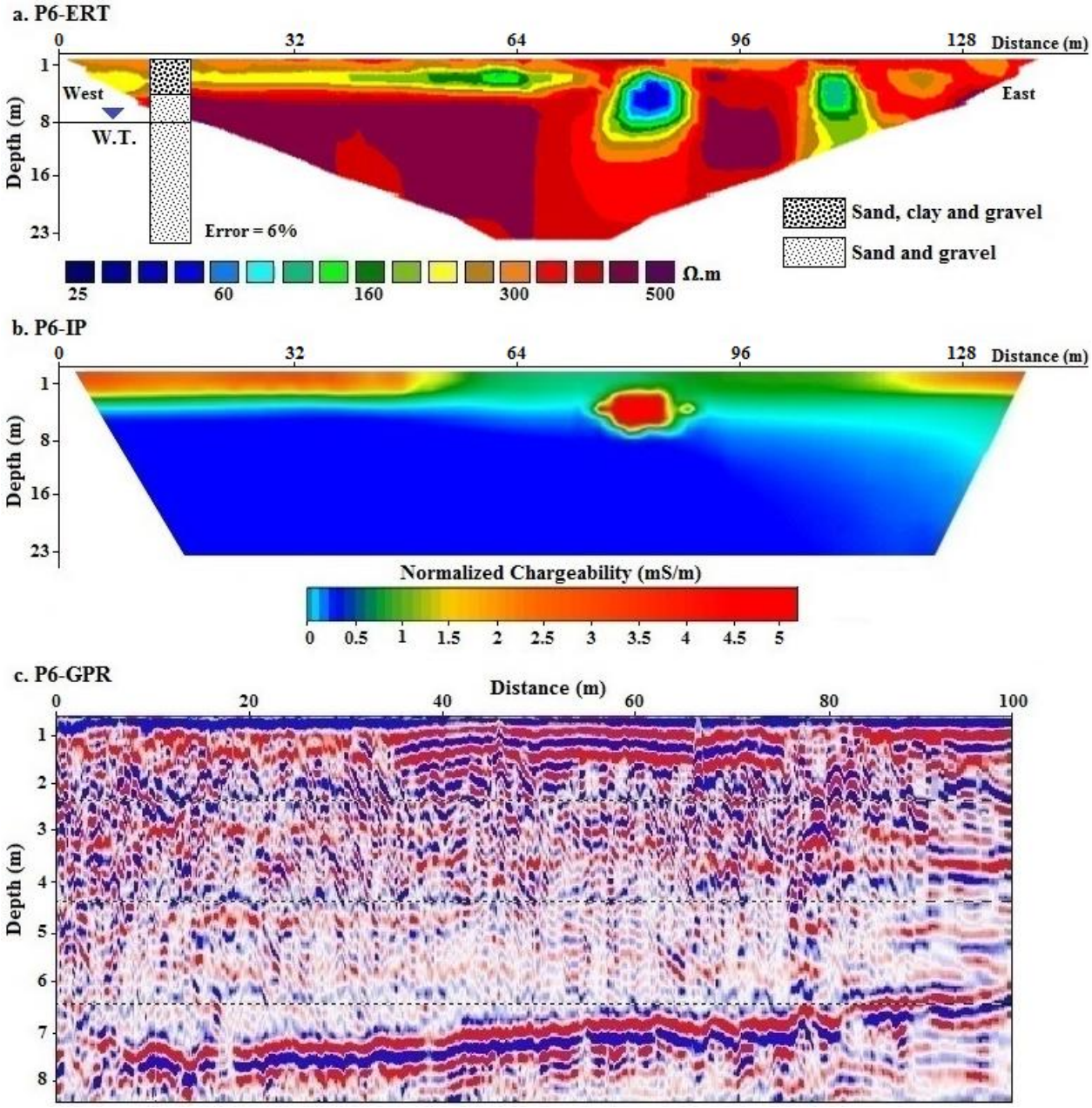

Figure 4.7: The ERT (a), IP (b) and GPR (c) data acquired along profile P6 which is located in the clean groundwater zone. This profile shows high resistivity values, low chargeability values and good GPR reflections.

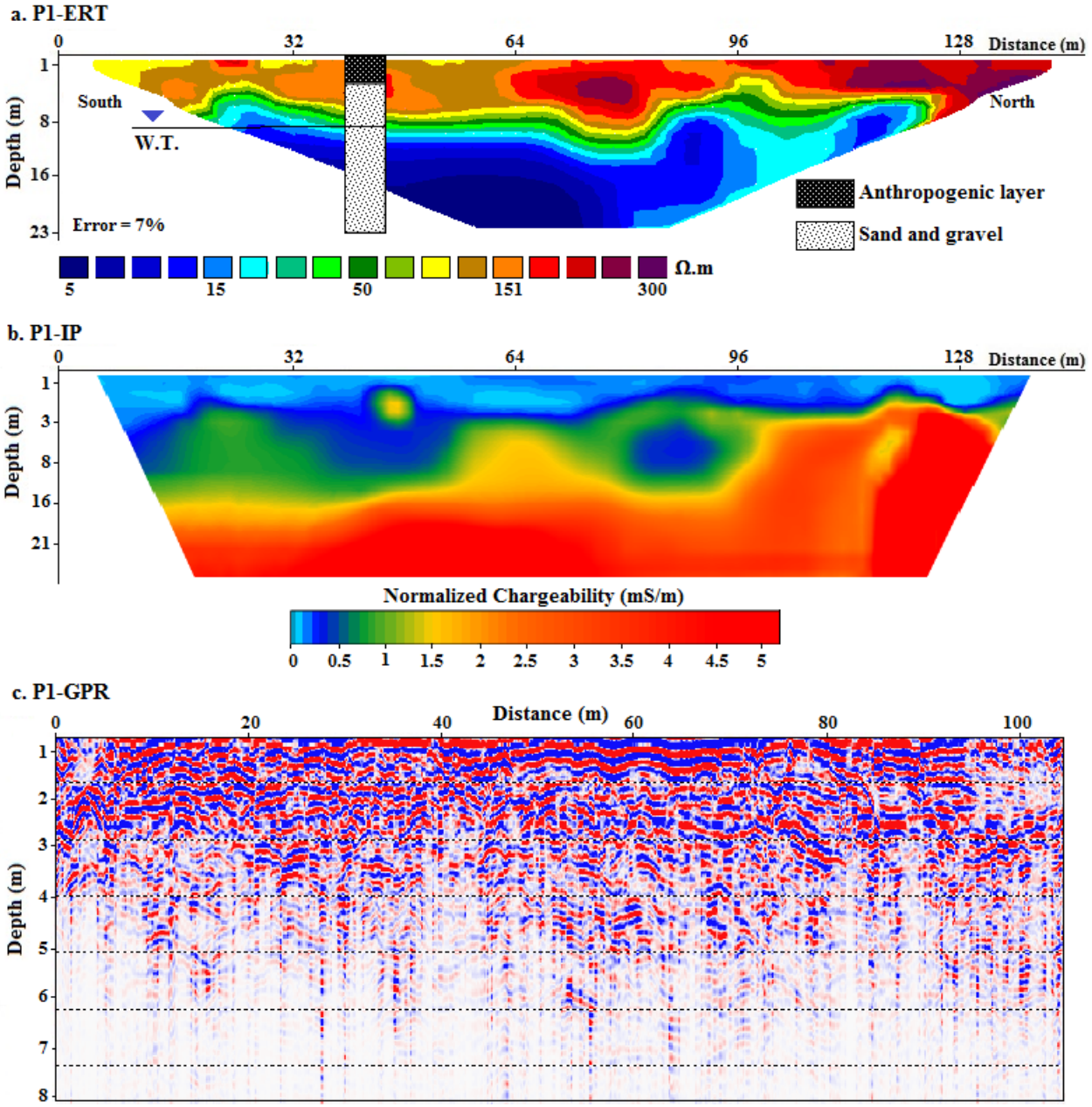

Figure 4.8: The ERT (a), IP (b) and GPR (c) data acquired along profile P1 which is located in the contaminated zone. This profile shows low resistivity and high chargeability values in the contaminated aquifer and attenuated GPR reflections starting at a depth of around 4 m.

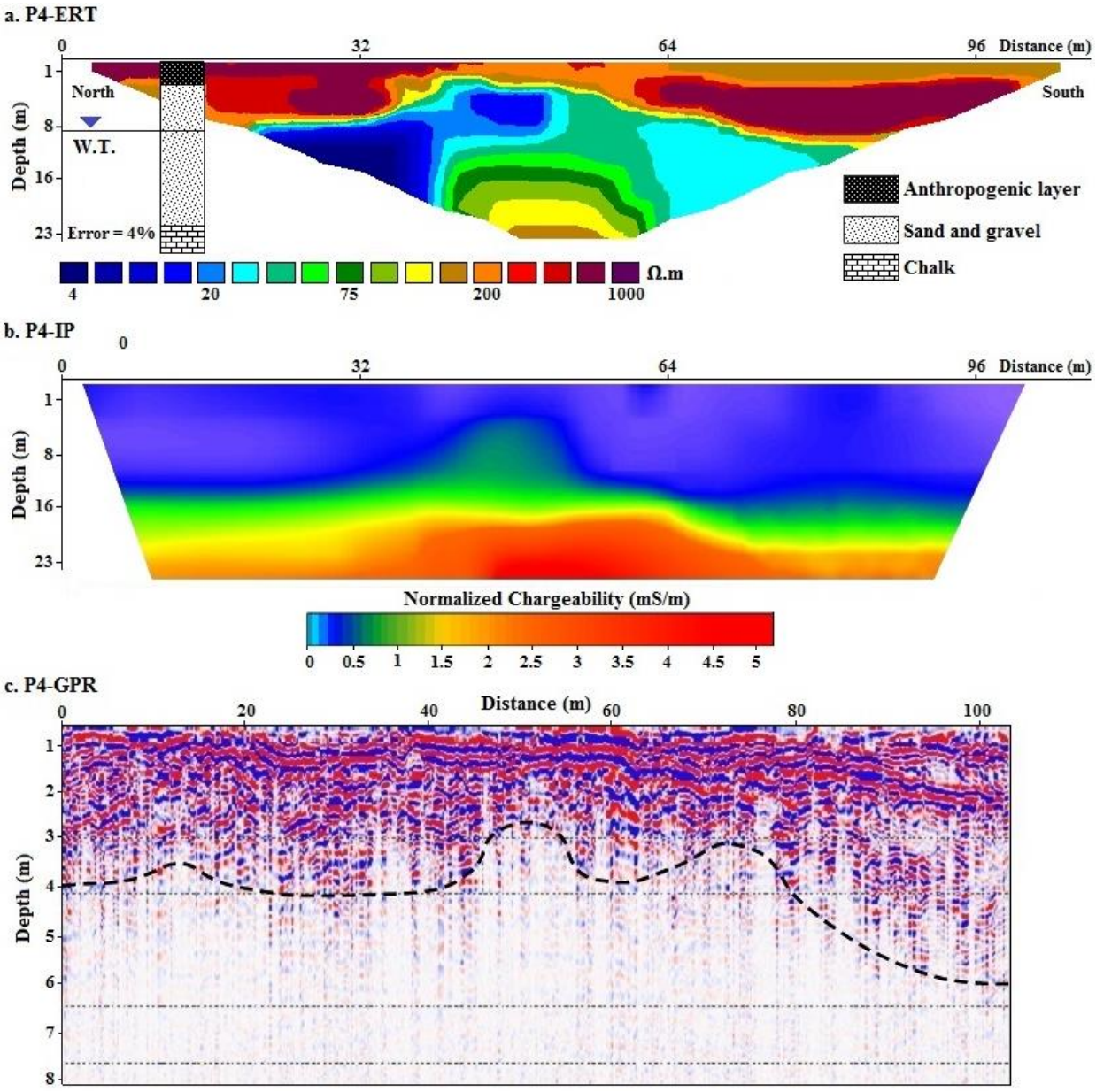

Figure 4.9: The ERT (a), IP (b) and GPR (b) data acquired along profile P4 which is located in the contaminated zone. This profile shows a low resistivity zone coincident with high chargeability values and GPR attenuated reflections.

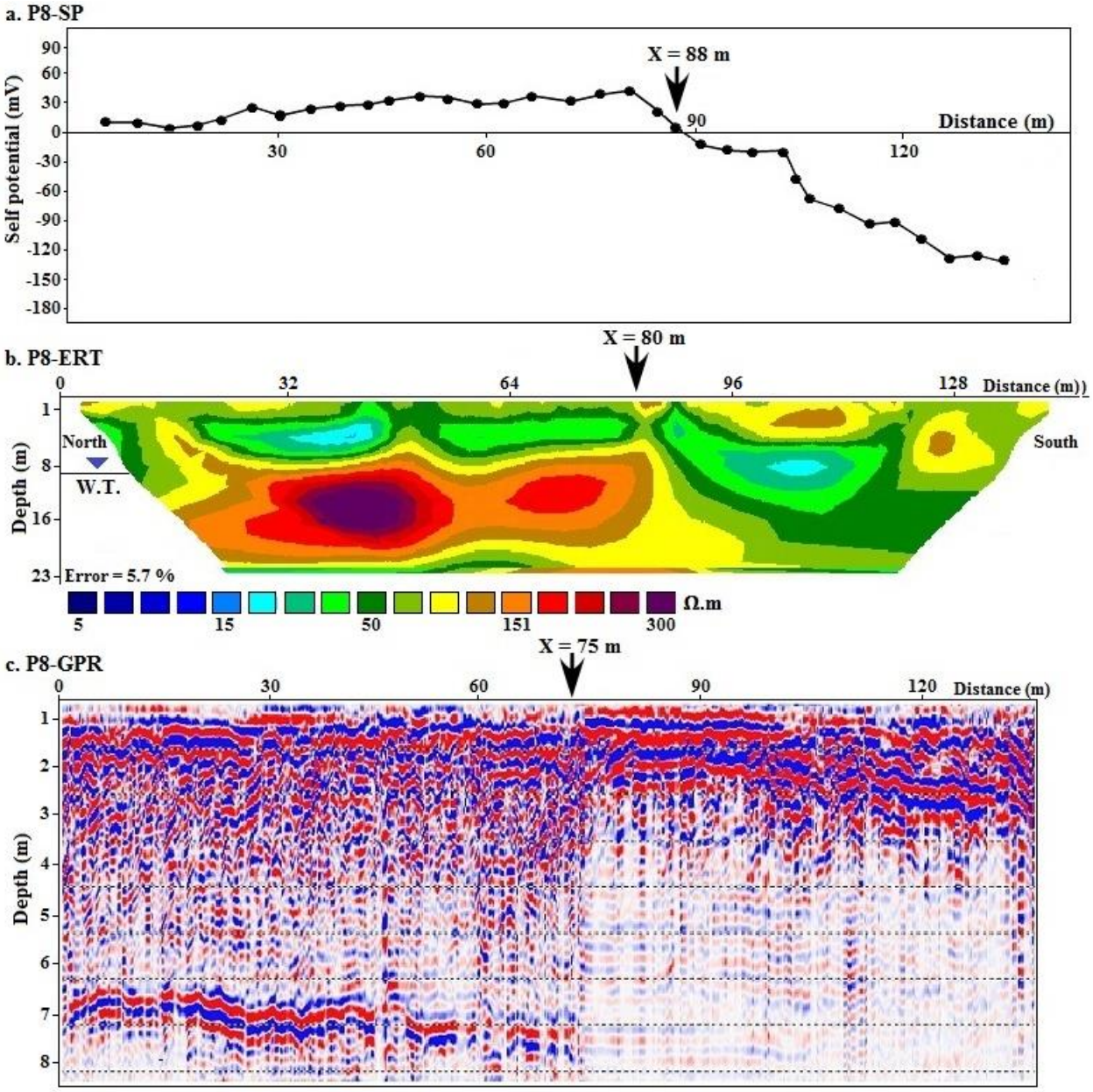

Figure 4.10: The SP (a), ERT (b) and GPR (c) data acquired along profile P8. This profile shows a transition between the contaminated (low resistivity/negative SP/ GPR attenuated reflections) and the clean (high resistivity/positive SP/strong GPR reflections) zones starting at X= 88 m in the SP profile, at X= 80 m in the ERT profile and at X= 75 m in the GPR profile.

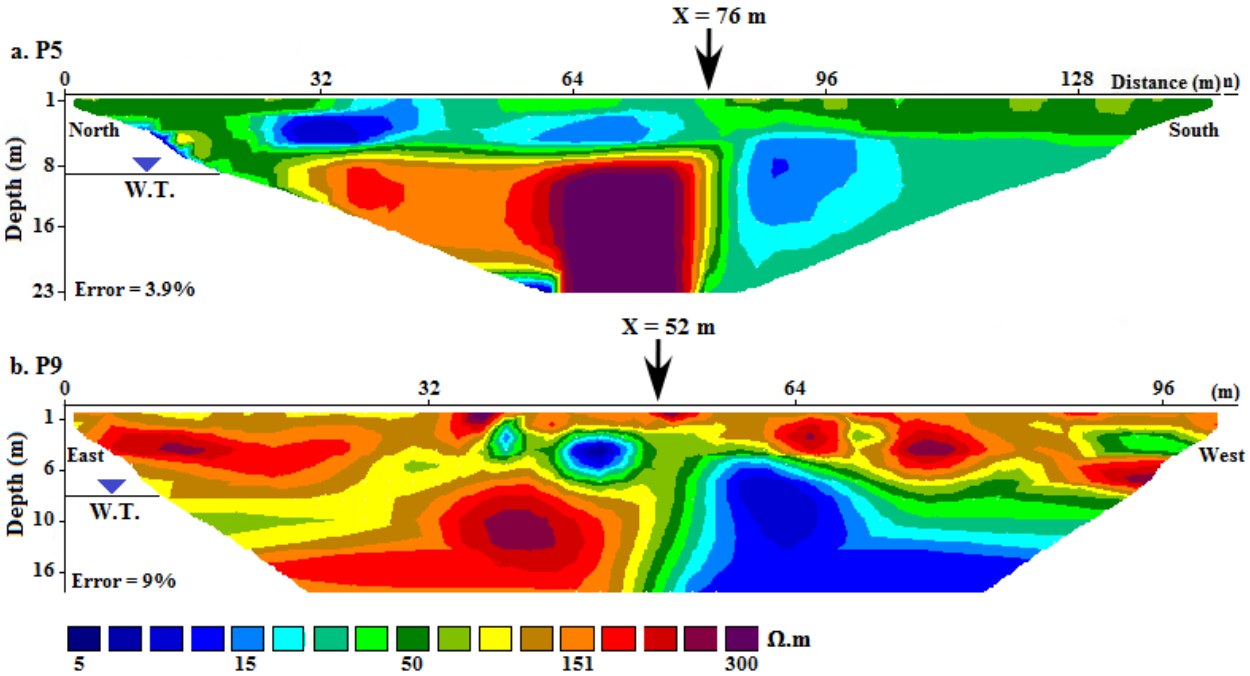

Figure 4.11: The ERT profiles P5 (a) and P9 (b) that extend from the clean to the contaminated zone. The profiles show a change in the electrical resistivity values from high to low at x=76 m in p5 and at x=52 m in P9.

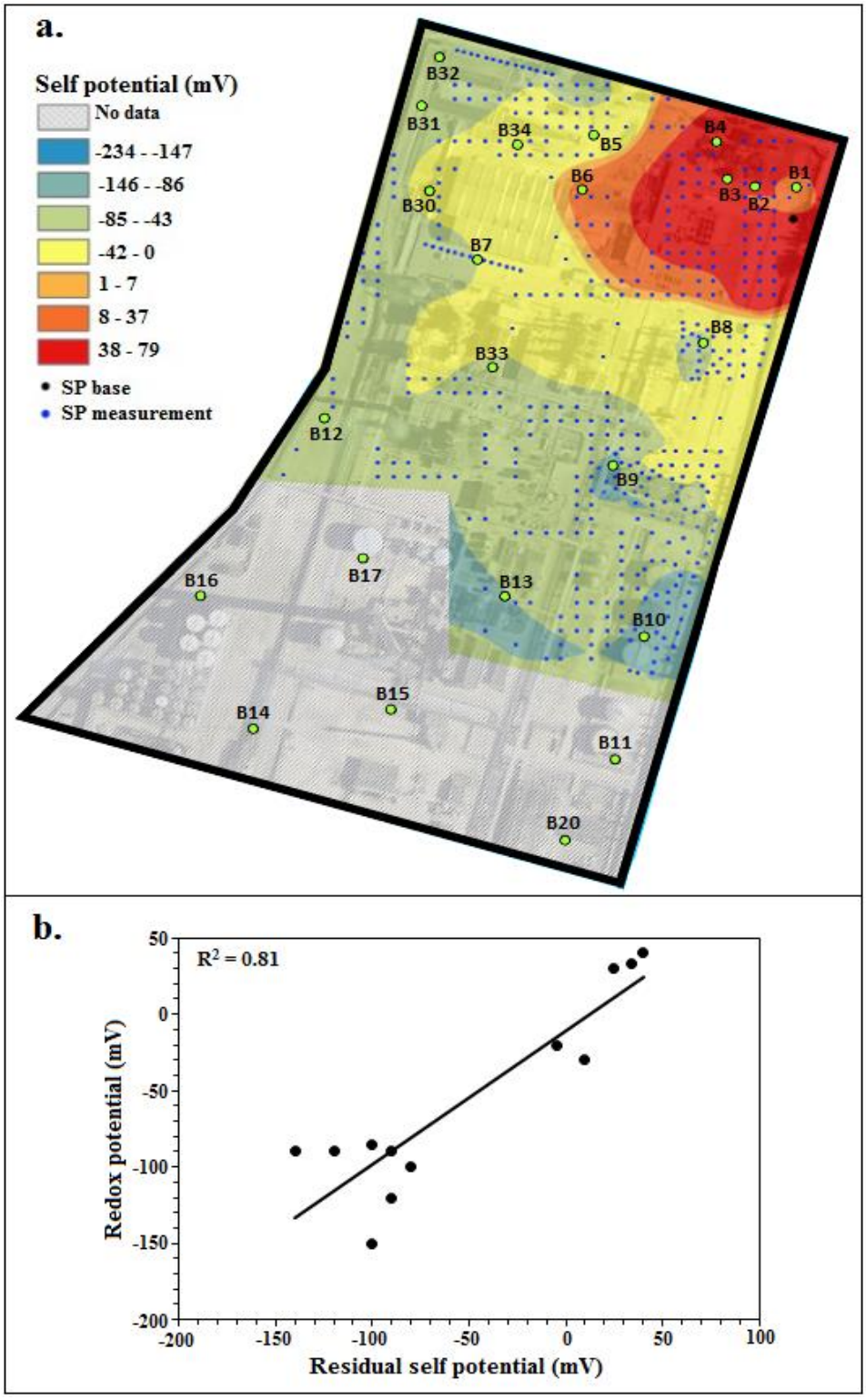

Figure 4.12: The SP map showing negative SP values in the contaminated zone and positive SP values in the clean zone (a). A good correlation (R^2 = 0.81) was observed between the SP values and the redox potential values of groundwater samples (b).

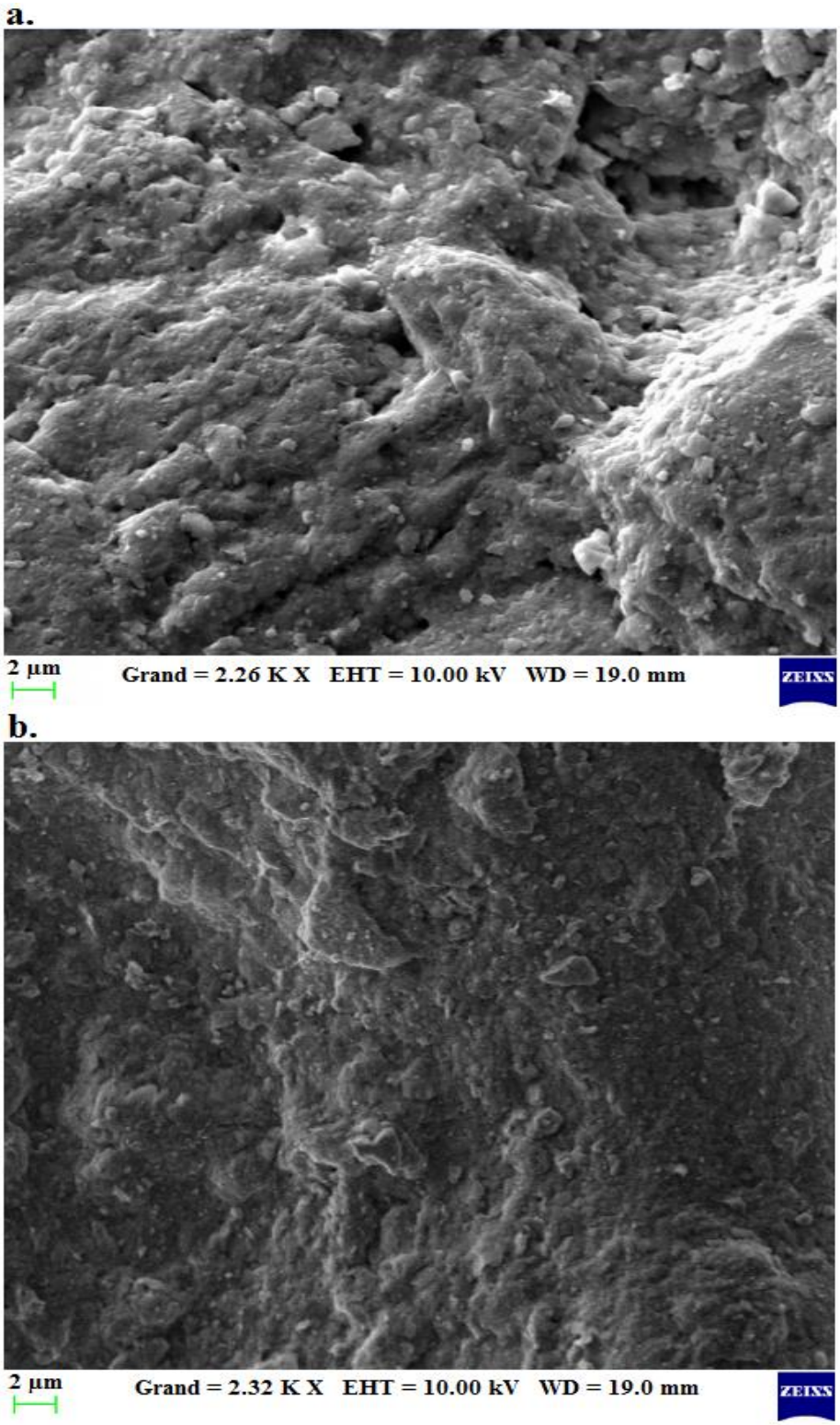

Figure 4.13: Scanning electron microscope images of a contaminated (a) and a clean (b) soil sample which were taken from the aquifer. The image of the contaminated sample shows etched pits and dissolution features which are absent in the image of the clean sample.

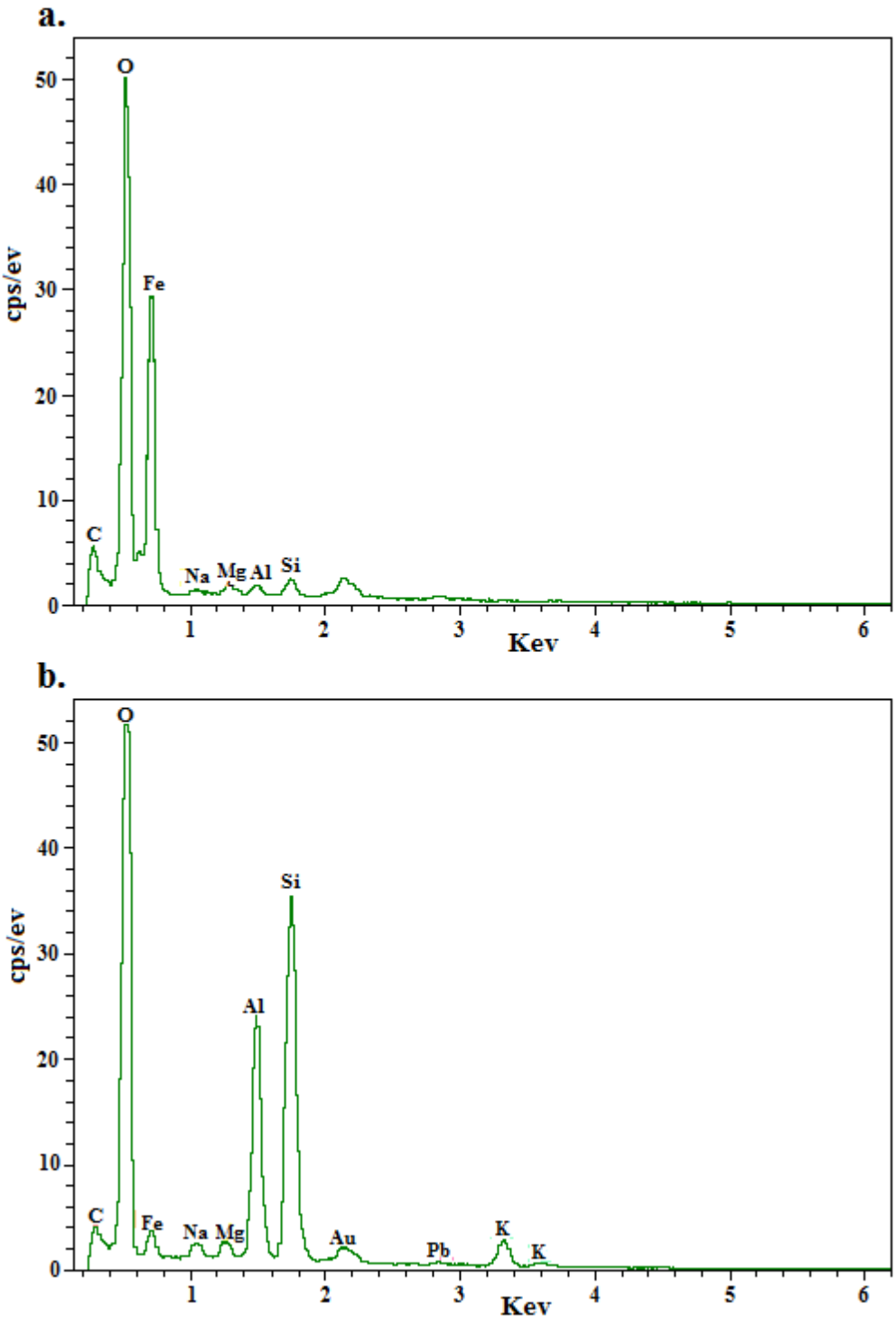

Figure 4.14: EDX results of a contaminated (a) and a clean (b) soil sample which were taken from the zone located directly above the groundwater table. The results show higher iron (Fe) peaks in the contaminated sample.

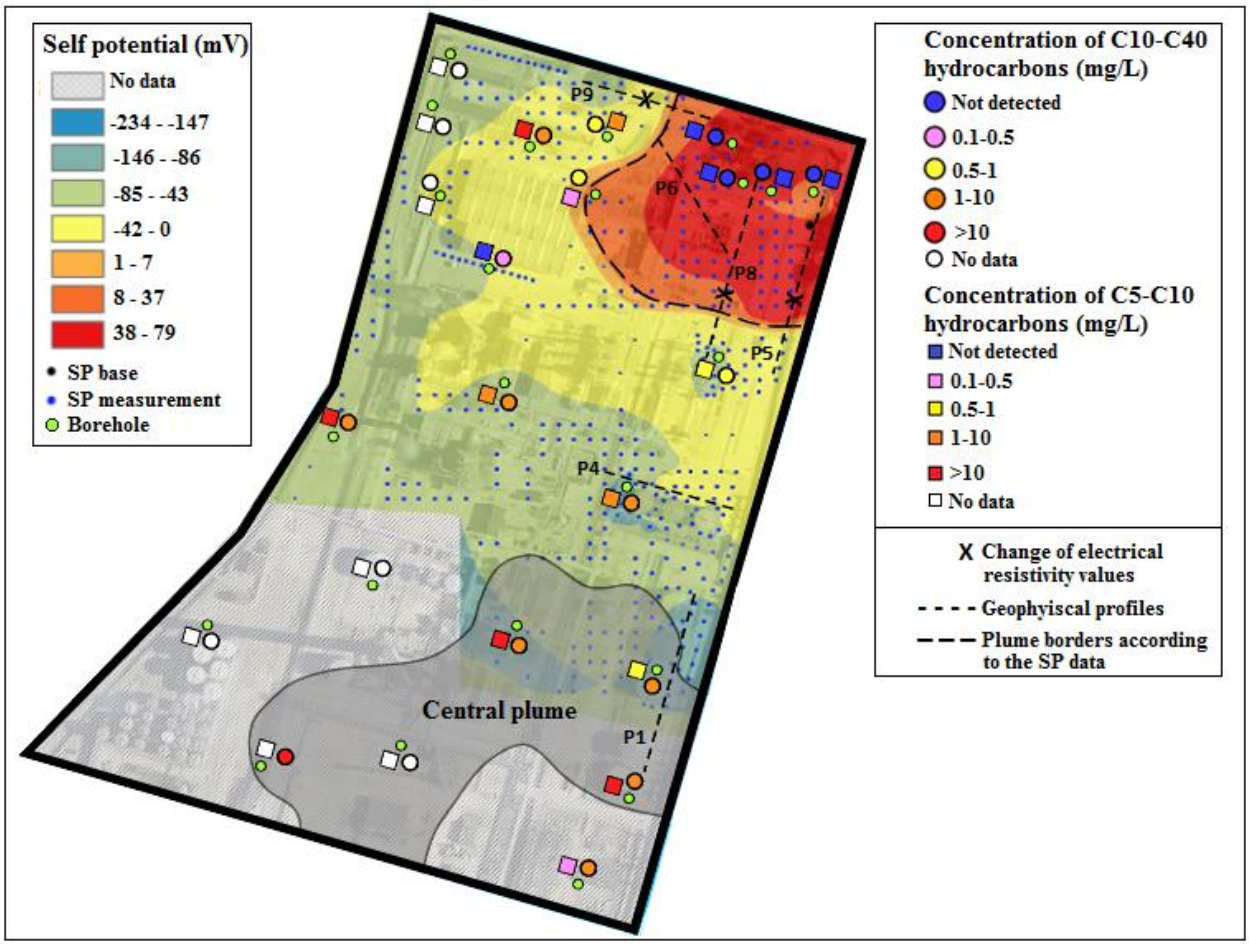

Figure 4.15: The SP map with respect to the hydrocarbons distribution and the conducted ERT profiles. The dotted curve depicts the estimated clean zone boundaries according to the shift of SP values from positive to negative. The "X" marks on the ERT profiles represent the locations at which the resistivity values changed from high in the clean zone to low in the contaminated zone.

Chapter 5

Redox Potential Distribution of an Organic-Rich Contaminated Site Obtained by the Inversion of Self-Potential Data

Paper 2 (Journal of Hydrology)

Redox potential distribution of an organic-rich contaminated site obtained by the inversion of self-potential data

M. Abbas[1], A. Jardani[1], A. Soueid Ahmed[2], A. Revil[2], L. Brigaud[1], Ph. Bégassat[3], and JP. Dupont[1]

(1) Université de Rouen, M2C, UMR 6143, CNRS, Morphodynamique Continentale et Côtière, Mont Saint Aignan, France.

(2) Université Savoie Mont Blanc, CNRS, IRD, IFSTTAR, ISTerre, F-73000 Chambéry, France.

(3) Agence de l'environnement et de la maîtrise de l'énergie (ADEME), 20 avenue du Grésillé, BP 90406, 49004 Angers cedex 1, France.

Corresponding author: abderrahim.jardani@univ-rouen.fr

Emails: abbas_mohammad@live.com; abderrahim.jardani@univ-rouen.fr; abdellahi.soueid-ahmed@univ-smb.fr; jean-paul.dupont@univ-rouen.fr; philippe.begassat@ademe.fr; andre.revil@univ-smb.fr

Journal of Hydrology (Accepted 21, September 2017)

Abstract

Mapping the redox potential of shallow aquifers impacted by hydrocarbon contaminant plumes is important for the characterization and remediation of such contaminated sites. The redox potential of groundwater is indicative of the biodegradation of hydrocarbons and is important in delineating the shapes of contaminant plumes. The self-potential method was used to reconstruct the redox potential of groundwater associated with an organic-rich contaminant plume in Northern France. The self-potential technique is a passive technique consisting in recording the electrical potential distribution at the surface of the Earth. A self-potential map is essentially the sum of two contributions, one associated with groundwater flow referred to as the electrokinetic component, and one associated with redox potential anomalies referred to as the electroredox component (thermoelectric and diffusion potentials are generally negligible). A groundwater flow model was first used to remove the electrokinetic component from the observed self-potential data. Then, a residual self-potential map was obtained. The source current density generating the residual self-potential signals was assumed to be associated with the position of the water table, an interface characterized by a change in both the electrical conductivity and the redox potential. The source current density was obtained through an inverse problem by minimizing a cost function including a data misfit contribution and a regularizer. This inversion algorithm allows the determination of the vertical and horizontal components of the source current density, taking into account the electrical conductivity distribution of the saturated and non-saturated zones obtained independently by the electrical resistivity tomography method. The redox potential distribution was finally determined from the inverted residual source current density. A redox map was successfully built and the estimated redox potential values correlated well with *in-situ* measurements.

5.1. Introduction

The increasing public concern with groundwater contamination problems has generated significant research activity, which aims to support the contaminant plumes characterization and remediation efforts (e.g., Rao et al., 2000; Craun et al., 2010). The redox potential is considered as a key-parameter for the characterization of organic-rich contaminant plumes because bacteria derive their energy through oxidizing organic carbon for their growth and reducing terminal electron acceptors (usually oxygen) for their respiration (Christensen et al., 2000; Tiehm and Schulze, 2003; Semple et al., 2007). Bacterial activity induces significant changes in the redox environment by playing the role of catalysts (Atlas, 1981; Revil et al., 2010; Atekwana and Atekwana, 2010; Vayenas et al., 2002). The consumption of electron acceptors by bacterial biodegradation processes in an organic-rich contaminant plume causes a change in the redox chemistry of the groundwater. Baedeker et al. (1993) have shown that the area within the plume is quickly becoming reducing and anoxic, whereas the area outside the plume is oxidizing and oxic.

Mapping the redox potential by classical geochemical methods is invasive (i.e., requiring boreholes), expensive and provides only scarce information. In addition, these measurements are time-consuming as they require a lot of precautions to avoid perturbing local equilibria by the introduction of oxygen. The need for cost-effective and fast methods to continuously characterize the contaminated groundwater has increased the interest of the concerned communities in the use of non-intrusive geophysical methods (Sauck, 2000; Atekwana et al., 2000; 2002; Buselli and Lu, 2001; Nimmer and Osiensky, 2002; Werkema et al., 2003, Revil and Jardani, 2013; Binley et al., 2015).

Several field and laboratory studies have shown a strong relationship between the self-potential method and the redox potential distribution in contaminated groundwater (Tim and Möller, 2001; Naudet et al., 2003, 2004; Naudet and Revil, 2005; Revil et al., 2010). The self-potential method is a passive geophysical technique that detects naturally occurring electrical currents by measuring the electrical potential distribution at the ground surface of the Earth. The method is sensitive to source current densities generated by pore water flow processes (electrokinetic component, e.g., Jardani et al., 2006) or by electrochemical processes such as oxidoreduction reactions (Nyquist and Corry 2002; Naudet et al., 2003) and temperature gradients (Revil et al., 2013). The contribution associated with groundwater flow is well-established and can be used to reconstruct the hydraulic properties of the subsurface during pumping tests (e.g., Soueid Ahmed et al., 2016a, b). Self-potential signals have been observed in a number of studies associated with organic-rich contaminant plumes (Hämmann et al., 1997; Vichabian et al., 1999, Nyquist and Corry, 2002; Naudet et al., 2003; Arora et al., 2007; Rittgers et al., 2013). Sandbox experiments have been conducted to better characterize this process (e.g., Naudet and Revil, 2005; Fachin et al., 2012; Rittgers et al., 2013). The changes in the redox environment associated with bacterial biodegradation of hydrocarbons establish zones with different redox potentials. In the presence of electronic conductors (abiotic conductors such as semi-conductors, e.g., pyrite and magnetite, and biotic conductors such as biofilms, see Delong, 2002; Tender et al., 2002), this

leads to the establishment of a natural geobattery (see Naudet et al., 2004). The biogeobattery theory was developed by Revil and co-worker (Naudet et al., 2004; Revil et al., 2010 and references therein). Support in favor of this biogeobattery theory has been developed since and validated by laboratory experiments (Risgaard-Petersen et al., 2012, 2014).

The above investigations illustrate the ability of the self-potential method to infer the redox potential and to monitor organic-rich contaminant plumes in shallow aquifers associated with active electrochemical source mechanisms. In the present study, a self-potential field survey was performed over a hydrocarbon contaminant plume in Northern France. We also modeled the electrokinetic contribution to remove it from the measured self-potential map. Our goal is to invert the residual self-potential map to estimate the distribution of the redox potential and to provide further support to the existence of biogeobatteries in such contaminant plumes. Note that the hydrocarbon contamination investigated in the present paper is very different from the contamination previously investigated at Entressen, which corresponds to leachates from a municipal landfill (Naudet et al., 2004).

5.2. Theory

5.2.1. Forward Problem

In an isotropic heterogeneous aquifer contaminated by hydrocarbons, the electrical source current density $\mathbf{j}_S$ (A m^{-2}) is responsible for the self-potential signal measured at the ground surface. This source current density can result from two contributions: (1) the streaming source current density component $\mathbf{j}_w$ which is caused by groundwater flow in porous media (electrokinetic component, see Sill, 1983) and (2) the redox source current density component $\mathbf{j}_R$ which is associated with the biogeobattery phenomenon (Naudet et al., 2004; Revil et al., 2010). The physical mechanisms that describe the self-potential anomalies are governed by a generalized Ohm's law, in which the total current density $\mathbf{j}$ is written as the sum of the conductive current density (given by Ohm's law) plus the source current density $\mathbf{j}_S$ mentioned above:

$$\mathbf{j} = -\sigma \nabla \psi + \mathbf{j}_S , \tag{1}$$

$$\mathbf{j}_S = \mathbf{j}_W + \mathbf{j}_R , \tag{2}$$

where ψ denotes the electrical potential (in V), $\mathbf{E} = -\nabla \psi$ (in V m^{-1}) describes the electrical field (induction is discarded because of the low frequency of the excitations), and $\boldsymbol{\sigma}$ denotes the electrical conductivity of the material (in S m^{-1}).

The streaming current density is linearly dependent on the Darcy velocity $\mathbf{u}$ (in m s^{-1}):

$$\mathbf{j}_W = \hat{Q}_V \mathbf{u} , \tag{3}$$

where $\hat{Q}_V$ (in C m^{-3}) denotes the effective charge density advectively carried along with the flow of the pore water. This charge density can be determined from the permeability itself k (in m^2) by using $\log_{10}\hat{Q}_V = -9.2 - 0.82\log_{10} k$ (Jardani et al., 2007; Revil and Mahardika, 2013) or from $\hat{Q}_V = -\sigma C \eta_f / k$ (where C is the electrokinetic coupling coefficient in V Pa^{-1} and η_f denotes the pore water viscosity in Pa s). The effect of the pore water conductivity (and therefore the ionic strength of the pore water) in the electrokinetic process is accounted for in the conduction term since the conductivity of the porous material is essentially proportional to the conductivity of the pore water.

The redox current density can be linearly related to the redox potential as (Revil et al., 2010; Rittgers et al., 2013):

$$\mathbf{j}_R = -\sigma \nabla E_H \,, \tag{4}$$

where E_H denotes the redox potential (generally determined from the activity of the Fe^{2+}/Fe^{3+} couple).

For the total current density, the continuity equation (conservation equation of the electrical charge) is:

$$\nabla \cdot \mathbf{j} = 0 \,. \tag{5}$$

The total current density is conservative. From equations (1) and (5), the electrical (self-) potential is therefore governed by a Poisson equation:

$$\nabla \cdot \left(\sigma \cdot \nabla \psi \right) = \Im \,. \tag{6}$$

where $\Im = \nabla \cdot \mathbf{j}_S = \nabla \cdot (\mathbf{j}_W + \mathbf{j}_R) = \nabla \cdot (\hat{Q}_V \mathbf{u} - \sigma \nabla E_H)$ (in A m^{-3}) appears as the driving source term (volumetric source current density). The computation of the electrical potential is therefore obtained through solving the Poisson equation by using, for instance, the finite elements method. In doing so, we need the spatial distribution of the electrical conductivity, the total current density sources $\mathbf{j}_W + \mathbf{j}_R$ and the boundary conditions. The electrical conductivity of the subsurface can be inferred independently by using the electrical resistivity tomography method (e.g., Binley et al., 1996). Regarding the boundary conditions for the self-potential problem, the Neumann and Dirichlets are:

$$\psi = 0 \text{ at } \Gamma_d \,, \tag{7}$$

$$-\boldsymbol{n} \cdot \left[\bar{\bar{\sigma}} \cdot \nabla \psi - \mathbf{j}_S \right] = 0 \text{ at } \Gamma_N \,. \tag{8}$$

The Neumann boundary condition (8) is imposed at the insulating air-ground interface Γ_N and the Dirichlet boundary condition (7) is imposed at all the remaining boundaries Γ_d far from the area of interest. Equation (6) can be also written in an integral form as:

$$\psi(\mathbf{r}) = \int_{\Omega_1} \mathbf{K}(\mathbf{r},\mathbf{r}')\mathbf{j}_S(r')dV\,, \tag{9}$$

where dV denotes a volume element around the current source point, Ω_1 denotes the source volume, $\mathbf{K(r,r')}$ denotes the kernel operator that incorporates the information on the variability of the electrical conductivity, boundary conditions and geometry of the studied domain. The Kernel matrix is composed by the Green functions of the problem. Since this kernel operator connects the distributions of both electrical current density sources ($\mathbf{j}_W$ and $\mathbf{j}_R$) that generate the electrical potential measured at the ground surface, the electrical potential given in equation (9) can be decomposed as:

$$\psi(\mathbf{r}) = \psi_R(\mathbf{r}) + \psi_W(\mathbf{r})\,, \tag{10}$$

with

$$\psi_R(\mathbf{r}) = \int_{\Omega_1} \mathbf{K}(\mathbf{r},\mathbf{r}')\mathbf{j}_R(r')dV\,, \tag{11}$$

$$\psi_W(\mathbf{r}) = \int_{\Omega_1} \mathbf{K}(\mathbf{r},\mathbf{r}')\mathbf{j}_W(r')dV\,, \tag{12}$$

For the purpose of delineating a contaminated area from the self-potential analysis, the electrical signature due to the redox potential can only be determined by removing the effect of the electrokinetic phenomena from the self-potential field observations. In other words, we need first to compute (e.g., Naudet et al., 2004):

$$\psi_R(\mathbf{r}) = \psi(\mathbf{r}) - \psi_W(\mathbf{r})\,. \tag{13}$$

The streaming potential can be estimated numerically by coupling the hydraulic and electric problems. At the first stage, the different wells present in the study site are employed to parameterize and calibrate the groundwater flow model (and therefore the associated electrokinetic component) by solving the following steady-state flow equations:

$$\nabla\cdot\mathbf{u} = 0\,, \tag{14}$$

$$\mathbf{u} = -K\nabla h \tag{15}$$

with the following boundary conditions:

$$h = h_D(x,y) \text{ at } \Gamma_d\,, \tag{16}$$

$$-\boldsymbol{n}\cdot\left[k\cdot\nabla h\right] = 0 \text{ at } \Gamma_N\,, \tag{17}$$

where h is the hydraulic head (in m), K is the hydraulic conductivity of the aquifer (in m s^{-1}), and $h_D(x,y)$ corresponds to the head imposed at the lateral boundaries (in m). A zero flux is fixed at the top and bottom boundaries of the domain of interest. Next, the self-potential distribution of the

Darcy velocity in the saturated zone is used to compute the streaming potential contribution from equation (3). Then the residual self-potential map is built by removing this electrokinetic contribution from the measured self-potential signals. Finally, the residual self-potential map is inverted as described in the next section.

5.2.2. Inverse problem

The self-potential signals measured at hydrocarbon contaminated sites are partially associated with an electrochemical component produced by oxido-reduction reactions. The processes by which this electrochemical signal is produced is described by the biogeobattery model (Naudet et al., 2004; Revil et al., 2010). The biogeobattery process typically occurs at the interface between the contaminated aquifer and the unsaturated zone (transition zone) where biofilms and minerals such as pyrite and magnetite can connect the anode of the biogeobattery (i.e., associated with the reducing zone) to the cathode (i.e., associated with the oxidizing zone) (see Figure 5.1). Electrons migration through biofilms and semi-conductors provides an electrical current through the capillary fringe (Linde and Revil, 2007). In this section, we will describe the different steps that will be followed to retrieve the redox potential by inverting the residual self-potential data. For this reason, the discretization of the current density vector will be performed only in the transition zone which is considered to have an arbitrary thickness of 1 m (see discussion below and see Linde and Revil, 2007).

The inverse problem relies on the minimization of the following objective (cost) function:

$$\Psi\left(\mathbf{J}_R\right)=\left\|\mathbf{W}_d\left(\mathbf{K}\mathbf{J}_R-\boldsymbol{\psi}_R\right)\right\|+\lambda\left\|\mathbf{J}_R-\mathbf{J}_R^0\right\|, \tag{18}$$

where $\boldsymbol{\psi}_R$ denotes a vector of the observed residual self-potential field, $\mathbf{W}_d=\sigma_d^2\times\mathbf{I}_{d\times d}$ denotes a diagonal covariance matrix to include in the optimization of the uncertainties of the SP data with σ_d^2 as variance. $\mathbf{J}_R=\left(\mathbf{J}_R^x,\mathbf{J}_R^y,\mathbf{J}_R^z\right)$ corresponds to the three components of the electrical current density associated with the redox contribution considered here as the unknown parameters to be estimated by the inversion algorithm. The matrix $\mathbf{K}=\left(\mathbf{K}_{ij}^x,\mathbf{K}_{ij}^y,\mathbf{K}_{ij}^z\right)$ denotes the kernel matrix (N × $3M$) where N denotes the number of the self-potential measurements recorded at the ground surface and M denotes the number of the elements that are discretized in order to assign the value of the electrical density. In equation (18), $\mathbf{J}_R^0$ denotes a priori electrical current density model. Such a priori model is used to avoid the potential presence of undesirable bias in the estimated model due to the non-uniqueness of the inverse problem, a problem that is inherent to all potential field problems. The *a priori* model can be derived from the gradient of the redox potential measurements obtained at different wells. In equation (18), λ denotes a regularization parameter that controls the weights of the data misfit term $\left\|\mathbf{K}\mathbf{J}_R-\boldsymbol{\psi}_R\right\|$ with respect to the regularizer

$\left\|\mathbf{J}_R - \mathbf{J}_R^0\right\|$ to find an optimal solution. In the present paper, we compute λ by using the L-curve technique (Hansen, 1998). Equation (18) corresponds to a linear problem for which the solution that minimizes the objective function (18) can be easily found as (Hansen, 1998):

$$\hat{\mathbf{J}}_R(\lambda) = \left[\mathbf{K}^T\mathbf{W}_D^T\mathbf{W}_D\mathbf{K} + \lambda^2 I\right]^{-1}\left(\mathbf{K}^T\boldsymbol{\psi}_R + \lambda\mathbf{J}_R^0\right). \quad (19)$$

This solution allows us to fit the (residual) self-potential data and reconstruct the spatial distribution of the redox potential via the following approximation (Linde and Revil, 2007):

$$E_h^s = -\frac{\mathrm{J}_R^Z\delta_z}{\sigma} + E_h^v, \quad (20)$$

where J_R^Z is the vertical component of the estimated electrical current density, δ_z is the arbitrary thickness of the transition zone, E_h^v is the redox potential of the unsaturated zone and E_h^s is the redox potential of the contaminated aquifer. As explained in details in Linde and Revil (2007), this procedure is independent of the thickness of the capillary fringe (transition zone).

5.3. Field investigations

5.3.1. Study site characterization

The area of investigation was an abandoned petroleum refinery located in the North-Western part of the Paris basin (France) and on an alluvial plain of the Seine River. The refinery was built in 1928, had an average refining activity of 7 million tons of crude oil per year and was shut down in 2013. Leakage from tanks and pipelines over the refinery operating years resulted in the seepage of light non-aqueous phase liquid (LNAPL) and dense non-aqueous phase liquid (DNAPL). Borehole data available over the area indicated that three different contamination phases exist: (1) a dissolved phase spreading down to a depth of 25 m; (2) a free phase present at different locations with a thickness ranging between 1 and 100 cm and (3) a residual phase consisting of the spill part which did not drain by gravity and residually saturated the pore spaces above the water table while the spill was traversing the vadose zone down to the aquifer (Atekwana and Atekwana, 2010). This phase is present at the source zones and at some other locations where the extended free phase can rise up due to the groundwater seasonal fluctuations caused by the nearby river. Note that the hydrocarbon contamination at this site is considered as mature (or aged) because enough time has elapsed for the biological processes to alter the hydrocarbons and their host environment after the contamination events, which started more than 80 years ago.

Geologically, the site is characterized by the first 2 m being an anthropogenic layer mainly composed of sandy soil with coarse grain diameter gravels. Below, there is a layer of fine to medium sand coarsening to gravel with depth, and with an average thickness ranging from 8 to 25 m. The site is characterized by one unconfined aquifer located in the sand and gravel layer

(between 4 and 11 m deep) and mainly fed by a karstified chalk aquifer which exists below at a depth ranging from 11 m to 25 m. In the alluvial aquifer, groundwater flows from the South-East to the North-West towards the Seine River.

A clean and a contaminated zone were identified according to the hydrocarbon analyses of groundwater samples (Figure 5.2). Samples taken from boreholes B34 and B12, located in the North-Western part of the site, recorded concentrations ranging from 1.2 to 4 mg L^{-1}. Higher concentrations ranging from 1.6 to 6.1 mg L^{-1} have been recorded in wells #B13 and B11, while values ranging between 1.3 and 2.6 mg L^{-1} were recorded in B33 and B9 located between the North-West and the center of the site. C5-C10 hydrocarbons measurements showed values ranging from 98 to 100 mg L^{-1} in B34 and B12; values ranging between 13 and 27 mg L^{-1} in B13 and B11 and values ranging between 1.4 and 3.7 mg L^{-1} in B33 and B9. Measurements conducted on groundwater samples taken from the boreholes located in the North-Eastern part of the site (wells #B1, B2, B3 and B4) recorded no hydrocarbons in the groundwater samples.

The measurements of groundwater geochemical parameters showed: increased total dissolved solids (TDS) concentrations (400-1000 mg/L); increased groundwater electrical conductivity values (400-2000 µS/cm) (Figure 5.3); negative redox potential values (-10 to -300 mV) (Figure 5.4) and depleted terminal electron acceptors (TEAs) concentrations (dissolved oxygen, sulfate and nitrate) within the contaminated aquifer boreholes (e.g., B7, B8, B9, B10, B11). In contrast, lower TDS concentrations (50-200 mg/L), lower groundwater electrical conductivity values (<400µS/cm), positive redox potential values (1-40 mV) and higher TEAs concentrations were observed in the clean groundwater zone boreholes (B1, B2, B3 and B4). The data provide evidence that biodegradation of organic matter is occurring at the site**.** Biodegradation is evidenced by (1) the increase of the TDS and groundwater electrical conductivity in the contaminated zone compared to the clean zone, (2) the change in redox conditions, and (3) the values of the dissolved oxygen concentrations in the contaminated zone. Furthermore, a change from negative redox potential to positive redox potential in the North-Eastern part of the site implies that a redox front exists at the boundary between the clean and contaminated zones.

5.3.2. Geophysical surveys

Electrical resistivity tomography can be used to image the subsurface in terms of electrical resistivity distribution by injecting direct current at the ground surface and measuring its corresponding electrical field (e.g., Samouëlian et al., 2005). 27 Two-dimensional (2-D) ERT profiles were acquired by using a Syscal Pro system (http://www.iris-instruments.com). Wenner and dipole-dipole arrays were used for each profile, with electrodes spacings of 1m, 2m, 3m and 5m according to the length of each profile. The electrical resistivity profiles were processed and filtered by the computer software Res2Dinv (Loke and Barker, 1996), which uses the field data to obtain a 2D model of the electrical resistivity distribution in the subsurface (Griffiths and Baker, 1993). The software subdivides the model into several small blocks and uses a lEast-square

inversion technique to obtain the resistivity value of each block (with a smoothness constraint). The 2-D ERT tomograms have been interpolated to obtain maps of the electrical resistivity distribution in the saturated and non-saturated zones.

To collect the self-potential data, two non-polarizable (Pb-$PbCl_2$) Petiau electrodes were used: one is fixed and referred to as the reference electrode, whereas the other can move into different measurement points with a rolling wire. The electrodes are rods of lead suspended in porous containers supersaturated with KCL/$PbCl_2$ solutions. The electrodes were placed in small holes filled with bentonite mud during the measurements. This ensures good electrical contact between the soil and the non-polarizable electrodes (Jardani et al., 2006). The measurements were performed by using a high input impedance (10 MΩ) voltmeter (MX20) which was connected to the electrodes to record their corresponding self-potential difference.

The self-potential survey was performed over a single day and no rain events happened during that day or in the two days prior the survey. The areas with no self-potential data correspond to the emplacement of facilities, buildings and pavements with a thick layer of asphalt. The base station of the self-potential survey was chosen in the clean zone and it was common to all the measurements which were done at 550 stations. To measure the drift between the two electrodes, the potential difference between the two electrodes was measured prior and after the survey. The difference was less than 1 mv indicating a minor and negligible drift. Note that the electrodes used for this survey were new. The temperature variation of the electrodes was not taken into account as the Petiau electrodes have a very small temperature sensitivity close to 0.2 mV/°C (Perrier et al., 1997; Petiau, 2000). Each station was measured up to 5 times and for each measurement, the scanning electrode was kept in the ground until a stable reading was achieved. The data reproducibility was tested by comparing the data presented in this paper to a self-potential map acquired one year earlier. The old map (not shown) did not cover the whole site and had fewer data points. The data showed however the same pattern with slight differences of less than 5 mV in the amplitudes of the signals.

5.4. Results and discussion

A representative electrical resistivity profile (ERT1) acquired in the contaminated zone is shown in Figure 5.5. The profile shows a simple geological structure with two main electrical resistivity domains: (1) a shallow resistive zone (100-300 Ω m) corresponding to the sand and gravel vadose zone and (2) a very conductive layer (<30 Ω m) starting at a depth of 9 m and corresponding to the contaminated alluvial aquifer. The map of the electrical resistivity distribution in the vadose zone (depth of 3 m) shows electrical resistivity values ranging from 100 to 400 Ω.m in the regions of contaminated and clean groundwater (Figure 5.6a). Figure 5.6b shows the electrical resistivity distribution is the site's saturated zone at a depth of 11m. The map is dominated by low electrical resistivity values (5-50 Ω m), except for the North-Eastern part of the

site, where higher electrical resistivity values (150-400 Ω m) appear in accordance with the clean groundwater zone (B1, B2, B3 and B4).

The low electrical resistivity values in the contaminated zone in comparison to the clean zone reflects the significant mineralization of groundwater which is responsible for the increase in TDS concentrations during the biodegradation of hydrocarbons (Atekwana et al., 2004). The etching and dissolution of minerals surfaces by biodegradation by products (e.g., organic and carbonic acids), in addition to the leaching of soluble salts (from grains surfaces) increase the concentrations of TDS and the groundwater electrical conductivity values in contaminated aquifers (McMahon et al., 1995; Atekwana et al., 2000; Sauck, 2000). Consequently, the increase of pore water electrical conductivity increases the bulk electrical conductivity and produces low resistivity anomalies in the impacted zones. The self-potential map (Figure 5.7) shows negative values ranging from -130 mV to -5 mV (with respect to the position of the reference) in the contaminated regions. Contrarily, the map shows positive values ranging from 10 to 70 mV in the clean region, located in the North-Eastern part of the site.

As mentioned earlier, the self-potential signal measured in the field includes two components: an electro-kinetic component associated with groundwater flow and an electrochemical component associated with redox processes. Other contributions (thermoelectric effects and diffusion potentials) are negligible in comparison to the electrokinetic and redox components, see discussions in Revil et al. (2009) and Revil et al. (2010). Redox-driven anomalies associated with buried metallic objects produced also strong but localized self-potential anomalies (see examples in Castermant et al., 2008, Rittgers et al., 2013) that can be filtered out easily (see Revil et al., 2012).

The first step of our analysis is the removal of the electrokinetic contribution from the recorded self-potential data. This step is important for isolating the self-potential signal produced by oxido-reduction reactions. This was carried out through the numerical computation of the electrokinetic contribution by solving the hydroelectric coupling problem as described previously in section (2.1). In the first step, the hydraulic head data collected from different wells were exploited to predict the distribution of the hydraulic head variations (Figure 5.8). This was done through estimating the hydraulic conductivity K of the aquifer (assumed here homogenous, $K=10^{-7}$ m s^{-1}) and defining the imposed boundary conditions for solving the diffusion equation. We acknowledge that this is a strong assumption that is probably not completely realistic. However, it seems to fit the head data pretty well in this special case study. In more complex environments, it will be better to invert the hydraulic conductivity or transmissivity fields first. Note that this assumption is not really needed however since the heads can be interpolated and we can use a single value of the apparent coupling coefficient as discussed by Arora et al. (2007). We also assume that the flow in the vadose zone is producing a negligible self-potential anomaly.

In the second step, we used the spatial distribution of the Darcy velocity of the groundwater flow which was determined numerically in the first step to compute the electrical current density of the confined aquifer. The electrical current density was neglected in the vadose zone. The charge

density parameter was calculated after determining the electrokinetic coupling coefficient C through a simple laboratory experiment (Figure 5.9a) described by Revil and Jardani (2013). The assumption of a single permeability value is consistent with the use of a single value for the effective charge density. For the streaming potential measurements, a graduated plastic tube, 50 cm long and 10 cm in diameter was used. A representative soil sample extracted from borehole B8 was placed at the bottom of the tube and two non-polarizable electrodes were placed at the bottom and the surface of the soil sample. The measurements were performed at ambient temperature (20°C±1C°C). A contaminated groundwater sample extracted from the same borehole with an electrical conductivity value of approximately 1000 $\mu S/cm$ was injected from the top of the tube. The measurement was repeated at different water head levels with an interval of 5 cm. Then the potential difference values were plotted against the water head levels in order to compute the electro-kinetic coupling coefficient *C*', which is represented in mV per meter of water head variation (Figure 5.9b). *C*' was determined to be -4.0±1 mV/m. These parameters, in addition to the electrical conductivity distribution in the saturated and unsaturated zones (determined from the ERT survey) were used to solve the Poisson equation to define the electrical signature (electrokinetic component) associated with groundwater flow (Figure 5.10). The electrokinetic component was determined to be very small and was removed from the self-potential data to produce the residual self-potential data. The residual self-potential map showed a similar pattern compared to the original field self-potential map, with positive self-potential values in the clean groundwater zone and negative self-potential values in the contaminated groundwater zone (Figure 5.11).

To predict the redox potential distribution in the aquifer, the self-potential data were inverted by using the approach introduced in the inverse problem description (section 2.2), where the heterogeneity of the electrical conductivity in the saturated and vadose zones is taken into account. This inversion is based on the estimation of the redox values from the vector of the electrical current density predicted through the inversion of the residual self-potential data. The electrical sources responsible for the self potential field were assumed to be located in the transition zone which was divided into 144 cells, with a dimension of "35 m × 56 m × 1 m for each (Figure 5.12). The electrical current density components that were predicted from the inversion of the self-potential data were assigned for each cell. The total number of the unknown parameters to invert was 3×144=432 and the total number of self-potential measurements was 350, so we dealt with an undeterminated inverse problem. The inverse problem was performed with a smooth constraint and the regularization parameter was determined through the L-curve approach. The retrieved current density components are illustrated in Figures 5.13 and 5.14. The figures show that the amplitudes of the horizontal components of the electrical current density J_x and J_y (Figure 5.13) are very small compared to the vertical component J_z (Figure 5.14). This was verified by comparing the correlation of the observed and numerical data obtained only from the vertical component (Figure 5.15a), with the correlation of the observed and numerical data obtained from the combination of the vertical and horizontal components (Figure 5.15b). Therefore, the

contributions of the horizontal components can be neglected. The distribution of the redox potential in the aquifer was then reconstructed from the vertical component of the current density by using equation (20) as described in section (2.2). Similar to the measured redox potential values, the predicted redox potential map showed positive values (10 to 40 mV) in the clean groundwater zone and negative values (0 to -150) in the contaminated groundwater zone (Figure 5.16a). The inverted redox potential values showed a good linear correlation (R^2 = 0.79) with the observed redox potential values (Figure 5.16b). This further supports the concept of biogebattery at this site with the source current density produced in the capillary fringe just above the water table**.** Note that the result shown in Figure 5.16 is free from the choice of the base station for the self-potential signals. It is only based on the relative amplitude of the residual self-potential anomaly with respect to the position of the reference electrode and the difference in redox potential between the contaminated zone and the background.

5.5. Conclusion

This study shows an application of the self-potential and electrical resistivity methods to estimate the redox potential at a site impacted by a mature hydrocarbon contamination undergoing biodegradation. The geophysical methods constrained by measurements of geochemical parameters provided useful information on the quality of groundwater, and indicated that biodegradation processes are occurring in the contaminated aquifer. An active (bio)geobattery process in which the redox potential gradient is the driving force of the self-potential electrochemical signal is suggested to be present in the contaminated portion of the site. This natural geobattery is created due to the existence of a strong redox potential gradient between the highly reducing conditions within the plume and the oxidizing conditions outside the plume. The associated current density occurred therefore in the capillary fringe of the unconfined aquifer.

The electrokinetic component of the observed self-potential signals was removed numerically from the field self-potential data to produce a residual self-potential map. For this purpose, a groundwater flow model was parameterized and calibrated to compute the spatial distribution of the Darcy velocity, which was used to calculate the streaming potential (electrokinetic component). A redox potential map was then reconstructed from the inversion of the residual self-potential data through the computation of the electrical current density components, taking into account the electrical conductivity distribution in the subsurface which was obtained from an electrical resistivity survey. The horizontal components were determined to be very small compared to the vertical component of the source current density. Therefore, the redox contribution in the contaminated aquifer can be explained by vertical dipoles distributed across the capillary fringe just above the water table, supporting further the mechanism of biogebattery at this site.

The predicted redox potential values showed a good correlation with the redox potential values measured independently in a set of wells. This good correlation illustrates the ability of the

self-potential method to delineate the redox front of the contaminant plume. Moreover, the self-potential equipment (voltmeter, electrodes and rolling wires) are inexpensive and stable over long periods of time. Therefore, the self-potential method can be considered as a cost-effective and fast method which could be used in the next stage of our research for the long term monitoring of the contaminant plume evolution during the remediation process. However, it would be necessary to undertake more biological and chemical investigations to characterize the biogeobattery mechanism (e.g., type of biofilms and bacteria, the precipitation of semi-conductors etc.) and define the more precisely the redox reactions (iron reduction, methanogenesis, etc.) occurring at this site.

5.6. References

Arora, T., Linde N., Revil, A., Castermant, J., 2007. Non-intrusive characterization of the redox potential of landfill leachate plumes from self-potential data. J. Contam. Hydrol. 92, 274–92. doi:10.1016/j.jconhyd.2007.01.018.

Atlas, R.M., 1981. Microbial degradation of petroleum hydrocarbons: an environmental prospective. Microbial. Rev., 45, 180-209.

Atekwana, E.A., Sauk, W.A., Werkema, D.D., 2000. Investigations of geoelectrical signatures at a hydrocarbon contaminated site. Appl. Geophys. 44, 167–180. doi:10.1016/S0926-9851(98)00033-0.

Atekwana, E. A., Sauk, W.A., Abdel Aal, G.Z., 2002. Geophysical investigation of vadose zone conductivity anomalies at a hydrocarbon contaminated site: Implications for the assessment of intrinsic bioremediation. Environ. Eng. Geophys., 7, 103–110.

Atekwana, E.A., Atekwana, E.A., 2010. Geophysical Signatures of Microbial Activity: A Review. Surv. Geophys., 31, 247–283. doi: 10.1007/s10712- 009 -9089 -8.

Baedecker, M.J., Cozzarelli, I.M., Eganhouse, R.M., Siegel, D.I., Bennett, P.C., 1993. Crude oil in a shallow sand and gravel aquifer: III. Biogeochemical reactions and mass balance modeling in anoxic groundwater. Applied Geochemistry 8, 569–586.

Buselli, G., Lu, K., 2001. Groundwater contamination monitoring with multichannel electrical and electromagnetic methods. J. Appl. Geophys.48, 11-23.

Binley, A., Henry-Poulter, S., Shaw, B., 1996. Examination of solute transport in an undisturbed soil column using electrical resistance tomography. Water Resour. Res., 32(4), 763–769.

Binley A., Hubbard S. S., Huisman J. A., Revil A., Robinson D. A., Singha K., Slater L. D., 2015. The emergence of hydrogeophysics for improved understanding of subsurface processes over multiple scales. Water Resour. Res., 51, 3837–3866, doi: 10.1002/2015WR017016.

Castermant J., Mendonça C.A., Revil A., Trolard F., Bourrié G., and Linde N., 2008. Redox potential distribution inferred from self-potential measurements associated with the corrosion of a burden metallic body. Geophysical Prospecting, 56, 269-282, doi:10.1111/j.1365-2478.2007.00675.x.

Christensen, T.H., Bjerg, P.L., Banwart, S.A., Jakobsen, R., Heron, G., Albrechtsen, H.-J., 2000. Characterization of redox conditions in groundwater contaminant plumes. J. Contam. Hydrol., 45, 165-241.

Corry, E., 1985. Spontaneous polarization associated with porphyry sulfide mineralization. Geophysics, 50, 1020-1034.

Craun, G.F., Brunkard, J.M., Yoder, J.S., Roberts, V.A., Carpenter, J., Wade, T., Calderon, R.L., Roberts, J.M., Beach, M.J., Roy, S.L., 2010. Causes of outbreaks associated with drinking water in the United States from 1971 to 2006. Clin Microbiol Rev., 23, 507-528.

Delong, E., 2002. L'électricité bactérienne, plus qu'une curiosité. La Recherché, 358, 17.

Fachin, S.J.S., Abreu, E.L., Mendonça, C.A., Revil, A., Novaes, G.C., Vasconcelos, S.S., 2012. Self-potential signals from an analog biogeobattery model, Geophysics, 77, 4, EN29-EN37, doi: 10.1190/GEO2011-0352.1, 2012.

Griffiths, D.H., Barker, R.D., 1993. Two-dimensional resistivity imaging and modeling in areas of complex geology. Journal of Applied Geophysics, 29, 211-226.

Hansen, P.C., 1998. Rank-Deficient and Discrete Ill-Posed Problems: Numerical aspects of Linear Inversion. 247 pp., SIAM, Philadelphia, Pa.

Hämmann, M., Maurer, H.R., Green, A.G., Horstmeyer, H., 1997. Self-Potential Image Reconstruction: Capabilities and Limitations. Eng. Geophys., 2, 21–35.

Jardani, A., Dupont, J., Revil, A., 2006. Self-potential signals associated with preferential groundwater flow pathways in sinkholes. J. Geophys. Res., 111, B09204, doi: 10.1029/2005JB004231.

Jardani, A., Revil, A., Bolève, A., Crespy, A., Dupont, J.P., Barrash, W., Malama, B., 2007. Tomography of the Darcy velocity from self-potential measurements. Geophys. Res. Lett. 34, L24403.

Linde, N., Revil, A., 2007. Inverting self-potential data for redox potentials of contaminant plumes. Geophysical Research Letters, 34, L14302, doi:10.1029/2007GL030084.

Loke, M.H., Barker, R.D., 1996. Practical techniques for 3D resistivity surveys and data inversion. Geophysical Prospecting, 44, 499-523.

McMahon, P.B., Vroblesky, D.A., Bradley, P.M., Chapelle, F.H., and Guller, C.D., 1995. Evidence of enhanced mineral dissolution in organic acid rich shallow ground water. Ground Water 33, 207–216.

Naudet, V., Revil, A., Bottero, J.-Y., Bégassat, P., 2003. Relationship between self-potential and redox conditions in contaminated groundwater. Geophys. Res. Lett. 30(21), 2091, doi: 10.1029/2003GL018096.

Naudet, V., Revil, A., Rizzo, E., Bottero, J.-Y., Bégassat, P., 2004. Groundwater redox conditions and conductivity in a contaminant plume from geoelectrical investigations. Hydrol. Earth Syst. Sci. 8, 8–22. doi:10.5194/hess-8-8-2004.

Naudet, V., Revil, A., 2005. A sandbox experiment to investigate bacteria-mediated redox processes on self-potential signals. Geophys. Res. Lett. 32, L11405, doi: 10.1029/2005GL022735.

Nimmer, R.E., Osiensky, J.L., 2002. Direct current and self-potential monitoring of an evolving plume in partially saturated fractured rock. Journal of Hydrology 267, 258–272.

Nyquist, J.E., Corry, C.E., 2002. Self-potential: the ugly duckling of environmental geophysics. The Leading Edge, 21, 446-451. doi:10.1190/1.1481251.

Perrier, F., Petiau G., Clerc G., Bogorodsky V., and Erkul E., 1997. A one year systematic study of electrodes for long period measurements of the electric field in geophysical environments. Journal of Geomagnetism and Geoelectricity 49, 1677–1696, doi: 10.5636/jgg.49.1677.

Petiau, G., 2000. Second generation of lead-lead chloride electrodes for geophysical applications. Pure and Applied Geophysics 157, 357–382, doi: 10.1007/s000240050004.

Rao, P.S., Jawitz J. W., Enfield C. G., Falta R. W., Annable M. D., and Wood A. L., 2002., Technology integration for contaminated site remediation: clean-up goals and performance criteria. Groundwater Quality: Natural and Enhanced Restoration of Groundwater Pollution (Proceedings of the Groundwater Quality 2001 Conference held at Sheffield, UK, June 2001). IAHS Publ. no. 275.

Risgaard-Petersen N., Revil, A., Meister, P., Nielsen, L.P., 2012. Sulfur, iron-, and calcium cycling associated with natural electric currents running through marine sediment. Geochimica et Cosmochimica Acta 92, 1–13.

Risgaard-Petersen, N., Damgaard, L.R., Revil, A., Nielsen, L.P., 2014. Mapping electron sources and sinks in a marine biogeobattery. Journal of Geophysical Research Biogeosciences, 119(8), 1475–1486, doi: 10.1002/ 2014JG002673.

Reppert, P.M., Morgan, F.D., 2001. Streaming potential collection and data processing techniques. J. Colloid Interface Sci. 233, 348–355.

Revil A., Trolard, F., Bourrié, G., Castermant, J., Jardani, A., Mendonça, C.A., 2009. Ionic contribution to the self-potential signals associated with a redox front. Journal of Contaminant Hydrology, 109(1-4), 27-39.

Revil, A., Mendonça, C.A., Atekwana, E.A., Kulessa, B., Hubbard, S.S., Bohlen, K.J., 2010. Understanding biogeobatteries: Where geophysics meets microbiology. J. Geophys. Res. 115, G00G02, doi:10.1029/2009JG001065.

Revil A., Karaoulis M., Johnson T., and Kemna A. 2012. Review: Some low-frequency electrical methods for subsurface characterization and monitoring in hydrogeology. Hydrogeology Journal 20, 4, 617-658, doi:10.1007/s10040-011-0819-x.

Revil, A. And Jardani, A., 2013. The Self-Potential Method, Theory and Applications in Environmental Geosciences, Cambridge University Press, Canbridge.

Revil A. and Mahardika H., 2013. Coupled hydromechanical and electromagnetic disturbances in unsaturated clayey materials. Water Resources Researc, 49(2), 744-766, doi:10.1002/wrcr.20092.

Revil A., Karaoulis, M., Srivastava, S., Byrdina, S., 2013. Thermoelectric self-potential and resistivity data localize the burning front of underground coal fires. Geophysics, 78, 5, B259–B273.

Revil, A., Jardani, A., 2013. The Self-Potential Method: Theory and Applications in Environmental Geosciences. Cambridge University Press. 383 pages.

Rittgers J. B., Revil, A., Karaoulis, M., Mooney, M.A., Slater, L.D., Atekwana, E.A., 2013. Self-potential signals generated by the corrosion of buried metallic objects with application to contaminant plumes. Geophysics, 78(5), EN65-EN82, doi: 10.1190/GEO2013-0033.1.

Samouëlian, A., Cousin, I., Tabbagh, A., Bruand, A., Richard, G., 2005. Electrical resistivity survey in soil science: a review. Soil and Tillage Research, 83, 2, September 2005, 173–193.

Sauck, W.A., 2000. A conceptual model for the geoelectrical response of LNAPL plumes in granular sediments. Journal of Applied Geophysics, 44, 151–165.

Semple, K.T., Doick, K.J., Wick, L.Y., Harms, H., 2007. Microbial interactions with organic contaminants in soil: definitions, processes and measurement. Environ. Pollut. 150, 166–76. doi:10.1016/j.envpol.2007.07.023.

Sill, W.R., 1983. Self-potential modeling from primary flows. Geophysics, 48, 76–86, doi:10.1190/1.1441409.

Soueid Ahmed, A., Jardani, A., Revil, A., Dupont, J.P., 2016a. Specific storage and hydraulic conductivity tomography through the joint inversion of hydraulic heads and self-potential data.Advances in Water Resources, 89, 80 90. http://dx.doi.org/10.1016/j.advwatres.2016.01.006.

Soueid Ahmed A., Jardani, A., Revil, A., Dupont, J.P., 2016b. Joint inversion of hydraulic head and self-potential data associated with harmonic pumping tests. Water Resources Research, 52(9), 6769–6791, doi: 10.1002/2016WR019058.

Tender, L.M., Reimers, C.E., Stecher, H.A., Holmes, D.E., Bond, D.R., Lowy, D.A., Pilobello, K., Fertig, S.J., Lovley, D., 2002. Harnessing microbially generated power on the seafloor. Nature Biotechnology, 20, 821-825.

Tiehm, A., Schulze, S., 2003. Intrinsic Aromatic Hydrocarbon Biodegradation for Groundwater Remediation. Oil Gas Sci. Technol. 58, 449–462. doi:10.2516/ogst: 2003028.

Timm, F., Möller, P., 2001. The relation between electrical and redox potential: an evidence from laboratory to field experiments. J. Geochem. Explor., 72, 115-127.

Vayenas, A.C., 2002. Visualization experiments of biodegradation in porous media and circulation of the biodegradation rate. Water Resour., 25, 203-219.

Vichabian, Y., Reppert, P.M., Morgan, F.D., 1999. Self potential mapping of contaminants. Proc. Symp. Appl. Geophys. to Eng. Environ. Probl. March 14-1.

Werkema, D.D., Atekwana, E.A., Enders, A., Sauck, W.A., Cassidy, D.P., 2003. Investigating the geoelectrical response of hydrocarbon contamination undergoing biodegradation. Geophysical Research Letters, 30, 1647, doi: 10.1029/2003GL017346.

Figures

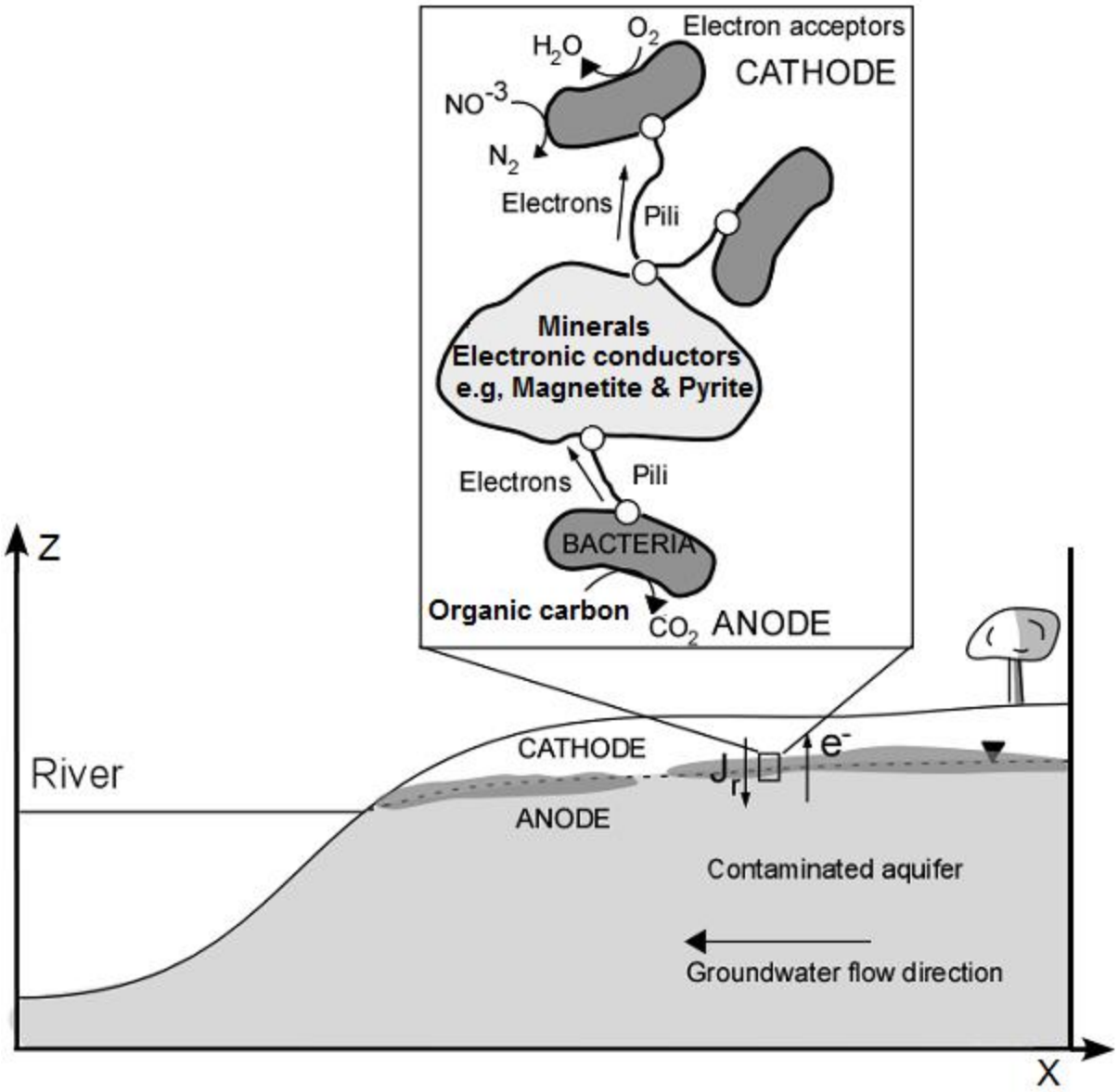

Figure 5.1: Sketch of the biogeobattery process that occurs at the water table located at the interface between the saturated and non-saturated zones. The diagram shows that mineral precipitates and bacterial biofilms transfer electrons between the cathode and the anode during the oxidation of organic carbon (modified from Revil et al., 2010). e- indicates the flux of electrons through biotic and/or abiotic electronic conductors located in the capillary fringe, and Jr indicates the source current density associated with the redox component of the self-potential field

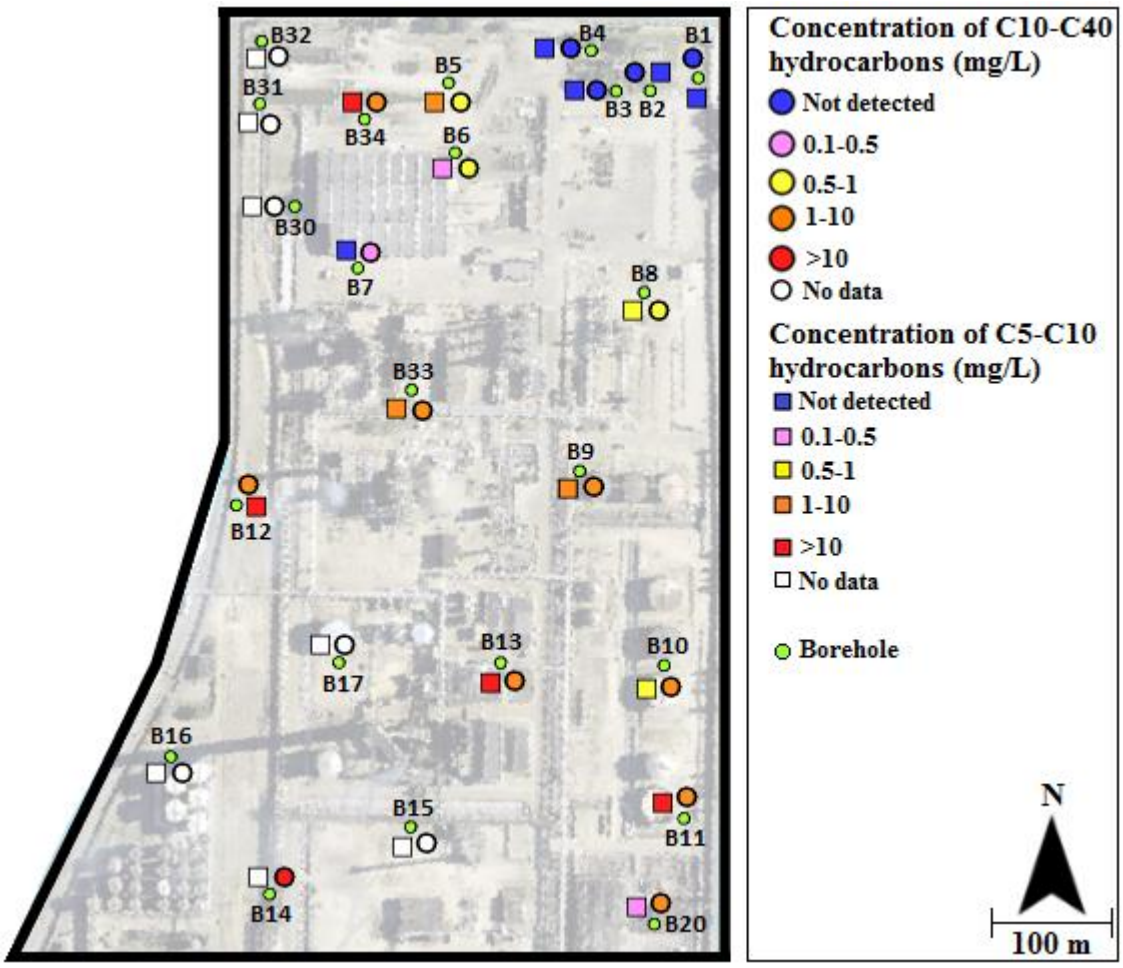

Figure 5.2: Borehole data showing the distribution of C10-C40 and C5-C10 hydrocarbons in groundwater overlaying an aerial photo of the site (Google Earth-© 2017 Google). The data shows a clean zone with zero concentrations of hydrocarbons in the North-Eastern part of the site (boreholes B1, B2, B3 and B4).

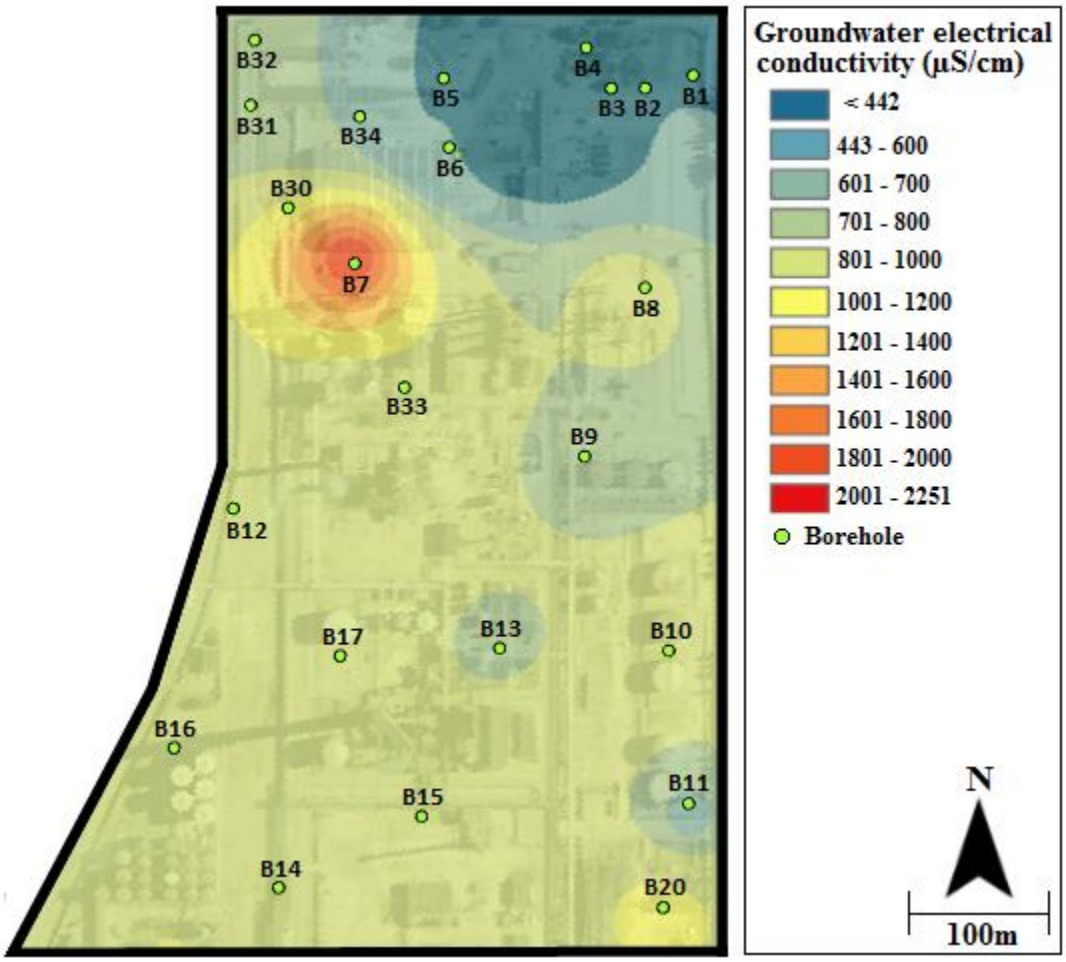

Figure 5.3: The distribution of groundwater electrical conductivity measured in the site boreholes (obtained by kriging with a linear variogram) overlaying an aerial photo of the site (Google Earth-© *2017 Google)*. The map shows higher electrical conductivity values close to the contaminated zone boreholes (e.g., B10, B13, B7, B8 and B33).

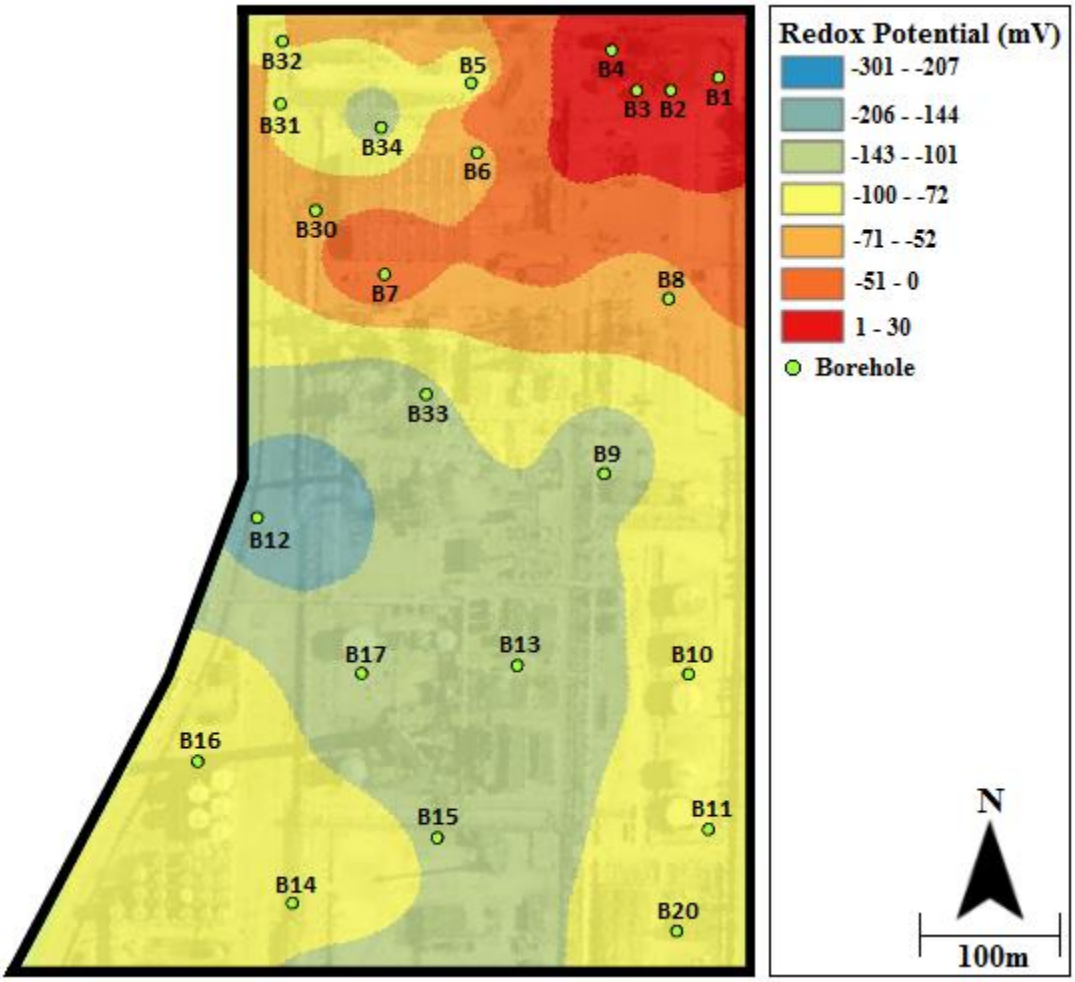

Figure 5.4: The distribution of redox potential measured in the site boreholes (obtained by kriging with a linear variogram) overlaying an aerial photo of the site (Google Earth-© *2017 Google)*. The map shows negative redox potential values close to the contaminated zone boreholes (e.g., B10, B13, B7, B8 and B33) and positive redox potential values close to the clean zone boreholes (e.g., B1, B2, B3 and B4).

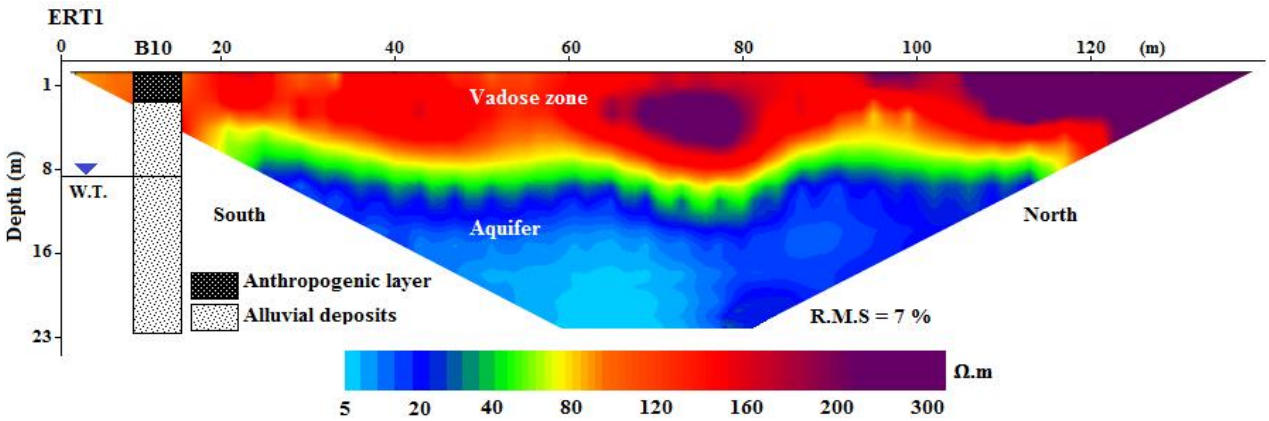

Figure 5.5: 2D-electrical resistivity tomography profile (Wenner configuration and 2 m electrodes spacing) acquired in the contaminated zone across borehole B10. Note that the shown location of the borehole is not its exact location on the profile (to avoid hiding profile features). The profile shows a high resistivity region in the non-saturated zone (150-300 Ω.m) and a low resistivity region in the saturated zone (5-30 Ω.m) which is located at a depth of approximately 9m.

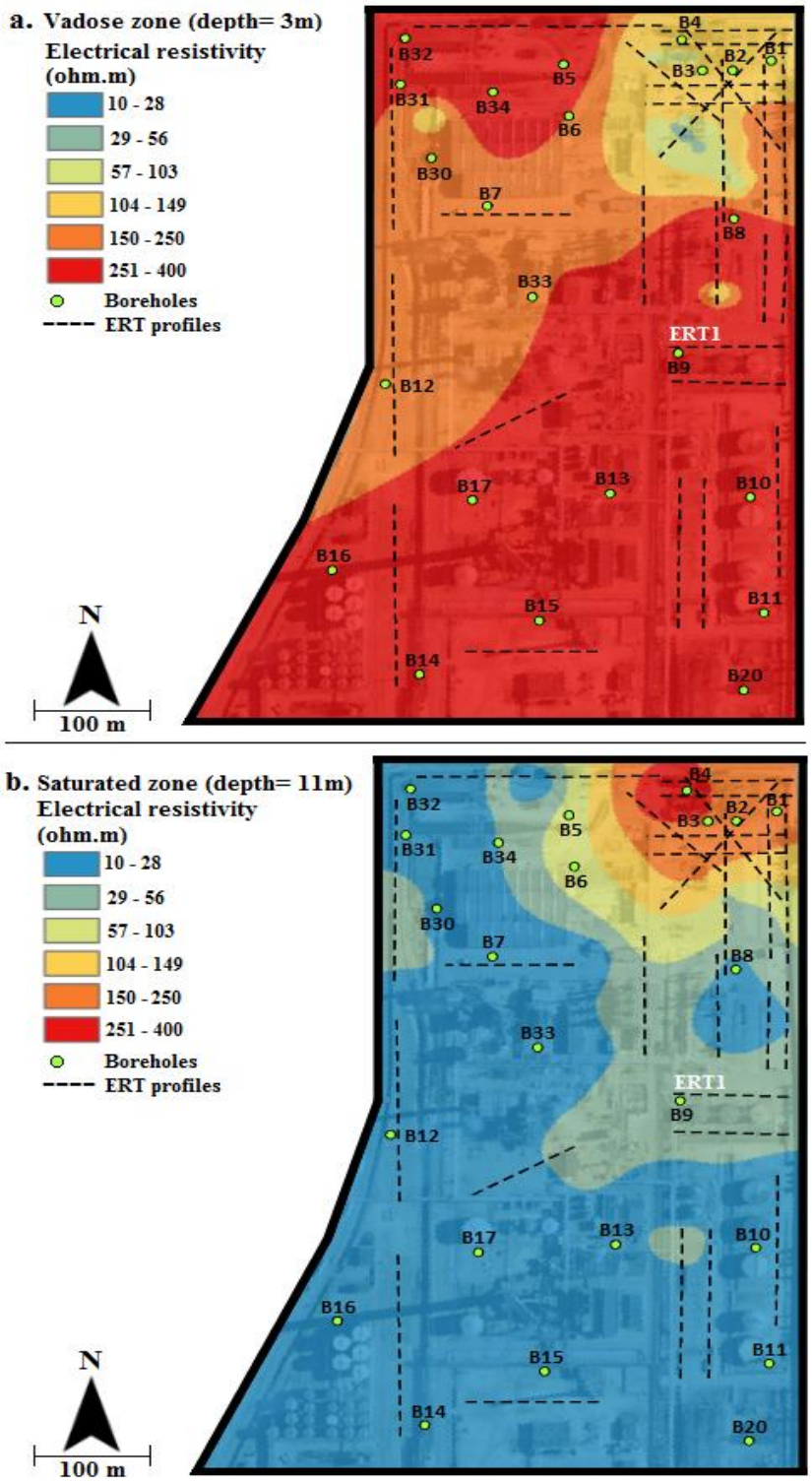

Figure 5.6: Distribution of electrical resistivity in the non-saturated (a) and saturated (b) zones overlaying an aerial photo of the site (Google Earth-© *2017 Google)*. The maps were obtained by the interpolation of data obtained from 27 electrical resistivity tomography profiles. The dashed lines represent the ERT profiles. ERT1 represents the location of the ERT profile shown in Figure 5.

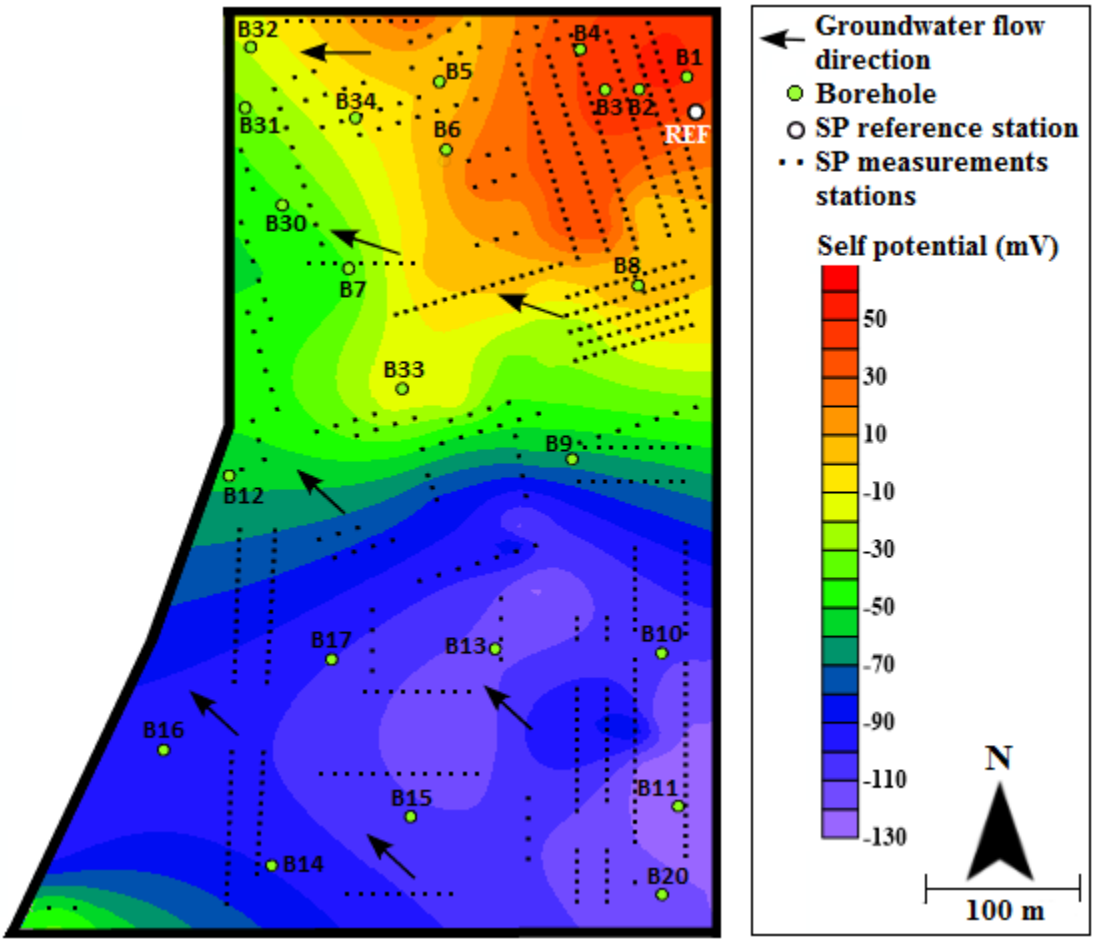

Figure 5.7: The measured self-potential map on the study site acquired in May 2016. The arrows show the direction of groundwater flow and the black dots correspond to the self-potential measurement stations made in the field. The white circle with the term 'REF' corresponds to the SP base (reference) station which was common for all the measurement stations. The self-potential map shows positive values close to the clean zone boreholes (B1, B2, B3 and B4) and negative values close to the contaminated zone boreholes (e.g., B7, B8, B9, B10, etc.).

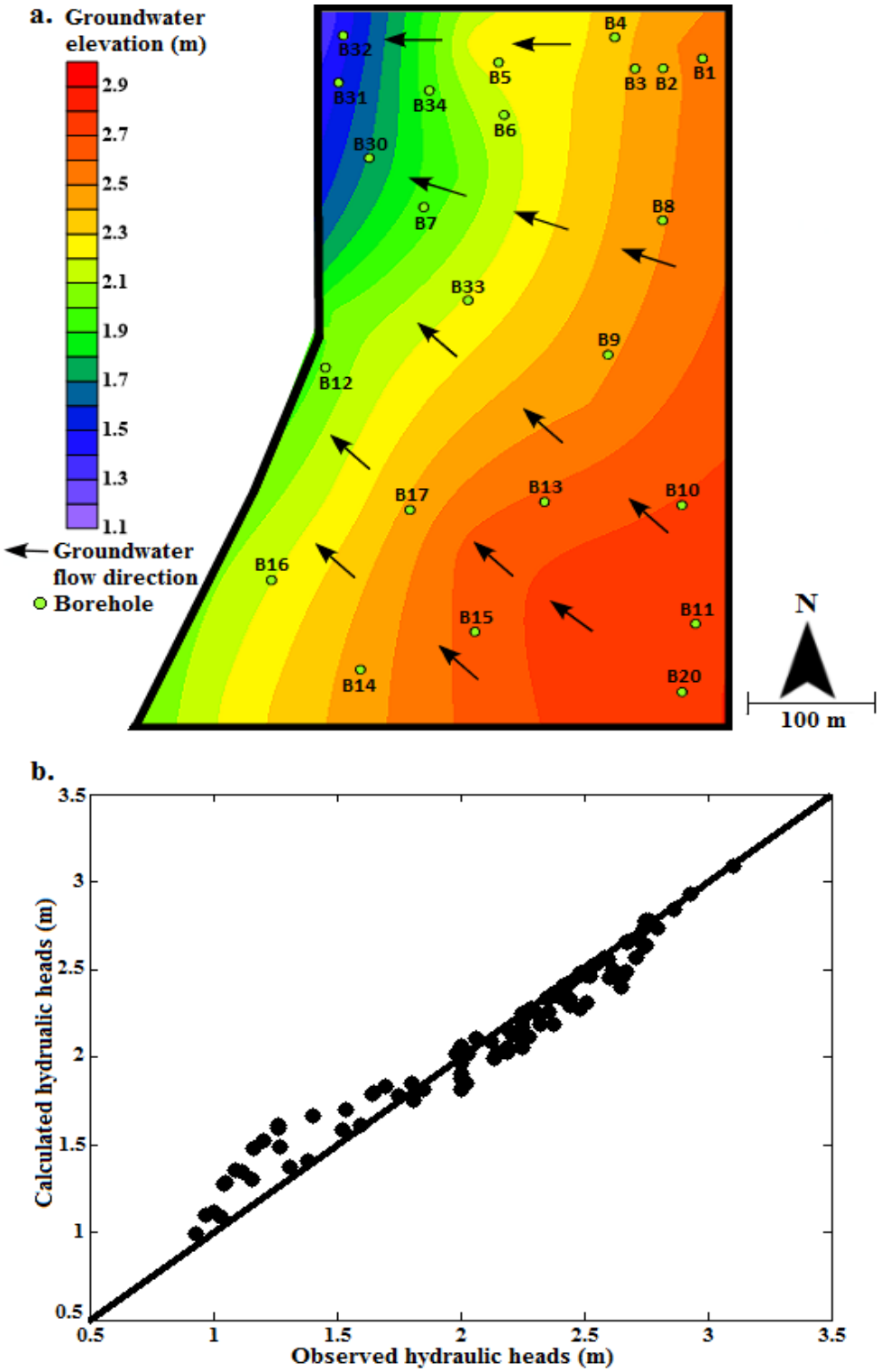

Figure 5.8: (a) The groundwater elevation in the study site. The arrows show the direction of groundwater flow. (b) Correlation between the hydraulic heads observed in boreholes (data points extracted from the interpolation of the data observed in the field) and the numerically predicted hydraulic heads which were used to calculate the electrokinetic self-potential component.

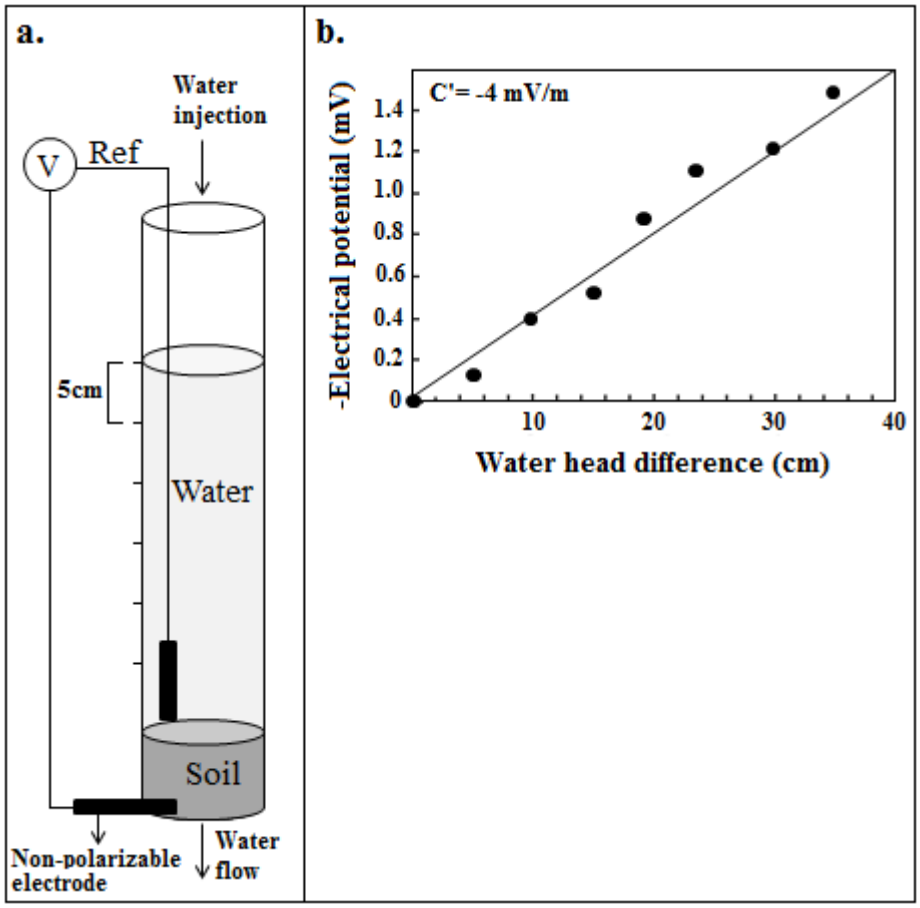

Figure 5.9: (a) The laboratory experiment used to calculate the electrokinetic coupling coefficient C' (Revil and Jardani, 2013). Two electrodes connected to a voltmeter were placed at the bottom and top of a soil sample. The arrows indicate the direction of water flow and the measurement was repeated at different water head levels with an interval of 5cm. (b) Plot of the water head difference against the measured electrical potential measured across the soil sample.

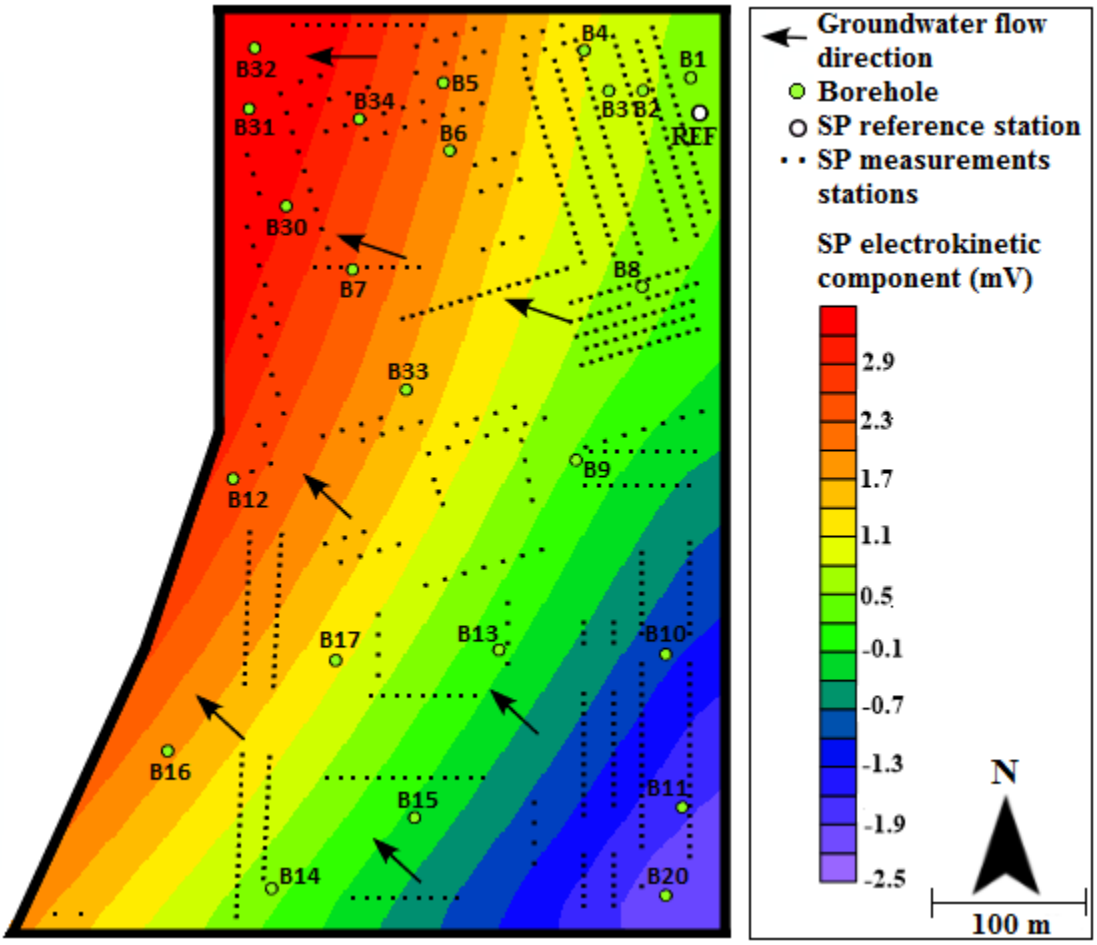

Figure 5.10: Map of the electrokinetic component of the self-potential data. The arrows represent the groundwater flow direction and the white circle with the term 'REF' corresponds to the SP base (reference) station.

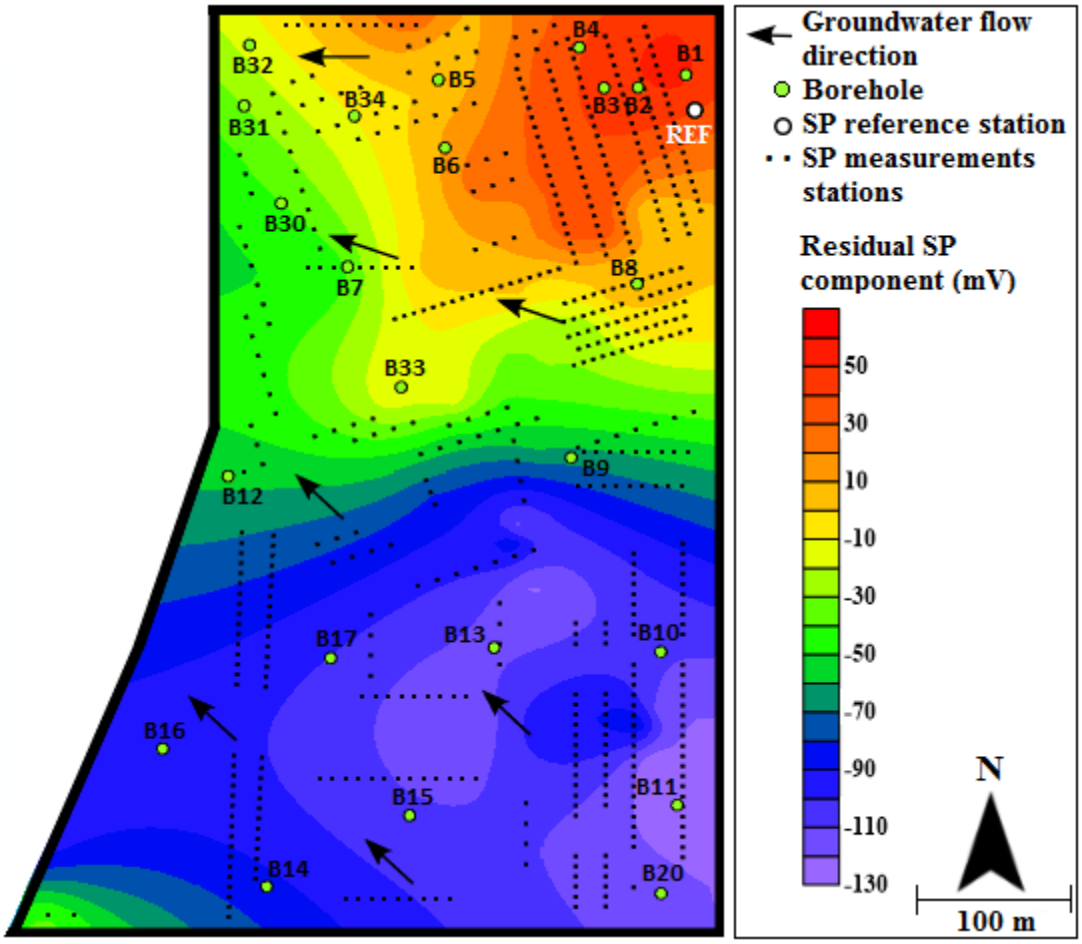

Figure 5.11: Map of the residual self-potential data (redox component) calculated by removing the electrokinetic component from the field self-potential data. The arrows represent the groundwater flow direction and the white circle with the term 'REF' corresponds to the SP base (reference) station.

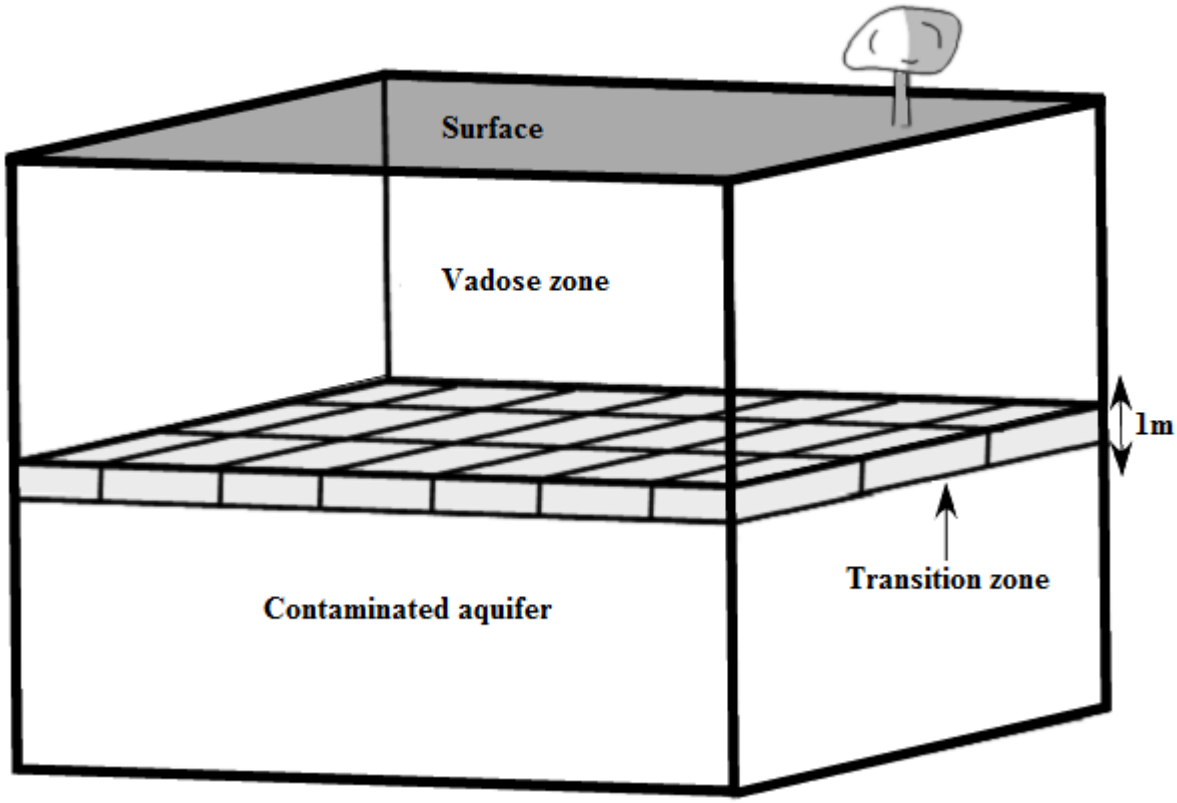

Figure 5.12: The position of the discretized domain used to invert the self-potential data. This domain corresponds to the transition zone, which separates the saturated zone from the non-saturated zone at a depth of 7.5m. The transition zone was considered to have a thickness of 1m.

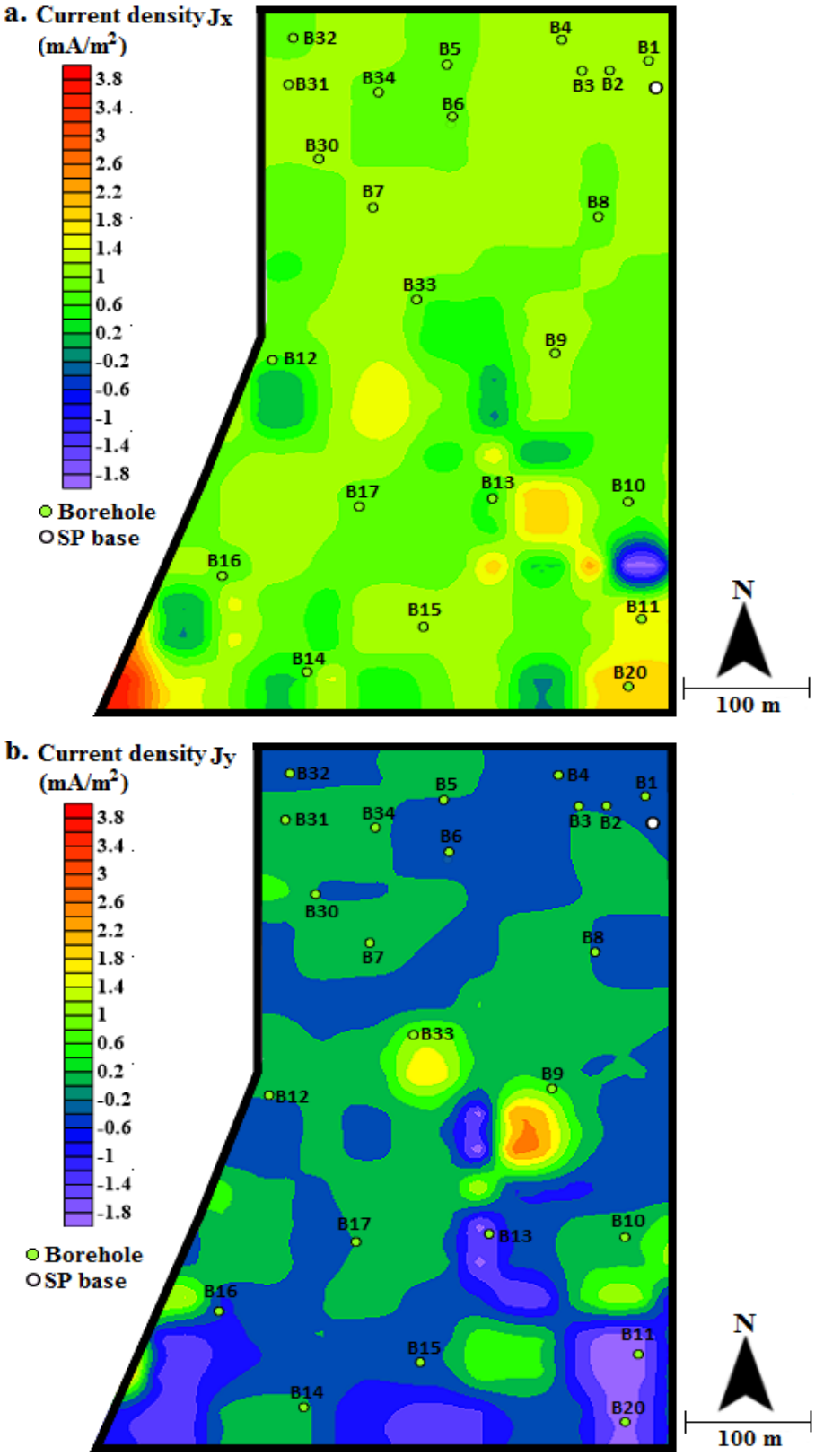

Figure 5.13: The inverted horizontal current density components (Jx and Jy).

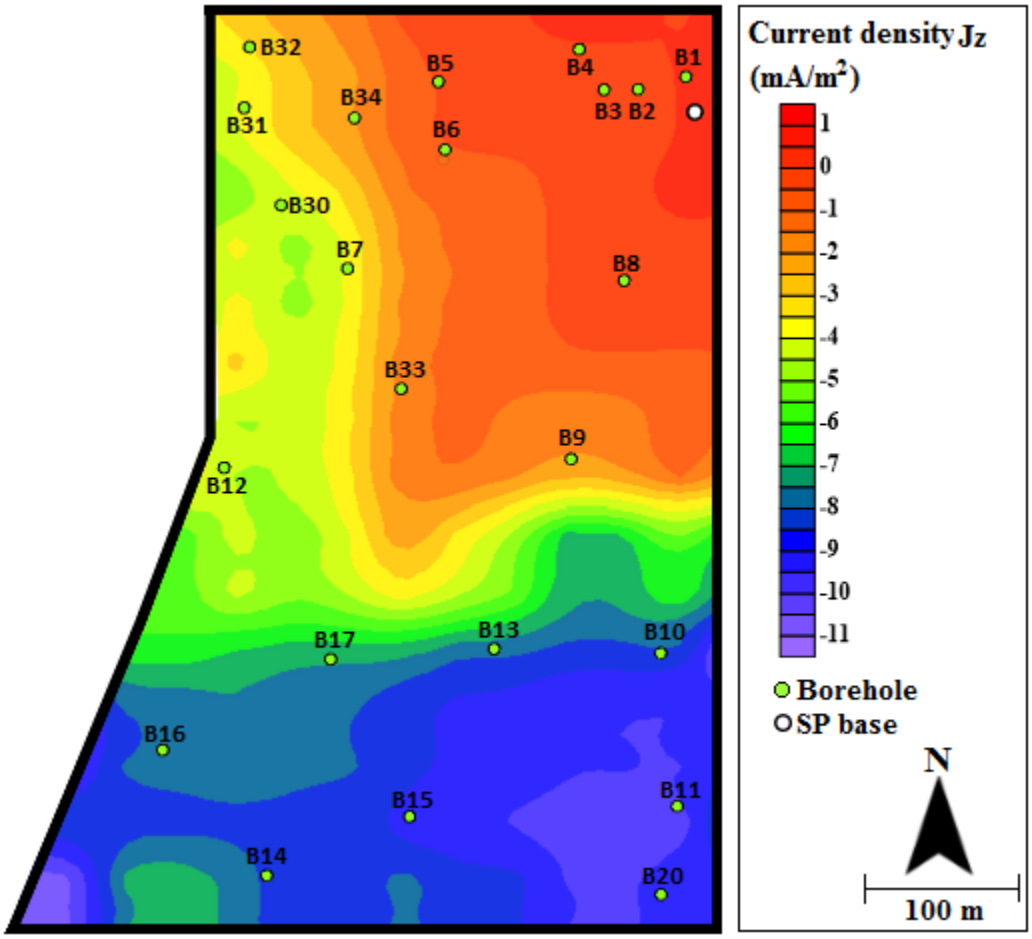

Figure 5.14: The inverted vertical current density component (Jz).

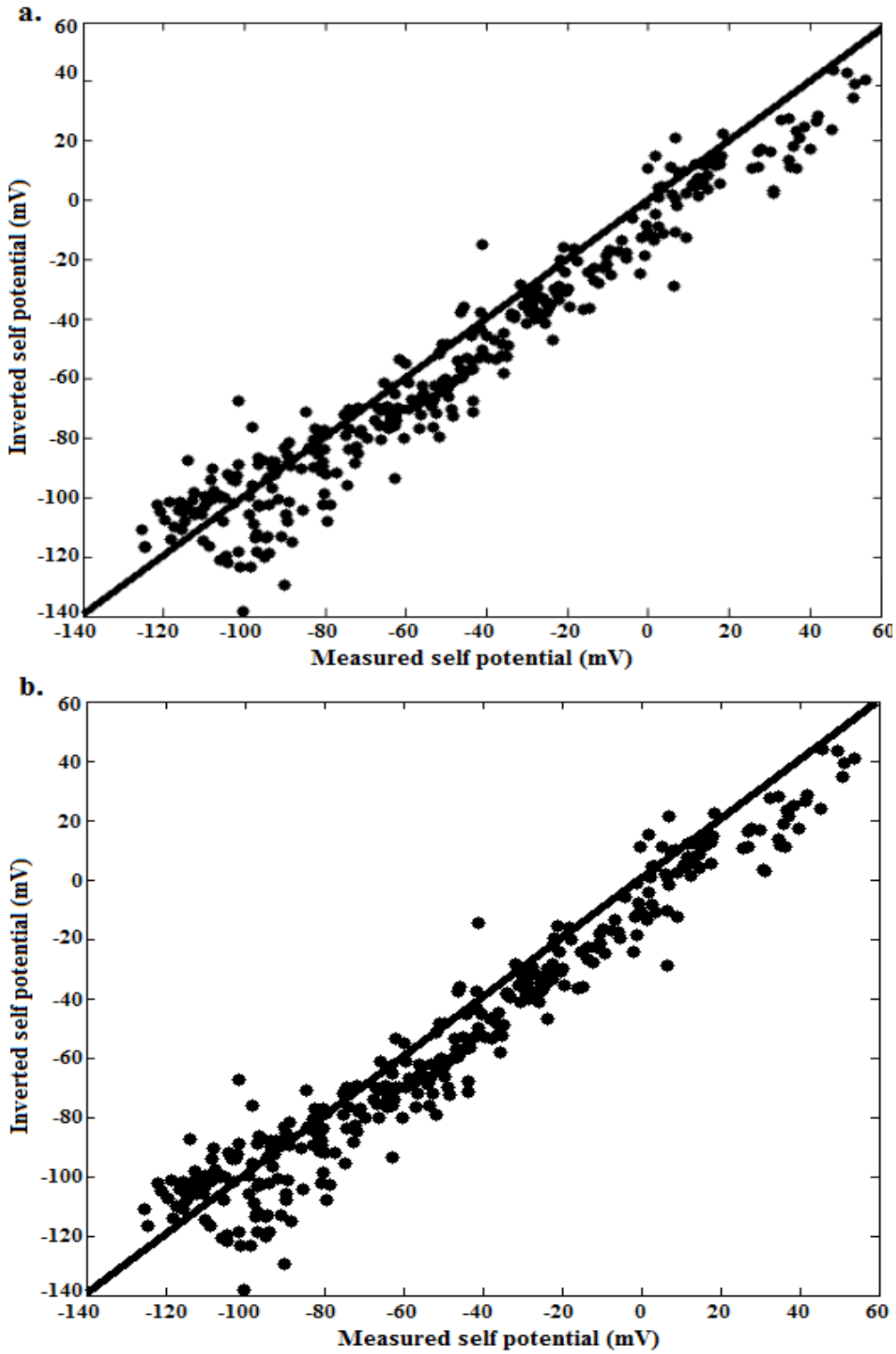

Figure 5.15: (a) Correlation between the measured and inverted self-potential data obtained by using only the vertical current density component (J_z). (b) Correlation between the measured and inverted self-potential data obtained from the combination of the three current density components (J_z J_x and J_y). The figure shows that the horizontal components are negligible compared to the vertical component.

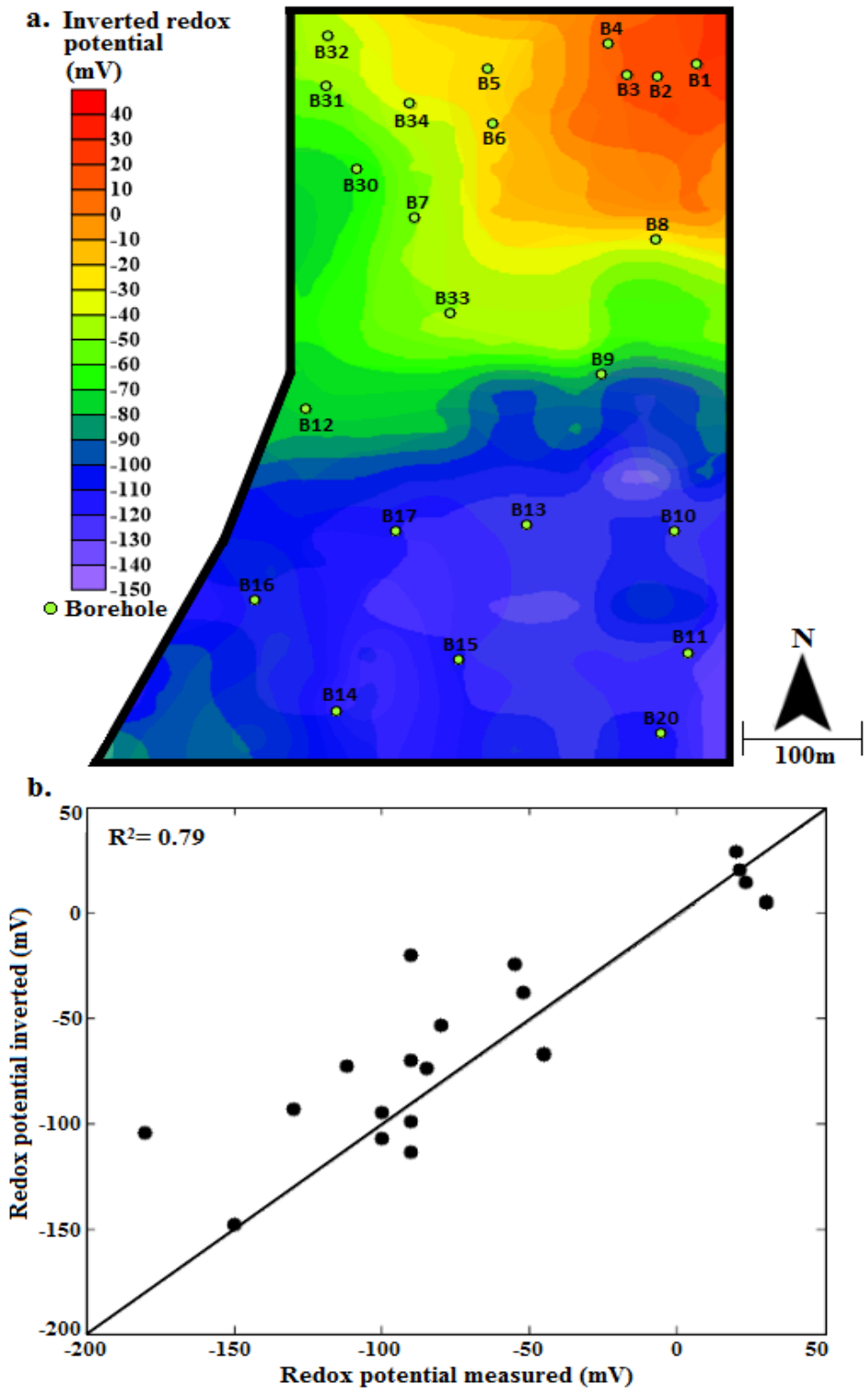

Figure 5.16: (a) The map of the predicted redox potential values obtained from the inversion of the residual self-potential data. (b) The linear correlation between the predicted redox potential values and the redox potential measured on boreholes showing a good correlation coefficient (R^2= 0.79).

Chapter 6

Magnetic Signatures of Hydrocarbon Contaminated Sediments (Paper 3)

Magnetic Signatures of Hydrocarbon Contaminated Sediments

M. Abbas[1], A. Jardani[1], M. Debret[1], S.Théodore[1] and J.P. Dupont[1]

(1) Université de Rouen, M2C, UMR 6143, CNRS, Morphodynamique Continentale et Côtière, Mont Saint Aignan, France.

Corresponding author: abbas_mohammad@live.com

Emails: abbas_mohammad@live.com; abderrahim.jardani@univ-rouen.fr; jean-paul.dupont@univ-rouen.fr: maxime.debret@univ-rouen.fr; solange.theodore@etu.univ-rouen.fr.

Abstract

Magnetic susceptibility and electrical resistivity methods were employed in order to investigate the effects of hydrocarbon contamination on the magnetic susceptibility of sediments at a contaminated petroleum refinery in Northern France. A shift of geoelectrical signature from resistive to conductive, together with geochemical analyses of groundwater and soil samples, indicated that biodegradation of hydrocarbons is occurring in the aquifer and transition zone contaminated sediments. We noticed that the magnetic susceptibility was much higher for hydrocarbon contaminated soil samples than for clean soil samples in the groundwater fluctuation zone. This magnetic susceptibility enhancement was attributed to iron transformation processes coupled to bacterial biodegradation of hydrocarbons. However, the contaminated and clean samples of the aquifer sediments showed the same low magnetic susceptibility despite the presence of oil contamination and biodegradation. This response was attributed to iron minerals dissolution which is favored in water saturated conditions. The shift of magnetic susceptibility and electrical resistivity was absent in the samples that were taken close to the contamination source which had high electrical resistivity and the same moderate magnetic susceptibility for clean and contaminated samples. The very high hydrocarbon content in these samples was thought to have produced a toxic environment for microorganisms, which suppressed the bacterial activity and prevented any significant shift in the geophysical signatures. Our results demonstrate that magnetic susceptibility of sediments can vary depending on the contamination extent, depth and sediment's biological conditions. Therefore, the combination of the magnetic susceptibility with electrical resistivity may provide a quick method to assess the hydrocarbon contamination, and to get primary information about the bacterial activity at our contaminated site.

6.1. Introduction

Hydrocarbon contamination of sediments remains a problem of major environmental concern. Cost-effective and fast methods are needed to continuously characterize the contaminated sediments and determine its chemical and biological properties. In the presence of hydrocarbon contamination, anaerobic Fe (III) reducing bacteria can use the hydrocarbons as a carbon source to transform iron oxides and hydroxides into crystalline Fe (II) containing different mineral phases. The reduction of iron oxides enhances the production of Fe (II) which in turn can react with Fe (III), HS^- or HCO_3 in the solution. This will result in the formation of different iron phase minerals such as magnetite, pyrite and siderite (Postma, 1981; Fredrickson et al., 1998). These biophysicochemical processes induce changes in the iron mineral content of soils and sediments that can display distinct magnetic susceptibility signatures (Kappler and Straub, 2005; Lovley and Anderson, 2000; Weber et al., 2006). Magnetic susceptibility (MS) of a natural material is a measure of its degree of magnetization in the presence of an external magnetic field and is directly proportional to the iron mineral content of sediments (Morris et al., 1994). The MS method has been used as an indicator of magnetic iron minerals and iron transformation processes at hydrocarbon contaminated sites, where the hydrocarbon biodegradation is coupled to iron reduction and organic carbon oxidation (Rijal et al., 2010, 2012; Mewafy et al., 2011).

Previous studies such as Hanesch and Scholger (2002) and Martins et al. (2007) observed a good correlation between hydrocarbons content and MS in hydrocarbon contaminated soil samples. After analyzing the MS variations in a hydrocarbon contaminated aquifer where iron reduction and methanogenesis are the main terminal electron acceptor processes, Mewafy et al. (2011) documented enhanced MS values associated with hydrocarbon contamination, and concluded that these enhancements are due to the precipitation of magnetite resulting from iron-reduction of bacterial anaerobic and aerobic processes. In a microcosm laboratory study, Porsch et al. (2010) investigated the variation of volume specific magnetic susceptibility with respect to the reduction of Ferrihydrite by Shewanella oneidensis MR-1 (iron reducing bacteria). The study reported a large initial increase of volume specific MS accompanied by an increase in the reduction of iron, followed by a slight decrease of MS at the end of the experiment. The X-ray diffraction patterns of the minerals formed during the reduction of Ferrihydrite showed that the initial increase of MS is associated with the formation of Magnetite. On the contrary, the slight decrease in MS was shown to be associated with the further reduction of magnetite to siderite; a paramagnetic mineral with low volume specific magnetic susceptibility. The increase in MS accompanied by the increase of iron reduction and magnetite formation occurred only in the microbial active microcosms, indicating microbial induced changes in the Fe-mineralogy which increased the MS.

The presence of hydrocarbons was essential for magnetite to form in a study done by Rijal et al. (2010), a clear decrease in the magnetite formation was observed outside the strongly contaminated zone. The enhanced magnetite formation in the contaminated zone was attributed to the intensive geo-microbiological activity. Given these studies, it was suggested that MS measurements are sensitive to microbial Fe transformation which can be coupled to hydrocarbons

biodegradation processes. Therefore, the MS method has high potential to serve as such less expensive and reliable tool to monitor oil contamination undergoing biodegradation coupled to iron transformation processes (Martins et al., 2007; Mewafy et al., 2011; Morris et al., 1994; Porsch et al., 2014).

During bacterial biodegradation of hydrocarbons, the attachment of microbial cells with large surface areas to mineral surfaces, and their alteration of the host environment through biogeochemical processes, can influence the grain surface resistivity (Atekwana and Atekwana, 2010). The biodegradation of hydrocarbons can increase the concentrations of total dissolved solids and groundwater electrical conductivity through minerals weathering processes and through adding ions directly into the solution (Sauck, 2000). These modifications can induce a change in the electrical resistivity signature from resistive in clean sediments to conductive in contaminated sediments (Atekwana et al., 2000; 2002; 2003; Werkema et al., 2000). Therefore, the electrical resistivity method is considered as an efficient tool in the study of hydrocarbon contaminated sediments and can be used as an indication of hydrocarbon biodegradation processes.

The main purpose of this study is to investigate the effects of hydrocarbon contamination and its consequent biodegradation on the magnetic susceptibility of sediments at a contaminated petroleum refinery in Northern France. The study aims to investigate the factors that might influence the MS response after examining samples taken from different depths and with different contamination extents. To achieve a better interpretation, the electrical resistivity method is used in combination with geochemical analyses of groundwater and soil samples to investigate the possible presence of hydrocarbon biodegradation, which could be coupled to iron transformation processes that can induce changes in the sediments iron content and magnetic susceptibility signatures.

6.2. Site description

The study site is an abandoned crude oil refinery located at 130 km North-West to Paris. The refinery which extends over an area of 260 hectares along the Seine River in the city of Petit Couronne was constructed in 1928. The site was contaminated by light non-aqueous phase liquid (LNAPL) and dense non-aqueous phase liquid (DNAPL) products due to leakage from tanks and pipelines. Three different contamination phases exist in the site subsurface including a dissolved phase, a free phase and a residual phase. Geologically, the site is characterized by the first 2 m being an anthropogenic layer mainly composed of sandy soil with coarse grain diameter gravels. Below, there is a layer of fine to medium sand coarsening to gravel with depth. This layer has an average thickness ranging from 8 to 25 m. The site is characterized by two aquifers: one alluvial unconfined aquifer located in the sand and gravel layer, between 4 and 11 m deep and a chalk aquifer at a depth ranging from 10 m to 25 m. A clean and a contaminated zone were identified according to the hydrocarbons content analyses of soil and groundwater that documented the presence of volatile and semi-volatile organic compounds such as benzene, toluene and xylenes.

6.3. Methods

Soil samples and cores

The soil samples were divided into 3 categories according to their sampling locations: category A, which contains soil samples taken from the zone located directly above the groundwater table (transition zone); category B, which contains soil samples taken from the water saturated zone and category C, which contains soil samples which were very close to the contamination source and were taken at a depth ranging between 0 and 2m. Additionally, two soil cores were taken from the zone above the groundwater table at two different locations. Core 1 is contaminated while core 2 is clean with no detected hydrocarbons. To determine the total hydrocarbons content, a series of analyses have been conducted on the soil samples:

(1) Methanol extraction and gas chromatography/mass spectrometry (GM/MS) to quantify the volatile C5-C10 hydrocarbons.

(2) Acetone extraction and gas chromatography with flame ionization detector (*GC-FID*) to quantify the total C10-C40 hydrocarbons.

(3) Head space gas chromatography/mass spectrometry (GM/MS) to quantify the BTEX and volatile organic compounds concentrations.

(4) Acetone/hexane extraction and gas chromatography/mass spectrometry (GM/MS) for the quantification of polycyclic aromatic hydrocarbons (PAH).

A Zeiss electron scanning microscope (SEM) was used to get images of the minerals surfaces in the order of 2µm and to perform chemical elemental composition analysis of soil samples by using the energy dispersive X-ray spectroscopy (EDX). To get information about the groundwater chemical parameters (e.g., total dissolved solids, groundwater electrical conductivity and dissolved oxygen), INW smart sensors were installed in the site boreholes. Additionally, *insitu* redox potential and PH measurements were done on groundwater samples.

Magnetic Susceptibility

The samples were preserved in coolers, oven dried, sieved and analyzed for MS by using a Bartington MS2 magnetic susceptibility system. The MS2 system relies on the change in the core permeability which changes the inductance in a wound inductor. Magnetic susceptibility is defined as the ability of a material to be magnetized in the presence of an external field. Therefore, the MS2 sensor operates on the principle of AC induction by supplying power to its oscillator circuit, which generates a low intensity alternating magnetic field. The oscillation frequency is determined by the inductance which is defined by the permeability of the material. The permeability $\boldsymbol{\mu_0}$ (permeability of free space in $N.A^2$) determines the inductance when the inductor contains only air. On the other hand, when the inductor is in contact with a soil sample, the inductance changes according to the change of the material permeability $\boldsymbol{\mu}$. The sensor measures the frequency values

of $\boldsymbol{\mu_0}$ and $\boldsymbol{\mu}$ and calculates the change in inductance which represents the relative permeability of a material ($\mu_r = \frac{\mu}{\mu_0}$). From the relative permeability $\boldsymbol{\mu_r}$, the MS meter calculates the volume magnetic susceptibility ($\boldsymbol{\chi_{vol}}$) from the following equation:

$$\chi_{vol} = \mu_r - 1.$$

The sensor was calibrated after each measurement to eliminate the thermally induced sensor drifts through obtaining a new $\boldsymbol{\mu_0}$ value which aims to reestablish the zero reference after each measurement. This was done through placing the sensor on the calibration cylinder and pressing the **Z** (calibrate) button after each measurement. To get high accuracy measurements, the sensor was kept 10 secs at each point until a stable value was reached. The measurement was repeated several times at each location, and the average of these measurements was considered as the MS value to be presented. For the soil cores, a measuring tape attached to the soil core was used to take the measurements at an interval of 0.5 cm.

6.4. Results and Discussion

The measurements of MS and electrical resistivity conducted on the soil samples showed different types of responses depending on the sampling location and contamination extent. Figure 6.1 shows the geophysical results of category A samples, which are samples that were situated at the groundwater fluctuation zone (referred to as the transition zone). The contaminated samples of category A recorded a total hydrocarbon content of approximately 20 mg/kg. We found that contaminated samples from category A had higher MS (100-250 SI) and lower electrical resistivity (50-100 Ω.m) in comparison to clean soil samples which exhibited values ranging from 2 to 10 (SI) for MS and from 300 to 400 (Ω.m) for electrical resistivity. In addition, soil core 1 taken from the same zone showed a transition of MS values from low (5-15 SI) in the clean sediments to higher values in the contaminated sediments (120-160 SI) (Figure 6.2a). The high values decreased to intermediate values (75-90 SI) starting from a depth of around 50 cm, where the blackish color which represents the hydrocarbon contamination decreased; indicating a decrease in MS values accompanied by the decrease in the contamination extent. On the other hand, the clean soil core (core 2) showed homogenous low MS values (2-15 SI) along the whole core (Figure 6.2b). To investigate the relationship between the observed MS values and the contamination extent, the MS values were correlated against the hydrocarbon content (Figure 6.3). As a result, a positive correlation was observed (R^2=0.80), indicating a direct relationship between the concertation of hydrocarbons and the MS values in the transition zone sediments.

The measurements of groundwater geochemical parameters shown in Table 1 demonstrated: increased total dissolved solids (TDS) concentrations (400-1000 mg/L); increased groundwater electrical conductivity (GEC) values (400-2000 µS/cm); negative redox potential values (-10 to -300 mV) and depleted dissolved oxygen concentrations within the contaminated zone boreholes. In contrast, lower TDS concentrations (100-300 mg/L), lower GEC values (<400µS/cm), positive

redox potential values (1-40 mV) and higher dissolved oxygen concentrations were observed in the clean zone boreholes. This observed contrast in the geochemical parameters values between the contaminated and clean zones provides evidence that biodegradation of organic matter is occurring at the site. Alterations of hydrocarbons by bacterial activity substantially modified the chemical and physical properties of the contaminated sediments and produced a dramatic shift in the electrical resistivity signatures from resistive in the clean state to conductive in the contaminated state (Sauck, 2000), as shown by the electrical resistivity results (Figure 6.1b). The transition zone has documented the highest values of bulk electrical conductivity in previous studies and was suggested to be the most biologically active in the presence of sufficient carbon source (Werkema et al., 2003).

The observed lower electrical resistivity values in the contaminated sediments compared to the clean sediments, in addition to the geochemical data, imply that biodegradation processes are occurring in the transition zone sediments. Our MS results support the findings of a study done by Rijal et al., (2010), who observed the highest MS in the top of the fluctuation zone at a hydrocarbon contaminated site. The MS measurements are sensitive to microbial iron transformation processes associated with the biodegradation of hydrocarbons in the biologically active transition zone. These processes could be responsible for the formation of iron minerals which enhanced the MS values of contaminated sediments in this zone. During Iron reduction coupled to biodegradation of hydrocarbons, Fe (III) is converted to Fe (II) which in turn can be oxidized by the protons of water to form magnetic minerals such as magnetite. Magnetite is considered as a Ferromagnetic material characterized by a high magnetic susceptibility (Mewafy et al., 2011). SEM images of samples taken from category A contaminated sediments show that mineral grain surfaces are intensively etched and pitted compared to images from uncontaminated soil samples (Figure 6.4). The remarkable dissolution features suggest intense mineral surface alteration by microbial processes in the contaminated sediments (Atekwana and Atekwana, 2010). In addition, the EDX data showed high iron peaks in the contaminated samples, whereas the data showed low Fe peaks in the clean soil samples (Figure 6.5).

To verify whether the enhanced MS values in the contaminated sediments are related to the degradation process and not directly to the presence of hydrocarbons, the clean soil core (Core 2) was contaminated by different fresh (not degraded) hydrocarbon products (benzene, diesel, toluene, etc..) and the MS measurements were repeated. The results of this experiment showed similar MS values to the previous measurement which was done on the same core in its clean state (Figure 6.6). The absence of MS values enhancement in the contaminated core suggests that this enhancement is related to the biodegradation processes of hydrocarbons and not to its direct presence.

Figure 6.7 shows the geophysical measurements done on soil samples of category B, which are mainly sediment samples that remained water saturated throughout the year. The contaminated samples of this category recorded a total hydrocarbon content similar to that of the category A samples, with concentrations of approximately 20 mg/kg. These samples exhibited low MS values

(5-20 SI) in both clean and contaminated samples. However, the clean samples recorded a significantly higher electrical resistivity (200-300 Ω.m) compared to contaminated samples (20-50 Ω.m). This electrical resistivity change in addition to the geochemical data indicate that biodegradation processes are occurring in the contaminated aquifer. Contaminated soil samples of category B had a much smaller MS in comparison to contaminated samples of category A, despite the presence of a similar amount of hydrocarbons. The total hydrocarbon content did not correlate well with the MS values (R^2=0.1) in the samples taken from the water saturated zone (Figure 6.8). The SEM images of contaminated sediments from this category showed similar weathering features to those occurring in the transition zone contaminated sediments (Figure 6.9). However, the EDX analysis didn't show any iron peaks in the contaminated sediments which recorded similar results as the clean sediments (Figure 6.10).

The low MS values of the contaminated sediments, the absence of a good correlation between the hydrocarbon content and MS and the absence of an iron peak in the EDX data despite the occurrence of bacterial biodegradation in the aquifer are probably attributed to the high mobility and to the complete water saturated conditions, which favors the dissolution of magnetic grains rather than the formation of new ones (Rijal et al., 2010). Support of this suggestion comes from studies such as Maher (1986), who documented lower MS values in soils that are seasonally water saturated. The authors suggested that the presence of organic matter in saturated and strongly reduced anoxic soils favors the depletion of magnetic minerals rather than the formation of new ones.

Soil samples of category C are samples that were situated in the top 2m soil layer and were taken close to the contamination source. The contaminated samples of this category had a dark blackish color due to the very high amount of total hydrocarbons which exceeded 10000 mg/kg. Both, hydrocarbon contaminated and clean samples exhibited similar MS values ranging from 20 to 50 SI (Figure 6.11a). On the other hand, electrical resistivity values ranging from 300 to 400 (Ω.m) were recorded in the clean sediments, whereas values ranging from 470 to 600 (Ω.m) were recorded in the contaminated sediments (Figure 6.11b). In contrast to the transition and saturated zones sediments which recorded a shift from high resistivity in clean sediments to lower resistivity in contaminated sediments, samples of this category recorded higher resistivity in contaminated sediments compared to clean sediments.

According to the insulating layer model, this response is attributed to the presence of non-degraded hydrocarbons (Benson et al., 1997; DeRyck et al., 1993). Hydrocarbons are considered as insulating materials having a higher electrical resistivity than the surrounding media in their natural non-altered state. The higher resistivity values in the contaminated sediments and the absence of the conductive electrical response indicate the absence of biodegradation processes at this location. As these samples had similar MS for both contaminated and clean sediments, and as they were taken from a very shallow depth, we expect that anthropogenic heavy metals input by atmospheric deposition which is common in industrial sites contributed to the slight enhancement of MS values, which is unlikely due to the bacterial activity as indicated by the electrical resistivity

results. The examination of metals concentrations in the samples of category C showed significant concentrations of Fe, Zn, Pb, Cu and Si, which may reflect the presence of anthropogenic metals contamination. Despite the presence of high amounts of hydrocarbons in the samples of category C, these geophysical responses are probably due to that the hydrocarbon concentration has been very high leading to a toxic effect on microorganisms. This can inhibit the biodegradation and the iron minerals transformation processes in these sediments. Note that, as the samples from categories A and B were taken from deeper depths, the influence of atmospheric deposition was neglected.

6.5. Conclusion

The study revealed a variable influence of hydrocarbon contamination on the MS measurements, depending on the sampling depth and sediments conditions. The electrical resistivity method constrained by geochemical measurements supported the MS investigations by providing an indication of biodegradation processes when recording a shift from high resistivity in clean sediments to lower resistivity in contaminated sediments. The highest MS values were recorded in the groundwater fluctuating zone contaminated sediments and were attributed to the enhanced bacterial activity at this zone as inferred from the electrical resistivity and geochemical measurements. The high mobility in the saturated zone, as well as the dissolution of magnetic minerals, might explain the low MS values recorded in the saturated zone sediments that had hydrocarbon content, electrical resistivity values and geochemical parameters concentrations similar to those of the transition zone sediments. The study also suggested that the very high hydrocarbons content produced a toxic environment for microorganisms and inhibited the biodegradation processes in the shallow (top soil) contaminated sediments. The slight MS enhancement in these sediments was attributed to anthropogenic atmospheric deposition of metals.

The presence of hydrocarbons in the contaminated sediments as a carbon source has played an important role and had a significant influence on the MS values due to the iron minerals transformation processes. Our results reveal that the combination of the magnetic susceptibility and electrical resistivity methods can be used to monitor the contamination, and can be considered as a proxy of bacterial activity in our contaminated site. However, the processes are complex and more field and laboratory chemical and biological studies (e.g., iron phases, bacterial populations, etc.) are required to complete this work. This will be done to precisely characterize the bacterial processes and the relationship between the different biological parameters and the magnetic susceptibility signatures.

6.6. References

Abdel Aal, G. Z., E. A. Atekwana, L. D. Slater, and E. A. Atekwana, 2004b, Effects of microbial processes on electrolytic and inter-facial electrical properties of unconsolidated sediments: Geophysical Research Letters 31, L12505, doi:10.1029/2004GL020030.

Atekwana, E. A., E. A. Atekwana, D. D. Werkema, J. P. Allen, L. A. Smart, J. W. Duris, D. P. Cassidy, W. A. Sauck, and S. Rossbach, 2004b, Evidence for microbial enhanced electrical conductivity in hydrocarbon-contaminated sediments: Geophysical Research Letters, 31, L23501, doi:10.1029/2004GL021359.

Atekwana, E.A. and E. A. Atekwana (2010). Geophysical Signatures of Microbial Activity: A Review. *Surv Geophysics*, 31, pp.247–283.

Fredrickson, J. K., J.M. Zachara, D.W. Kennedy, H. Dong, T. C. Onstott, N.W. Hinman, and S.M. Li (1998), Biogenic iron-mineralization accompanying the dissimilatory reduction of hydrous ferric oxide by a groundwater bacterium, Geochim. Cosmochim. Acta, 62, 3239–3257.

Hanesch, M. and R. Scholger (2002). Mapping of heavy metal loadings in soils by means of magnetic susceptibility measurements. *Environmental Geology*, 42(8), pp.857–870. Available at: http://link.springer.com/10.1007/s00254-002-0604-1.

Kappler, A., and K. L. Straub (2005), Geomicrobiological cycling of iron, in Molecular Geomicrobiology, vol. 59, edited by J. F. Banfield, J. Cervini-Silva, and K. H. Nealson, pp. 85–108, The Mineralogical Society of America, Chantilly, Va.and K. H. Nealson, pp. 85–108, The Mineralogical Society of America, Chantilly, Va.

Lovley, D.R. and R. T. Anderson (2000). Influence of dissimilatory metal reduction on fate of organic and metal contaminants in the subsurface. *Hydrogeology Journal*, 8(Iii), pp.77–88.

Maher, B. A. (1986). Characterization of soils by mineral magnetic measurements. *Phys Earth Planet Inter*, 42, pp.76–92.

Martins C.C., M. M. Mahiques, M. C. Bícego, M. M. Fukumoto, and R. C. Montone, 2007. Comparison between anthropogenic hydrocarbons and magnetic susceptibility in sediment cores from the Santos Estuary, Brazil. *Mar. Pollut. Bull.*, **54**, 240□246.

Mewafy, F. M., E. A. Atekwana, D. D. Werkema Jr., L. D. Slater, D. Ntarlagiannis, A. Revil, M. Skold, and G. N. Delin (2011), Magnetic susceptibility as a proxy for investigating microbially mediated iron reduction, Geophys. Res. Lett., 38, L21402, doi: 10.1029/2011GL049271.

Morris W.A., Versteeg J.K., Marvin C.H., McCarry B.E. and Rukavina N.A., 1994. Preliminary comparisons between magnetic susceptibility and polycyclic aromatic hydrocarbon content in sediments from Hamilton Harbour, Western Lake Ontario. Sci. Tot. Environ., 152, 153□160.

Naudet, V., A. Revil, E. Rizzo, J. Y. Bottero, and P. Bégassat, 2004. Groundwater redox conditions and conductivity in a contaminant plume from geoelectrical investigations. Hydrol. Earth Syst. Sci. 8, 8–22. Doi: 10.5194/hess-8-8-2004.

Postma, D. (1981), Formation of siderite and vivianite and the pore-water composition of a recent bog sediment in Denmark, Chem. Geol., 31, 225–244.

Porsch K., M. L. Rijal, T. Borch, L. D. Troyerd, S. Behrensa, F. Wehlande, E. Appel, A. Kappler, 2014. Impact of organic carbon and iron bioavailability on the magnetic susceptibility of soils. *Geochimica et Cosmochimica Acta*, 128, pp.44–57.

Porsch K., U. Dippon, M. L. Rijal, E. Appel, A. Kappler, 2010. In-situ magnetic susceptibility measurements as a tool to follow geomicrobiological transformation of Fe minerals Environ. Sci. Technol., 44 (2010), pp. 3846–3852.

Rijal M. L., E. Appel, E. Petrovský , and U. Blaha, 2010. Change of magnetic properties due t fluctuations of hydrocarbon contaminated groundwater in unconsolidated sediments. *Environ. Pollut.*, **158**, 1756□1762.

Sauck, W. A., 2000. A conceptual model for the geoelectrical response of LNAPL plumes in granular sediments: Journal of Applied Geo-physics, 44, 151–165.

Weber, K. A., L. A. Achenbach, and J. D. Coates, 2006. Microorganisms pumping iron: anaerobic microbial iron oxidation and reduction. *Nature reviews. Microbiology*, 4(10), pp.752–764.

Werkema, D. D., E. A. Atekwana, W. A. Sauck, S. Rossbach, and J . Duris, 2000. Vertical Distribution of Microbial Abundances and Apparent Resistivity at an LNAPL Spill Site. Proc. Symp. Appl. Geophys. to Eng. Environ. Probl. 669–678.

Werkema, D. D., E. A. Atekwana, A. Enders, W. A. Sauck, and D. P. Cassidy, 2003. Investigating the geoelectrical response of hydrocarbon contamination undergoing biodegradation: Geophysical Research Letters, 30, 1647, doi:10.1029/2003GL017346.

Figures

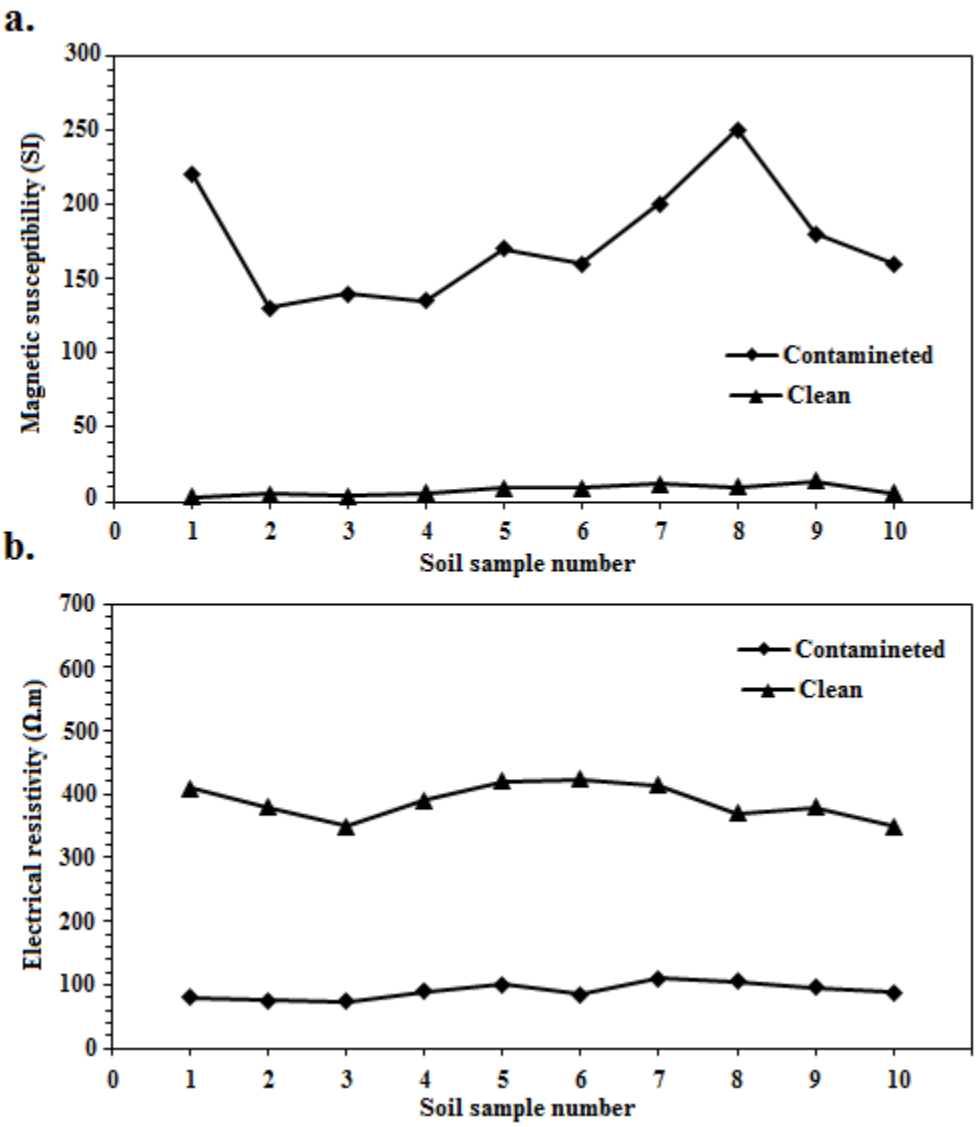

Figure 6.1: Plot of the magnetic susceptibility (a) and electrical resistivity (b) of clean and contaminated soil samples from category A, which were sampled from the transition zone.

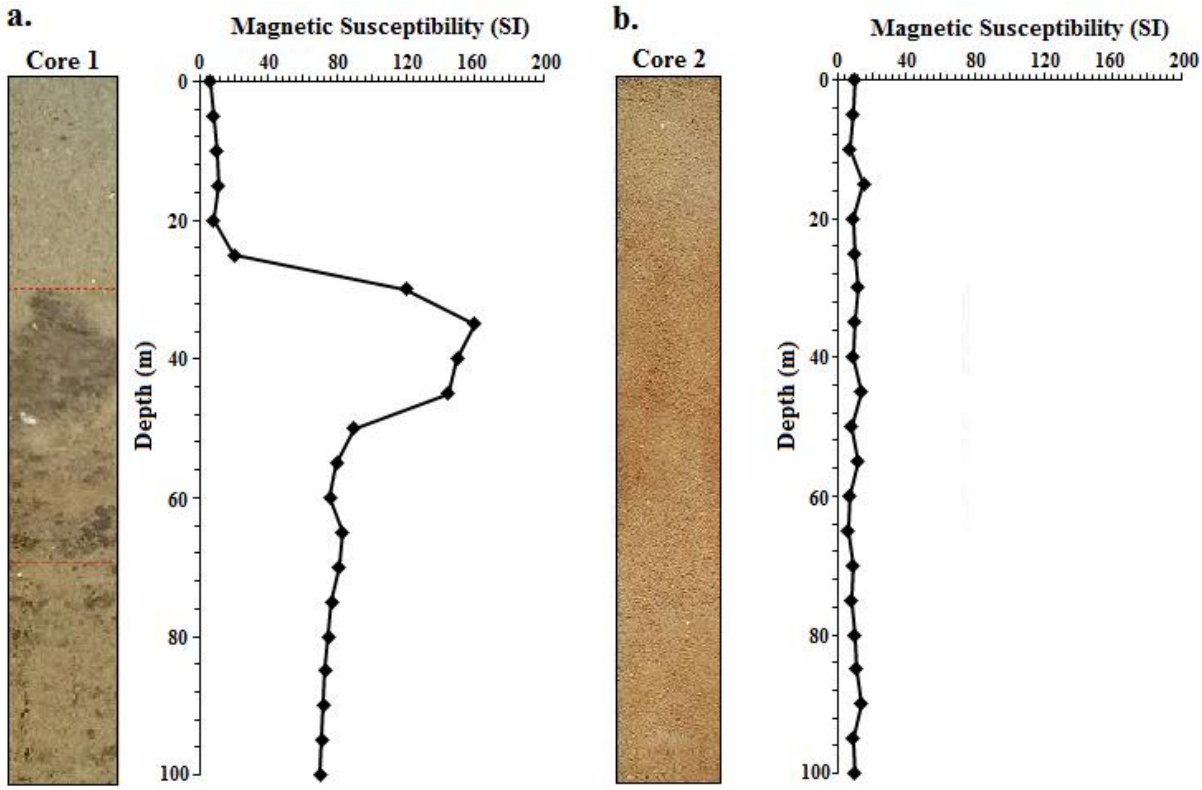

Figure 6.2: Magnetic susceptibility results of contaminated (a) and clean (b) soil cores taken from the transition zone. The figure shows higher MS values in the presence of hydrocarbon contamination (represented by blackish colored sediments).

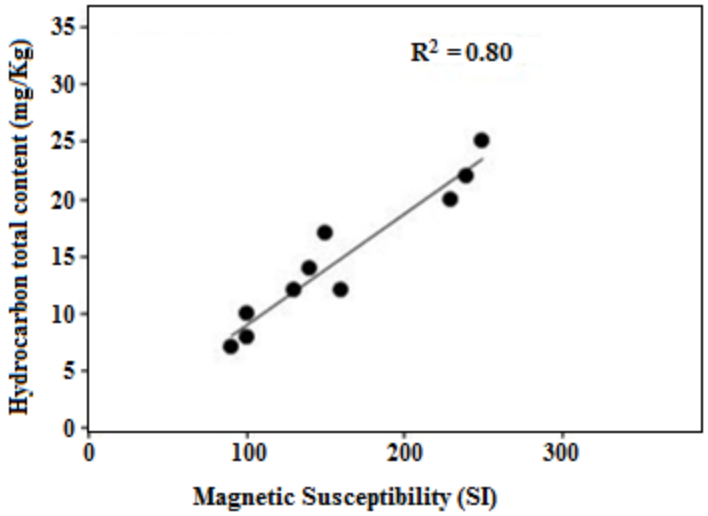

Figure 6.3: The correlation between the hydrocarbons content and the magnetic susceptibility of category A soils samples. A good correlation with a determination coefficient (R^2) of 0.80 was observed.

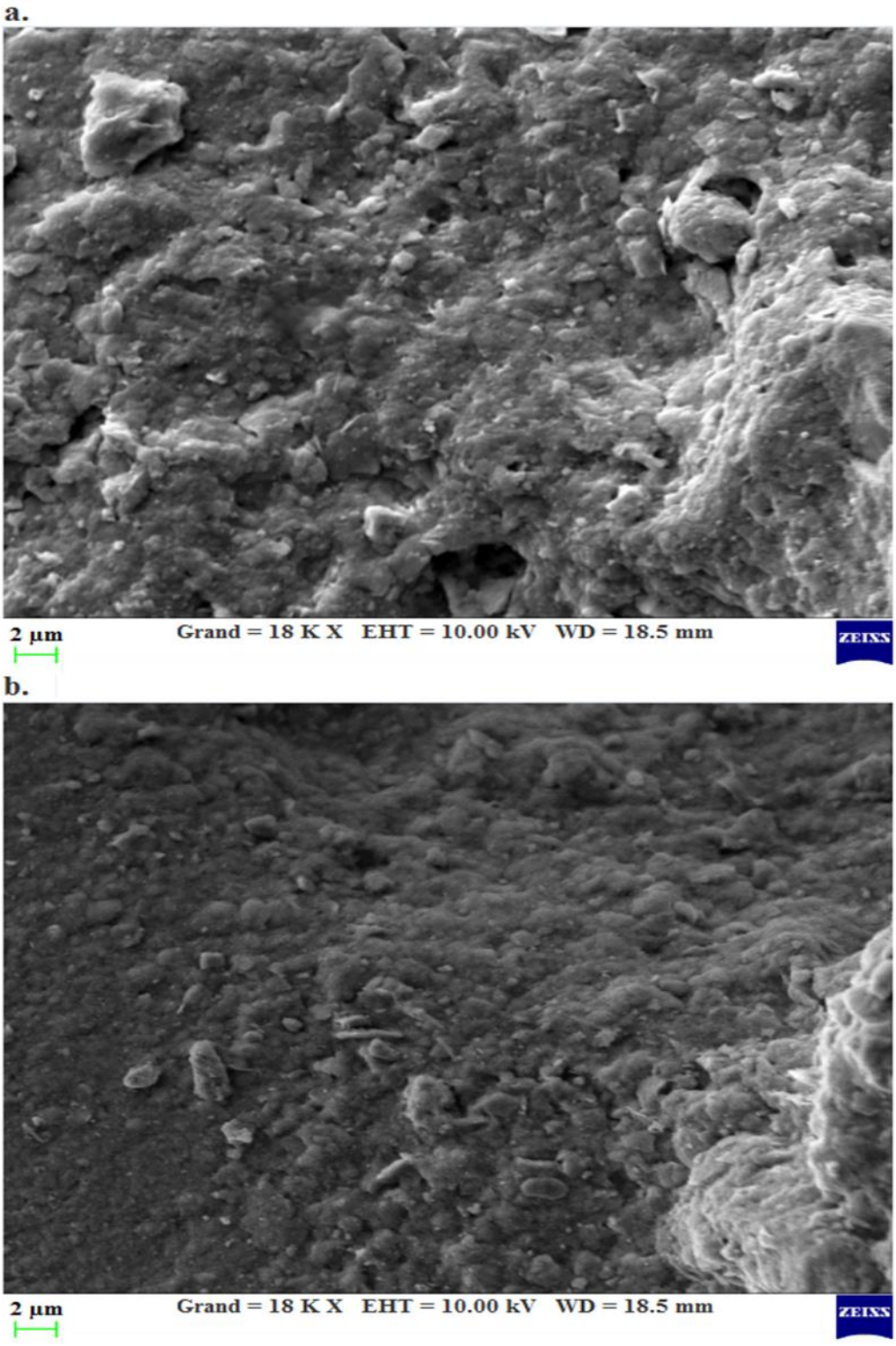

Figure 6.4: Scanning electron microscope images if a contaminated (a) and a clean (b) soil sample taken from the transition zone (category A). The images show etched pits and mineral weathering features in the contaminated sample.

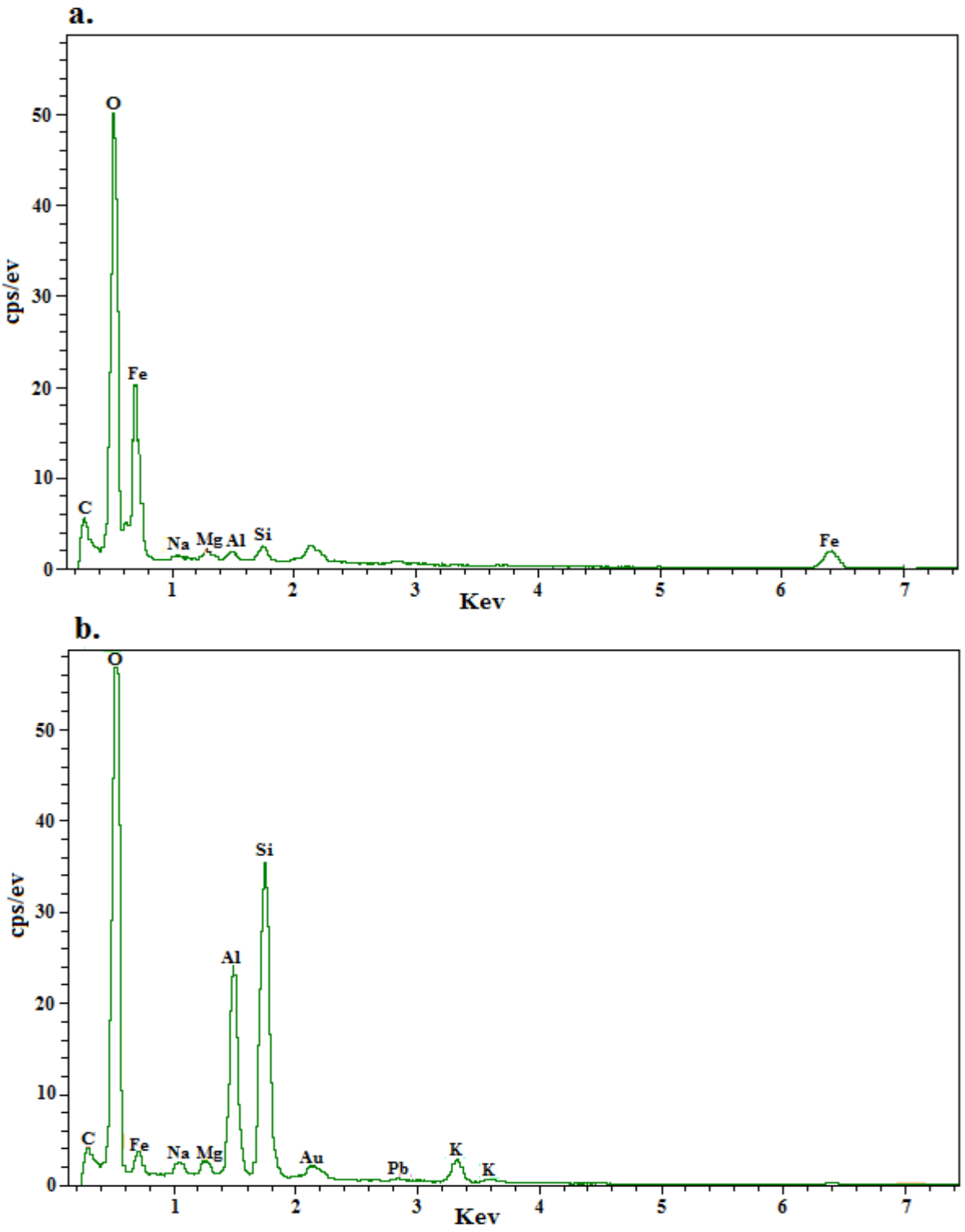

Figure 6.5: EDX analysis results of a contaminated (a) and a clean (b) soil sample taken from the transition zone. The results show higher iron (Fe) peaks in the contaminated sample.

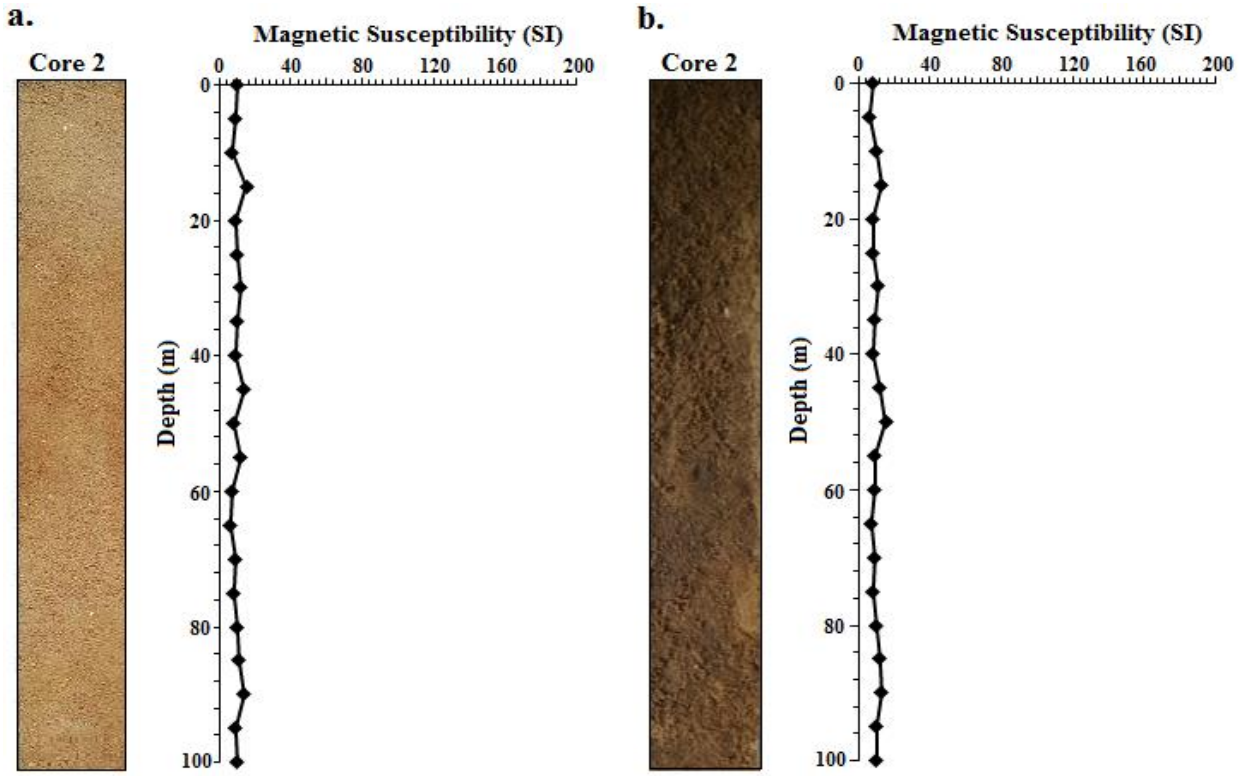

Figure 6.6: Core 2 before (a) and after (b) the addition of fresh hydrocarbons. The results show similar MS values before and after the addition of hydrocarbons to the clean soil core which was taken from the transition zone.

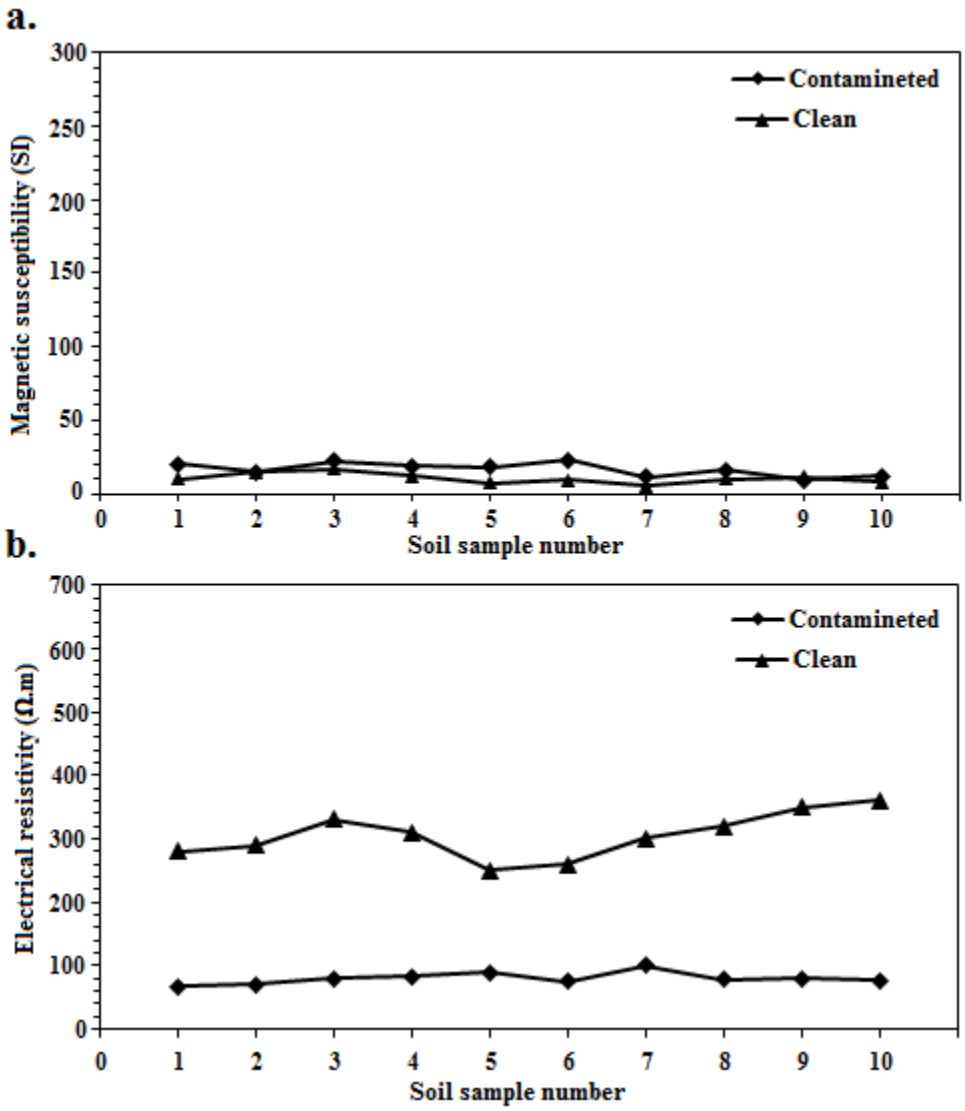

Figure 6.7: Plots of Magnetic susceptibility (a) and electrical resistivity (b) of clean and contaminated samples of category B, which were taken from the aquifer.

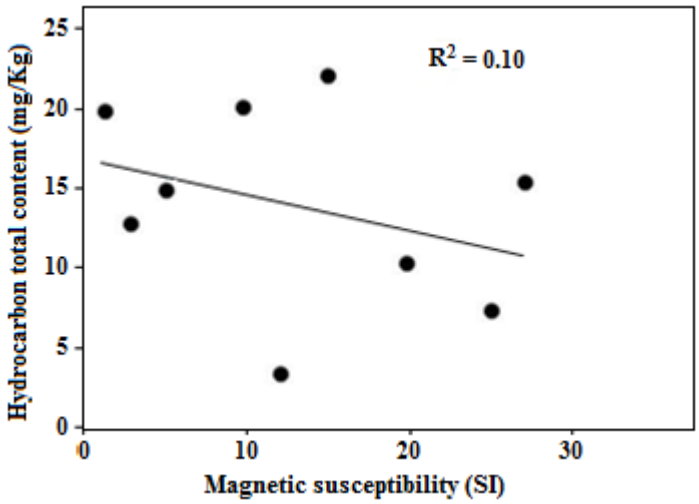

Figure 6.8: Linear scatter plot between the magnetic susceptibility and the total hydrocarbons content of category B samples. R^2 denotes the coefficient of determination which was determined to be very small (0.10).

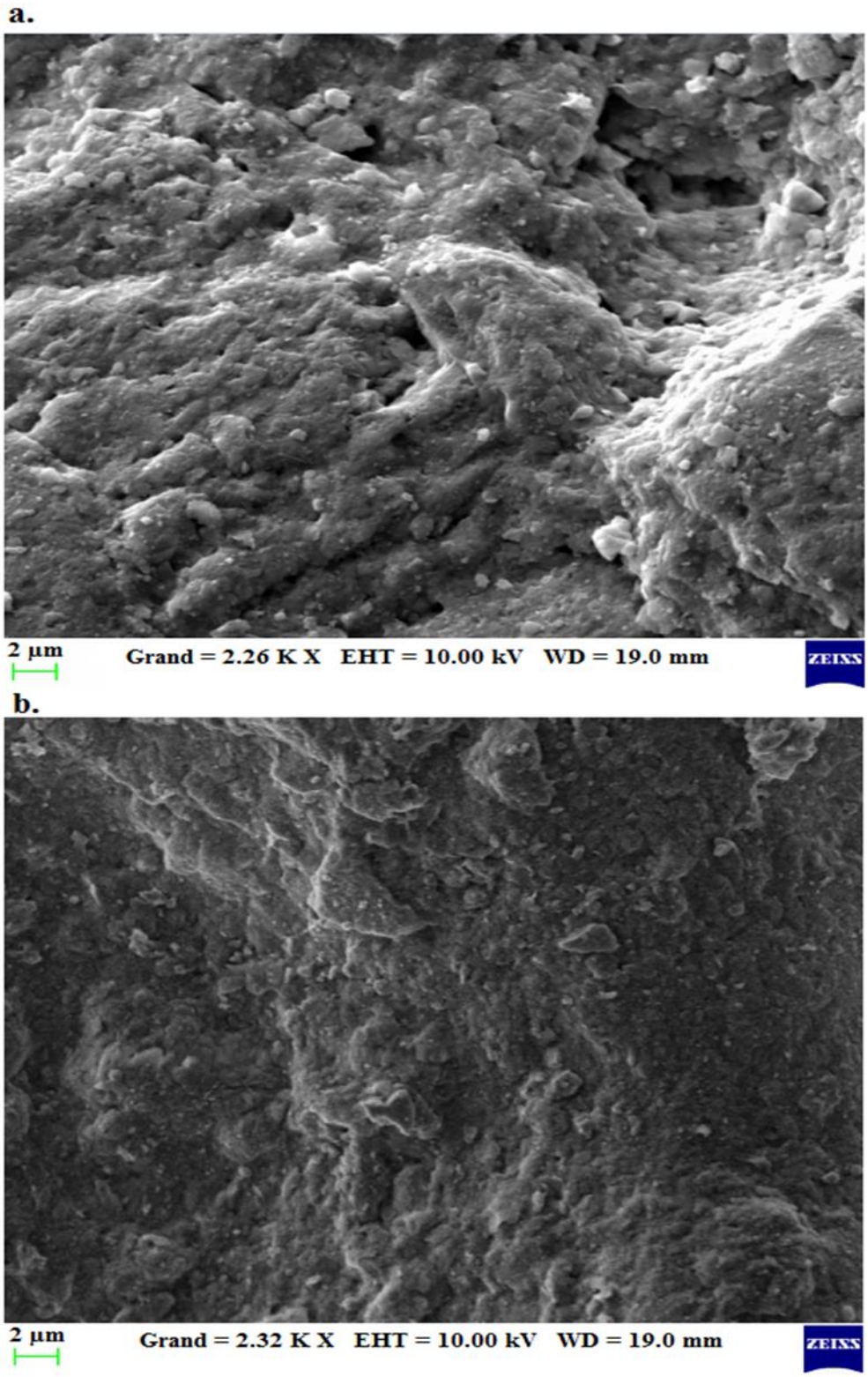

Figure 6.9: Scanning electron microscope images of a contaminated (a) and a clean (b) soil sample taken from the aquifer. The images show etched pits and minerals weathering features in the contaminated sample.

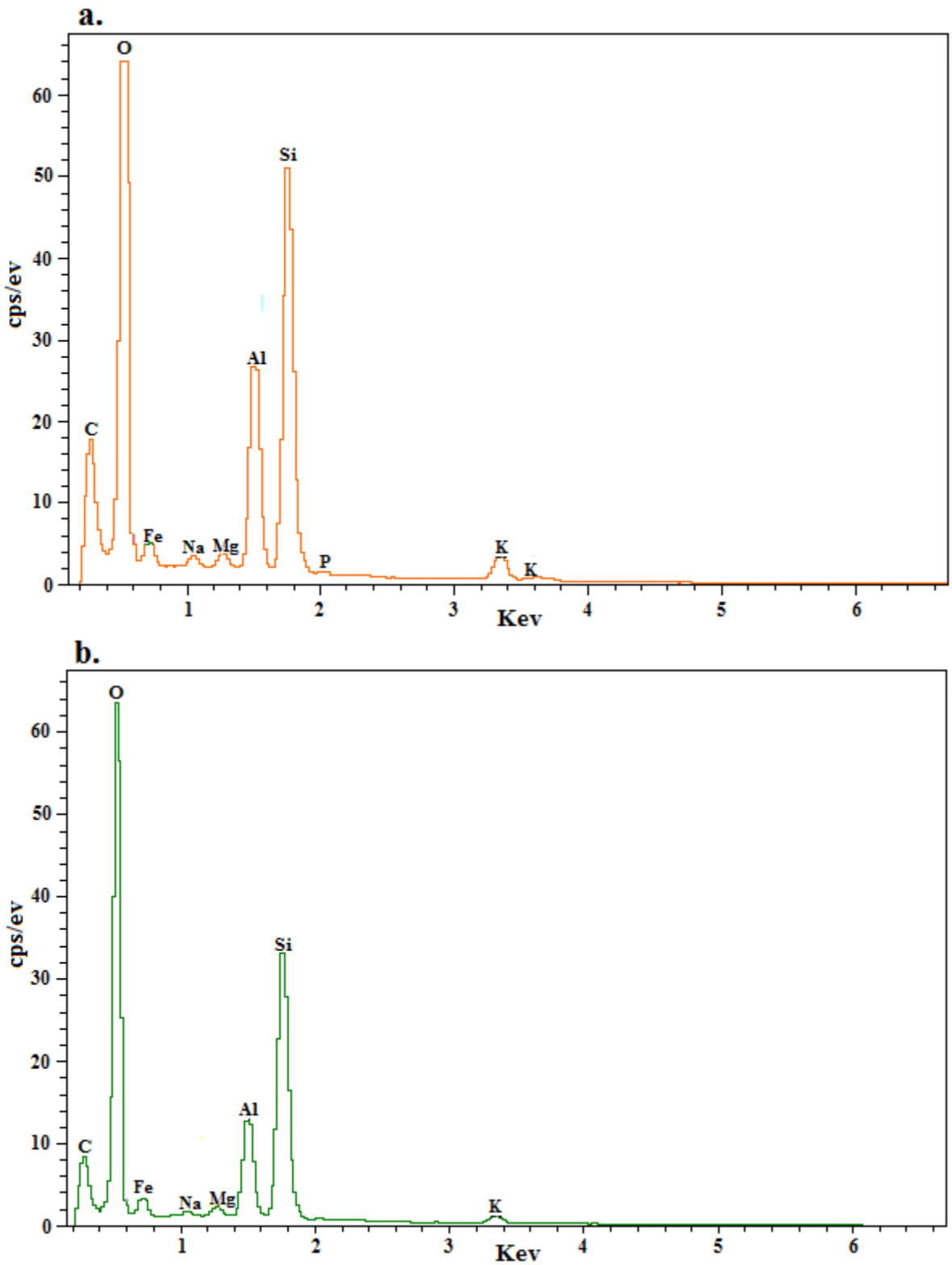

Figure 6.10: EDX analysis results of a contaminated (a) and a clean (b) soil sample taken from the aquifer. The results show similar elements composition in both samples.

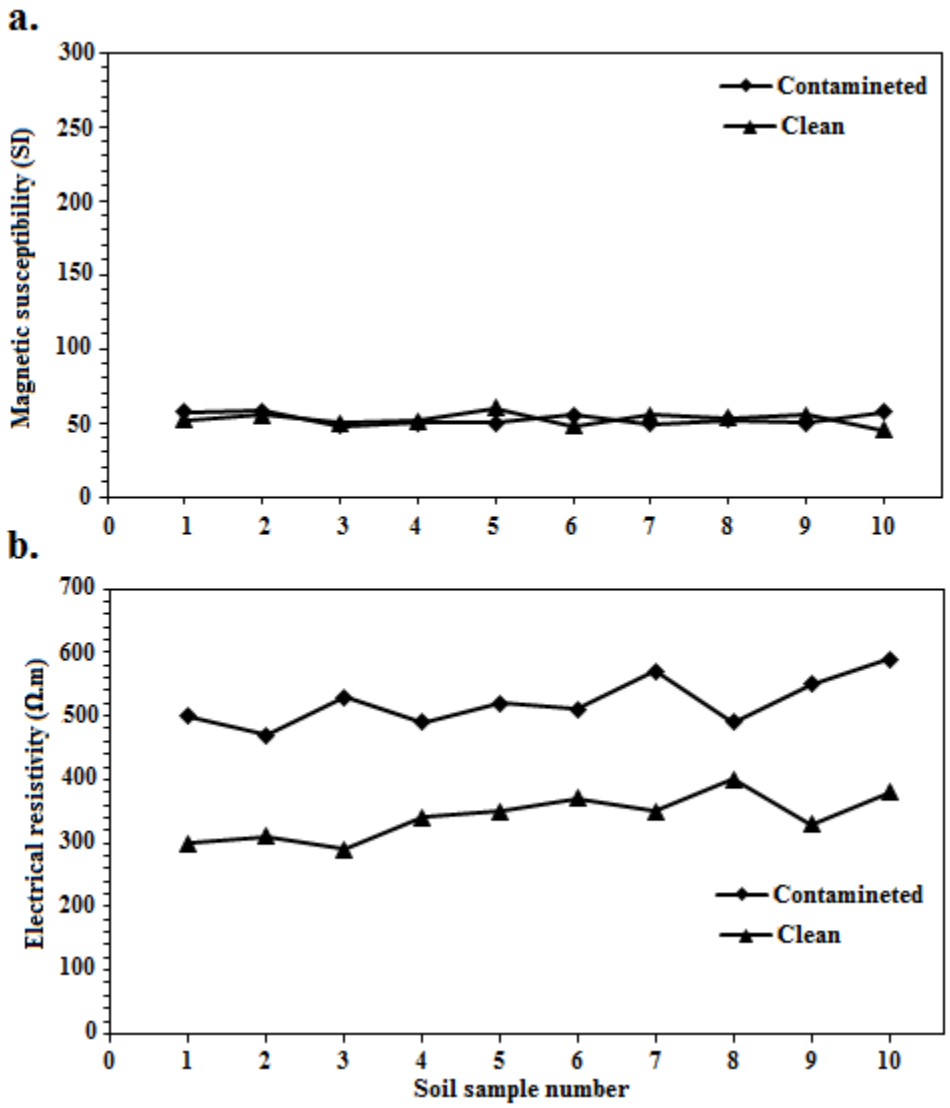

Figure 6.11: Plot of magnetic susceptibility (a) and electrical resistivity (b) of clean and contaminated samples from category C, which were sampled close to the surface.

Table 1: Geochemical parameters of groundwater in contaminated and clean zones boreholes. The data shows higher values of parameters such as the total dissolved solids (TDS) and groundwater electrical conductivity (***σ***) in the contaminated boreholes compared the clean ones. The data also show positive redox potential in the clean boreholes and negative redox potential in the contaminated boreholes.

Borehole	*Zone*	*Eh (mV)*	*O2 (mg/L)*	*TDS (mg/L)*	σ_e *(µS/cm)*	PH
B1	Clean	22	≈ 2	228	456	7.41
B2	Clean	21	≈ 2	220	450	7.12
B7	Contaminated	-26	0.53	992	1983	6.39
B8	Contaminated	-75	0.79	440	880	6.71
B9	Contaminated	-119	-	380	761	6.44
B11	Contaminated	-87	0.9	328	656	6.66
B12	Contaminated	-220	-	404	809	6.33
B13	Contaminated	-149	-	361	722	6.07
B15	Contaminated	-83	0.4	433	856	6.31
B20	Contaminated	-100	-	556	1112	6.72

Chapter 7

Application of the GPR method for mapping subsurface utilities and planning boreholes installations

7.1. Introduction

Oil contamination of the shallow subsurface is a major problem of environmental concern. Boreholes installation is considered as a crucial step for delineating contamination plumes, studying the groundwater properties and proceeding with the remediation processes. Gathering information about the shallow subsurface utility infrastructure is important for safe and cost-effective boreholes installation. Non-destructive and accurate techniques are therefore needed to acquire knowledge about the shallow structures which could affect the boreholes installation and produce any potential hazards during the process. Geophysical methods have been shown as effective and non-destructive techniques which could explore the shallow subsurface in a fast and accurate way. Among all geophysical methods, the GPR is considered as the most efficient tool which can be used for utility detection and has been extensively used for a variety of applications including archeological, hydrogeological and civil engineering investigations (Enes et al., 2010; Jeng et al., 2011).

The GPR uses high frequency electromagnetic waves to detect subsurface features whose electromagnetic properties differ from those of the surrounding media. Numerous successful applications of the GPR which successfully detected buried utilities in the shallow subsurface have been documented (e.g., Cheng et al., 2013; Metwaly, 2015; Reynolds et al., 1997). However, the application of the GPR in industrial areas characterized by intensive urban activities is still a challenge because of the complicated infrastructure, which could contain noise sources that can impact the acquired data. The GPR method is less effective in heterogeneous environments and in conductive media such as clayey soils, which can decrease the penetration depth through introducing conductive absorptive losses which can cause the attenuation of the GPR signal (Cassidy, 2007).

In this study, we applied the GPR method to produce a map of potential safe positions of boreholes locations, which will be used for the remediation process in the contaminated petroleum refinery of Petit-Couronne. The shallow subsurface in this site is characterized by the presence of different types of utilities including, electrical cables, pipelines and concrete slabs at a depth ranging from 30 to 200 cm. There exist no accurate background information about the utilities in this area, therefore the GPR was used to locate the existing utilities before starting the boreholes installations process in order to avoid any potential problems such as pipelines and cables destruction. This study also aims to reduce the drilling cost by reducing the number of non-successful attempts which could result from the presence of such utilities. The electrical resistivity tomography method was also used to get more information about the geological structures of the study area.

7.2. Boreholes planning and GPR data acquisition

The study zone extends over an area of 5600 m^2 in the center of the refinery (Figure 7.1). An initial plan of boreholes locations was established with a number of 20 boreholes having a distance of approximately 10 m between each. Figure 7.2 shows the initial boreholes locations plan and the GPR profiles conducted across these locations. 17 vertical and horizontal GPR profiles were conducted using a Mala Geoscience X3M radar system coupled to a shielded antenna. Antennas with central frequencies of 250 MHz and 100 MHz were used. A recording tape was used to accurately measure the distance along the surveyed profiles and the radar antenna was moved along the profiles lines which were delineated by the measuring tape. For data acquisition, we used a wheel mode with a recording interval of 0.10 meters, time windows of 70 ns and 200ns (in order to get information from deeper sources), and a number of 512 stacks per trace. Each profile was repeated in the reverse direction for higher data accuracy.

Figure 7.1: The location of the study zone (Google Earth). The study zone is located in the center of the refinery and covers an area of around 5600 m^2.

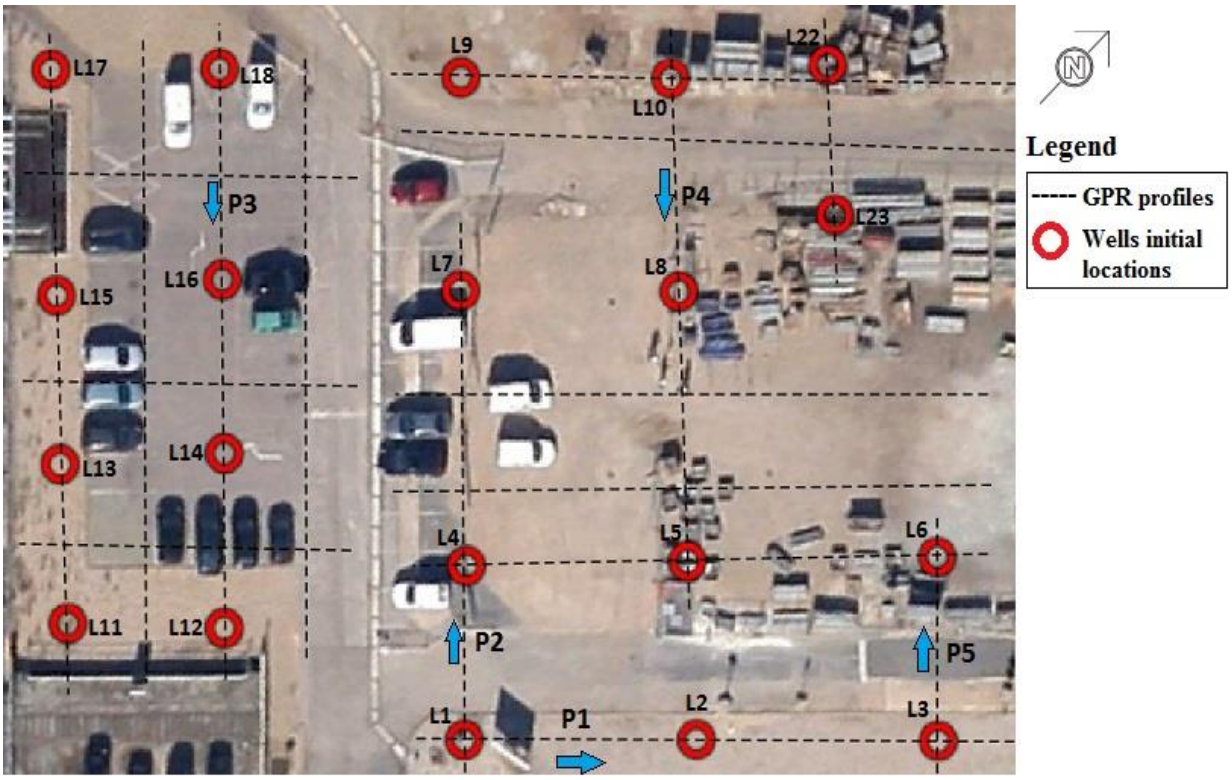

Figure 7.2: Well initial locations map. The red circles show the wells locations and the blue arrows show the direction of the GPR profiles.

7.3. Data processing

The data processing process was started by a dewow filtering to remove the initial direct current signal. This was followed by a time-zero correction to overcome the time zero point jump caused by equipment instability. This step is done to find the true ground surface reflection. The traces were multiplied by a gain function to overcome the effects of geometrical spreading losses and improve the visual quality of the data by enhancing the low amplitude reflections. Filtering the data constituted of applying a band pass filter that improves the signal quality by improving the signal to noise ratio. This step has to be done carefully to avoid signal alterations which can result in removing reflections that represent subsurface structures. According to the information observed in the amplitude spectra of the raw data, a band pass filter of 150 MHz to 250 MHz was applied to the profiles which were acquired by using the 250 MHz antennae. Whereas, a 50 MHz to 150 MHz band pass filter was applied to the profiles acquired by using the 100 MHz antenna. The mean velocities of the electromagnetic waves were estimated by: (1) velocity adaptation through fitting the continuous reflections with the geological layers identified by the ERT profiles and available geological data, and (2) by determining the velocity through fitting hyperbolic reflections originating from point sources.

7.4. Results and discussion

The profiles showed a complex pattern with reflections from different subsurface utilities buried in the shallow part of the subsurface (0-1 m). These reflections included responses from pipes, cables, concrete slabs and interfaces such as the interface between the filling and the original soils. The profiles showed many hyperbolic reflected signals which correspond to buried pipes. Based on the size of the hyperbola, we could classify two types of buried pipes as follows: (1) the wider hyperbolas correspond to reflections from large diameter oil pipes and (2) and the narrower hyperbolas correspond to smaller diameter water supply pipes. The reflections from buried pipes were recorded in profiles P1, P2, P4 and P5. Profile 1 showed the hyperbolic reflections at x=8m, x=13 m and x=21 m, at a depth ranging from 0.8 to 1.2 m (Figure 7.3). The wide hyperbolic reflection below location L2 corresponds to a large diameter oil supply pipe. Therefore the L2 location was marked as “bad location”. The straight continuous reflector at a depth of 1.5 m corresponds to the interface between the surface dry sandy gravel layer and the below contaminated sand humid layer. This was validated by the geological and ERT data which showed a change in sediments and electrical resistivity values at the same depth (Figure 7.4). The lower resistivity values which appear below this interface corresponds to humid contaminated sediments. As discussed in the previous chapters, the hydrocarbon biodegradation processes are considered to be responsible for the soil elevated electrical conductivity, which limited the penetration depth of the GPR.

Another important feature observed along the GPR profiles P2, P3, P4 and P5 is characterized by a strong large diameter ringing reflection starting at a shallow depth (Figures 7.5, 7.6 and 7.7). This ringing pattern corresponds to buried concrete slabs. The reflections from subsurface electrical cables are those observed in profiles P2 and P4, and characterized by strong multiple reflections that extend to the maximum depth of investigation. Several excavations were done to validate our interpretations and relate the observed reflections to the buried utilities. Figure 7.8 shows an excavation done at x=10 m along profile P5 showing a buried concrete slab at a depth of around 1m. This observation agreed well with the position of the wide ringing reflection in the GPR profile which started at the same depth. Another two excavations were done at x= 8 m and x= 13 m along profile P1 (Figure 7.9). These excavations showed two types of buried pipes (oil and water pipes) reflected in the GPR profile as narrow and wide hyperbolic reflections.

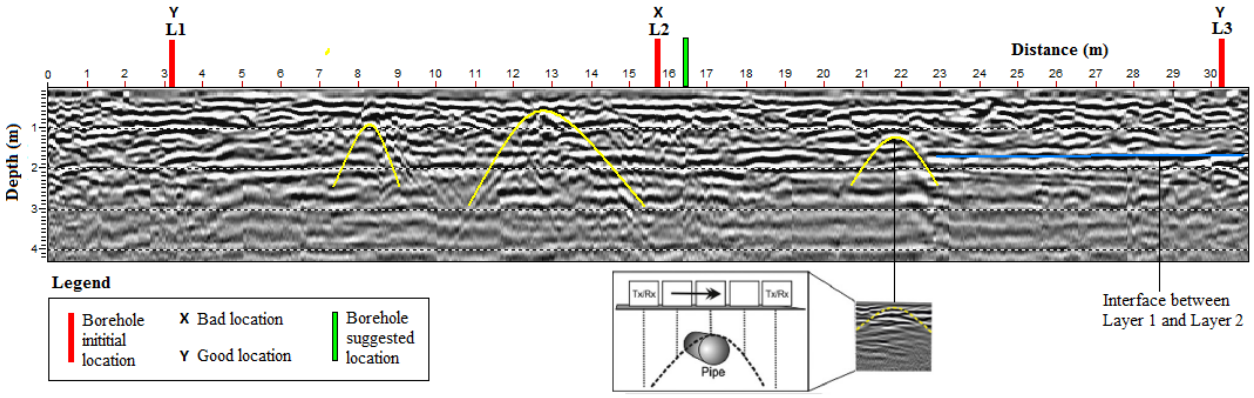

Figure 7.3: GPR profile acquired along profile P1. The GPR profile shows several hyperbolic reflections corresponding to buried water and oil supply pipes (reflection template adapted from Metwaly et al., 2015).

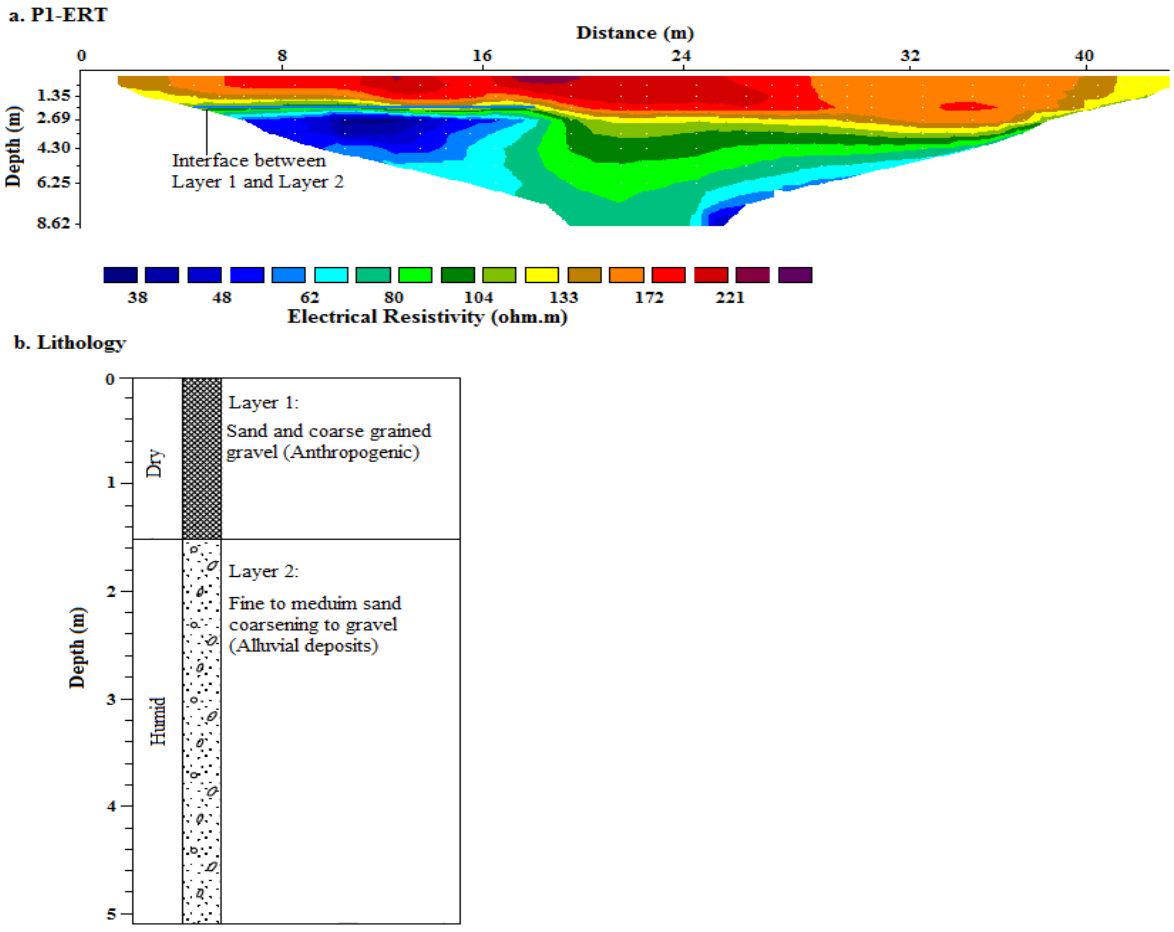

Figure 7.4: ERT profile (a) and geological data (b) acquired along profile P1. The blue line in the ERT profile represents the interface between layers 1 and 2 which are shown in the lithology profile.

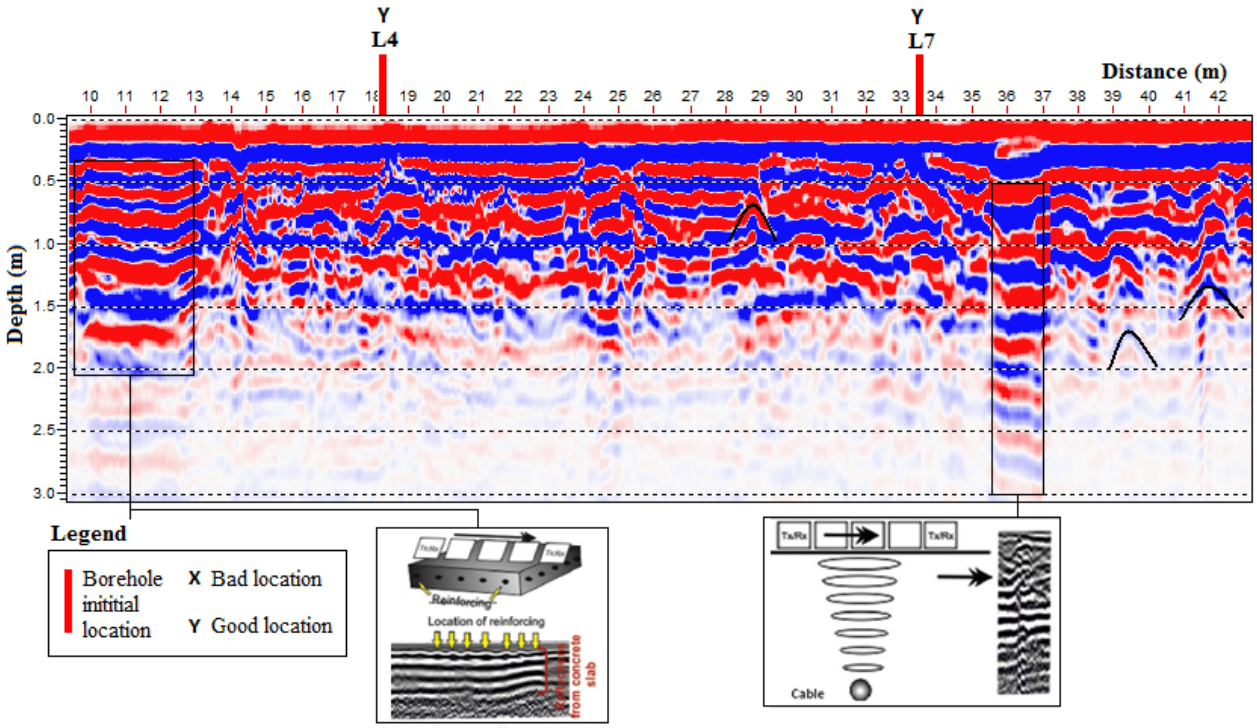

Figure 7.5: GPR profile P2 showing ringing reflections from a buried concrete slab and from an electrical cable (the reflections templates are adapted from Metwaly et al., 2015).

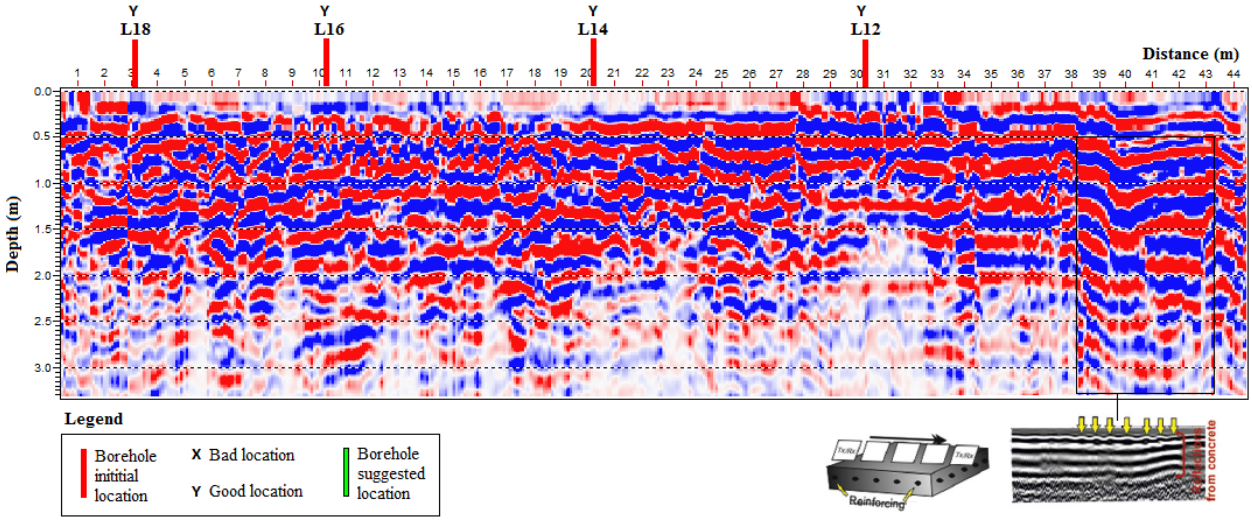

Figure 7.6: The GPR profile P3 showing ringing reflections from a buried concrete slab (the reflections templates are adapted are from Metwaly et al., 2015).

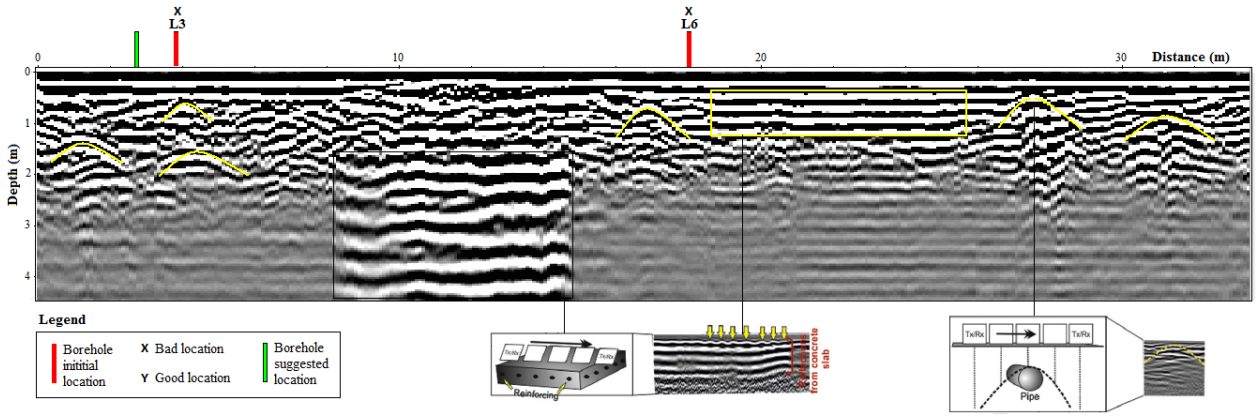

Figure 7.7: The GPR profile P5 showing reflections from buried concrete slabs and pipes (the reflections templates are adapted from Metwaly et al., 2015).

Figure 7.8: An excavation done along profile P5 showing a buried concrete slab at a depth of around 1m.

a. Large diameter oil pipe

b.Small diameter water pipes

Figure 7.9: Excavations done along profile P1 showing buried water and oil supply pipes. The narrow hyperbolas in the GPR profiles represent the water supply pipes while the wide hyperbolas represent the oil pipes.

7.5. New boreholes locations

According to the GPR profiles, we could state whether the initial locations of the boreholes are suitable or not. The locations were marked unsuitable when observed to be above or close to a

buried utility. In this case, the initial locations were moved to a position where we have no reflections from buried utilities in the GPR profiles. Therefore, according to the obtained results, locations L2, L3, L6, L10 and L17 were moved on the new locations map as shown in Figure 7.10.

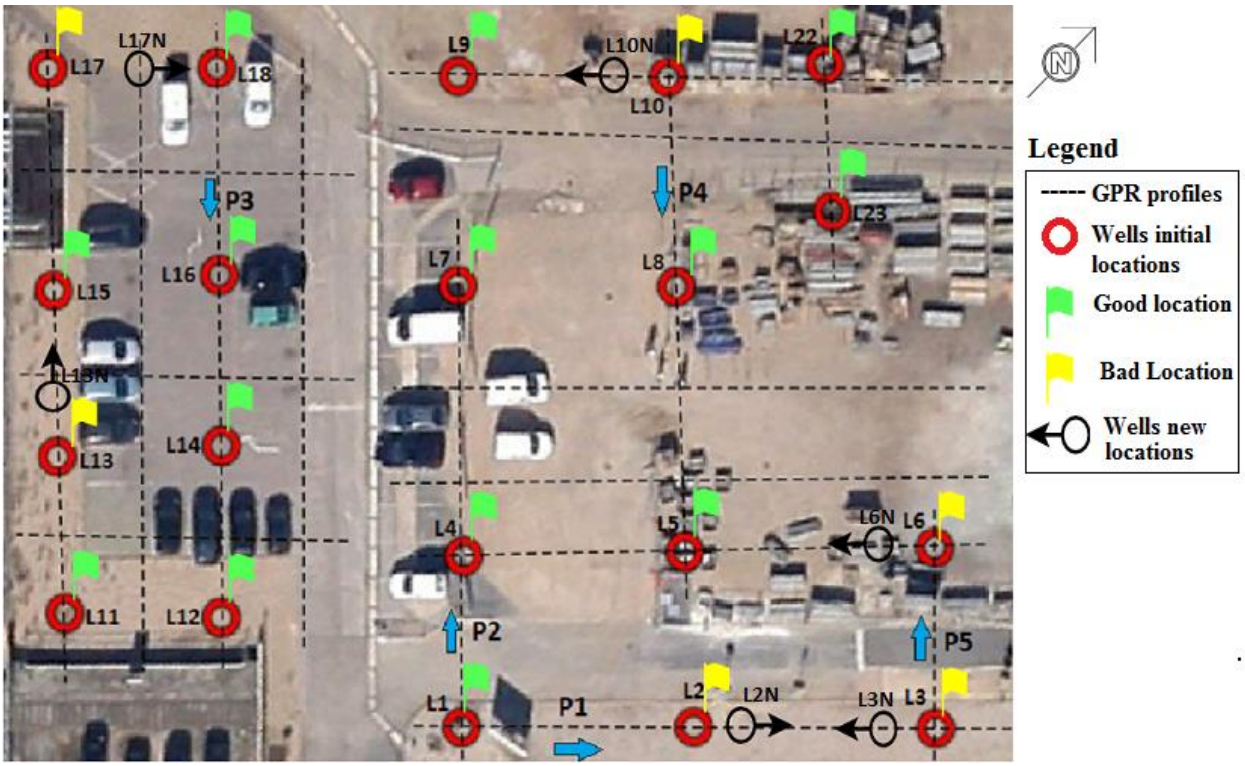

Figure 7.10: New boreholes locations map according to the GPR data. The green and yellow flags correspond to good and bad locations respectively and the blue arrows show the direction of the GPR profiles. The Letter N corresponds to the new location and the black arrows represent the direction in which the initial locations were moved.

7.6. References

Cassidy, N. J., 2007. Evaluating LNAPL contamination using gpr signal attenuation analysis and dielectric property measurements: Practical implications for hydrological studies. Journal of Contaminant Hydrology, 94, 49–75.

Cheng, N. F., H.C. Tang, and C. Chan, 2013. Identification and positioning of underground utilities using ground penetrating radar (GPR), Sustainable Environmen. Res. 23 (2013) 141–152.

Enes, Y., D. Sevket, and O. Caner, 2010. On the imaging application of ground penetrating radar, in: Proceedings of the URSI International Symposium on Electromagnetic Theory, Berlin, Germany, 16–19 August, 2010.

Jeng, Y., C. H. Lin, Y. W. Li, C. S. Chen, and H.M. Yu, 2011. Application of sub-image multiresolution analysis of ground penetrating radar data in a study of shallow structure, J. Appl. Geophys. 73 (2011) 251–260.

Metwaly, M., 2015. Application of GPR technique for subsurface utility mapping: A case study from urban area of Holy Mecca, Saudi Arabia Measurement 60 (2015) 139–145.

Reynolds, J. M., 1997. An Introduction to Applied and Environmental Geophysics, John Wiley & Sons, Chichester.

Chapter 8

Conclusion

The application of geophysical methods for monitoring hydrocarbon contaminated sites has been the subject for many research activities in the last two decades. This is driven by the need for obtaining large scale spatial data, given that the classical geochemical investigations are expensive, time consuming and provide only small scale point measurements. However, the application of geophysical methods to contaminated sites could face many obstacles. One of which is getting access to such sites, despite the presence of numerous contaminated sites in Europe and particularly in France. This could be due to confidentiality issues and to conflicts between the different scientific and engineering communities (e.g., environmental engineers, geochemists, geophysicists, etc.), as each one of them has his own language, understandings and theories. Therefore, the application of geophysical methods in this thesis was limited to the one site which we could have the access to; the refinery of Petit-Couronne.

The main objective of this work was to contribute to the development of the application of geophysical methods to hydrocarbon contaminated sites investigations. In this sense, the objective of this thesis was to characterize the hydrocarbon contamination and investigate its effects on the soil and groundwater geophysical and geochemical properties in an abandoned petroleum refinery contaminated by different hydrocarbon products (e.g., LNAPL and DNAPL products). For that, five geophysical methods including ERT, GPR, IP, SP and MS were applied and combined with geochemical data acquired from the site boreholes. The comparison between the contaminated and clean zones showed that the contamination changed the chemical and biological properties of soil and groundwater. This was shown through recording increased TDS concentrations, increased groundwater electrical conductance, a change of redox potential values from positive to negative, increased ions concentrations and depleted concentrations of electron acceptors such as oxygen, nitrate and sulfate.

These geochemical changes, which are evidences of microbial biodegradation of hydrocarbons were reflected in the different geophysical signatures. Generally, the geophysical responses recorded by the different methods supported the findings of Sauck (2000), who suggested that biological alterations of hydrocarbons can substantially modify the pore water biogeochemistry, producing a temporal shift in the geoelectrical signature from resistive to conductive. Apparently, the leaching of soluble salts and the mineral dissolution processes associated with the production of organic acids during the biodegradation of hydrocarbons increased the TDS concentrations, and as a result, increased the groundwater electrical conductivity. These modifications in the chemical properties of pore fluids modified the ohmic and capacitive parts of the electrical conduction in contaminated sediments. This was reflected as an increase of electrical conductivity and chargeability in the zones impacted by the dissolved phase of the contamination. A change of the electrical resistivity signature form resistive in the clean background aquifers ($\approx$300 Ω.m) to conductive in the contaminated aquifers (<50 Ω.m) was observed. The ERT and IP methods provided information about the extent of the contamination in the aquifer due to the dissolved phase, where the low resistivity anomalies extended to a depth of around 23m. Thus these methods can be used to obtain spatial information on the groundwater

quality and chemical conditions. Furthermore, the increase in the soil electrical conductivity effected the GPR measurements which showed attenuated reflections amplitudes (shadow zones) in the zones impacted by the residual phase of the contamination.

The changes in groundwater redox chemistry due to the utilization of electron acceptors during the redox processes were reflected in the SP data, where an active biogeobattery process was suggested to be present in the contaminated portion of the site. This natural geobattery was created due to the existence of a strong redox potential gradient between the highly reducing conditions within the plume and the oxidizing conditions outside the plume. This created a driving force for the self-potential electrochemical signal. A residual self-potential map was first produced through removing the electrokinetic component from the observed self-potential signals. This was done by calibrating a groundwater flow model to compute the spatial distribution of the Darcy velocity, which was used to calculate the streaming potential; referred to as the electrokinetic component of the SP signal. An inversion algorithm was then used to obtain the current density components from the residual self potential data. The horizontal components were determined to be very small compared to the vertical component of the source current density which was used to construct a redox potential map of the site. Therefore, vertical dipoles distributed across the capillary fringe were suggested to be responsible for the redox effect in the SP signal. A good correlation was shown between the predicted redox potential values and redox potential values measured independently in a set of wells. This good correlation illustrates the ability of the self-potential method to delineate the borders between the contaminated and clean zones according to the contrast in the redox conditions created due to the biodegradation process.

The iron minerals transformation processes, particularly the precipitation or iron minerals was reflected as changes in the magnetic susceptibility signature. The MS measurements recorded variable values according to the sediments biological conditions and depth. The biologically active transition zone exhibited high MS values in contaminated locations compared to clean ones. This response was attributed to the precipitation of iron minerals coupled to the biodegradation process which was evidenced by the geochemical and electrical resistivity measurements. On the other hand, low MS values were observed in the contaminated aquifer sediments, despite the occurrence of biodegradation, evidenced by the electrical resistivity values and geochemical parameters concentrations. This response was attributed to the dissolution of magnetic minerals and their high mobility in the saturated zone. The top soil layer showed no differences in MS values between contaminated and clean sediments. This was explained by the absence of biological activity at this zone due to the presence of a very high hydrocarbons content, which produced a toxic environment for the microorganisms. Therefore, the presence of hydrocarbons in the contaminated sediments as a carbon source has played an important role and had a significant influence on the MS values due to the iron minerals transformation processes.

Throughout this study, the geochemical and geophysical data were in great agreement. The geophysical methods consistently showed the same behavior in the contaminated zones where biodegradation is occurring as inferred from the geochemical data. The contaminated zones

(according to hydrocarbon concentrations analyses done on groundwater samples) recorded lower resistivity anomalies and negative redox potential values compared to the clean zone which recorded higher resistivity values and positive self potential values. Therefore, the hydrocarbon contamination of groundwater was delineated according to the geophysical contrast between the contaminated and clean zones. The plume borders, which were delineated according to the geophysical data were in great agreement with the boreholes geochemical data, as the borders of the contaminated zone were detected between the contaminated and the clean boreholes.

The given results illustrate the ability of geophysical methods to characterize and delineate the contamination at the site. The combination of the different geophysical methods reduced the ambiguity in the interpretations by recording consistent results that showed a clear geophysical contrast between contaminated and clean zones. Additionally, this combination provided insight on the different processes that might have modified the contaminated sediments chemical and biological properties. By using these 5 methods, it will be possible to follow the remediation process and assess the changes in groundwater geochemical properties over time. This will be done through observing the temporal evolution of the geophysical signatures (Figure 8.1).

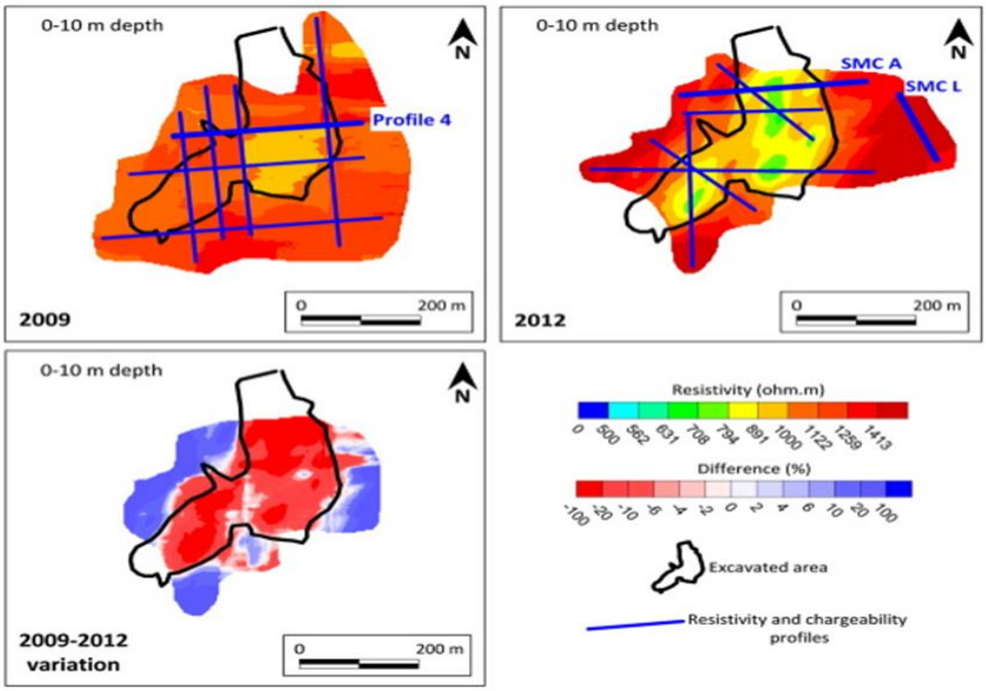

Figure 8.1: An example showing the variation of electrical resistivity over time at a hydrocarbon contaminated site (Blondel et al., 2014).

This approach, combined with few geochemical point measurements will help evaluate the remediation process and delineate the contaminant plume evolution in a time-lapse manner. As the GPR proved to be more sensitive to small changes in the bulk electrical conductivity occurring in the contamination residual phase, this method will be first used to locate the unknown source zones through high-resolution scanning of the site. Then time-lapse GPR measurements will be used to

follow the changes of electrical conductivity in the residual zones as the remediation proceeds. The SP method proved to be sensitive to changes in the redox conditions which are in turn related to the contaminant distribution in groundwater. Therefore, fixed SP electrodes connected to an automated system will be used to follow the evolution of the contaminant plume over time.

Besides, it is necessary to conduct laboratory experiments in parallel to the field ones in order to better understand the geoelectrical response of each type of contaminant, and to fully understand the associated biological and chemical mechanisms. It is also important to define the duration and concentration at which the different hydrocarbon compounds alter the sediments biogeochemical properties and consequently the geophysical signal. For this purpose, a sand box experiment has been constructed to follow the evolution of the geophysical response with respect to the contaminant type and concentration, and with respect to the variations of the different geochemical parameters (Figure 8.2).

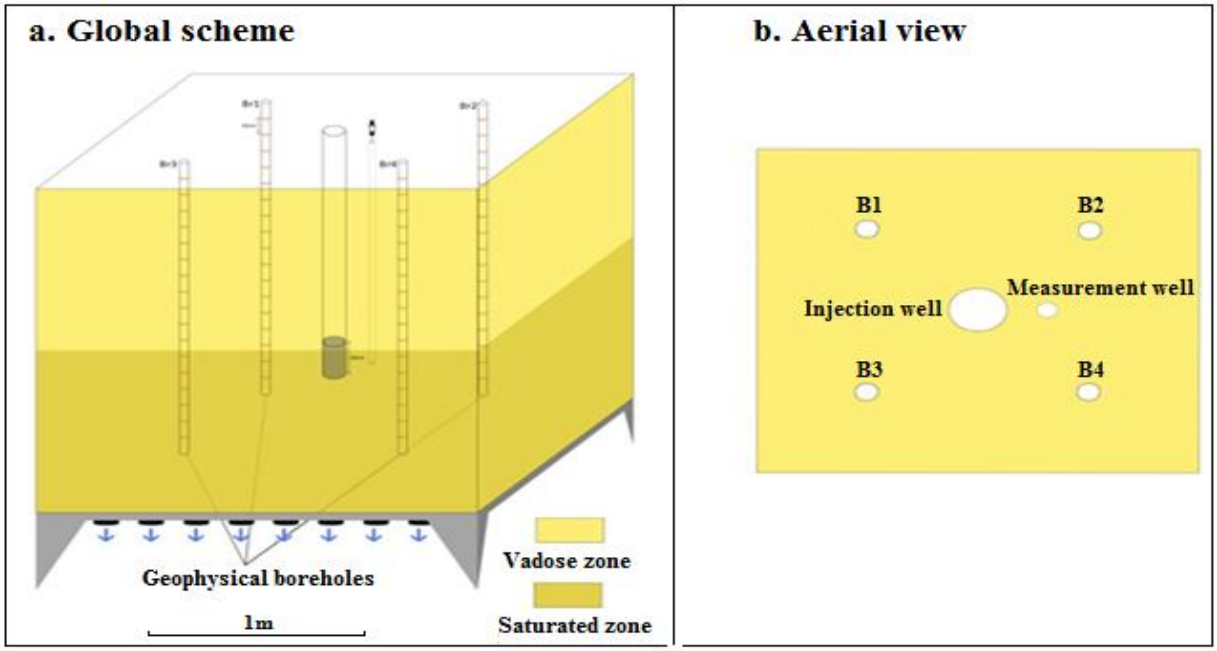

Figure 8.2: The global scheme and the aerial view of the sand box experimental setup. The setup constitutes of a sand box containing a saturated and a non-saturated zone and 5 boreholes which will be used for the geophysical and geochemical measurements.

The sand-box simulates field conditions with a saturated and a non-saturated zone and contains boreholes which enable high-resolution imaging of the electrical resistivity vertical changes. The sandbox will be injected by an oil spill extracted from the site contaminant plume and the biological conditions in the sandbox will be monitored by adding a mix of bacterial populations and nutrients to activate the biodegradation process. The temporal effects of the contamination on the geoelectrical response will be followed by conducting time-lapse geophysical and geochemical measurements.

Another obstacle which faces the application of geophysical methods at contaminated sites is the noise which can be produced in the geophysical data when acquired at industrial sites. This

problem was a subject of research for many studies which aimed to improve the quality of such data by improving the signal to noise ratio. The numerous field geophysical measurements conducted during this thesis could lead to improving the methodology (e.g., acquisition, processing, interpretation, etc.) of geophysical data acquired in industrial sites. However, more efforts should be done to improve the quality of geophysical measurements on the field. An example would be working on the development and the use of boreholes measurements. Conducting geoelectrical measurements in boreholes allows acquiring data with higher vertical resolution and a better signal to noise ratio. Moreover, this kind of measurements could be done in boreholes which were initially installed for geochemical and hydrogeological monitoring of the site. This approach will increase the choices for geophysical methods in terms of setup (surface or borehole) and resolution (vertical and horizontal). This will make it possible to extend the scope of geophysical methods and overcome the obstacles encountered at urban sites. By applying the different geophysical techniques at both the laboratory and field scales, combined with geochemical investigations, contamination diagnoses and remediation monitoring can be more efficient and less time consuming.

Appendices

Journal of Hydrology 554 (2017) 111–127

Contents lists available at ScienceDirect

Journal of Hydrology

journal homepage: www.elsevier.com/locate/jhydrol

Research papers

Redox potential distribution of an organic-rich contaminated site obtained by the inversion of self-potential data

M. Abbas [a], A. Jardani [a,*], A. Soueid Ahmed [b], A. Revil [b], L. Brigaud [a], Ph. Bégassat [c], J.P. Dupont [a]

[a] Université de Rouen, M2C, UMR 6143, CNRS, Morphodynamique Continentale et Côtière, Mont Saint Aignan, France
[b] Université Savoie Mont Blanc, CNRS, IRD, IFSTTAR, ISTerre, F-73000 Chambéry, France
[c] Agence de l'environnement et de la maîtrise de l'énergie (ADEME), 20 avenue du Grésillé, BP 90406, 49004 Angers cedex 1, France

ARTICLE INFO

Article history:
Received 4 July 2017
Received in revised form 28 August 2017
Accepted 30 August 2017
Available online 21 September 2017
This manuscript was handled by P. Kitanidis, Editor-in-Chief, with the assistance of Niklas Linde, Associate Editor

Keywords:
Self-potential
Inverse problem
Contaminated site
Redox potential
Hydrogeophysics, biogeophysics

ABSTRACT

Mapping the redox potential of shallow aquifers impacted by hydrocarbon contaminant plumes is important for the characterization and remediation of such contaminated sites. The redox potential of groundwater is indicative of the biodegradation of hydrocarbons and is important in delineating the shapes of contaminant plumes. The self-potential method was used to reconstruct the redox potential of groundwater associated with an organic-rich contaminant plume in northern France. The self-potential technique is a passive technique consisting in recording the electrical potential distribution at the surface of the Earth. A self-potential map is essentially the sum of two contributions, one associated with groundwater flow referred to as the electrokinetic component, and one associated with redox potential anomalies referred to as the electroredox component (thermoelectric and diffusion potentials are generally negligible). A groundwater flow model was first used to remove the electrokinetic component from the observed self-potential data. Then, a residual self-potential map was obtained. The source current density generating the residual self-potential signals is assumed to be associated with the position of the water table, an interface characterized by a change in both the electrical conductivity and the redox potential. The source current density was obtained through an inverse problem by minimizing a cost function including a data misfit contribution and a regularizer. This inversion algorithm allows the determination of the vertical and horizontal components of the source current density taking into account the electrical conductivity distribution of the saturated and non-saturated zones obtained independently by electrical resistivity tomography. The redox potential distribution was finally determined from the inverted residual source current density. A redox map was successfully built and the estimated redox potential values correlated well with *in-situ* measurements.

1. Introduction

The increasing public concern with groundwater contamination problems has generated significant research activity, which aims to support the contaminant plumes characterization and remediation efforts (e.g., Rao et al., 2002; Craun et al., 2010). The redox potential is considered as a key-parameter for the characterization of organic-rich contaminant plumes because bacteria derive their energy through oxidizing organic carbon for their growth and reducing terminal electron acceptors (usually oxygen) for their respiration (Christensen et al., 2000; Tiehm and Schulze, 2003; Semple et al., 2007). Bacterial activity induces significant changes in the redox environment by playing the role of catalysts (Atlas, 1981; Revil et al., 2010; Atekwana and Atekwana, 2010; Vayenas, 2002). The consumption of electron acceptors by bacterial biodegradation processes in an organic-rich contaminant plume causes a change in the redox chemistry of the groundwater. Baedecker et al. (1993) have shown that the area within the plume is quickly becoming reducing and anoxic, whereas the area outside the plume is oxidizing and oxic.

Mapping the redox potential by classical geochemical methods is invasive (i.e., requiring boreholes), expensive and provides only scarce information. In addition, these measurements are time-consuming as they require a lot of precautions to avoid perturbing local equilibria by the introduction of oxygen. The need for cost-effective and fast methods to continuously characterize the contaminated groundwater has increased the interest of the

* Corresponding author.
E-mail addresses: abbas_mohammad@live.com (M. Abbas), abderrahim.jardani@univ-rouen.fr (A. Jardani), abdellahi.soueid-ahmed@univ-smb.fr (A. Soueid Ahmed), andre.revil@univ-smb.fr (A. Revil), philippe.begassat@ademe.fr (Ph. Bégassat), jean-paul.dupont@univ-rouen.fr (J.P. Dupont).

http://dx.doi.org/10.1016/j.jhydrol.2017.08.053
0022-1694/

concerned communities in the use of non-intrusive geophysical methods (Sauck, 2000; Atekwana et al., 2000, 2002; Buselli and Lu, 2001; Nimmer and Osiensky, 2002; Werkema et al., 2003, Revil and Jardani, 2013a,b; Binley et al., 2015).

Several field and laboratory studies have shown a strong relationship between the self-potential method and the redox potential distribution in contaminated groundwater (Timm and Möller, 2001; Naudet et al., 2003, 2004; Naudet and Revil, 2005; Revil et al., 2010). The self-potential method is a passive geophysical technique that detects naturally occurring electrical currents by measuring the electrical potential distribution at the ground surface of the Earth. The method is sensitive to source current densities generated by pore water flow processes (electrokinetic component, e.g., Jardani et al., 2006) or by electrochemical processes such as oxidoreduction reactions (Nyquist and Corry, 2002; Naudet et al., 2003) and temperature gradients (Revil et al., 2013). The contribution associated with groundwater flow is well-established and can be used to reconstruct the hydraulic properties of the subsurface during pumping tests (e.g., Soueid Ahmed et al., 2016a,b). Self-potential signals have been observed in a number of studies associated with organic-rich contaminant plumes (Hämmann et al., 1997; Vichabian et al., 1999, Nyquist and Corry, 2002; Naudet et al., 2003; Arora et al., 2007; Rittgers et al., 2013). Sandbox experiments have been conducted to better characterize this process (e.g., Naudet and Revil, 2005; Fachin et al., 2012; Rittgers et al., 2013). The changes in the redox environment associated with bacterial biodegradation of hydrocarbons establish zones with different redox potentials. In the presence of electronic conductors (abiotic conductors such as semiconductors, e.g., pyrite and magnetite, and biotic conductors such as biofilms, see Delong, 2002; Tender et al., 2002), this leads to the establishment of a natural geobattery (see Naudet et al., 2004). The biogeobattery theory was developed by Revil and coworker (Naudet et al., 2004; Revil et al., 2010 and references therein). Support in favor of this biogeobattery theory has been developed since and validated by laboratory experiments (Risgaard-Petersen et al., 2012, 2014).

The above investigations illustrate the ability of the self-potential method to infer the redox potential, and to monitor organic-rich contaminant plumes in shallow aquifers associated with active electrochemical source mechanisms. In the present study, a self-potential field survey was performed over a hydrocarbon contaminant plume in northern France. We also modeled the electrokinetic contribution to remove it from the measured self-potential map. Our goal is to invert the residual self-potential map to estimate the distribution of the redox potential and to provide further support to the existence of biogeobatteries in such contaminant plumes. Note that the hydrocarbon contamination investigated in the present paper is very different from the contamination previously investigated at Entressen, which corresponds to leachates from a municipal landfill (Naudet et al., 2004).

2. Theory

2.1. Forward problem

In an isotropic heterogeneous aquifer contaminated by hydrocarbons, the electrical source current density $\mathbf{j}_S$ (A m^{-2}) is responsible for the self-potential signal measured at the ground surface. This source current density can result from two contributions: (1) The streaming source current density component $\mathbf{j}_\mathbf{w}$ which is caused by groundwater flow in porous media (electrokinetic component, see Sill, 1983), and (2) The redox source current density component $\mathbf{j}_\mathbf{R}$ which is associated with the biogeobattery phenomenon (Naudet et al., 2004; Revil et al., 2010). The physical mechanisms that describe the self-potential anomalies are governed by a generalized Ohm's law, in which the total current density $\mathbf{j}$ is written as the sum of the conductive current density (given by Ohm's law) plus the source current density $\mathbf{j}_S$ mentioned above:

$$\mathbf{j} = -\sigma\nabla\psi + \mathbf{j}_S, \tag{1}$$

$$\mathbf{j}_S = \mathbf{j}_W + \mathbf{j}_\mathbf{R}, \tag{2}$$

where ψ denotes the electrical potential (in V), $\mathbf{E} = -\nabla\psi$ (in V m^{-1}) describes the electrical field (induction is discarded because of the low frequency of the excitations), and σ denotes the electrical conductivity of the material (in S m^{-1}).

The streaming current density is linearly dependent on the Darcy velocity $\mathbf{u}$ (in m s^{-1}):

$$\mathbf{j}_W = \hat{Q}_V\mathbf{u}, \tag{3}$$

where $\hat{Q}_V$ (in C m^{-3}) denotes the effective charge density advectively carried along with the flow of the pore water. This charge density can be determined from the permeability itself k (in m^2) by using $\log_{10}\hat{Q}_V = -9.2 - 0.82\log_{10}k$ (Jardani et al., 2007; Revil and Mahardika, 2013) or from $\hat{Q}_V = -\sigma C\eta_f/k$ (where C is the electrokinetic coupling coefficient in V Pa^{-1} and η_f denotes the pore water viscosity in Pa s). The effect of the pore water conductivity (and therefore the ionic strength of the pore water) in the electrokinetic process is accounted for in the conduction term since the conductivity of the porous material is essentially proportional to the conductivity of the pore water.

The redox current density can be linearly related to the redox potential as (Revil et al., 2010; Rittgers et al., 2013):

$$\mathbf{j}_R = -\sigma\nabla E_H, \tag{4}$$

where E_H denotes the redox potential (generally determined from the activity of the Fe^{2+}/Fe^{3+} couple).

For the total current density, the continuity equation (conservation equation of the electrical charge) is

$$\nabla\cdot\mathbf{j} = 0. \tag{5}$$

The total current density is conservative. From Eqs. (1) and (5), the electrical (self-) potential is therefore governed by a Poisson equation:

$$\nabla\cdot(\sigma\cdot\nabla\psi) = \Im. \tag{6}$$

where $\Im = \nabla\cdot\mathbf{j}_S = \nabla\cdot(\mathbf{j}_W + \mathbf{j}_R) = \nabla\cdot(\hat{Q}_V\mathbf{u} - \sigma\nabla E_H)$ (in A m^{-3}) appears as the driving source term (volumetric source current density). The computation of the electrical potential is therefore obtained through solving the Poisson equation by using, for instance, the finite elements method. In doing so, we need the spatial distribution of the electrical conductivity, the total current density sources $\mathbf{j}_W + \mathbf{j}_R$ and the boundary conditions. The electrical conductivity of the subsurface can be inferred independently by using the electrical resistivity tomography method (e.g., Binley et al., 1996). Regarding the boundary conditions for the self-potential problem, the Neumann and Dirichlets are:

$$\psi = 0 \text{ at } \Gamma_d, \tag{7}$$

$$-\boldsymbol{n}\cdot\left[\overline{\overline{\sigma}}\cdot\nabla\psi - \mathbf{j}_S\right] = 0 \text{ at } \Gamma_N. \tag{8}$$

The Neumann boundary condition (8) is imposed at the insulating air-ground interface Γ_N and the Dirichlet boundary condition (7) is imposed at all the remaining boundaries Γ_d far from the area of interest. Eq. (6) can be also written in an integral form as:

$$\psi(\mathbf{r}) = \int_{\Omega_1}\mathbf{K}(\mathbf{r},\mathbf{r}')\mathbf{j}_S(\mathbf{r}')\mathrm{dV}, \tag{9}$$

where dV denotes a volume element around the current source point, Ω_1 denotes the source volume, $\mathbf{K}(\mathbf{r},\mathbf{r}')$ denotes the kernel operator that incorporates the information on the variability of the electrical conductivity, boundary conditions and geometry of the studied domain. The Kernel matrix is composed by the Green functions of the problem. Since this kernel operator connects the distributions of both electrical current density sources ($\mathbf{j}_W$ and $\mathbf{j}_R$) that generate the electrical potential measured at the ground surface, the electrical potential given in Eq. (9) can be decomposed as:

$$\psi(\mathbf{r}) = \psi_R(\mathbf{r}) + \psi_W(\mathbf{r}), \tag{10}$$

with

$$\psi_R(\mathbf{r}) = \int_{\Omega_1} \mathbf{K}(\mathbf{r},\mathbf{r}')\mathbf{j}_R(\mathrm{r}')\mathrm{dV} \tag{11}$$

$$\psi_W(\mathbf{r}) = \int_{\Omega_1} \mathbf{K}(\mathbf{r},\mathbf{r}')\mathbf{j}_W(\mathrm{r}')\mathrm{dV} \tag{12}$$

For the purpose of delineating a contaminated area from the self-potential analysis, the electrical signature due to the redox potential can only be determined by removing the effect of the electrokinetic phenomena from the self-potential field observations. In other words, we need first to compute (e.g., Naudet et al., 2004):

$$\psi_R(\mathbf{r}) = \psi(\mathbf{r}) - \psi_W(\mathbf{r}). \tag{13}$$

The streaming potential can be estimated numerically by coupling the hydraulic and electric problems. At the first stage, the different wells present in the study site are employed to parameterize and calibrate the groundwater flow model (and therefore the associated electrokinetic component) by solving the following steady-state flow equations:

$$\nabla \cdot \mathbf{u} = 0, \tag{14}$$

$$\mathbf{u} = -K\nabla h, \tag{15}$$

with the following boundary conditions:

$$h = h_D(x,y) \text{ at } \Gamma_d, \tag{16}$$

$$-\boldsymbol{n} \cdot [k \cdot \nabla h] = 0 \text{ at } \Gamma_N, \tag{17}$$

where h is the hydraulic head (in m), K is the hydraulic conductivity of the aquifer (in m s^{-1}), and $h_D(x,y)$ corresponds to the head imposed at the lateral boundaries (in m). A zero flux is fixed at the top and bottom boundaries of the domain of interest. Next, the self-potential distribution of the Darcy velocity in the saturated zone is used to compute the streaming potential contribution from equation (3). Then the residual self-potential map is built by removing this electrokinetic contribution from the measured self-potential signals. Finally, the residual self-potential map is inverted as described in the next section.

2.2. Inverse problem

The self-potential signals measured at hydrocarbon contaminated sites are partially associated with an electrochemical component produced by oxido-reduction reactions. The process by which this electrochemical signal is produced is described by

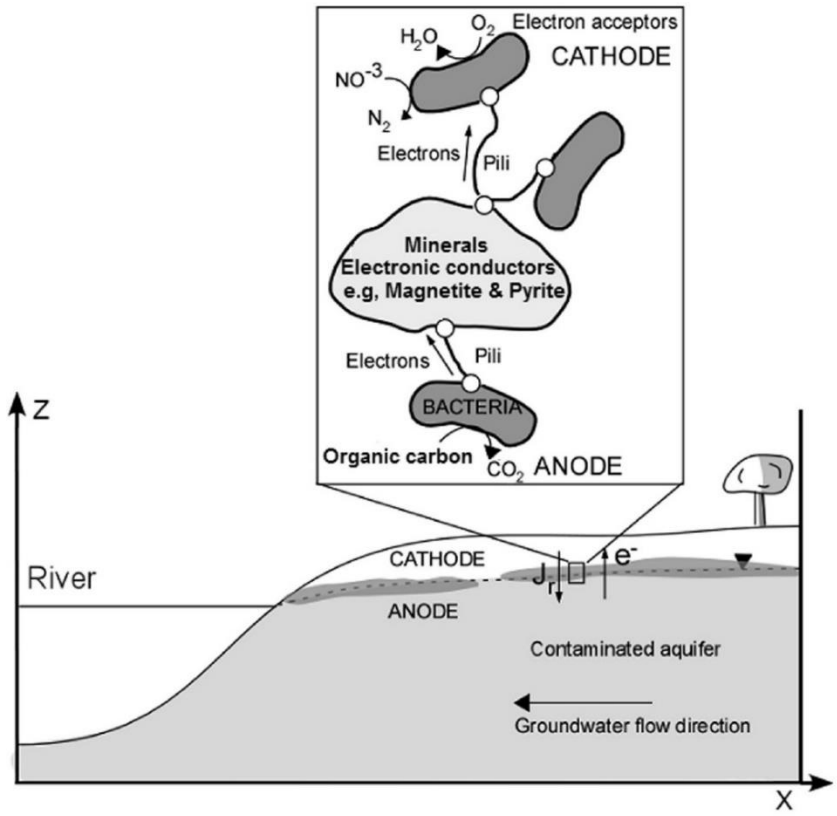

Fig. 1. Sketch of the biogeobattery process that occurs at the water table located at the interface between the saturated and non-saturated zones. The diagram shows that mineral precipitates and bacterial biofilms transfer electrons between the cathode and the anode during the oxidation of organic carbon (modified from Revil et al., 2010). e^- indicates the flux of electrons through biotic and/or abiotic electronic conductors located in the capillary fringe, and Jr indicates the source current density associated with the redox component of the self-potential field.

the biogeobattery model (Naudet et al., 2004; Revil et al., 2010). The biogeobattery process typically occurs at the interface between the contaminated aquifer and the unsaturated zone (transition zone) where biofilms and minerals such as pyrite and magnetite can connect the anode of the biogeobattery (i.e., associated with the reducing zone) to the cathode (i.e., associated with the oxidizing zone) (see Fig. 1). Electrons migration through biofilms and semi-conductors provides an electrical current through the capillary fringe (Linde and Revil, 2007). In this section, we will describe the different steps that will be followed to retrieve the redox potential by inverting the residual self-potential data. For this reason, the discretization of the current density vector will be performed only in the transition zone which is considered to have an arbitrary thickness of 1 m (see discussion below and see Linde and Revil, 2007).

The inverse problem relies on the minimization of the following objective (cost) function:

$$\Psi(\mathbf{J}_R) = \|\mathbf{W}_d(\mathbf{K}\mathbf{J}_R - \boldsymbol{\psi}_R)\| + \lambda\|\mathbf{J}_R - \mathbf{J}_R^0\|, \tag{18}$$

where $\boldsymbol{\psi}_R$ denotes a vector of the observed residual self-potential field, $\mathbf{W}_d = \sigma_d^2 \times \mathbf{I}_{d\times d}$ denotes a diagonal covariance matrix to include in the optimization of the uncertainties of the SP data with σ_d^2 as variance. $\mathbf{J}_R = (\mathbf{J}_R^x, \mathbf{J}_R^y, \mathbf{J}_R^z)$ corresponds to the three components of the electrical current density associated with the redox contribution considered here as the unknown parameters to be estimated by the inversion algorithm. The matrix $\mathbf{K} = \left(\mathbf{K}_{ij}^x, \mathbf{K}_{ij}^y, \mathbf{K}_{ij}^z\right)$ denotes the kernel matrix ($N \times 3M$) where N denotes the number of the self-potential measurements recorded at the ground surface and M denotes the number of the elements that are discretized in order to assign the value of the electrical density. In Eq. (18), $\mathbf{J}_R^0$ denotes a priori electrical current density model. Such a priori model is used to avoid the potential presence of undesirable bias in the estimated model due to the non-uniqueness of the inverse problem, a problem that is inherent to all potential field problems. The *a priori* model can be derived from the gradient of the redox potential measurements obtained at different wells. In Eq. (18), λ denotes a regularization parameter that controls the weights of the data misfit term $\|\mathbf{K}\mathbf{J}_R - \boldsymbol{\psi}_R\|$ with respect to the regularizer $\|\mathbf{J}_R - \mathbf{J}_R^0\|$ to find an optimal solution. Here, we compute λ by using the L-curve technique (Hansen, 1998). Eq. (18) corresponds to a linear problem for which the solution that minimizes the objective function (18) can be easily found as (Hansen, 1998):

$$\hat{\mathbf{J}}_R(\lambda) = \left[\mathbf{K}^T\mathbf{W}_D^T\mathbf{W}_D\mathbf{K} + \lambda^2 I\right]^{-1}\left(\mathbf{K}^T\boldsymbol{\psi}_R + \lambda\mathbf{J}_R^0\right). \tag{19}$$

This solution allows us to fit the (residual) self-potential data and reconstruct the spatial distribution of the redox potential via the following approximation (Linde and Revil, 2007):

$$E_h^s = -\frac{\mathrm{J}_R^Z \delta_z}{\sigma} + E_h^v, \tag{20}$$

where J_R^Z is the vertical component of the estimated electrical current density, δ_z is the arbitrary thickness of the transition zone, E_h^v is the redox potential of the unsaturated zone and E_h^s is the redox potential of the contaminated aquifer. As explained in detail in

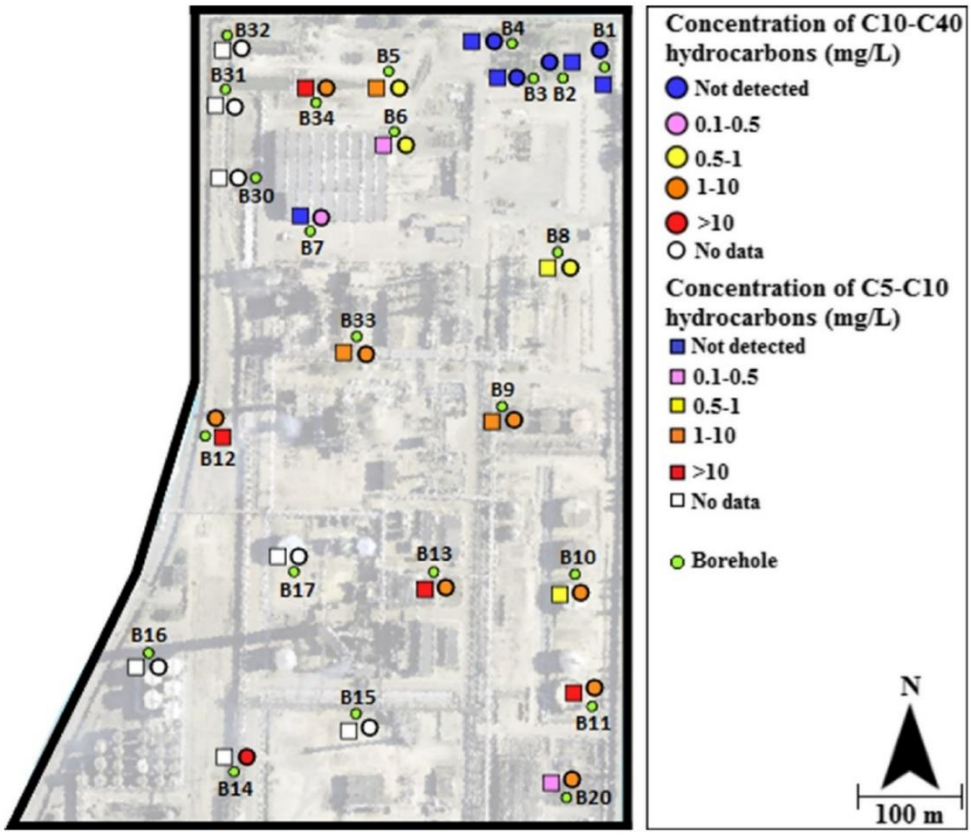

Fig. 2. Borehole data showing the distribution of C10-C40 and C5-C10 hydrocarbons in groundwater overlaying an aerial photo of the site (Google Earth-© 2017 Google). The data shows a clean zone with zero concentrations of hydrocarbons in the north-eastern part of the site (boreholes B1, B2, B3 and B4).

Linde and Revil (2007), this procedure is independent of the thickness of the capillary fringe (transition zone).

3. Field investigations

3.1. Study site characterization

The area of investigation was an abandoned petroleum refinery located in the north-western part of the Paris basin (France), and on an alluvial plain of the Seine River. The refinery was built in 1928, had an average refining activity of 7 million tons of crude oil per year and was shut down in 2013. Leakage from tanks and pipelines over the refinery operating years resulted in the seepage of light non-aqueous phase liquid (LNAPL) and dense non-aqueous phase liquid (DNAPL). Borehole data available over the area indicated that three different contamination phases exist: (1) a dissolved phase spreading down to a depth of 25 m; (2) a free phase present at different locations with a thickness ranging between 1 and 100 cm and (3) a residual phase consisting of the spill part which did not drain by gravity and residually saturated the pore spaces above the water table while the spill was traversing the vadose zone down to the aquifer (Atekwana and Atekwana, 2010). This phase is present at the source zones and at some other locations where the extended free phase can rise up due to the groundwater seasonal fluctuations caused by the nearby river. Note that the hydrocarbon contamination at this site is considered as mature (or aged) because enough time has elapsed for the biological processes to alter the hydrocarbons and their host environment after the contamination events, which started more than 80 years ago.

Geologically, the site is characterized by the first 2 m being an anthropogenic layer mainly composed of sandy soil with coarse grain diameter gravels. Below, there is a layer of fine to medium sand coarsening to gravel with depth, and with an average thickness ranging from 8 to 25 m. The site is characterized by one unconfined aquifer located in the sand and gravel layer (between 4 and 11 m deep), and mainly fed by a karstified chalk aquifer which exists below at a depth ranging from 11 m to 25 m. In the alluvial aquifer, groundwater flows from the south-east to the north-west towards the Seine River.

A clean and a contaminated zone were identified according to the hydrocarbon analyses of groundwater samples (Fig. 2). Samples taken from boreholes B34 and B12, located in the northwestern part of the site, recorded concentrations ranging from 1.2 to 4 mg L^{-1}. Higher concentrations ranging from 1.6 to 6.1 mg L^{-1} have been recorded in wells #B13 and B11, while values ranging between 1.3 and 2.6 mg L^{-1} were recorded in B33 and B9 located between the northwest and the center of the site. C5-C10 hydrocarbons measurements showed values ranging from 98 to 100 mg L^{-1} in B34 and B12; values ranging between 13 and 27 mg L^{-1} in B13 and B11 and values ranging between 1.4 and 3.7 mg L^{-1} in B33 and B9. Measurements conducted on groundwater samples taken from the boreholes located in the northeastern part of the site (wells #B1, B2, B3 and B4) recorded no hydrocarbons in the groundwater samples.

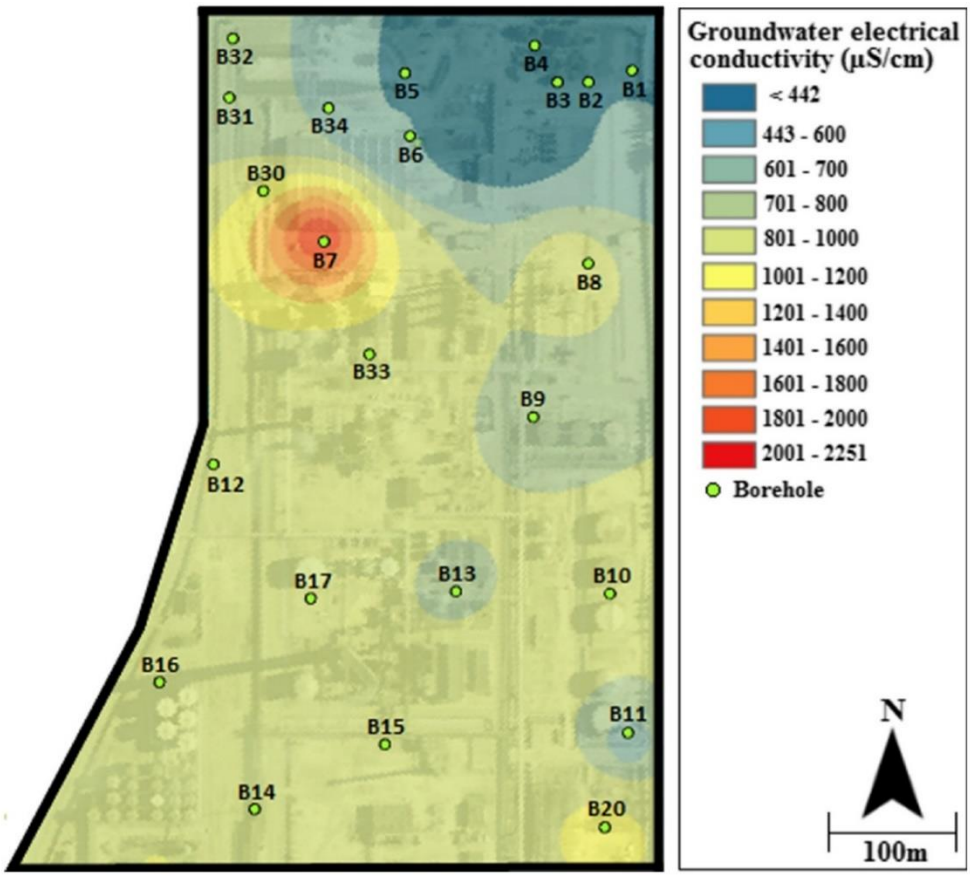

Fig. 3. The distribution of groundwater electrical conductivity measured in the site boreholes (obtained by kriging with a linear variogram) overlaying an aerial photo of the site (Google Earth-© 2017 Google). The map shows higher electrical conductivity values close to the contaminated zone boreholes (e.g., B10, B13, B7, B8 and B33).

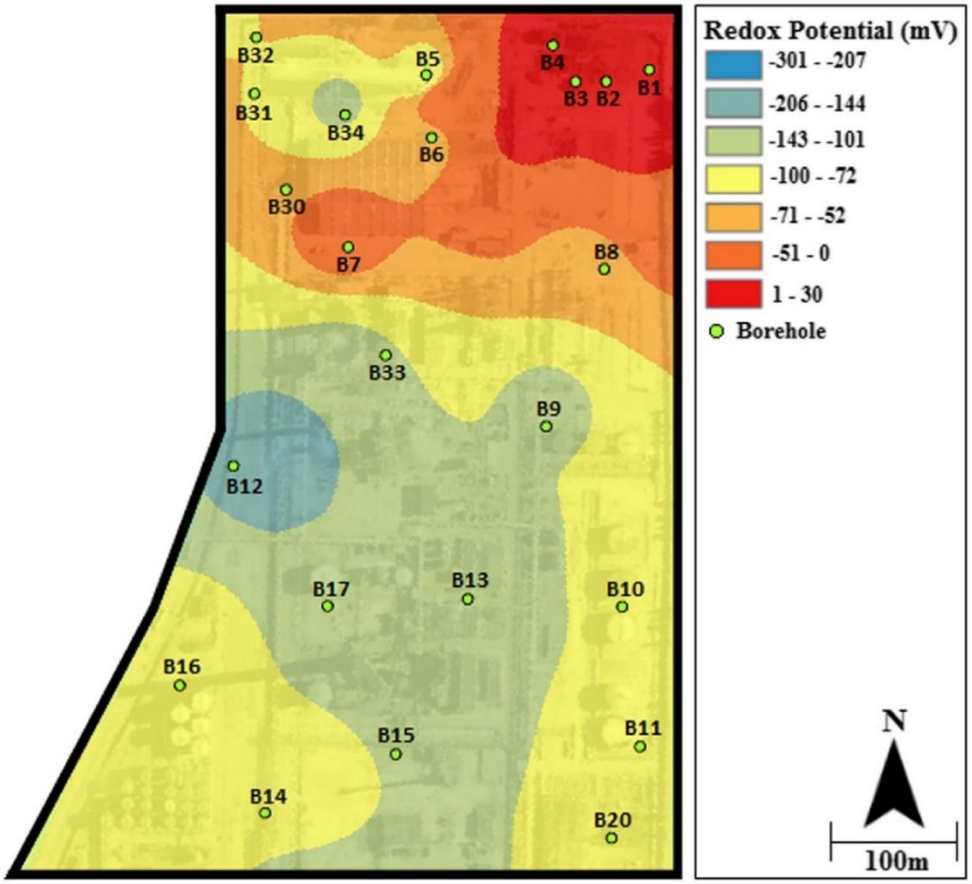

Fig. 4. The distribution of redox potential measured in the site boreholes (obtained by kriging with a linear variogram) overlaying an aerial photo of the site (Google Earth-© 2017 Google). The map shows negative redox potential values close to the contaminated zone boreholes (e.g., B10, B13, B7, B8 and B33) and positive redox potential values close to the clean zone boreholes (e.g., B1, B2, B3 and B4).

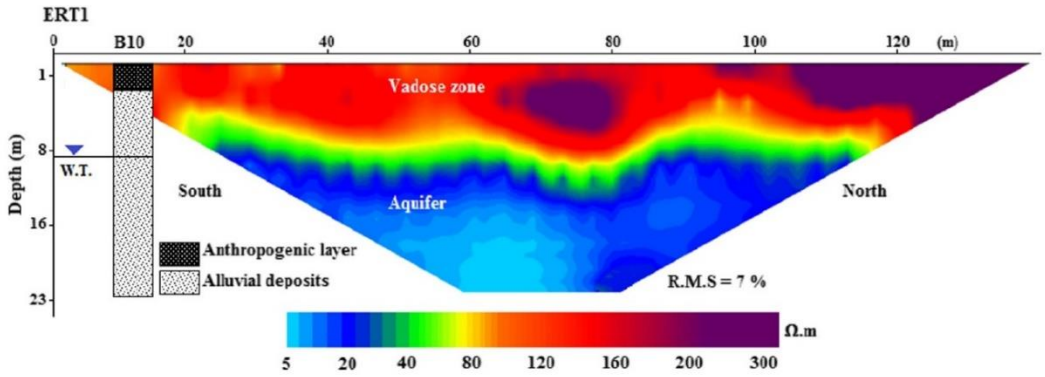

Fig. 5. 2D-electrical resistivity tomography profile (Wenner configuration and 2 m electrodes spacing) acquired in the contaminated zone across borehole B10. Note that the shown location of the borehole is not its exact location on the profile (to avoid hiding profile features). The profile shows a high resistivity region in the non-saturated zone (150–300 Ω.m) and a low resistivity region in the saturated zone (5–30 Ω.m) which is located at a depth of approximately 9 m. W.T. stands for the water table.

The measurements of groundwater geochemical parameters showed: increased total dissolved solids (TDS) concentrations (400–1000 mg/L); increased groundwater electrical conductivity values (400–2000 μS/cm) Fig. 3; negative redox potential values (−10 to −300 mV) (Fig. 4) and depleted terminal electron acceptors (TEAs) concentrations (dissolved oxygen, sulfate and nitrate) within the contaminated aquifer boreholes (e.g., B7, B8, B9, B10, B11). In contrast, lower TDS concentrations (50–200 mg/L), lower

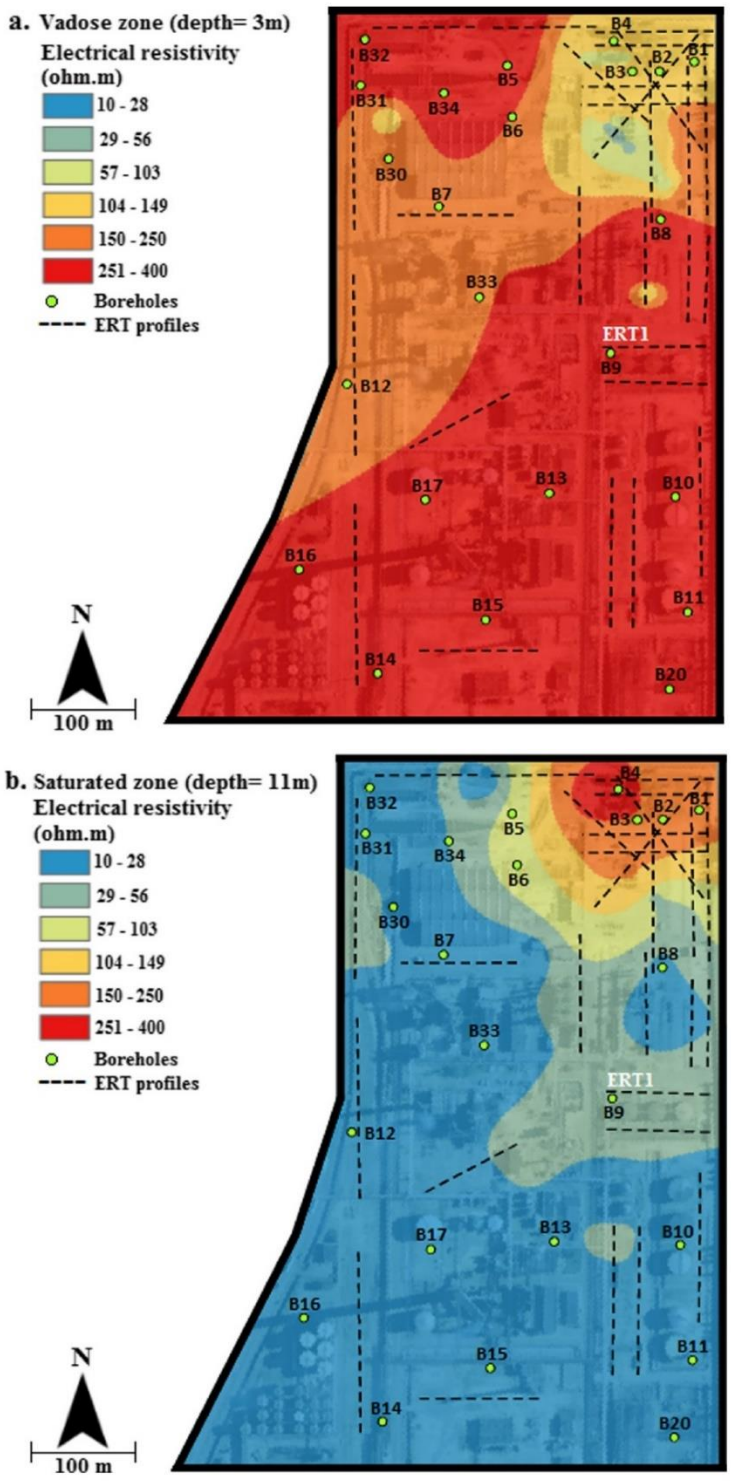

Fig. 6. Distribution of electrical resistivity in the non-saturated (a) and saturated (b) zones overlaying an aerial photo of the site (Google Earth-© 2017 Google). The maps were obtained by the interpolation of data obtained from 27 electrical resistivity tomography profiles. The dashed lines represent the ERT profiles. ERT1 represents the location of the ERT profile shown in Fig. 5.

groundwater electrical conductivity values (<400 μS/cm), positive redox potential values (1–40 mV) and higher TEAs concentrations were observed in the clean groundwater zone boreholes (B1, B2, B3 and B4). The data provide evidence that biodegradation of organic matter is occurring at the site. Biodegradation is evidenced by (1) the increase of the TDS and groundwater electrical

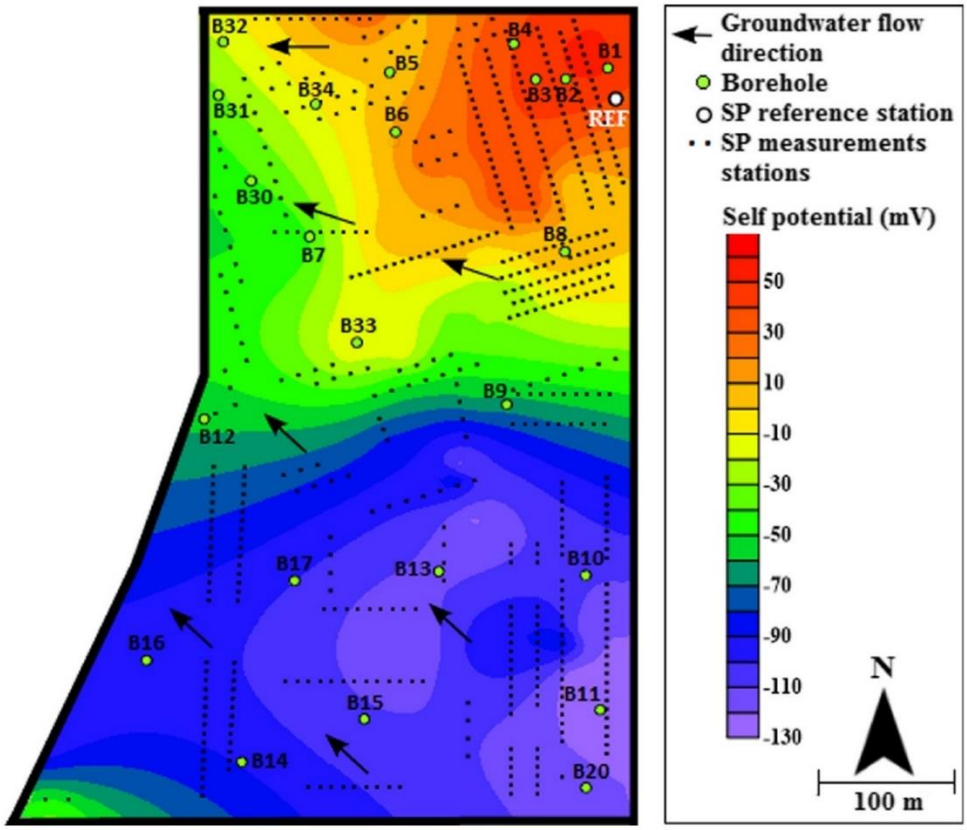

Fig. 7. The measured self-potential map on the study site acquired in May 2016. The arrows show the direction of groundwater flow and the black dots correspond to the self-potential measurement stations made in the field. The white circle with the term 'REF' corresponds to the SP base (reference) station which was common for all the measurement stations. The self-potential map shows positive values close to the clean zone boreholes (B1, B2, B3 and B4) and negative values close to the contaminated zone boreholes (e.g., B7, B8, B9, B10, etc.).

conductivity in the contaminated zone compared to the clean zone, (2) the change in redox conditions, and (3) the values of the dissolved oxygen concentrations in the contaminated zone. Furthermore, a change from negative redox potential to positive redox potential in the north-eastern part of the site implies that a redox front exists at the boundary between the clean and contaminated zones.

3.2. Geophysical surveys

Electrical resistivity tomography can be used to image the subsurface in terms of electrical resistivity distribution by injecting direct current at the ground surface and measuring its corresponding electrical field (e.g., Samouëlian et al., 2005). 27 Two-dimensional (2-D) ERT profiles were acquired by using a Syscal Pro system (http://www.iris-instruments.com). Wenner and dipole-dipole arrays were used for each profile, with electrodes spacings of 1 m, 2 m, 3 m and 5 m according to the length of each profile. The electrical resistivity profiles were processed and filtered by the computer software Res2Dinv (Loke and Barker, 1996), which uses the field data to obtain a 2D model of the electrical resistivity distribution in the subsurface (Griffiths and Barker, 1993). The software subdivides the model into several small blocks and uses a least-square inversion technique to obtain the resistivity value of each block (with a smoothness constraint). The 2-D ERT tomograms have been interpolated to obtain maps of the electrical resistivity distribution in the saturated and non-saturated zones.

To collect the self-potential data, two non-polarizable (Pb-$PbCl_2$) Petiau electrodes were used: one is fixed and referred to as the reference electrode, whereas the other can move into different measurement points with a rolling wire. The electrodes are rods of lead suspended in porous containers supersaturated with $KCl/PbCl_2$ solutions. The electrodes were placed in small holes filled with bentonite mud during the measurements. This ensures good electrical contact between the soil and the non-polarizable electrodes (Jardani et al., 2006). The measurements were performed by using a high input impedance (100 MΩ) voltmeter (MX20) which was connected to the electrodes to record their corresponding self-potential difference.

The self-potential survey was performed over a single day and no rain events happened during that day or in the two days prior the survey. The areas with no self-potential data correspond to the emplacement of facilities, buildings and pavements with a thick layer of asphalt. The base station for the self-potential survey was chosen in the clean zone and it was common to all the measurements which were done at 550 stations. To measure the drift between the two electrodes, the potential difference between the two electrodes was measured prior and after the survey. The difference was less than 1 mv indicating a minor and negligible drift. Note that the electrodes used for this survey were new. The temperature variation of the electrodes was not taken into account as the Petiau electrodes have a very small temperature sensitivity close to 0.2 mV/°C (Perrier et al., 1997; Petiau, 2000). Each station was measured up to 5 times and for each measurement, the

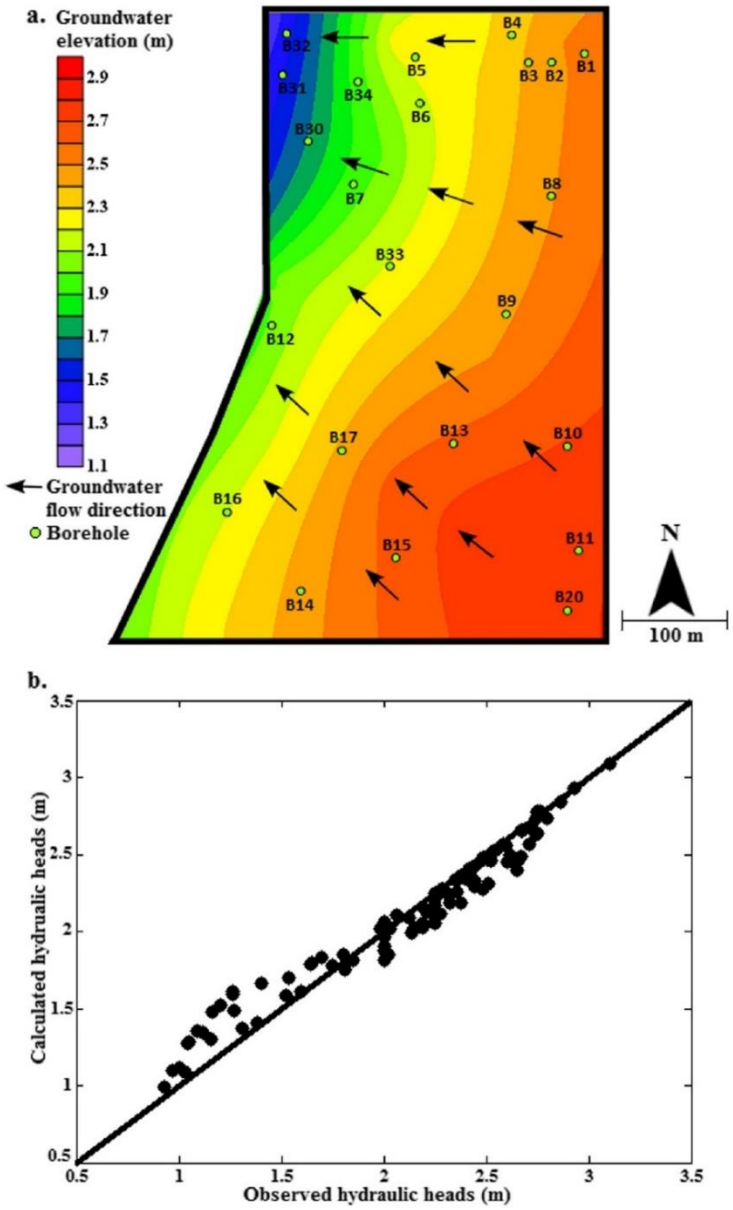

Fig. 8. (a) The groundwater elevation in the study site. The arrows show the direction of groundwater flow. (b) Correlation between the hydraulic heads observed in boreholes (data points extracted from the interpolation of the data observed in the field) and the numerically predicted hydraulic heads which were used to calculate the electrokinetic self-potential component.

scanning electrode was kept in the ground until a stable reading was achieved. The data reproducibility was tested by comparing the data presented in this paper to a self-potential map acquired one year earlier. The old map (not shown) did not cover the whole site and had fewer data points. The data showed however the same pattern with slight differences of less than 5 mV in the amplitudes of the signals.

4. Results and discussion

A representative electrical resistivity profile (ERT1) acquired in the contaminated zone is shown in Fig. 5. The profile shows a simple geological structure with two main electrical resistivity domains: (1) a shallow resistive zone (100–300 Ω m) corresponding to the sand and gravel vadose zone and (2) a very conductive layer (<30 Ω m) starting at a depth of 9 m and corresponding to the contaminated alluvial aquifer. The map of the electrical resistivity distribution in the vadose zone (depth of 3 m) shows electrical resistivity values ranging from 100 to 400 Ω.m in the regions of contaminated and clean groundwater (Fig. 6a). Fig. 6b shows the electrical resistivity distribution is the site's saturated zone at a depth of 11m. The map is dominated by low electrical resistivity values (5–50 Ω m), except for the north-eastern part of the site, where higher electrical resistivity values (150–400 Ω m) appear in accordance with the clean groundwater zone (B1, B2, B3 and B4). The low electrical resistivity values in the contaminated zone in comparison to the clean zone reflects the significant mineralization of groundwater which is responsible for the increase in TDS

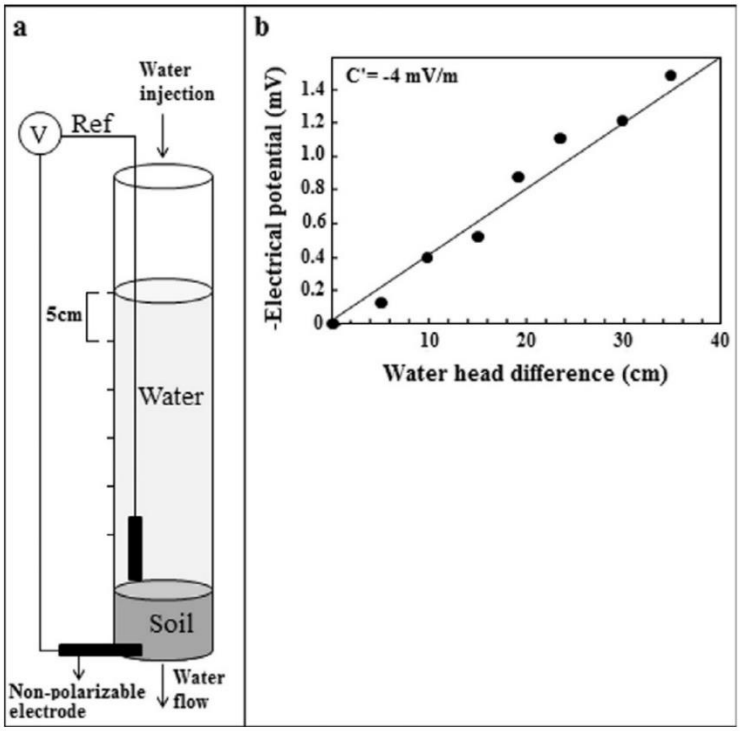

Fig. 9. (a) The laboratory experiment used to calculate the electrokinetic coupling coefficient C′ (Revil and Jardani, 2013a,b). Two electrodes connected to a voltmeter were placed at the bottom and top of a soil sample. The arrows indicate the direction of water flow and the measurement was repeated at different water head levels with an interval of 5 cm. (b) Plot of the water head difference versus the measured electrical potential measured across the soil sample.

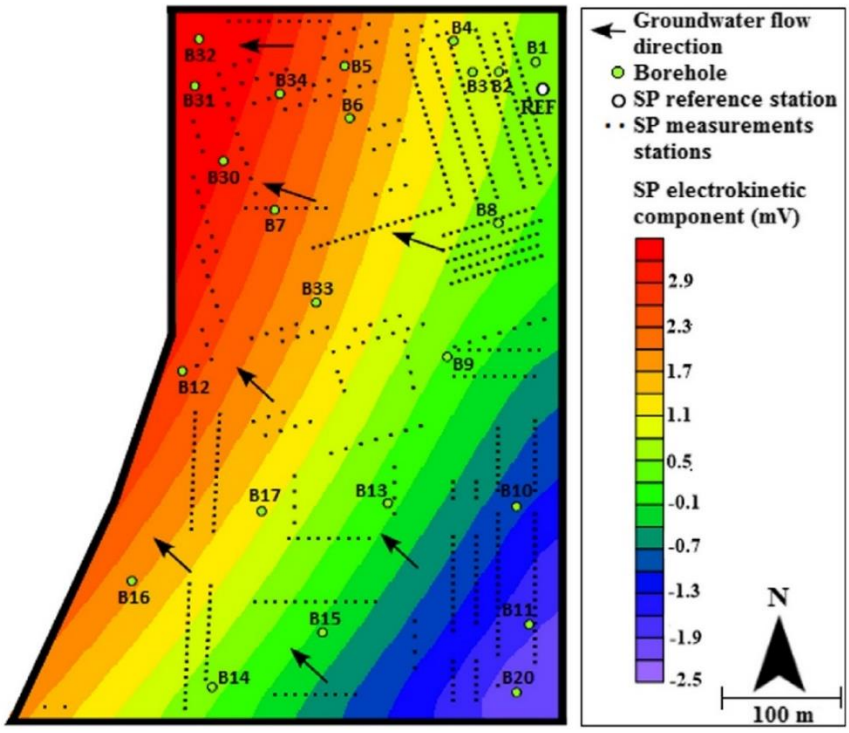

Fig. 10. Map of the electrokinetic component of the self-potential data. The arrows represent the groundwater flow direction and the white circle with the term 'REF' corresponds to the SP base (reference) station.

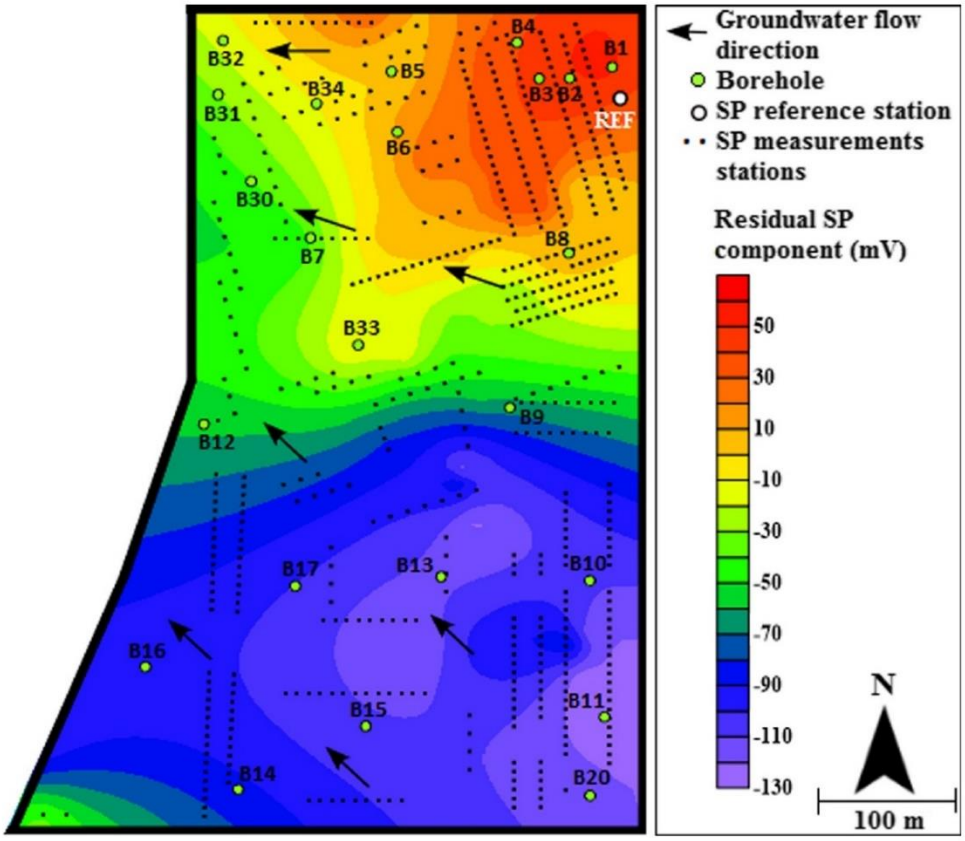

Fig. 11. Map of the residual self-potential data (redox component) calculated by removing the electrokinetic component from the field self-potential data. The arrows represent the groundwater flow direction and the white circle with the term 'REF' corresponds to the SP base (reference) station.

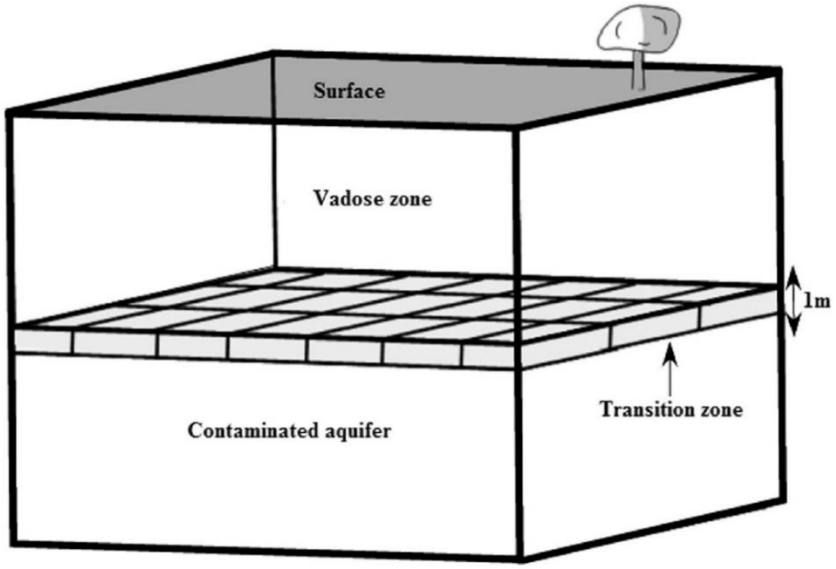

Fig. 12. The position of the discretized domain used to invert the self-potential data. This domain corresponds to the transition zone, which separates the saturated zone from the non-saturated zone at a depth of 7.5 m. The transition zone was considered to have a thickness of 1 m.

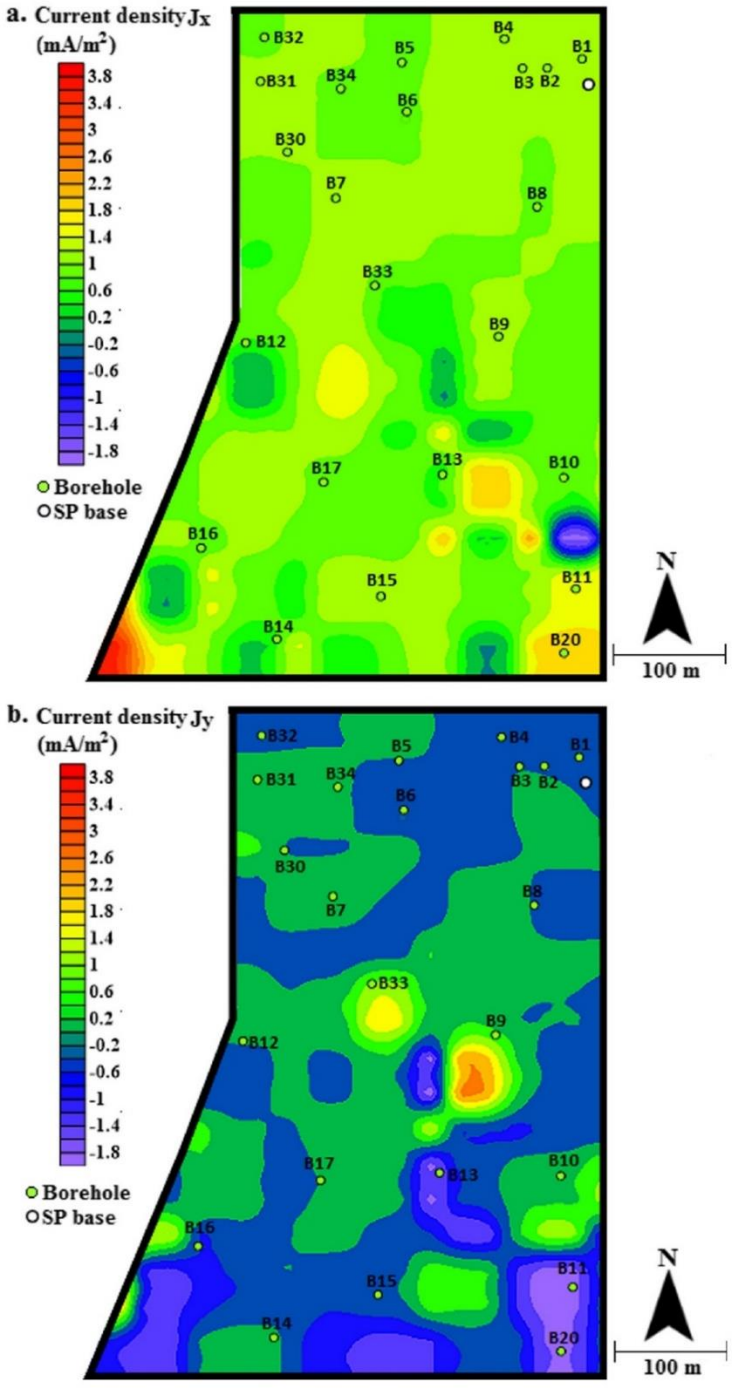

Fig. 13. The inverted horizontal current density components (Jx and Jy).

concentrations during the biodegradation of hydrocarbons (Atekwana et al., 2000). The etching and dissolution of minerals surfaces by biodegradation by products (e.g., organic and carbonic acids), in addition to the leaching of soluble salts (from grains surfaces) increase the concentrations of TDS and the groundwater electrical conductivity values in contaminated aquifers (McMahon et al., 1995; Atekwana et al., 2000; Sauck, 2000). Consequently, the increase of pore water electrical conductivity increases the bulk electrical conductivity and produces low resistivity anomalies in the impacted zones. The self-potential map (Fig. 7) shows negative values ranging from −130 mV to −5 mV (with respect to the position of the reference) in the contaminated regions. Contrarily, the

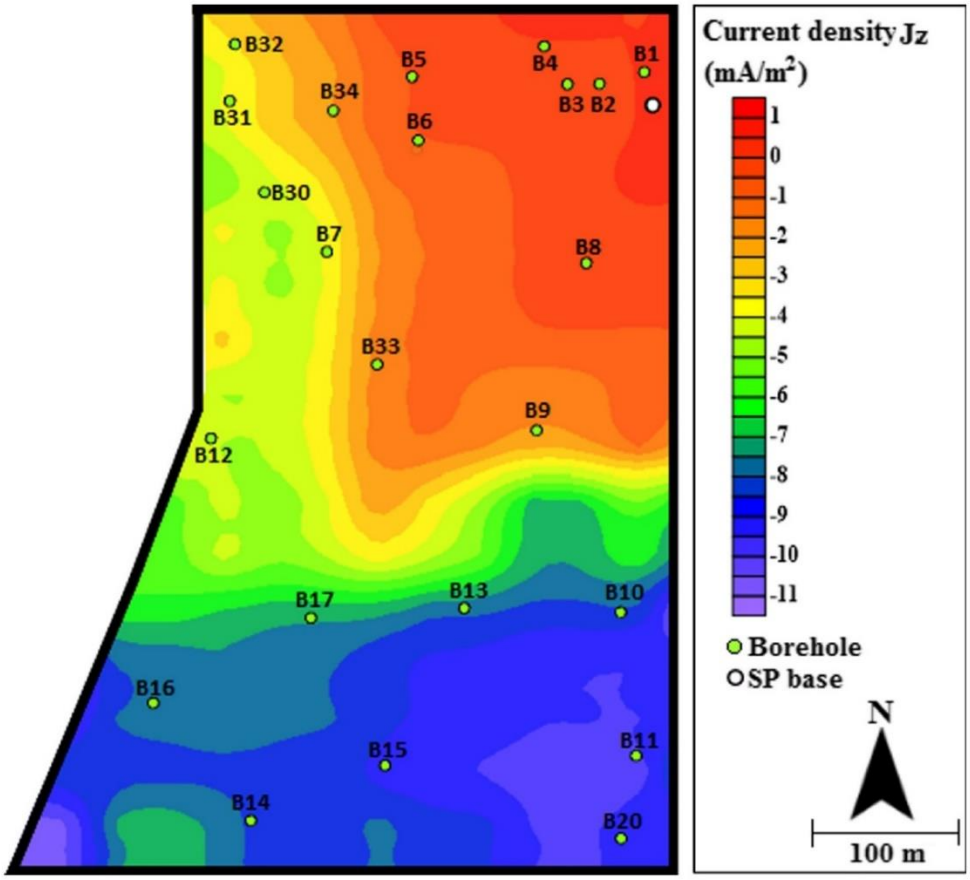

Fig. 14. The inverted vertical current density component (Jz).

map shows positive values ranging from 10 to 70 mV in the clean region, located in the north-eastern part of the site.

As mentioned earlier, the self-potential signal measured in the field includes two components: an electro-kinetic component associated with groundwater flow and an electrochemical component associated with redox processes. Other contributions (thermoelectric effects and diffusion potentials) are negligible in comparison to the electrokinetic and redox components, see discussions in Revil et al. (2009) and Revil et al. (2010). Redox-driven anomalies associated with buried metallic objects produced also strong but localized self-potential anomalies (see examples in Castermant et al., 2008, Rittgers et al., 2013) that can be filtered out easily (see Revil et al., 2012).

The first step of our analysis is the removal of the electrokinetic contribution from the recorded self-potential data. This step is important for isolating the self-potential signal produced by oxido-reduction reactions. This was carried out through the numerical computation of the electrokinetic contribution by solving the hydroelectric coupling problem as described previously in Section 2.1. In the first step, the hydraulic head data collected from different wells were exploited to predict the distribution of the hydraulic head variations (Fig. 8). This was done through estimating the hydraulic conductivity K of the aquifer (assumed here homogenous, $K = 10^{-7}$ m s^{-1}) and defining the imposed boundary conditions for solving the diffusion equation. We acknowledge that this is a strong assumption that is probably not completely realistic. However, it seems to fit the head data pretty well in this special case study. In more complex environments, it will be better to invert the hydraulic conductivity or transmissivity fields first. Note that this assumption is not really needed however since the heads can be interpolated and we can use a single value of the apparent coupling coefficient as discussed by Arora et al. (2007). We also assume that the flow in the vadoze zone is producing a negligible self-potential anomaly.

In the second step, we used the spatial distribution of the Darcy velocity of the groundwater flow which was determined numerically in the first step to compute the electrical current density of the confined aquifer. The electrical current density was neglected in the vadose zone. The charge density parameter $\hat{Q}_V$ was calculated after determining the electrokinetic coupling coefficient C through a simple laboratory experiment (Fig. 9a) described by Revil and Jardani (2013a,b). The assumption of a single permeability value is consistent with the use of a single value for the effective charge density. For the streaming potential measurements, a graduated plastic tube, 50 cm long and 10 cm in diameter was used. A representative soil sample extracted from borehole B8 was placed at the bottom of the tube and two non-polarizable electrodes were placed at the bottom and the surface of the soil sample. The measurements were performed at ambient temperature (20°C ± 1C°C). A contaminated groundwater sample extracted from the same borehole with an electrical conductivity value of approximately 1000 μS/cm was injected from the top of the tube. The measurement was repeated at different water head levels with an interval of 5 cm. Then the potential difference values were plotted against

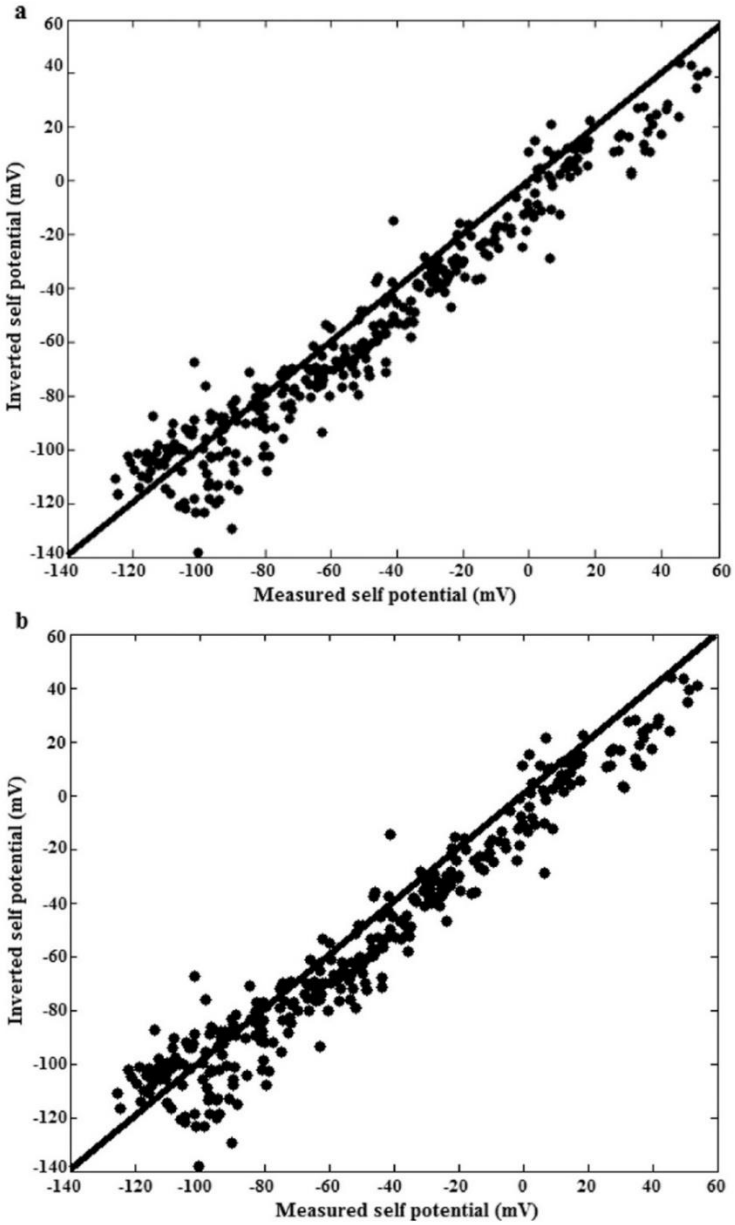

Fig. 15. (a) Correlation between the measured and inverted self-potential data obtained by using only the vertical current density component (J_z). (b) Correlation between the measured and inverted self-potential data obtained from the combination of the three current density components (J_z J_x and J_y). The figure shows that the horizontal components are negligible compared to the vertical component.

the water head levels in order to compute the electro-kinetic coupling coefficient C, which is represented in mV per meter of water head variation (Fig. 9b). C was determined to be -4.0 ± 1 mV/m. These parameters, in addition to the electrical conductivity distribution in the saturated and unsaturated zones (determined from the ERT survey) were used to solve the Poisson equation to define the electrical signature (electrokinetic component) associated with groundwater flow (Fig. 10). The electrokinetic component was determined to be very small and was removed from the self-potential data to produce the residual self-potential data. The residual self-potential map showed a similar pattern compared to the original field self-potential map, with positive self-potential values in the clean groundwater zone and negative self-potential values in the contaminated groundwater zone (Fig. 11).

To predict the redox potential distribution in the aquifer, the self-potential data were inverted by using the approach introduced in the inverse problem description (Section 2.2), where the heterogeneity of the electrical conductivity in the saturated and vadose zones is taken into account. This inversion is based on the estimation of the redox values from the vector of the electrical current density predicted through the inversion of the residual self-potential data. The electrical sources responsible for the self potential field were assumed to be located at the transition zone which was divided into 144 cells, with a dimension of "35 m $\times$ 56 m $\times$ 1 m for each (Fig. 12).

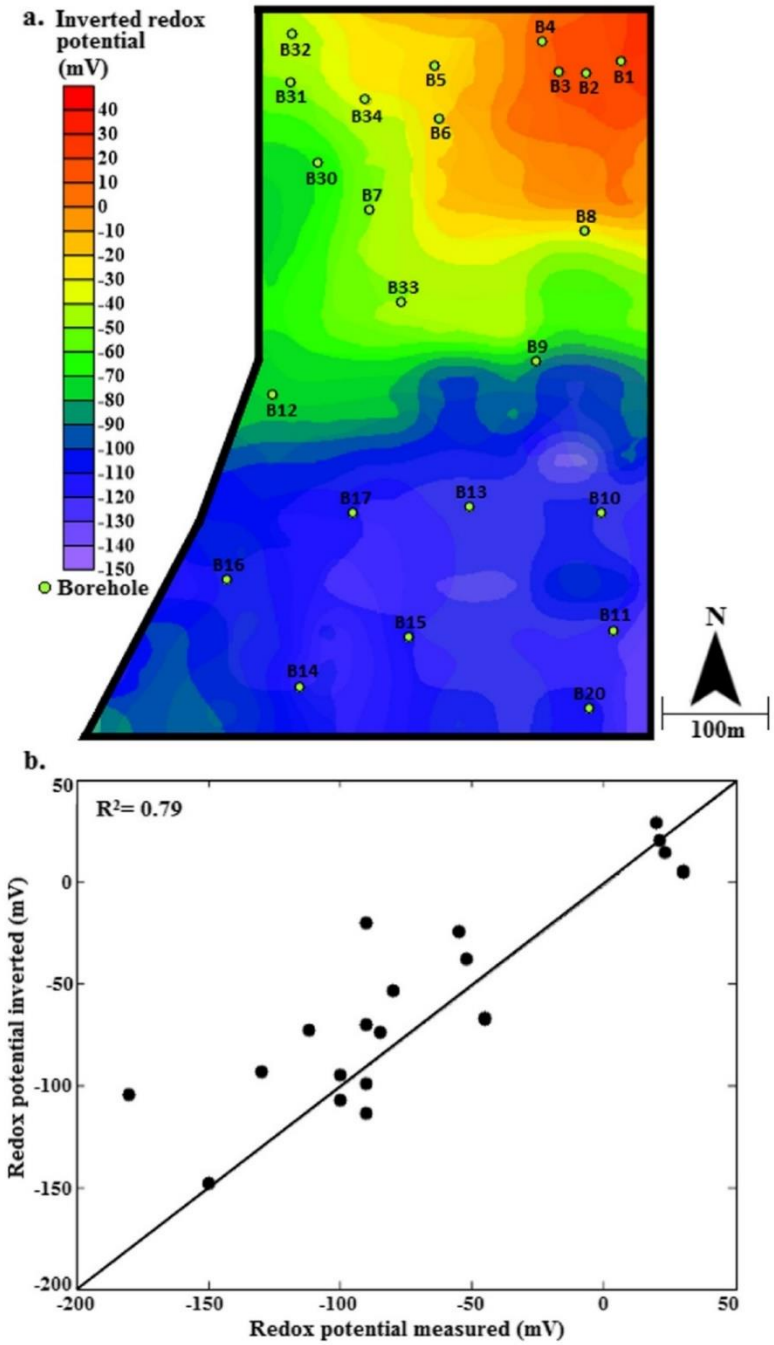

Fig. 16. (a) The map of the predicted redox potential values obtained from the inversion of the residual self-potential data. (b) The linear correlation between the predicted redox potential values and the redox potential measured on boreholes showing a good correlation coefficient (R^2 = 0.79).

The electrical current density components that were predicted from the inversion of the self-potential data were assigned for each cell. The total number of the unknown parameters to invert was $3 \times 144 = 432$ and the total number of self-potential measurements was 350, so we dealt with an undeterminated inverse problem. The inverse problem was performed with a smallest constraint and the regularization parameter was determined through the L-curve approach. The retrieved current density components are illustrated in Figs. 13 and 14. The figure shows that the amplitudes of the horizontal components of the electrical current density J_x and J_y (Fig. 13) are very small compared to the vertical component J_z (Fig. 14). This was verified by comparing the correlation of the observed and numerical data obtained only from the vertical component (Fig. 15a), with the correlation of the observed and numerical data obtained from the combination of the vertical and horizontal components (Fig. 15b). Therefore, the contributions of the horizontal components can be neglected. The distribution of the redox potential in the aquifer was then reconstructed from the

vertical component of the current density by using Eq. (20) as described in Section 2.2. Similar to the measured redox potential values, the predicted redox potential map showed positive values (10–40 mV) in the clean groundwater zone and negative values (0 to −150) in the contaminated groundwater zone (Fig. 16a). The inverted redox potential values showed a good linear correlation (R^2 = 0.79) with the observed redox potential values (Fig. 16b). This further supports the concept of biogebattery at this site with the source current density produced in the capillary fringe just above the water table. Note that the result shown in Fig. 16 is free from the choice of the base station for the self-potential signals. It is only based on the relative amplitude of the residual self-potential anomaly with respect to the position of the reference electrode and the difference in redox potential between the contaminated zone and the background.

5. Conclusion

This study shows an application of the self-potential and electrical resistivity methods to estimate the redox potential at a site impacted by a mature hydrocarbon contamination undergoing biodegradation. The geophysical methods constrained by measurements of geochemical parameters provided useful information on the quality of groundwater, and indicated that biodegradation processes are occurring in the contaminated aquifer. An active (bio)-geobattery process in which the redox potential gradient is the driving force of the self-potential electrochemical signal is suggested to be present in the contaminated portion of the site. This natural geobattery is created due to the existence of a strong redox potential gradient between the highly reducing conditions within the plume and the oxidizing conditions outside the plume. The associated current density occurred therefore in the capillary fringe of the unconfined aquifer.

The electrokinetic component of the observed self-potential signals was removed numerically from the field self-potential data to produce a residual self-potential map. For this purpose, a groundwater flow model was parametrized and calibrated to compute the spatial distribution of the Darcy velocity, which was used to calculate the streaming potential (electrokinetic component). A redox potential map was then reconstructed from the inversion of the residual self-potential data through the computation of the electrical current density components, taking into account the electrical conductivity distribution in the subsurface which was obtained from an electrical resistivity survey. The horizontal components were determined to be very small compared to the vertical component of the source current density. Therefore, the redox contribution in the contaminated aquifer can be explained by vertical dipoles distributed across the capillary fringe just above the water table, supporting further the mechanism of biogebattery at this site.

The predicted redox potential values showed a good correlation with the redox potential values measured independently in a set of wells. This good correlation illustrates the ability of the self-potential method to delineate the redox front of the contaminant plume. Moreover, the self-potential equipment (voltmeter, electrodes and rolling wires) are inexpensive and stable over long periods of time. Therefore, the self-potential method can be considered as a cost-effective and fast method which could be used in the next stage of our research for the long term monitoring of the contaminant plume evolution during the remediation process. However, it would be necessary to undertake more biological and chemical investigations to characterize the biogeobattery mechanism (e.g., type of biofilms and bacteria, the precipitation of semiconductors etc.) and define the more precisely the redox reactions (e.g., iron reduction, methanogenesis) occurring at this site.

Acknowledgments

We thank the 'Agence de l'Environnement et de la Maîtrise de l'Energie' (ADEME) for funding the project Geoplus and the region of Normandy for funding the Project GEOCARE. Valgo is thanked for providing access to the site. We thank the Associate Editor, Dr. Niklas Linde, and the two referees for their constructive and useful comments.

References

Arora, T., Linde, N., Revil, A., Castermant, J., 2007. Non-intrusive characterization of the redox potential of landfill leachate plumes from self-potential data. J. Contam. Hydrol. 92, 274–292. http://dx.doi.org/10.1016/j.jconhyd.2007.01.018.

Atlas, R.M., 1981. Microbial degradation of petroleum hydrocarbons: an environmental prospective. Microbial. Rev. 45, 180–209.

Atekwana, E.A., Sauk, W.A., Werkema, D.D., 2000. Investigations of geoelectrical signatures at a hydrocarbon contaminated site. Appl. Geophys. 44, 167–180. http://dx.doi.org/10.1016/S0926-9851(98)00033-0.

Atekwana, E.A., Sauk, W.A., Abdel Aal, G.Z., 2002. Geophysical investigation of vadose zone conductivity anomalies at a hydrocarbon contaminated site: implications for the assessment of intrinsic bioremediation. Environ. Eng. Geophys. 7, 103–110.

Atekwana, E.A., Atekwana, E.A., 2010. Geophysical signatures of microbial activity: a review. Surv. Geophys. 31, 247–283. http://dx.doi.org/10.1007/s10712- 009 -9089 -8.

Baedecker, M.J., Cozzarelli, I.M., Eganhouse, R.M., Siegel, D.I., Bennett, P.C., 1993. Crude oil in a shallow sand and gravel aquifer: III. Biogeochemical reactions and mass balance modeling in anoxic groundwater. Appl. Geochem. 8, 569–586.

Buselli, G., Lu, K., 2001. Groundwater contamination monitoring with multichannel electrical and electromagnetic methods. J. Appl. Geophys. 48, 11–23.

Binley, A., Henry-Poulter, S., Shaw, B., 1996. Examination of solute transport in an undisturbed soil column using electrical resistance tomography. Water Resour. Res. 32 (4), 763–769.

Binley, A., Hubbard, S.S., Huisman, J.A., Revil, A., Robinson, D.A., Singha, K., Slater, L. D., 2015. The emergence of hydrogeophysics for improved understanding of subsurface processes over multiple scales. Water Resour. Res. 51, 3837–3866. http://dx.doi.org/10.1002/2015WR017016.

Castermant, J., Mendonça, C.A., Revil, A., Trolard, F., Bourrié, G., Linde, N., 2008. Redox potential distribution inferred from self-potential measurements associated with the corrosion of a burden metallic body. Geophys. Prospecting 56, 269–282. http://dx.doi.org/10.1111/j.1365-2478.2007.00675.x.

Christensen, T.H., Bjerg, P.L., Banwart, S.A., Jakobsen, R., Heron, G., Albrechtsen, H.-J., 2000. Characterization of redox conditions in groundwater contaminant plumes. J. Contam. Hydrol. 45, 165–241.

Craun, G.F., Brunkard, J.M., Yoder, J.S., Roberts, V.A., Carpenter, J., Wade, T., Calderon, R.L., Roberts, J.M., Beach, M.J., Roy, S.L., 2010. Causes of outbreaks associated with drinking water in the United States from 1971 to 2006. Clin. Microbiol. Rev. 23, 507–528.

Delong, E., 2002. L'électricité bactérienne, plus qu'une curiosité. La Recherché 358, 17.

Fachin, S.J.S., Abreu, E.L., Mendonça, C.A., Revil, A., Novaes, G.C., Vasconcelos, S.S., 2012. Self-potential signals from an analog biogeobattery model. Geophysics 77 (4), EN29–EN37. http://dx.doi.org/10.1190/GEO2011-0352.1.

Griffiths, D.H., Barker, R.D., 1993. Two-dimensional resistivity imaging and modeling in areas of complex geology. J. Appl. Geophys. 29, 211–226.

Hansen, P.C., 1998. Rank-Deficient and Discrete Ill-Posed Problems: Numerical aspects of Linear Inversion. 247 pp., SIAM, Philadelphia, Pa.

Hämmann, M., Maurer, H.R., Green, A.G., Horstmeyer, H., 1997. Self-potential image reconstruction: capabilities and limitations. Eng. Geophys. 2, 21–35.

Jardani, A., Dupont, J., Revil, A., 2006. Self-potential signals associated with preferential groundwater flow pathways in sinkholes. J. Geophys. Res. 111, B09204. http://dx.doi.org/10.1029/2005JB004231.

Jardani, A., Revil, A., Bolève, A., Crespy, A., Dupont, J.P., Barrash, W., Malama, B., 2007. Tomography of the Darcy velocity from self-potential measurements. Geophys. Res. Lett. 34, L24403.

Linde, N., Revil, A., 2007. Inverting self-potential data for redox potentials of contaminant plumes. Geophys. Res. Lett. 34, L14302. http://dx.doi.org/10.1029/2007GL030084.

Loke, M.H., Barker, R.D., 1996. Practical techniques for 3D resistivity surveys and data inversion. Geophys. Prospecting 44, 499–523.

McMahon, P.B., Vroblesky, D.A., Bradley, P.M., Chapelle, F.H., Guller, C.D., 1995. Evidence of enhanced mineral dissolution in organic acid rich shallow ground water. Ground Water 33, 207–216.

Naudet, V., Revil, A., Bottero, J.-Y., Bégassat, P., 2003. Relationship between self-potential and redox conditions in contaminated groundwater. Geophys. Res. Lett. 30 (21), 2091. http://dx.doi.org/10.1029/2003GL018096.

Naudet, V., Revil, A., Rizzo, E., Bottero, J.-Y., Bégassat, P., 2004. Groundwater redox conditions and conductivity in a contaminant plume from geoelectrical investigations. Hydrol. Earth Syst. Sci. 8, 8–22. http://dx.doi.org/10.5194/hess-8-8-2004.

Naudet, V., Revil, A., 2005. A sandbox experiment to investigate bacteria-mediated redox processes on self-potential signals. Geophys. Res. Lett. 32, L11405. http://dx.doi.org/10.1029/2005GL022735.

Nimmer, R.E., Osiensky, J.L., 2002. Direct current and self-potential monitoring of an evolving plume in partially saturated fractured rock. J. Hydrol. 267, 258–272.

Nyquist, J.E., Corry, C.E., 2002. Self-potential: the ugly duckling of environmental geophysics. The Leading Edge 21, 446–451. http://dx.doi.org/10.1190/1.1481251.

Perrier, F., Petiau, G., Clerc, G., Bogorodsky, V., Erkul, E., 1997. A one year systematic study of electrodes for long period measurements of the electric field in geophysical environments. J. Geomagnetism Geoelectricity 49, 1677–1696. http://dx.doi.org/10.5636/jgg.49.1677.

Petiau, G., 2000. Second generation of lead-lead chloride electrodes for geophysical applications. Pure Appl. Geophys. 157, 357–382. http://dx.doi.org/10.1007/s000240050004.

Rao, P.S., Jawitz, J.W., Enfield, C.G., Falta, R.W., Annable, M.D., Wood, A.L., 2002., Technology integration for contaminated site remediation: clean-up goals and performance criteria. Groundwater Quality: Natural and Enhanced Restoration of Groundwater Pollution (Proceedings of the Groundwater Quality 2001 Conference held at Sheffield, UK, June 2001). IAHS Publ. no. 275.

Risgaard-Petersen, N., Revil, A., Meister, P., Nielsen, L.P., 2012. Sulfur, iron-, and calcium cycling associated with natural electric currents running through marine sediment. Geochim. Cosmochim. Acta 92, 1–13. http://dx.doi.org/10.1016/j.gca.2012.05.036.

Risgaard-Petersen, N., Damgaard, L.R., Revil, A., Nielsen, L.P., 2014. Mapping electron sources and sinks in a marine biogeobattery. J. Geophys. Res.Biogeosci. 119 (8), 1475–1486. http://dx.doi.org/10.1002/2014JG002673.

Revil, A., Trolard, F., Bourrié, G., Castermant, J., Jardani, A., Mendonça, C.A., 2009. Ionic contribution to the self-potential signals associated with a redox front. J. Contaminant Hydrol. 109 (1–4), 27–39.

Revil, A., Mendonça, C.A., Atekwana, E.A., Kulessa, B., Hubbard, S.S., Bohlen, K.J., 2010. Understanding biogeobatteries: where geophysics meets microbiology. J. Geophys. Res. 115, G00G02. http://dx.doi.org/10.1029/2009JG001065.

Revil, A., Karaoulis, M., Johnson, T., Kemna, A., 2012. Review: some low-frequency electrical methods for subsurface characterization and monitoring in hydrogeology. Hydrogeol. J. 20 (4), 617–658. http://dx.doi.org/10.1007/s10040-011-0819-x.

Revil, A., Jardani, A., 2013a. The Self-Potential Method, Theory and Applications in Environmental Geosciences. Cambridge University Press, Canbridge.

Revil, A., Mahardika, H., 2013. Coupled hydromechanical and electromagnetic disturbances in unsaturated clayey materials. Water Resour. Res. 49 (2), 744–766. http://dx.doi.org/10.1002/wrcr.20092.

Revil, A., Karaoulis, M., Srivastava, S., Byrdina, S., 2013. Thermoelectric self-potential and resistivity data localize the burning front of underground coal fires. Geophysics 78 (5), B259–B273.

Revil, A., Jardani, A., 2013b. The Self-Potential Method: Theory and Applications in Environmental Geosciences. Cambridge University Press. 383 pages.

Rittgers, J.B., Revil, A., Karaoulis, M., Mooney, M.A., Slater, L.D., Atekwana, E.A., 2013. Self-potential signals generated by the corrosion of buried metallic objects with application to contaminant plumes. Geophysics 78 (5), EN65–EN82. http://dx.doi.org/10.1190/GEO2013-0033.1.

Samouëlian, A., Cousin, I., Tabbagh, A., Bruand, A., Richard, G., 2005. Electrical resistivity survey in soil science: a review. Soil Tillage Res. 83 (2), 173–193.

Sauck, W.A., 2000. A conceptual model for the geoelectrical response of LNAPL plumes in granular sediments. J. Appl. Geophys. 44, 151–165.

Semple, K.T., Doick, K.J., Wick, L.Y., Harms, H., 2007. Microbial interactions with organic contaminants in soil: definitions, processes and measurement. Environ. Pollut. 150, 166–176. http://dx.doi.org/10.1016/j.envpol.2007.07.023.

Sill, W.R., 1983. Self-potential modeling from primary flows. Geophysics 48, 76–86. http://dx.doi.org/10.1190/1.1441409.

Soueid Ahmed, A., Jardani, A., Revil, A., Dupont, J.P., 2016a. Specific storage and hydraulic conductivity tomography through the joint inversion of hydraulic heads and self-potential data. Adv. Water Resour. 89 (80), 90. http://dx.doi.org/10.1016/j.advwatres.2016.01.006.

Soueid Ahmed, A., Jardani, A., Revil, A., Dupont, J.P., 2016b. Joint inversion of hydraulic head and self-potential data associated with harmonic pumping tests. Water Resour. Res. 52 (9), 6769–6791. http://dx.doi.org/10.1002/2016WR019058.

Tender, L.M., Reimers, C.E., Stecher, H.A., Holmes, D.E., Bond, D.R., Lowy, D.A., Pilobello, K., Fertig, S.J., Lovley, D., 2002. Harnessing microbially generated power on the seafloor. Nat. Biotechnol. 20, 821–825.

Tiehm, A., Schulze, S., 2003. Intrinsic aromatic hydrocarbon biodegradation for groundwater remediation. Oil Gas Sci. Technol. 58, 449–462. http://dx.doi.org/10.2516/ogst: 2003028.

Timm, F., Möller, P., 2001. The relation between electrical and redox potential: an evidence from laboratory to field experiments. J. Geochem. Explor. 72, 115–127.

Vayenas, A.C., 2002. Visualization experiments of biodegradation in porous media and circulation of the biodegradation rate. Water Resour. 25, 203–219.

Vichabian, Y., Reppert, P.M., Morgan, F.D., 1999. Self potential mapping of contaminants. In: Proc. Symp. Appl. Geophys. to Eng. Environ. Probl. March 14-1.

Werkema, D.D., Atekwana, E.A., Enders, A., Sauck, W.A., Cassidy, D.P., 2003. Investigating the geoelectrical response of hydrocarbon contamination undergoing biodegradation. Geophys. Res. Lett. 30, 1647. http://dx.doi.org/10.1029/2003GL017346.

Groundwater

Application of Large-Scale Inversion Algorithms to Hydraulic Tomography in an Alluvial Aquifer

by P. Fischer[1], A. Jardani[2], A. Soueid Ahmed[2], M. Abbas[2], X. Wang[3], H. Jourde[4], and N. Lecoq[2]

Abstract

Large-scale inversion methods have been recently developed and permitted now to considerably reduce the computation time and memory needed for inversions of models with a large amount of parameters and data. In this work, we have applied a deterministic geostatistical inversion algorithm to a hydraulic tomography investigation conducted in an experimental field site situated within an alluvial aquifer in Southern France. This application aims to achieve a 2-D large-scale modeling of the spatial transmissivity distribution of the site. The inversion algorithm uses a quasi-Newton iterative process based on a Bayesian approach. We compared the results obtained by using three different methodologies for sensitivity analysis: an adjoint-state method, a finite-difference method, and a principal component geostatistical approach (PCGA). The PCGA is a large-scale adapted method which was developed for inversions with a large number of parameters by using an approximation of the covariance matrix, and by avoiding the calculation of the full Jacobian sensitivity matrix. We reconstructed high-resolution transmissivity fields (composed of up to 25,600 cells) which generated good correlations between the measured and computed hydraulic heads. In particular, we show that, by combining the PCGA inversion method and the hydraulic tomography method, we are able to substantially reduce the computation time of the inversions, while still producing high-quality inversion results as those obtained from the other sensitivity analysis methodologies.

Introduction

In hydrogeology, the assessment of hydraulic properties of subsurface aquifers, such as transmissivity, storage coefficient and solute transport parameters, is a key issue to an adequate management and protection of groundwater resources. Generally, aquifer characterization is based on the interpretation of hydraulic observations data collected during pumping, infiltration, or tracer tests (Carrera and Neuman 1986b; Rao et al. 2003; Lee and Kitanidis 2014; Pool et al. 2015). Therefore, hydraulic tomography is considered as one of the most effective approaches for characterizing the spatial distribution of hydraulic transmissivity of an aquifer (Cardiff et al. 2009; Berg and Illman 2013; Cardiff et al. 2013; Soueid Ahmed et al. 2015; Zha et al. 2015; Wang et al. 2016). This method relies on a set of hydraulic head responses recorded during cross-hole pumping experiments. Then, the interpretation can be achieved through the use of an inverse algorithm to image the spatially varying hydraulic properties in the subsurface.

The inverse problem for estimating hydraulic parameters involves a formulation of a forward problem, which sets up the link between the hydraulic observations and the unknown hydraulic parameters (Tarantola and Valette 1982). For a hydraulic tomography inversion, the forward modeling is based on a numerical method (e.g., the finite element, finite-difference and finite volume methods) used to solve the partial differential equation of the groundwater flow. The forward problem operator can be formulated as:

$$\mathbf{d} = f(\mathbf{s}) + \boldsymbol{\eta} \tag{1}$$

where $\mathbf{d}$ represents the hydraulic responses of the model, $\mathbf{s}$ is the logarithm of the m unknown hydraulic transmissivities, to be estimated from a set of n observed data $\mathbf{d}_{\text{obs}}$ and a nonlinear forward modeling application $f : \mathbb{R}^m \rightarrow \mathbb{R}^n$. $\boldsymbol{\eta}$ is an additive noise of the numerical modeling.

In a probabilistic framework, the inverse problem maximizes a posterior probability density function $\pi_{\text{post}}(\mathbf{s}|\mathbf{d})$. Generally, the problem is ill-posed and the

[1]Corresponding author: UNIROUEN, UNICAEN, CNRS, M2C, Normandie University, 76000 Rouen, France; +33(0)235147181; fax: +33(0)235147022; pierre.fischer1@univ-rouen.fr

[2]UNIROUEN, UNICAEN, CNRS, M2C, Normandie University, 76000 Rouen, France.

[3]Department of Earth Science and Engineering, Imperial College London, London SW7 2AZ, UK.

[4]CNRS, Laboratoire Hydrosciences, Université de Montpellier, 34000 Montpellier, France.

Article impact statement: Efficiency comparison of different largescale inversion methodologies associated with hydraulic tomography to model an alluvial aquifer.

Received March 2016, accepted August 2016.

doi: 10.1111/gwat.12457

solution is non-unique, therefore additional a priori information is required in order to find one physically meaningful solution (Carrera and Neuman 1986a). Furthermore, in our case, the problem is under-determined, it involves a small number of measurements but a large number of unknown parameters ($n \ll m$). The inverse problem corresponds to recovering the "best fitting" model parameters $\hat{\mathbf{s}}$ which allow the model responses to match the observed data, and at the same time respect the constraints imposed by the a priori information on the model. Using the Bayes' formula, the posterior probability density function can be expressed as (Elsheikh et al. 2014):

$$\pi_{\text{post}}(\mathbf{s}|\mathbf{d}) \propto exp\left[-\frac{1}{2}(f(\mathbf{s})-\mathbf{d})^{\mathrm{T}}\mathbf{R}^{-1}(f(\mathbf{s})-\mathbf{d}) - \frac{1}{2}\left(\mathbf{s}-\mathbf{s}_{\text{prior}}\right)^{\mathrm{T}}\mathbf{Q}^{-1}\left(\mathbf{s}-\mathbf{s}_{\text{prior}}\right)\right] \quad (2)$$

where $\mathbf{s}_{\text{prior}}$ denotes the a priori model; $\mathbf{Q}$ is a $m \times m$ covariance matrix of the model parameters, which can include geostatistical information about the distribution trend or pattern of the unknowns parameters (in that case $\mathbf{Q}$ is defined in a matrix where elements of the matrix represent the variogram function associated with the distance between cells of the model) and $\mathbf{R}$ denotes a $n \times n$ diagonal covariance matrix which accounts for the errors occurred in the data measurements.

The aim of the inversion problem is to find a set of parameter which maximizes the density of probability, $\pi_{\text{post}}(\mathbf{s}|\mathbf{d})$. This corresponds to a model of high probability with respect to the measurements and the imposed a priori model (Tarantola and Valette 1982). To solve the inverse problem, two main groups of iterative methods are often employed: (1) the deterministic methods which assume that the algorithm converges to a local minimum by performing a linearization of an objective function and (2) the stochastic methods which converge to a global minimum by selecting different randomly generated parameters fields as probable solutions to the model (Pool et al. 2015). Several deterministic and stochastic inversion algorithms have been widely applied in hydrogeology, but they are time- and memory-expensive, particularly for the cases which involve a fine discretization of the parameter grid and/or a large amount of observational data (Kitanidis and Lee 2014). Thereby, one of the main trends in the development of inversion theory during the last few years was to develop algorithms which are able to solve inversion models with a large number of unknown parameters and data.

Recently, several time- and memory-saving methods have been developed to reduce the memory cost and the computation time of the usually large matrices involved in the inversion algorithms. One way for reducing the computational and memory demands is to use some approximation methods on matrix operations, such as the fast multipole method (FMM) (Greengard and Rokhlin 1987), which is based on Legendre polynomial expansions and spherical harmonics. The FMM was associated with the hierarchical matrices approach (Hackbusch and Börm 2002) to compute matrix-vector products for a large-scale application in seismic imaging (Ambikasaran et al. 2013). Another way is through using the MINRES Krylov subspace method (Paige and Saunders 1975) which can be combined with the fast fourier transform (FFT) (Nowak et al. 2003) to iteratively solve inversions of large matrix systems. This method has recently been applied to 3-D large-scale transient hydraulic tomography problems (Liu et al. 2014). The two approaches mentioned above avoid the calculation of the full Jacobian matrix of the forward model at each iteration. A new method has recently been developed by Lieberman et al. (2013), in an application of an inversion algorithm for a large-scale 3-D transient contaminant transport. The authors used a proper orthogonal decomposition method (POD) to compute a projection basis with the eigenvectors associated to the highest eigenvalues of the Hessian matrix of the forward problem. The inverse problem was then solved in a reduced projected subspace.

In this paper, we have attempted to achieve an efficient site hydraulic characterization (i.e., to obtain high-resolution transmissivity fields at a low computational cost) by applying a recently developed geostatistical inversion method, the principal component geostatistical approach (PCGA) (Lee and Kitanidis 2014). This method can considerably reduce the computation time and the memory cost of inversions by using an approximation of the covariance matrix $\mathbf{Q}$ based on a singular value decomposition method (SVD), and by avoiding the computation of the Jacobian matrix through the use of a matrix-free product based on a finite-difference method.

This paper presents an application of the PCGA method, combined with a hydraulic tomography investigation, for a large-scale inverse modeling of the hydraulic transmissivity field of an alluvial aquifer. First, we present the methodology of the geostatistical approach (GA) algorithm, and the modifications for large-scale application (PCGA). Then, we describe the hydrogeological background of the experimental field site, from which the hydraulic measurements were taken, and present the numerical model setup. Finally, we show our inversion results. In particular, we compare these results to those obtained by applying the classical GA method with two different methods in Jacobian matrix computation (i.e., an adjoint-state and a finite-difference methods), which do not use a covariance matrix approximation. We have evaluated the computation times, and the sensitivities and accuracies of the inversion results for the three different methodologies. Using a hydraulic tomography field application on a porous aquifer, we show the advantages of the PCGA inversion method for efficient large-scale inverse modeling in hydrogeology.

Principal Component Geostatistical Approach

In the GA (Kitanidis and Vomvoris 1983; Hoeksema and Kitanidis 1984; Kitanidis 1995), the prior probability density function of the m model parameters $\mathbf{s}$ is set as a multivariate Gaussian with a mean $E(\mathbf{s}) = \mathbf{X}\boldsymbol{\beta}$ where $\mathbf{X}$

is an $m \times p$ known matrix and $\boldsymbol{\beta}$ a $p \times 1$ vector to be determined during the inversion process (generally $p = \mathbf{1}$), and a covariance, $E\left[(\mathbf{s} - \mathbf{X}\boldsymbol{\beta})(\mathbf{s} - \mathbf{X}\boldsymbol{\beta})^{\mathrm{T}}\right] = \mathbf{Q}(\boldsymbol{\theta})$.

The posterior probability density function $\Psi = -ln[\pi(\mathbf{s}|\mathbf{d})]$ (also called in inversion problems the objective function) then becomes:

$$\Psi = \frac{1}{2}(f(\mathbf{s}) - \mathbf{d})^{\mathrm{T}}\mathbf{R}^{-1}(f(\mathbf{s}) - \mathbf{d}) + \frac{1}{2}(\mathbf{s} - \mathbf{X}\boldsymbol{\beta})^{\mathrm{T}}\mathbf{Q}^{-1}(\mathbf{s} - \mathbf{X}\boldsymbol{\beta}) \quad (3)$$

The best approximation $\hat{\mathbf{s}}$ for the model parameters, taking into account the a priori information and the observed data, can be found as being the model maximizing the density of probability in (Equation 2), which is also equivalent to minimize the argument of its exponential. Thus, $\hat{\mathbf{s}}$ is found by minimizing the objective function Ψ (Equation 3). This minimization can be achieved by using a Newton linearization iterative approach on $\mathbf{s}$. The iterative process initializes at a reasonable $\mathbf{s}_0$. Then, at iteration step $\mathbf{j}+1$, the new value $\mathbf{s}_{j+1}$ is found in the vicinity of the previous model $\mathbf{s}_j$ using a first-order Taylor approximation:

$$f(\mathbf{s}_{j+1}) = f(\mathbf{s}_j) + \mathbf{F}_j(\mathbf{s}_{j+1} - \mathbf{s}_j) \quad (4)$$

Here $\mathbf{F}_j$ is the $n \times m$ Jacobian matrix of the forward problem f for s_j : $\mathbf{F}_j = \left.\frac{\partial f}{\partial \mathbf{s}}\right|_{\mathbf{s}=\mathbf{s}_j}$.

After some matrix manipulations, the updated solution of the parameters in the iterative process, found by minimizing the objective function, can be written as (Kitanidis 1995):

$$\mathbf{s}_{j+1} = \mathbf{X}\boldsymbol{\beta}_j + \mathbf{Q}\mathbf{F}_j^{\mathrm{T}}\boldsymbol{\xi}_j \quad (5)$$

where the $p \times 1$ vector $\boldsymbol{\beta}_j$ and the $n \times 1$ vector $\boldsymbol{\xi}_j$ are solutions of the following matrix system (Kitanidis 1995):

$$\begin{bmatrix} \mathbf{F}_j\mathbf{Q}\mathbf{F}_j^{\mathrm{T}} + \mathbf{R} & \mathbf{F}_j\mathbf{X} \\ (\mathbf{F}_j\mathbf{X})^{\mathrm{T}} & \mathbf{0} \end{bmatrix} \begin{bmatrix} \boldsymbol{\xi}_j \\ \boldsymbol{\beta}_j \end{bmatrix} = \begin{bmatrix} \mathbf{d} - f(\mathbf{s}_j) + \mathbf{F}_j\mathbf{s}_j \\ \mathbf{0} \end{bmatrix} \quad (6)$$

Note that here $\mathbf{0}$ represents a $p \times p$ matrix of zeros on the left-hand side and a $p \times 1$ vector of zeros on the right-hand side.

At the end of the iterative process, to quantify the model parameter's uncertainty after optimization, we can compute the posterior covariance of s derived as:

$$\mathbf{Q}_{\mathbf{post}} = \mathbf{Q} - \begin{bmatrix} \mathbf{F}_j\mathbf{Q} \\ \mathbf{X}^{\mathrm{T}} \end{bmatrix}^{\mathrm{T}} \begin{pmatrix} \mathbf{F}_j\mathbf{Q}\mathbf{F}_j^{\mathrm{T}} + \mathbf{R} & \mathbf{F}_j\mathbf{X} \\ (\mathbf{F}_j\mathbf{X})^{\mathrm{T}} & \mathbf{0} \end{pmatrix}^{-1} \begin{bmatrix} \mathbf{F}_j\mathbf{Q} \\ \mathbf{X}^{\mathrm{T}} \end{bmatrix} \quad (7)$$

The GA method as presented above needs the computation of the Jacobian matrix $\mathbf{F}$ for each iteration in order to solve the system (Equation 6), which can usually be done by solving the forward problem $m+1$ times using a finite-difference method, or $n+1$ times using an adjoint-state method. Even if the adjoint-state method may considerably decrease the computation time for underdetermined problems (see Cardiff and Kitanidis 2008 for a comparison of the finite-difference and adjoint-state method computation times), it is not efficient for large-scale problems with a large number of measurements and parameters. Another problem which appears in the GA method is that when the number of data and/or parameters is high, it requires a significant computational power for the calculation and storage of the covariance matrix $\mathbf{Q}$ (which can be alleviated by FFT, H-matrices, or FMM). To overcome these difficulties, Kitanidis and Lee have developed the PCGA, on the basis of the GA method.

In this new approach, the computational and memory costs associated with the manipulation of matrix $\mathbf{Q}$ are reduced using a low-rank approximation of a chosen truncation order $K \ll m$ through a SVD:

$$\mathbf{Q}_K = \mathbf{U}\mathbf{S}\mathbf{V}^{\mathrm{T}} \quad (8)$$

where $\mathbf{S}$ is a $K \times K$ diagonal matrix containing the singular values of $\mathbf{Q}$ sorted in descending order, $\mathbf{U}$ is a $m \times K$ matrix and $\mathbf{V}$ is an $m \times K$ matrix. As $\mathbf{Q}$ is defined as a symmetric matrix, its SVD simplifies to: $\mathbf{Q}_K = \mathbf{V}\mathbf{S}\mathbf{V}^{\mathrm{T}}$.

This decomposition can also be written as:

$$\mathbf{Q}_K = \sum_{i=1}^{K} \boldsymbol{\zeta}_i\boldsymbol{\zeta}_i^{\mathrm{T}} \text{ with } \boldsymbol{\zeta}_i = \sqrt{\lambda_i}\mathbf{V}_i \quad (9)$$

where λ_i is the ith singular value (also $\mathbf{S}(i,i)$) and $\mathbf{V}_i$ is the ith column vector of $\mathbf{V}$ associated to λ_i. The error arising from this K-rank decomposition equals to the $K+1$th singular value (λ_{K+1}) of $\mathbf{Q}$.

However, this decomposition is a good approximation only for a matrix $\mathbf{Q}$ in which the most of its information is contained in its few highest eigenvalues and eigenvectors, meaning a relatively smooth pattern. One can also use an eigen-decomposition if $\mathbf{Q}$ is a matrix defined by positive eigenvalues or a randomized decomposition approach which is efficient for high-dimensional matrices with $m \sim$ 1,000,000 (Halko et al. 2011).

In addition, the PCGA method also avoids the full Jacobian matrix calculation at each iteration. When performing a matrix product, such as $\mathbf{F}_j\mathbf{u}$ (where $\mathbf{F}_j$ is the $n \times m$ Jacobian matrix and $\mathbf{u}$ is a $m \times 1$ vector), instead of computing it directly, the method finds an approximation to its accurate form using a first-order Taylor series:

$$f\left(\mathbf{s}_j + \frac{\delta\|\mathbf{s}_j\|}{\|\mathbf{u}\|}\mathbf{u}\right) = f(\mathbf{s}_j) + \frac{\delta\|\mathbf{s}_j\|}{\|\mathbf{u}\|}\mathbf{F}_j\mathbf{u} + \sigma(\delta^2) \quad (10)$$

$$\mathbf{F}_j\mathbf{u} \approx \frac{\|\mathbf{u}\|}{\delta\|\mathbf{s}_j\|}\left[f\left(\mathbf{s}_j + \frac{\delta\|\mathbf{s}_j\|}{\|\mathbf{u}\|}\mathbf{u}\right) - f(\mathbf{s}_j)\right] \quad (11)$$

where δ is a finite-difference interval and $\|\mathbf{u}\|$ and $\|\mathbf{s}_j\|$ are the norm of the vectors $\mathbf{u}$ and $\mathbf{s}_j$.

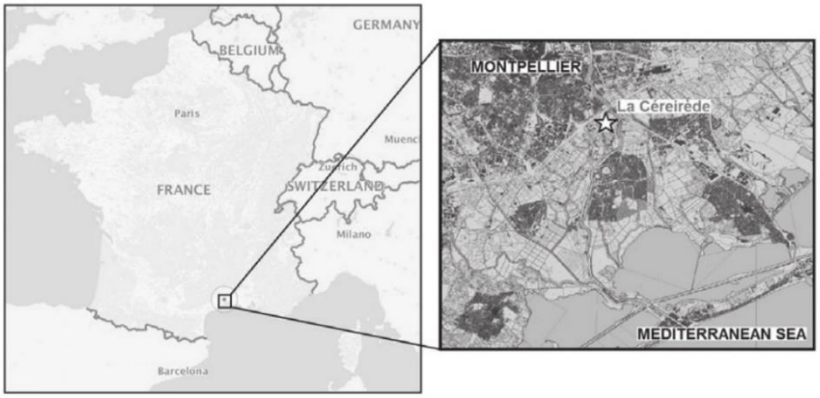

Figure 1. Location of the studied experimental site "La Céreirède" (map and aerial photography from geoportail.fr) occupying an area of 720 m^2. It is situated in the South of France, near the town of Montpellier and the Mediterranean Sea.

Thus, in the matrix system (Equation 6) of the GA algorithm the calculation of the full Jacobian $\mathbf{F}$ is avoided by approximating the computation of $\mathbf{F}_j\mathbf{s}_j$, $\mathbf{F}_j\mathbf{X}$, $\mathbf{F}_j\mathbf{Q}\mathbf{F}_j^{\mathrm{T}}$ and $\mathbf{Q}\mathbf{F}_j^{\mathrm{T}}$ with (Kitanidis and Lee 2014):

$$\mathbf{F}_j\mathbf{s}_j = \frac{1}{\delta}\left[f\left(\mathbf{s}_j + \delta\mathbf{s}_j\right) - f\left(\mathbf{s}_j\right)\right] \tag{12}$$

$$\mathbf{F}_j\mathbf{X}_i = \frac{\|\mathbf{X}_i\|}{\delta\|\mathbf{s}_j\|}\left[f\left(\mathbf{s}_j + \frac{\delta\|\mathbf{s}_j\|}{\|\mathbf{X}_i\|}\mathbf{X}_i\right) - f\left(\mathbf{s}_j\right)\right] \quad \text{with } \boldsymbol{X}_i \text{ the } \boldsymbol{i}\text{th column of } \boldsymbol{X} \tag{13}$$

$$\mathbf{F}_j\mathbf{Q}\mathbf{F}_j^{\mathrm{T}} \approx \mathbf{F}_j\mathbf{Q}_K\mathbf{F}_j^{\mathrm{T}} = \mathbf{F}_j\sum_{i=1}^{K}\boldsymbol{\zeta}_i\boldsymbol{\zeta}_i^{\mathrm{T}}\mathbf{F}_j^{\mathrm{T}} = \sum_{i=1}^{K}\left(\mathbf{F}_j\boldsymbol{\zeta}_i\right)\left(\mathbf{F}_j\boldsymbol{\zeta}_i\right)^{\mathrm{T}} = \sum_{i=1}^{K}\boldsymbol{\eta}_i\boldsymbol{\eta}_i^{\mathrm{T}} \tag{14}$$

$$\mathbf{Q}\mathbf{F}_j^{\mathrm{T}} \approx \mathbf{Q}_K\mathbf{F}_j^{\mathrm{T}} = \sum_{i=1}^{K}\boldsymbol{\zeta}_i\boldsymbol{\zeta}_i^{\mathrm{T}}\mathbf{F}_j^{\mathrm{T}} = \sum_{i=1}^{K}\boldsymbol{\zeta}_i\left(\mathbf{F}_j\boldsymbol{\zeta}_i\right)^{\mathrm{T}} = \sum_{i=1}^{K}\boldsymbol{\zeta}_i\boldsymbol{\eta}_i^{\mathrm{T}} \tag{15}$$

where $\boldsymbol{\eta}_i = \mathbf{F}_j\boldsymbol{\zeta}_i = \frac{\|\boldsymbol{\zeta}_i\|}{\delta\|\mathbf{s}_j\|}\left[f\left(\mathbf{s}_j + \frac{\delta\|\mathbf{s}_j\|}{\|\boldsymbol{\zeta}_i\|}\boldsymbol{\zeta}_i\right) - f\left(\mathbf{s}_j\right)\right]$.

If we now consider the number of forward model evaluations needed per iteration for the calculation of the Jacobian matrix, there are $K + p + 2$ runs. One run is needed for evaluating $f\left(\mathbf{s}_j\right)$, one is needed for assessing $f\left(\mathbf{s} + \delta\mathbf{s}_j\right)$, K runs are needed for calculating $\boldsymbol{\eta}_i$ and p runs are needed for computing $\mathbf{X}_i$. It can be observed that, with this method, the number of forward model runs per iteration is no longer dependent on m or n. Hence, the number of parameters and observed data can increase without increasing the run time of the algorithm. However, if the number of parameter increases, the low-rank approximation order K might also need to be increased slightly in order to maintain a small truncation error for $\mathbf{Q}_K$.

The algorithm iteratively updates the parameters set in Equation 5 by solving the matrix system of Equation 6 with the PCGA approximations until the optimum $\hat{\mathbf{s}} = \mathbf{s}_{\mathrm{post}}$ is achieved, that is, the objective function has iteratively converged to a local minimum.

Application to an Experimental Site

We have applied the PCGA large-scale method as presented in the previous part to an experimental site, named "la Céreirède." The field site is located in Montpellier in the South of France, on the alluvium of the Lez river, which flows toward the Mediterranean Sea a few kilometers downstream (Figure 1).

At the field site, the alluvial deposit is composed of a 12-m thick formation of unconsolidated sands and silts lying on a 2-m thick layer of pebbles and gravels. Beneath these Quaternary formations, there exist clayey sands of the Pliocene, marls of the Miocene, and limestone of the Jurassic (Figure 2). Three porous aquifer formations have been characterized in this site:

- a low permeability aquifer in the upper part of the alluvium (unconsolidated sands and silts),
- a semi-confined aquifer in the pebbles and gravel,
- a semi-confined to confined aquifer in the clayey sands of Pliocene.

The field site comprises 12 wells which fully penetrate the three aforementioned aquifers in an area of 36×20 m^2 (Figure 3). The hydraulic data were collected by performing two pumping tests in PZ 2 (5 L/min), and in PZ 11 (5 L/min), respectively, while measuring hydraulic head variations in the other 10 wells. The pumping was performed at the depth of the pebbles and gravel layer, which is the most productive aquifer, because its transmissivity is considerably higher than the

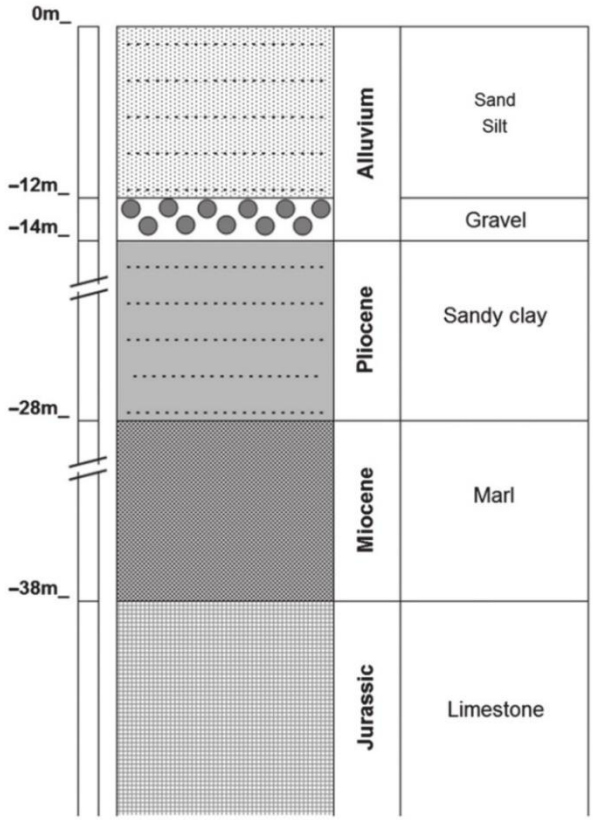

Figure 2. Schematic geological section of the experimental site "La Céreirède." Three aquifers formations have been characterized in the sands and silts alluvium, in the gravels and in the clayey sands.

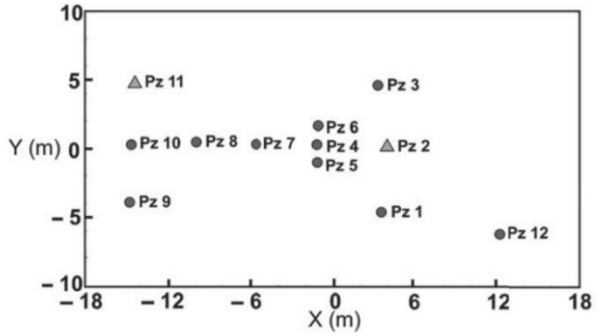

Figure 3. Well pattern on the experimental site "La Céréirède" (circles represent the 10 measurement wells and triangles represent the 2 pumping wells). As Hydraulic drawdowns in the pumping wells are not measured, the tomography provided 20 observed data.

Table 1
Values of Variables Used to Perform the PCGA Inversion on a Model of the Site for 25,600 Parameters and 20 Observed Data. Results of This Inversion Are Shown in Figures 4 and 5

Geometry	$X\ (m) = [-18, 18]$; $Y\ (m) = [-10, 10]$
Grid (number of parameters)	160×160 cells
Uncertainty on data	$\sigma = 0.001$ m; $\mathbf{R} = \sigma.Id\ (n)$
Experimental variogram function	$Var\ (\text{distance}) = 0.11 \times \left[1 - exp\left(-\frac{\text{distance}}{8}\right)\right]$
Finite-difference step	$\delta = 10^{-5}$

transmissivities in silts and clayed sands. We considered that the contribution of the two others aquifers to the water pumped is negligible compared to the contribution from the pebbles and gravel aquifer. From a classic hydrogeological analysis of the soil of each well, we could also estimate values of the field transmissivity at these points. Using these punctual values of transmissivities and their positions in the field as input in a MATLAB variogram routine ("variogramfit" by W. Schwanghart), we were able to obtain the transmissivity field variogram function, which will be used in the inversion algorithm to create the covariance matrix **Q** (Table 1). The variogram function is of type exponential with a sill of 0.11 and a range of 8 m.

The PCGA inversion algorithm was implemented in MATLAB and connected to the flow modeling software COMSOL Multiphysics, which solves the forward problem. The inversion algorithm performs, at the end of each iteration, a linear minimum research ("fminsearch" MATLAB function) to accelerate the convergence of Equation 3 to a local minima.

The 2-D flow model is discretized as a grid of $\sqrt{m} \times \sqrt{m}$ transmissivity cells in a rectangular zone. This local model is enclosed by a larger buffer zone of 100×100 m^2 with a constant transmissivity of 10^{-5} m^2/s (average value of locally estimated transmissivities at the field site) and a 0 m constant head condition at the boundaries (no drawdown induced by the pumping wells). This buffer zone was set up in order to minimize the impact of the boundary conditions. The flow simulations were performed under steady-state conditions. The inversion of the model is set up using the 2×10 drawdown observed during the pumping tests (10 measurement wells for each of the 2 pumping tests) representing the observed data in the inversion algorithm. The inversion aims to reconstruct the spatially varying T distribution in the local region producing the observational data set.

Results

We have applied the PCGA to assess the equivalent transmissivity field of the multi-layered aquifer at the Céreirède field site. The most transmissive part of the aquifer is the pebbles and gravels part, but the alluvium and the clayey sands might also be the cause of some variations in the estimated equivalent transmissivity field. The inputs to the inversion models are given in Table 1.

The inversions were performed on a uniform fine-scale discretization grid (160×160). A constant initial transmissivity field was considered in the inverse models. The Kth order of truncation for the covariance matrix **Q**

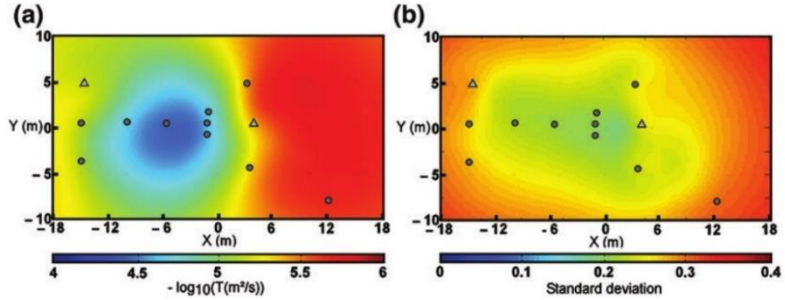

Figure 4. Maps of the log-transmissivity (a, on the left) and parameter's a posteriori standard deviation (b, on the right) for a PCGA inversion method with 25,600 parameters, 20 observed data and a covariance matrix decomposition of order $K = 128$ applied to the experimental site. The transmissivities vary around a mean of 10^{-5} m²/s which is consistent with transmissivity values estimated from pumping test analysis. The aquifer is less transmissive in the eastern part and more in the western part especially in a zone around PZ 7 (see Figure 3). But we got a better precision in zones with more information: at the center and the western part of the map, while in the eastern part where we did not have piezometers, the results show a larger standard deviation.

was selected such that the first truncated singular value of the matrix (the low-rank approximation error) fall below 1. This corresponds to an order of $K = 128$. We will show that this choice of truncation order is acceptable and allows the significant information about the prior model structure to be preserved. The low-rank covariance matrix was calculated and then imported to the inversion algorithm. The parallelized computation of the low-rank decomposition takes only a few minutes (it even takes less than 1 min with a 32 cores parallelization). The inversion then converged in 2 h 45 min on an Intel Xeon QuadCore 2.8GHz with 12Go RAM.

The results from the inversion are shown in Figures 4 and 5. First, from the distribution of model parameters (given as negative log transmissivity in Figure 4), it can be seen that the value of the inverted transmissivity takes the mean value 10^{-5} m²/s, which is the mean of the transmissivity measurements on the site. A clear contrast in T is observed between the two regions on the east and west sides of boreholes PZ1, PZ2, and PZ3. Overall, the eastern part which is closer to the Lez river, is slightly less transmissive than the western part (T are approximately 2×10^{-6} m²/s and 1×10^{-5} m²/s, respectively). An area with a highest T (3×10^{-5} m²/s) is also highlighted within the western part, around PZ 7. But it has to be noticed that the boreholes and pumping wells are not homogeneously distributed over the site, thus some parts of the site (especially on the eastern side) might give more uncertain results. Therefore, it is interesting to estimate the values of the transmissivity field uncertainties.

Figure 4b presents a map of the uncertainty for each parameter value (given by the diagonal entries of the posterior covariance matrix $\mathbf{Q}_{\text{post}}$). The standard deviation for the log-transmissivity varies between 0.2 for the parameter cells near the investigation wells, and 0.33 in both the area with very few information and close to the model's boundaries. In particular, the uncertainty in the eastern part, where the number of wells is small, is much higher.

Good correlations between the calculated and measured hydraulic heads were obtained (Figure 5). The root

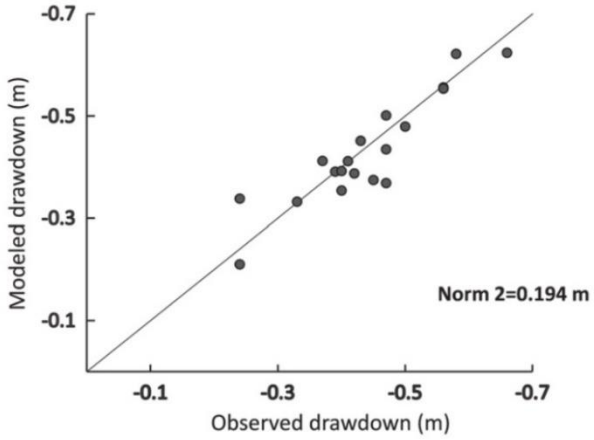

Figure 5. Graph showing the differences between the 20 observed drawdowns and modeled drawdowns after convergence of a PCGA inversion method with 25,600 parameters and a covariance matrix decomposition of order $K = 128$ applied to the experimental site. The drawdowns are globally well reproduced.

mean square error calculated at the end of the inversion was computed as 0.194 m. The hydraulic heads with the most significant difference between the inverted and the measured values are observed on PZ1 and PZ9.

It is clear that the PCGA method is reliable for the modeling of the porous aquifer considered in this work because it produces a set of good inversion results with a high resolution (each cell represents a rectangle of 22.5cm × 12.5 cm on the site) from a few measurements (20 observed data for 720 m²) in less than 3 h. However, the main problem of this method is that the SVD of the covariance matrix needs a considerably large amount of time and memory. The computational demands increase squarely with the number of model parameters, m. In this work, the decomposition was only performed once before the inversion, and the resulting low-rank covariance matrix was used at all iteration steps throughout the inversion (i.e., the variogram function remaining the same). Otherwise, if a variable variogram model is desired

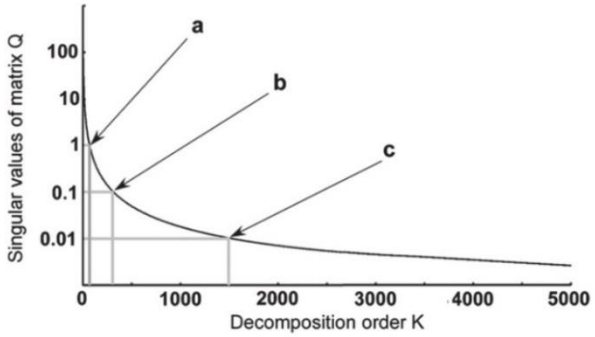

Figure 6. Covariance matrix singular values decrement curve for 10,000 parameters. Three decomposition order (a to c) corresponding to truncation error of 1, 0.1, and 0.01 have been chosen for the results comparison of the PCGA inversion method (see Figure 7).

at different iteration steps, the computation of the covariance matrix decomposition can also be accelerated by specific linear algebra methods (FFT, FMM, and H-matrices) and a parallelization on several cores to achieve a reasonable computational time (Lee and Kitanidis 2014).

Comparison of Results between PCGA Simulations with Different Decomposition Order, and between PCGA and GA Simulations

In addition to the PCGA experimental application presented above, several other inversions were also conducted for the same field site but with a smaller number of parameters and using different methods for the computation of sensitivity matrix (input for each inversion is shown in Table 1). These numerical experiments allows us to compare (1) the results from PCGA with varied low-rank truncation K and (2) the results from PCGA to those obtained from the GA method with a first-order finite-difference Jacobian matrix computation, and an adjoint-state Jabobian matrix computation (the integral was solved using the Gauss-Legendre quadratic method as described in Soueid Ahmed et al. 2014) The inversion results are compared with respect to the total computation time and relative accuracy of the results.

Comparison of Inversion Results for Using Different Decomposition Order

First, we assess the effect of the chosen truncation order for the covariance matrix. Three PCGA inversions, with 10,000 parameters and using different K-order truncations of the covariance matrix corresponding to singular values (truncation errors) of $\lambda_{K+1} \simeq 1$ ($K = 69$), $\lambda_{K+1} \simeq 0.1$ ($K = 313$) and $\lambda_{K+1} \simeq 0.01$ ($K = 1532$), were performed. Figure 6 shows a relationship between the singular value and the truncation order, on which the position of the three K orders that were adopted in our inversions are indicated. Figure 7 shows the results obtained from these inversions. Note that very similar T fields (e.g., similar trend and location of high T zones) were obtained from the inversions using different truncation order. Therefore, the influence of reducing the

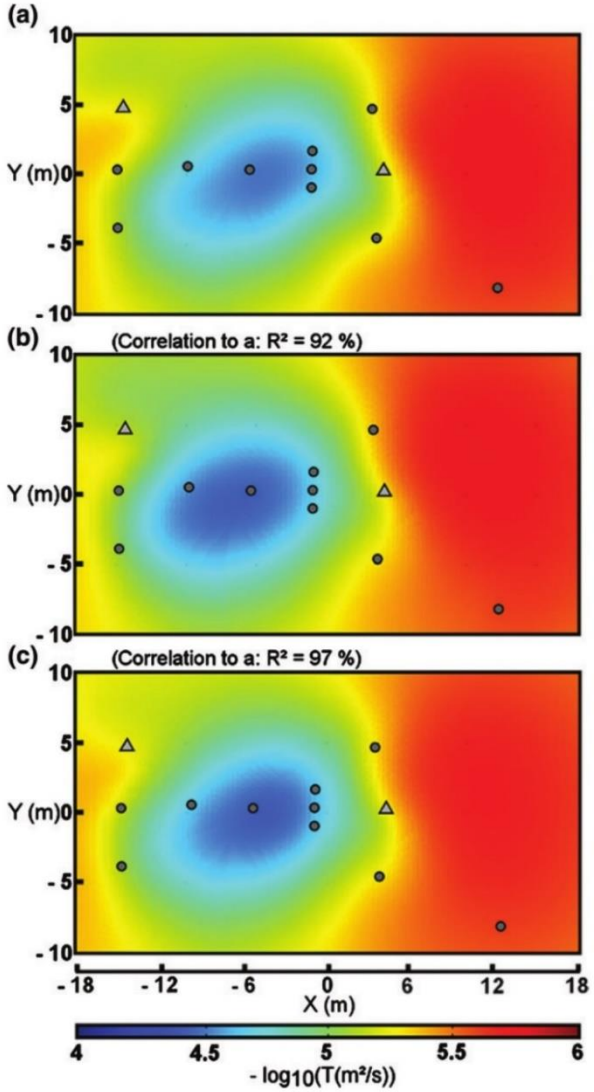

Figure 7. Maps of the log-transmissivity for a PCGA inversion method with 10,000 parameters, 20 observed data and three different covariance matrix decomposition applied to the experimental site. The map (a) was obtained for $K = 69$, the map (b) for $K = 313$ and the map (c) for $K = 1532$ (see Figure 6). The results obtained for these three decomposition are relatively the same (same transmissivity values, same zones) so, for this site, there is no significant loss of information when using a truncation order corresponding to an error of 1 (map (a)) for the covariance matrix which allows us to reduce the computation time of the inversion without decreasing the accuracy of the results.

K-order, as long as the truncation error is below 1, on the inversion results is mild. The most information regarding the spatial structure of the prior model is preserved in its first few singular values, so it is acceptable to consider a truncation order for a truncation error $\lambda_{K+1} \simeq 1$ for the covariance matrix.

PCGA and GA Results Comparison

In this section, we compare the inversion results obtained for the PCGA method using an approximated $\mathbf{Q}$ matrix, with those of the GA method using two different

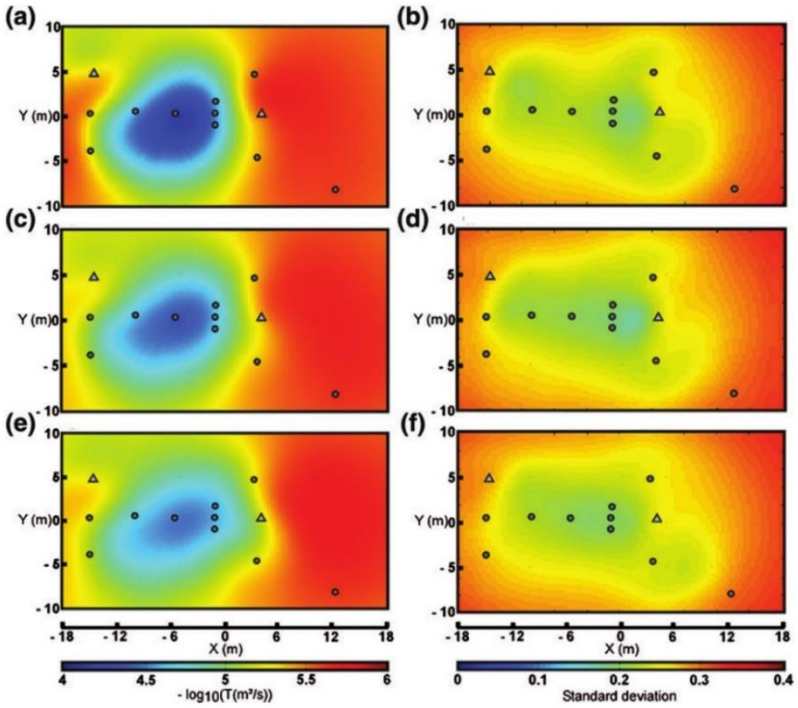

Figure 8. Maps of the log-transmissivity (a, c, e) and parameter's a posteriori standard deviation (b, d, f) for three different inversion methods with 10,000 parameters and 20 observed data applied to the experimental site. The maps (a) and (b) were obtained with the GA-adjoint-state method, the maps (c) and (d) with the GA-finite-difference method and the maps (e) and (f) with the PCGA method with a covariance matrix decomposition of order $K = 69$. The three methods provide relatively the same results for this site. The GA-adjoint-state method leads to a better data matching (see Figure 9) due to its slightly higher contrast of transmissivity distribution, but regarding the calculation time the PCGA inversion is much more efficient (see Table 2).

methods for Jacobian matrix computation (i.e., the finite-difference and adjoint-state methods), where the entirety of the **Q** matrix were used. All the inverse simulations were performed on a 100 × 100 grid. Figure 8 shows the inverted transmissivity distributions and the corresponding distributions of standard deviation of each model parameter. It can be seen that in the three transmissivity fields, the calculated T value for each cell varies around the mean 10^{-5} m^2/s. In general, the three approaches produced similar spatial distribution of the transmissivity; however, the range of the inverted transmissivities from the GA-adjoint-state method (i.e., 2×10^{-6} to 1×10^{-4} m^2/s) is larger than that of the PCGA and that of the GA-finite-difference method (i.e., 2×10^{-6} to 3×10^{-5} m^2/s). Since the PCGA method is based on a finite-difference matrix vector product approximation, it is expected to obtain a similar parameter range from this method and the GA-finite-difference method. The difference between the results from these two methods and the GA-adjoint-state method may come from the definition of the finite-difference step δ. In addition, the resolved transmissivity field from PCGA is smoother compared to that from the method where an adjoint-state method is used to compute the sensitivity matrix. This is caused by the low-rank truncation in PCGA and also the finite-difference approach, which tends to reduce the heterogeneity of the inverted T field.

The spatial distributions of the standard deviation of the inverted parameters are shown in Figure 8. For each method, the uncertainty of the reconstruction is mainly dependent on the number and position of the wells. The correlation between inverted and measured hydraulic head data for the three inversion models are shown in the cross-plots of Figure 9. It can be seen that, with the same inversion inputs, the GA-adjoint-state method generated a slightly better correlation compared to the other two methods, which is reflected by the smaller RMSE values (0.165 m compared to 0.182 and 0.188 m). The performance of the three methods in terms of simulation time is compared in Table 2.

A significant reduction in computational time is observed for the GA-adjoint-state method compared to the GA-finite-difference method (Table 3). This reduction is mainly related to the calculation of the Jacobian sensitivity matrix (Cardiff and Kitanidis 2008). As the grid discretization increases, the significance of reduction in computational time of the GA-adjoint-state method compared to the GA-finite-difference-based method become more apparent. However, an even more significant time reduction was observed in using the PCGA method. Note that in Table 3 the computation time for PCGA includes the time from both the covariance matrix decomposition and the inversion calculation. The computational time of PCGA is observed to be 10

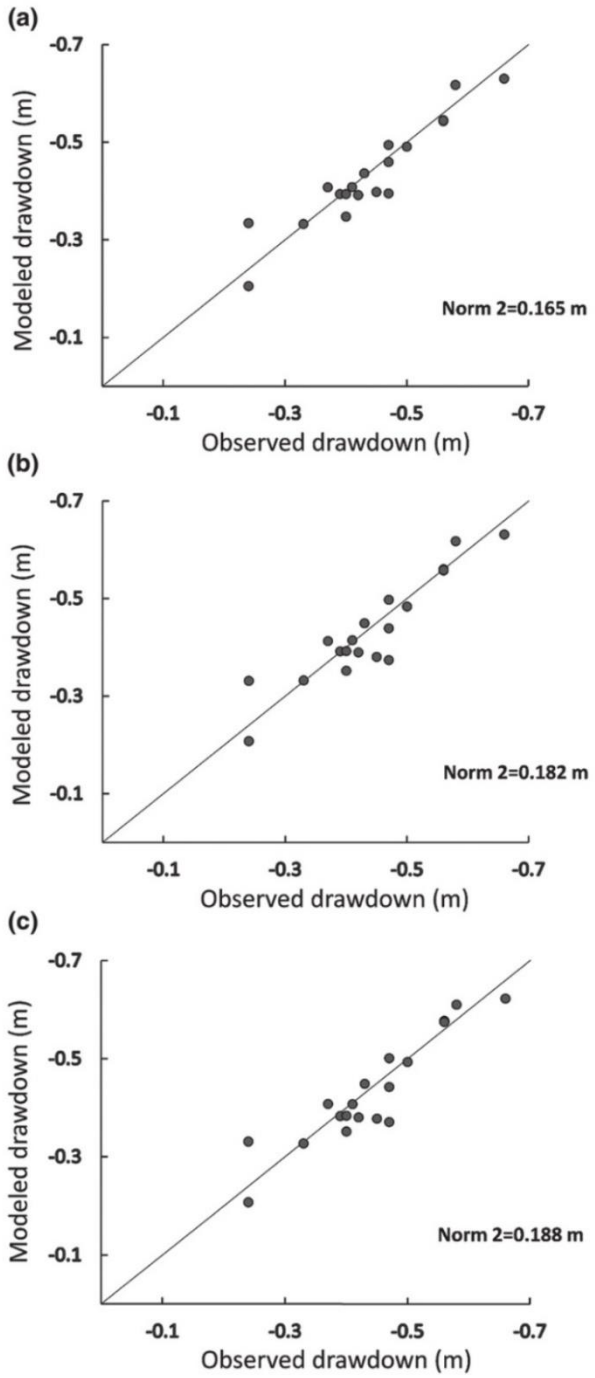

Figure 9. Graphs showing the differences between the 20 observed drawdowns and modeled drawdowns after convergence of three different inversion methods with 10,000 parameters applied to the experimental site. The graph (a) was obtained with the GA-adjoint-state method, the graph (b) with the GA-finite-difference method, and the graph (c) with the PCGA method with a covariance matrix decomposition of order $K = 69$. Regarding the mathematical norm 2 the GA-adjoint-state method has a slightly better convergence on the data than the other methods but the PCGA inversion method is much more efficient for the calculation time (see Table 2).

Table 2

Comparison of the Efficiency between Three Algorithm of Geostatistical Inversion Methods (GA-Adjoint-State, GA-Finite-Difference, and PCGA) on a Same Under-Determined Modeling. Results of These Inversions Are Shown in Figures 8 and 9. The Convergence on Data Was Slightly Better for an Adjoint-State Method but the Calculation Time Was Considerably Reduced by Using a PCGA Method

	GA-Adjoint-State Method	GA-Finite-Difference Method	PCGA Method (Truncation Order $K = 69$)
Number of parameters	100 × 100	100 × 100	100 × 100
Computation time	10 h 43 min	72 h 10 min	1 h 33 min
Value of objective functionto be minimized after convergence	23.0602	26.6526	27.4641
ℓ_2-norm between observed and modeled data	0.165 m	0.182 m	0.188 m

Table 3

Convergence Times for Different Methods Using Different Grid Sizes. An Intel Xeon QuadCore 2.8GHz with 12Go RAM Has Been Used to Perform the Computations. The PCGA Method (with a Truncation Error of Approximately 1) Is Always the Fastest because It Involves Less Forward Problems than the GA-Finite-Difference Method and That the Gauss-Legendre Resolution of the Integral in the GA-Adjoint-State Method Requires a Calculation of a Number of Nodes Proportional to the Number of Cells in the Grid in Each Forward Problem

Grid Resolution	GA-Adjoint-State Method	GA-Finite-Difference Method	PCGA Method (Truncation Error $\lambda_{K+1} \simeq 1$)
10 × 10	5 min	16 min	1 min
30 × 30	9 min	1 h 40 min	3 min
50 × 50	45 min	8 h 21 min	6 min
80 × 80	3 h 19 min	41 h 44 min	29 min
100 × 100	10 h 43 min	72 h 10 min	1 h 33 min

times less than that of the GA-adjoint-state method and 70 times less than that of the GA-finite-difference method. Altogether, the advantage of PCGA in obtaining a fast solution without compromising the inversion quality makes it a promising candidate in solving large-scale inversion problems.

Conclusion

The GA-finite-difference method is useful and straightforward for inversions with a few parameters and a large number of observational data. In contrast, the GA-adjoint-state method is advantageous in dealing with inversion models with a few observational data but a relatively large parameters set. On the contrary, the PCGA is an efficient method for both cases. It is also helpful for extremely under-determined problems where a large number of unknown parameters is present. In fact, the time and memory required by this method to perform the iterative process of the inversion is less sensitive to the number of parameters or measurements, but more dependent on the approximation order of the covariance matrix chosen by the modeler. A higher order approximation will lead to higher computational costs but the error introduced in the inversions will be much smaller.

The comparison of different methodologies has shown that PCGA approach appears to be the most efficient strategy for carrying out large-scale inversions in porous aquifers. We noticed that, in the studied case, the errors introduced by the approximation in the PCGA methods were not significant. Thus, we obtained the same accuracy in results from the PCGA inverse modeling compared to the GA inverse modeling. Thereby, with this strategy, only the principal components of the covariance matrix are kept in the inversion process, and the computational and memory costs necessary for the inversion algorithm are optimized. Additionally, the PCGA method significantly reduces the computational time. With the PCGA method we divided the computation time by seven compared to the GA-adjoint-state method, and by 50 compared to the GA-finite-difference method.

In summary, by applying the PCGA for a hydraulic tomography in a porous aquifer, we found an especially adapted strategy, which produces accurate inversion results with a good resolution in a reduced time, and which manages optimally the computer memory involved in the inversion algorithm. Nevertheless, the PCGA method is efficient specifically for models with a smooth distribution of the targeted parameters (which could typically be used for a good average representation of porous aquifers) so that the covariance matrix can be approximated by much smaller matrices.

Acknowledgments

We would like to thanks Pr. Michael Cardiff and two others anonymous reviewers for their relevant comments on this article. We also thank the region Normandy for financially supporting the PhD of Pierre Fischer.

References

Ambikasaran, S., J.Y. Li, P.K. Kitanidis, and E. Darve. 2013. Large-scale stochastic linear inversion using hierarchical matrices. *Computers & Geosciences* 17: 913–927.

Berg, S.J., and W.A. Illman. 2013. Field study of subsurface heterogeneity with steady-state hydraulic tomography. *Groundwater* 51, no. 1: 29–40.

Cardiff, M., and P.K. Kitanidis. 2008. Efficient solution of nonlinear, underdetermined inverse problems with a generalized PDE model. *Computers & Geosciences* 34: 1480–1491.

Cardiff, M., W. Barrash, P.K. Kitanidis, B. Malama, A. Revil, S. Straface, and E. Rizzo. 2009. A potential-based inversion of unconfined steady-state hydraulic tomography. *Groundwater* 47, no. 2: 259–270.

Cardiff, M., W. Barrash, and P.K. Kitanidis. 2013. Hydraulic conductivity imaging from 3-D transient hydraulic tomography at several pumping/observation densities. *Water Resources Research* 49: 7311–7326.

Carrera, J., and S.P. Neuman. 1986a. Estimation of aquifer parameters under transient and steady state conditions: 1. Maximum likelihood method incorporating prior information. *Water Resources Research* 22, no. 2: 199–210.

Carrera, J., and S.P. Neuman. 1986b. Estimation of aquifer parameters under transient and steady state conditions: 3. Application to synthetic and field data. *Water Resources Research* 22, no. 2: 228–242.

Elsheikh, A.H., M.F. Wheeler, and I. Hoteit. 2014. Hybrid nested sampling algorithm for Bayesian model selection applied to inverse subsurface flow problems. *Journal of Computational Physics* 258: 319–337.

Greengard, L., and V. Rokhlin. 1987. A fast algorithm for particle simulations. *Journal of Computational Physics* 73, no. 2: 325–348.

Hackbusch, W., and S. Börm. 2002. Data-sparse approximation by adaptive $\mathcal{H}^2$-matrices. *Computing* 69, no. 1: 1–35.

Halko, N., P.G. Martinsson, and J.A. Tropp. 2011. Finding structure with randomness: probabilistic algorithms for constructing approximate matrix decompositions. *SIAM Review* 53, no. 2: 217–288.

Hoeksema, R.J., and P.K. Kitanidis. 1984. An application of the geostatistical approach to the inverse problem in two-dimensional groundwater modeling. *Water Resources Research* 20, no. 7: 1003–1020.

Kitanidis, P.K. 1995. Quasi-linear geostatistical theory for inversing. *Water Resources Research* 31, no. 10: 2411–2419.

Kitanidis, P.K., and J. Lee. 2014. Principal component geostatistical approach for large-dimensional inverse problem. *Water Resources Research* 50, no. 7: 5428–5443.

Kitanidis, P.K., and E.G. Vomvoris. 1983. A geostatistical approach to the inverse problem in groundwater modeling (steady state) and one-dimensional simulations. *Water Resources Research* 19, no. 3: 677–690.

Lee, J., and P.K. Kitanidis. 2014. Large-scale hydraulic tomography and joint inversion of head and tracer data using the principal component geostatistical approach (PCGA). *Water Resources Research* 50, no. 7: 5410–5427.

Lieberman, C., K. Fidkowski, K. Willcox, and B. van Bloemen Waanders. 2013. Hessian-based model reduction: large-scale inversion and prediction. *International Journal for Numerical Methods in Fluids* 71: 135–150.

Liu, X., Q. Zhou, P.K. Kitanidis, and J.T. Birkholzer. 2014. Fast iterative implementation of large-scale nonlinear geostatistical inverse modeling. *Water Resources Research* 50: 198–207.